Direct Integration and Interface Studies of 2D Materials and Dielectric Oxide Films

---

A
Dissertation
Presented to
the faculty of the School of Engineering and Applied Science
University of Virginia

---

in partial fulfillment
of the requirements for the degree

Doctor of Philosophy in
Materials Science and Engineering

by

Maria Gabriela Sales

August 2023

APPROVAL SHEET

This
Dissertation
is submitted in partial fulfillment of the requirements
for the degree of

Doctor of Philosophy

Author: Maria Gabriela Sales

Advisor: Stephen McDonnell

Committee Member: Jon Ihlefeld

Committee Member: Petra Reinke

Committee Member: Gaurav Giri

Committee Member: Sina Najmaei

Accepted for the School of Engineering and Applied Science:

Jennifer L. West, School of Engineering and Applied Science
August 2023

Abstract

The mechanism of how any electronic device works relies on the intrinsic properties of the material layers that comprise the stack and the interfaces between them. In this work, we focus on studying the integration and properties of oxide/semiconductor interfaces for emerging field-effect transistor (FET) device architectures, specifically those used for memory and data storage. The materials that we focus our investigations on are HfO_2 as the gate oxide, and 2D transition metal dichalcogenides (TMDCs) as the semiconducting channel.

Since the 2000's, HfO_2 has been established as an alternative linear dielectric material to SiO_2, as it allows for dielectric layers that avoid leakage without sacrificing capacitance and device performance. Furthermore, in 2011, HfO_2 was found to possess ferroelectricity in the thin film geometry, making it attractive for use in scaled memory devices, such as ferroelectric FETs (FeFETs). In this work, we interface HfO_2 thin films with semiconducting TMDCs, which have amassed wide research interest due to their unique and versatile physical and electronic properties. TMDCs, with chemical formula MX_2, are a class of 2D materials, in which X-M-X stacks form strongly bonded layers in-plane, which are held in the out-of-plane direction by weak van der Waals forces. Due to their van der Waals nature, TMDCs are stable at atomic-scale thicknesses, which allows device scalability, and are free of surface dangling bonds, which offers the promise of high-quality interfaces when applied to a device. However, as we demonstrate through in-depth spectroscopic studies of commercial TMDC single-crystals used by most of the 2D materials community, these single-crystal flakes suffer from high impurity concentrations which would impact their promising material and electronic properties. This necessitates methods for direct growth and integration of these TMDCs that allow for proper control of material properties.

Through direct integration studies, we aim to investigate and engineer the interface chemistry of semiconducting 2D TMDCs with dielectric and ferroelectric HfO_2-based films, and to correlate this interface chemistry with the functional properties of FETs. Specifically, we have the following design schemes: 1) TMDC-on-Dielectric, where TMDCs are grown directly onto dielectrics by molecular beam epitaxy (MBE), and 2) Dielectric-on-TMDC, where we investigate interfaces formed by the deposition of dielectrics and ferroelectrics onto semiconducting TMDCs by atomic layer deposition (ALD). All of this work is carried out with the goal of providing fundamental insights into how device performance relates to processing and interface chemistry so that intelligent device optimization can be achieved.

To Tito Dondo, the original and arguably more practical doctor in the family.

You are so loved and incredibly missed.

Acknowledgements

My first acknowledgement goes to my advisor, Professor Stephen McDonnell, for the innumerable ways he has been the best mentor I could have asked for throughout this PhD journey. Anything I have accomplished in graduate school was in large part because of his constant guidance, encouragement, and enormous belief in me. Stephen, I am forever indebted for everything I have learned from you, and know that I will carry these with me in every step of my career. Thank you for your mentorship and for setting an example of what it means to be an effective researcher and scientist, both in and out of the lab.

The work presented in this dissertation would not have been possible without the help of numerous collaborators whom I have had the pleasure and privilege of working with. It is impossible to name all of these intelligent scientists, students, and professors, but I would be remiss not to give a few special thanks. To the Nano Team at ARL, especially to Dr. Sina Najmaei, Dr. Alex Mazzoni, Dr. Wendy Sarney, and Seth Pearson, thank you for all of your valuable contributions, helpful discussions, and fun company whenever I would visit ARL. To Sina, thank you for believing in me and trusting me to be part of the NeuroPipe project, which has been a key factor in allowing me to finish my research and this dissertation. To Professor Jon Ihlefeld and his research group, especially Dr. Shelby Fields and Sam Jaszewski, thank you very much for your countless contributions in the early parts of this work. Our work together has been really impactful to me and the trajectory of my research, so thank you for introducing me to the HfO_2 world. And to every collaborator/co-author I have worked on projects with, professors I have TA'ed for, professors I have taken classes from, NMCF staff who have trained me with equipment and greatly helped with my research, and members of the MSE UVA community, thank you for everything. My experiences with each and every one of you has definitely helped shape me into the scientist that I am today, so for that, I extend my sincerest thanks.

I have so much gratitude for the members of the McDonnell group, whom I have shared the good, the bad, and the ugly with. And through it all, these people have turned from co-workers/labmates to really good friends. Keren, thank you for being a mentor, friend, and confidante literally since the very first day I set foot in Wilsdorf Hall, unaware of the journey that was to come. Your insights and wisdom, both in science and life in general, are always incredibly thoughtful and genuinely helpful. Peter, though you may not believe me when I say this, I will always be thankful that I ended up sitting next to you in that basement office through most of grad

school. Whether questions about UHV, cars, or everything in between, thank you for being a reliable go-to colleague and friend. Gaby, thank you for being patient with all my daily rants and unsolicited grad school advice. It's been awesome to have someone I can easily talk to about Filipino and women-in-STEM things. And of course, thank you for being my UHV troubleshooting partner-in-crime. Lee, thank you for being someone I can count on to give me a boost of positivity, especially when it is most needed, whether in the form of cheese, desserts, or funny videos. Your thoughtfulness definitely does not go unnoticed. Victor, thank you for being a trusty and smart voice of reason for me. You have been a really dependable labmate and advice-giver, be it for small stuff like choosing colors on Origin, to bigger stuff like choosing career paths. I am very thankful that in this lab group, I have met some of the best people to work, laugh, celebrate wins, and learn from failure with, day in and day out.

I have been lucky to form many treasured friendships throughout my time in Charlottesville. Having these people by my side made this challenging journey less so, and made the struggles easier to take on. Luke, Jonathan, Rebecca, Pedro, Carolina, Anna, Katie, thank you for all the fun adventures and fond memories through all these years. From sunrise hikes to wine nights, beaches in the summer to mountains in the fall, thank you for being my source of solace through the ups and downs of grad school. Peter, Adrian, Eli, thank you for the pizza sharing, the coffee drinking, and all the serious and silly conversations in between. Your support through these crazy times was always felt from near or far. And to Will, thank you for being my rock. Thank you for your unwavering support, immense patience, goofiness, and calm amidst the chaos.

Last but not the least, literally, I would like to thank my crazy big family. My relatives, titos, titas, who, despite being in every corner of the world, are incredibly supportive of everything I try to do in life. I have also had several homes away from home in the form of my cousins who lived in the same state. To Ate Michelle, Kuya Kong, Ate Kim, Ate Macy, and Patrick, thank you for always being welcoming of me visiting and hanging out whenever I needed it; I feel very fortunate to have had you all close by. To my siblings, Pepe, Ado, and Raya, thank you for always being supportive and so helpful. I look at you guys sometimes and ponder how it's possible that I am the oldest, yet you are all smarter and show more maturity than me at times. And finally, Mama and Tatay, I have way too much to thank you for. Thank you for all the opportunities you have provided me that led me to this path. Thank you for surrounding me with love and encouragement, which is what I lean on with every challenge I face. I could not have done any of this without you.

Table of Contents

List of Tables

List of Figures

1 Introduction

1.1 Background and Motivation

The 2020 International Roadmap for Devices and Systems (IRDS) [1] More Moore targets for node scaling every 2-3 years are based on "PPAC" – performance, power, area, and cost. Specifically, these targets are: >15% more operating frequency at scaled supply voltage (performance), >30% less energy per switching at a given performance (power), >30% less chip area footprint (area), and <30% more wafer cost (cost). These scaling targets in the IRDS are the industry drivers for materials and process innovation for logic and memory devices. Such technological advancements that are expected to come from the IRDS targets include alternative high-κ gate dielectrics, alternative high-mobility channel materials, new device architectures, and new integration schemes. Shown in Figure 1.1 is the IRDS More Moore roadmap's projected evolution of device architectures.

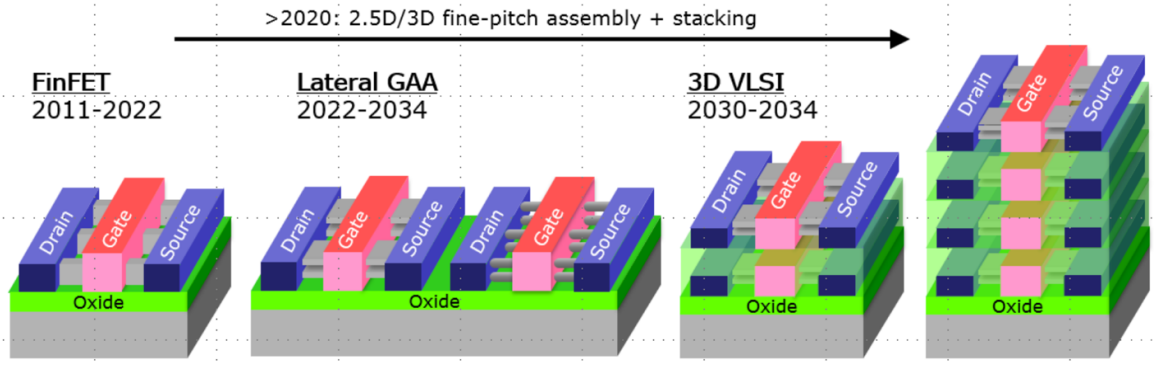

Figure 1.1. New device architectures from the IRDS More Moore roadmap: fin field-effect transistors (finFET), lateral gate-all-around (GAA), and three-dimensional very large scale integration (3D VLSI) [1].

The mechanism of any electronic device is based upon the intrinsic properties of the layers comprising the device stack and the interfaces between them, so the material interfaces play a key role in determining device functionality. The contribution of interfaces to the overall current flow and performance also becomes even more substantial as device dimensions are scaled down. Thus, it is critical to study the properties of these material interfaces pertinent to emerging device

architectures and investigate different integration schemes that make these device configurations a reality. Additionally, it is evident that with the PPAC scaling targets, and since architectures require more device components to be stacked over a small chip area, there are also an increased number of material interfaces, which further motivates the need to understand their properties and limitations. In this dissertation, we focus specifically on the interface between the dielectric oxide and the semiconducting channel in devices that are used for data storage.

Memory technologies are generally classified into two categories – volatile and non-volatile. Volatile memories cannot store data while the power supply is off, while non-volatile memories (NVM) can retain information even without a power supply. For non-volatile applications requiring more permanent mass storage, the current state-of-the-art in the market is flash memory. The digital storage element in most consumer flash memories is a floating gate field-effect transistor (FGFET), also called charge trap flash (CTF) memory. For FGFETs, shown in Figure 1.2(b), write and erase processes for data storage are based on carrier injection into and tunneling out of the conductive floating gate/charge trap layer. [2] These processes are schematically shown in the figure as the low resistance state (LRS) and high resistance state (HRS), respectively. [3] While flash memory has been highly successful and widely distributed as a consumer memory technology, it is expected to soon reach its physical and technical limitations. Since the mechanism of FGFET/CTF memory cells rely on consecutive electron tunneling, traps are generated in the dielectric oxide after high write/erase cycles, resulting in less charge transferred to and from the floating gate, and an overall reduced efficiency of the memory cell. Current flash memories thus suffer from poor endurance and retention capacity, especially after high write/erase cycles, and slow rewrite speeds. [4] These limitations necessitate the development of NVM devices that perform at high speeds, require low power, and have better endurance, while being cost-effective and scalable. [5, 6]

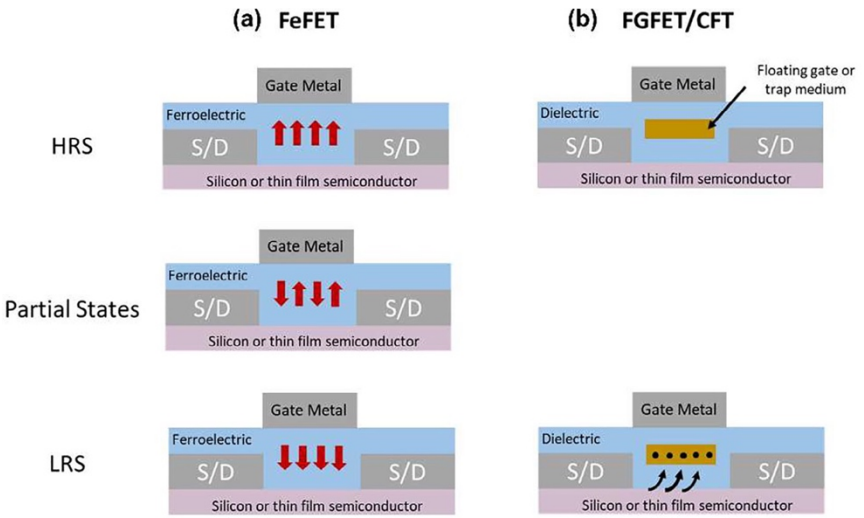

Figure 1.2. Structure and mechanism of selected NVM devices: (a) ferroelectric field-effect transistor, and (b) floating gate field-effect transistor or charge trap flash memory [3].

Several emerging NVM architectures have been proposed in literature, each with their own advantages and disadvantages. An emerging NVM device that we focus our attention on is the ferroelectric field-effect transistor (FeFET). In FeFETs, the high resistance and low resistance states (HRS and LRS) responsible for data storage are based upon the polarization state of the ferroelectric layer, schematically shown by the red arrows in Figure 1.2(a). [3] The main advantages of FeFETs are its 1T (one-transistor) cell structure, which requires less accessory circuit elements compared to traditional random-access memories (Figure 1.3), the high stability and performance of its memory states, which arise from ferroelectric polarization, and its low-power field-driven switching mechanism [6]. Shown in Figure 1.3 is the 1T1C (one-transistor-one-capacitor) cell structure typical for a dynamic random-access memory (DRAM) cell, wherein data storage occurs by storing charge in the capacitor, and the connected transistor acts as a switch to access the capacitor (to read/write charge). The advantage of the 1T cell structure of FeFETs (as well as flash memory) is that data storage occurs in the transistor itself, resulting in a smaller footprint for each individual memory cell, and thus allowing enhanced memory densities per chip area. [7]

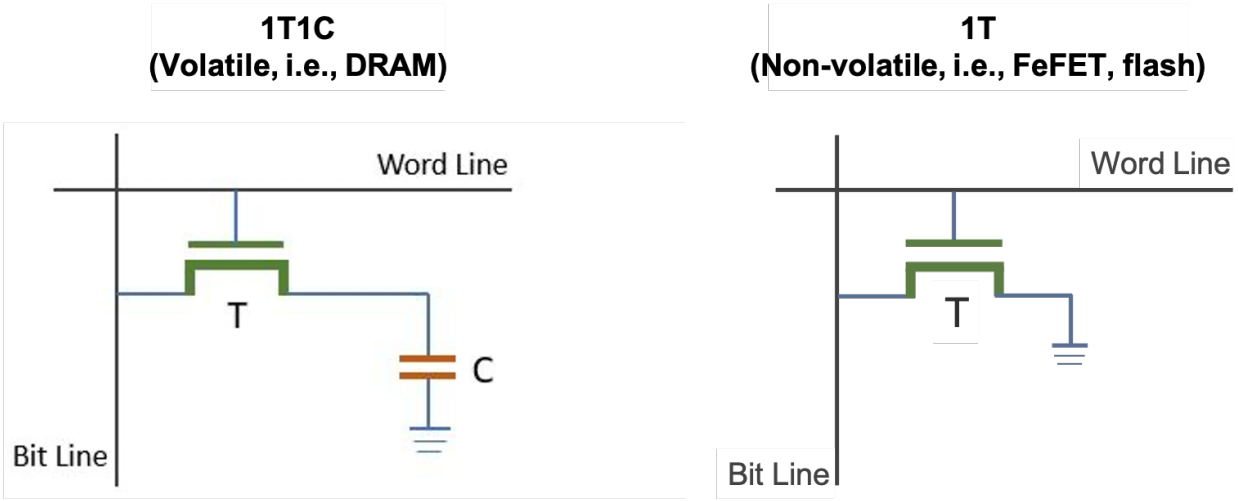

Figure 1.3. Memory cell circuit structures: 1T1C for DRAM, and 1T for FeFET and flash memory. The word line is connected to the transistor gate, and the bit line is connected to the source. [8]

The ferroelectric and floating gate FETs shown in Figure 1.2(a) and (b) are both examples of a metal-oxide-semiconductor field-effect transistor (MOSFET), the most prevalent semiconductor-based device structure used in integrated circuits. At a simplistic level, an MOS transistor is basically an on-off switch wherein the applied gate voltage determines current flow between the source and drain (S/D). [9] A key component in any MOS transistor, as the name implies, is the oxide/semiconductor interface, depicted in Figure 1.2 as the interface between the blue gate dielectric (or ferroelectric) and the purple semiconductor layers. To turn on the transistor, a gate voltage is applied through the gate dielectric/ferroelectric layer, inducing a polarization in the dielectric that then attracts charge carriers in the semiconductor to the interface, and causes current flow in the semiconducting channel. The role of the insulating oxide or gate dielectric layer is then to modulate the conductance in the semiconducting channel.

1.2 HfO_2 Thin Films

1.2.1 HfO_2 as an Established Linear Dielectric

The gate oxide material that we choose to study in this work is HfO_2. HfO_2 has been the state-of-the-art dielectric layer in many technologies because of its high relative permittivity (high-

κ) exceeding that of SiO_2. [10] The capacitance (C) of a dielectric material, which is a measure of its ability to store charge, is directly proportional to its relative permittivity (κ), as shown in Eq. 1,

$$C = \kappa\varepsilon_0 \frac{A}{t} \qquad (1)$$

where ε_0 is the permittivity of free space, A is the oxide area in contact with the channel, and t is the dielectric oxide thickness. The capacitance of the dielectric in a MOSFET is critical for maximizing device current and circuit speed because the current flow in the channel depends on the capacitance of the gate dielectric oxide in contact with it. A higher capacitance translates to a higher field effect and higher device current, which means a more efficient MOSFET. [11, 12] As can be seen in Eq. 1, the capacitance can be improved by decreasing the oxide thickness, t. However, due to current technological demands, we reached the physical scaling limitations of SiO_2 more than a decade ago. Further thinning of SiO_2 layers beyond 2 nm [13, 14] resulted in significant leakage currents through tunneling of carriers across the thin SiO_2 layer. This tunneling effect, which occurs as an electron encounters a potential barrier at the oxide interface that causes the electron wavefunction amplitude to decay exponentially, is demonstrated schematically in Figure 1.4. The rectangular potential barrier shown in this figure is analogous to the SiO_2 layer, with the barrier height being representative of its band offset with the adjacent conducting or semiconducting layer. It can be seen that the electron wavefunction decays but is able to penetrate across the width of the barrier, which represents the thickness of the dielectric layer. This means that the probability of finding the electron on the other side of the barrier is nonzero, thus the electron is said to tunnel through the barrier. This tunneling phenomenon can be avoided by having a wider barrier, that is, a thicker dielectric. [15]

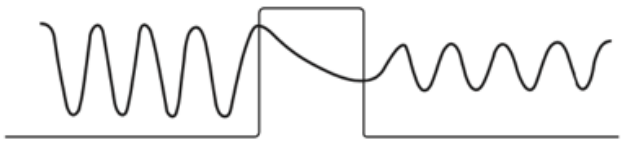

Figure 1.4. Tunneling through a rectangular potential barrier [15].

HfO_2, with its higher relative permittivity, has emerged as an alternative to SiO_2 in commercial devices [16, 17]. The equivalent oxide thickness (EOT), defined as the thickness of SiO_2 that would produce the same capacitance as a high-κ dielectric, is given by Eq. 2.

$$EOT = t_{hi\kappa} \frac{\kappa_{SiO_2}}{\kappa_{hi\kappa}} \qquad (2)$$

Using Eq. 2, the relative permittivity of SiO_2 ($\kappa_{SiO_2} = 3.9$), and the typical relative permittivity of HfO_2 ($\kappa_{hi\kappa} = 25$) [18], which we note can vary depending on processing conditions, it can be seen that a HfO_2 layer that is 6.5 nm thick ($t_{hi\kappa}$) has an EOT of 1 nm; this means it can achieve the same capacitance as a 1 nm layer of SiO_2. The use of HfO_2 instead of SiO_2 has thus allowed the implementation of thicker dielectrics to avoid leakage, without sacrificing device performance. Given the high-κ properties of HfO_2, processes have been established to widely integrate this material and make it compatible with complementary metal-oxide-semiconductor (CMOS) fabrication [19].

1.2.2 HfO_2 as an Emerging Ferroelectric

In addition to its excellent dielectric properties and CMOS compatibility, in 2011, HfO_2 was found to possess ferroelectricity in the thin film geometry (sub-20 nm) when doped or alloyed with other atoms [20]. Ferroelectricity can be defined as the characteristic of a material that has a permanent spontaneous polarization which can be reoriented; ferroelectric materials are thus a subset of dielectric materials [21]. The polarization in ferroelectrics is typically orders of magnitude larger than in regular dielectrics, and it can be switched or reoriented by applying an electric field less than the dielectric breakdown field. Even when the applied electric field is removed, ferroelectrics retain their polarization state, which is what makes these materials attractive for NVM applications. The polarization value at a zero applied electric field is called the remanent polarization. The origin of ferroelectricity in materials is a crystal structure that has no inversion symmetry, also called non-centrosymmetric crystal structures. Their non-centrosymmetric nature induces a permanent dipole moment in the crystal because the net positive charge (from cations) and net negative charge (from anions) in the unit cell are displaced with respect to each other. [22]

In HfO_2, the non-centrosymmetric crystal structure that exhibits ferroelectricity is its orthorhombic phase. Shown in Figure 1.5 are the unit cells of the thermodynamically stable monoclinic phase (left), the metastable tetragonal phase (right), and the metastable orthorhombic phase possessing ferroelectricity (center). The green circles represent the metal or Hf atoms, and in red are the O atoms. In the orthorhombic phase, the oxygen anions responsible for the polarization are shown in gold. As depicted in the figure, the location of these O atoms in gold can be shifted within the unit cell, inducing a change in the polarization (P) direction of the crystal.

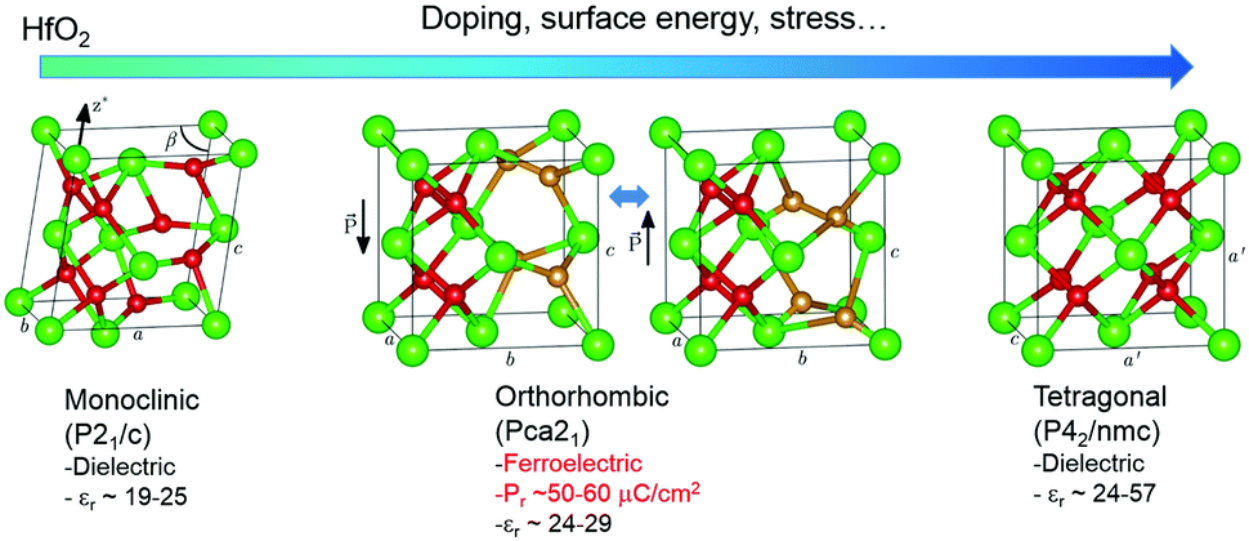

Figure 1.5. Unit cells of various HfO_2 phases and their electrical characteristics. ε_r denotes the relative permittivity, and P_r is the remanent polarization of the ferroelectric orthorhombic phase. [23]

The top of Figure 1.5 indicates several driving factors for stabilizing the orthorhombic phase over the equilibrium monoclinic phase. These include using reduced film thickness and/or constrained grain size [24, 25], applying biaxial stress [26-28], introducing oxygen vacancies [29, 30], and adding dopants, such as Si, Al, Y, Gd, and Zr [20, 31-34]. For parts of this dissertation aimed at investigating interfaces with ferroelectric oxides, we use HfO_2 thin films alloyed with Zr, which we abbreviate as HZO (hafnium zirconium oxide). The choice of Zr as the alloying element to make ferroelectric HfO_2 comes with advantages that make it particularly attractive, such as a large compositional space (Hf:Zr content) allowing orthorhombic phase formation and a low crystallization temperature [27, 34-38]. While pure HfO_2 exhibits the monoclinic phase at equilibrium, pure ZrO_2 thin films crystallize into the tetragonal phase. In an alloy of HZO, the

presence of some amount of ZrO_2 provides a tetragonal to orthorhombic phase transition pathway during cooling, resulting in the presence of the ferroelectric orthorhombic phase in HZO thin films. [34]

The implications of this work are not limited to the NVM devices described in Chapter 1.1. As a scalable and CMOS-compatible dielectric/ferroelectric, thin films of HfO_2 and HfO_2 alloys are highly versatile for use as a gate oxide in various MOS transistor devices. Our studies of its interface with emerging semiconducting materials allow for applicability of the implications of this work not just to currently realized NVM devices (as in Chapter 1.1), but also to other types of electronic devices making use of the same oxide/semiconductor interfacial stacks.

1.3 Semiconducting 2D Materials

In this dissertation, we interface our dielectric and ferroelectric oxides with semiconducting transition metal dichalcogenides (TMDCs), which are a specific class of materials belonging to the two-dimensional (2D) material family. The interest in using 2D materials for electronics rapidly rose after the first demonstration of the isolation of graphene, a single-atomic-layer-thick sheet of carbon atoms, in 2004 [39]. This discovery won the team (Andre Geim and Konstantin Novoselov) the Nobel Prize in Physics in 2010 [40]. The 2D nature of graphene, in which the carbon atoms are held by strong sp^2 bonds in-plane, with stacked graphene layers being stabilized in the out-of-plane direction by weak van der Waals forces, brought about interesting physics and unique electronic properties, which gave rise to vast interest in the field of 2D materials for electronics. Particularly, 2D materials are promising as an alternative channel material that doesn't suffer from degraded carrier mobility with decreasing thickness, and provides excellent gate electrostatic control during FET operation due to the in-plane directionality of carrier transport. [41, 42] However, a limitation of graphene is that it is a semimetal, i.e., the valence and conduction bands intersect. The absence of a band gap results in graphene transistors with poor switching behavior (on/off ratio < 30) due to the thermal excitation of carriers. [39]

This has led to research into other classes of 2D materials, such as TMDCs. TMDCs are composed of a transition metal (M), i.e., typically a group IV, V, or VI element, sandwiched between two chalcogen atoms (X), i.e., S, Se, or Te. This three-atom stack makes up each TMDC layer, and similar to graphene, each layer is held in-plane by strong covalent bonds, while multi-

layer interaction (out-of-plane) is weaker and held only by van der Waals forces. The structure of a generic TMDC is schematically shown in Figure 1.6.

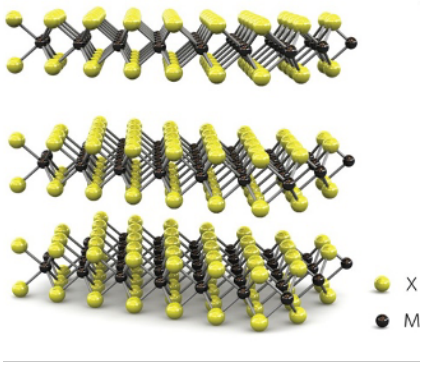

Figure 1.6. Schematic representation of a generic TMDC with chemical formula MX_2 [43].

In general, the equilibrium structures of Mo- and W-based TMDCs (specifically their sulfides, selenides, and monolayer tellurides [44]) have semiconducting properties, while others, like NbX_2 and TaX_2, are metals in equilibrium. The band gaps of semiconducting TMDCs are typically within 1-2 eV, which are comparable to traditional semiconductors like Si, thus making these TMDCs more suitable than graphene as an FET channel. For this dissertation, we chose to study MoS_2 and WSe_2 as our 2D semiconductors, as they are the two pioneering and most widely used TMDC channels in FET devices. [43]

One of the first uses of TMDCs as channels, reported in 2004, was with bulk WSe_2 crystals, which had mobilities (in p-type conduction) comparable to the best single-crystal Si FETs and on/off ratios of ~10^4, which were orders of magnitude higher than that of graphene FETs [45]. In 2007, back-gated FETs with few-layer MoS_2 channels were demonstrated, which had room-temperature mobilities ranging from 10 to 50 $cm^2\ V^{-1}\ s^{-1}$, and on/off ratios of at least 10^5 [46]. The properties of TMDC-based FETs were shown to dramatically improve in the first report of a top-gated FET with a single-layer MoS_2 channel, which was published by Radisavljevic et al. in 2011 [47]. It should be noted that the first report of exfoliation of single-layer MoS_2 came in 1986 (Joensen et al. [48]), more than two decades before the seminal Radisavljevic et al. paper on single-layer MoS_2 FETs. The method used in the 1986 study was Li intercalation of bulk MoS_2 powder followed by reaction with water to exfoliate out free-standing MoS_2 monolayer particles in solution. Almost twenty years later, Novoselov et al. reported on their dry technique of isolation

and identification of single-layer TMDCs using the same process as their work on the isolation of graphene – mechanically exfoliating/cleaving bulk crystals by repeated peeling of layers with tape [49]. This "scotch tape method" has been the exfoliation technique widely adapted by many research groups for device fabrication using single- or few-layer TMDCs, and was the method employed by Radisavljevic et al. [47] to realize the first monolayer MoS_2-based FET.

In the report by Radisavljevic et al. [47], the theoretical room-temperature mobility of MoS_2 (at least 200 $cm^2\ V^{-1}\ s^{-1}$) was achieved by providing dielectric screening through the top gate dielectric, and in addition, these FETs also had significantly improved on/off ratios of 10^8. Similarly top-gated FETs using single-layer WSe_2 have since been fabricated and shown to have excellent properties, with room-temperature mobilities of ~250 $cm^2\ V^{-1}\ s^{-1}$ and on/off ratios of at least 10^6 [50].

One of the reasons that MoS_2 and WSe_2 are the two prototypical TMDCs is their different charge carrier properties. MoS_2 has excellent electron conduction (n-type), while hole conduction (p-type) dominates in WSe_2. Because of this, n-channel and p-channel FETs are typically demonstrated using MoS_2 and WSe_2, respectively. Furthermore, the electronic properties of TMDCs have unique tunability. Changes in the number of TMDC layers results in changes in their band structure due to quantum confinement effects and orbital rehybridization. Mo- and W-based TMDCs undergo a transition from an indirect band gap in their bulk or multi-layer form to a direct band gap for monolayers. This direct band gap in the monolayer form opens up many potential applications for these MoX_2 and WX_2 TMDCs in photonics and optoelectronics. [43]

For the purposes of device integration, which is the ultimate goal of our studies, the 2D van der Waals nature of TMDCs, wherein the basal plane is ideally free of dangling bonds, offers the promise of a high-quality interface with the gate dielectric in an FET [51]. Thus, common issues with semiconductor integration, such as intermixing of constituents across interfaces and mobility degradation due to carrier scattering at the surface/interface (from roughness and dangling bonds), are avoided [42, 52, 53]. These advantages of semiconducting 2D TMDCs over traditional bulk semiconductors are pictorially shown in Figure 1.7.

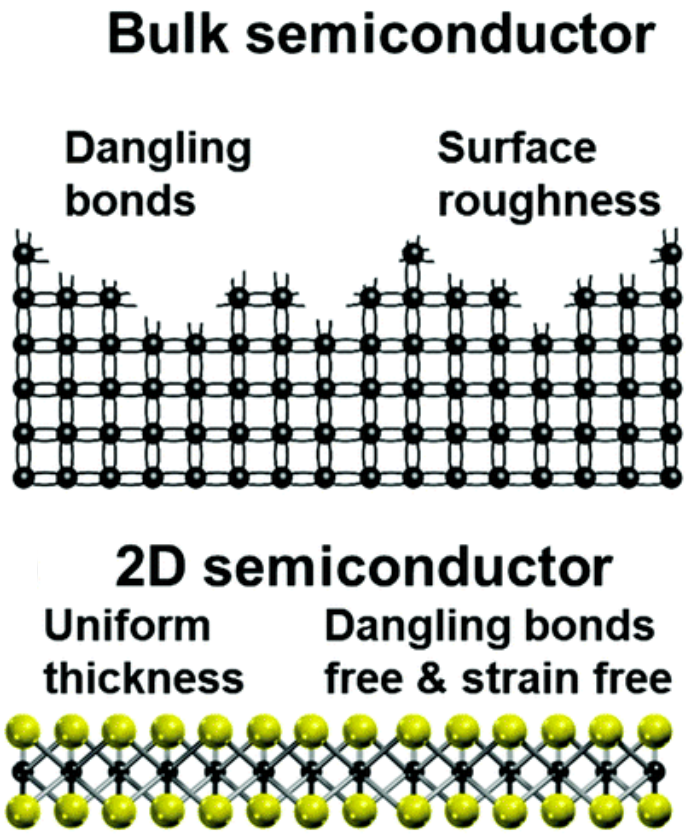

Figure 1.7. Schematic illustration of the issues with bulk 3D semiconductors and the advantages of semiconducting 2D materials [41].

Much of the device-focused work on TMDC-based FETs utilize exfoliated flakes of TMDCs from geological or chemical vapor transport (CVT) grown bulk crystals [54-59], using Geim and Novoselov's scotch tape method. While this is an excellent way to generate proof-of-concept devices, the process is not scalable to wafer processing. As such, many of the challenges with materials integration and interface formation during traditional semiconductor processing methods are circumvented despite being critical to industrially relevant technologies. Also, as we will show in Chapter 3, CVT-grown and geological TMDC crystals that are used as source material for exfoliation suffer from high impurity concentrations, which may dominate the material properties and prevent intrinsic starting material.

Studying direct growth methods allows investigation of the process-structure-property relationships at play in these devices with particular relevance to scalable technologies. Moreover, direct integration removes any need for transfer processes which can introduce residual

contaminants that may obscure and modify the behavior of these devices [60-64]. In the work we present in this dissertation, we specifically focus on direct growth methods and integration techniques that are back end of the line (BEOL) compatible and relevant to current industrial processes.

1.4 Dissertation Overview

The goals of this body of work are to investigate and engineer the interface chemistry of semiconducting 2D TMDCs with dielectric and ferroelectric HfO_2-based films, and to correlate this interface chemistry with the functional properties of FETs. Specifically, we have the following design schemes: 1) TMDC-on-Dielectric, where TMDCs are grown directly onto dielectrics by molecular beam epitaxy (MBE), and 2) Dielectric-on-TMDC, where we investigate interfaces formed by the deposition of dielectrics and ferroelectrics onto semiconducting TMDCs by atomic layer deposition (ALD). All of this work is carried out with the goal of providing fundamental insights into how device performance relates to processing and interface chemistry so that intelligent device optimization can be achieved.

This dissertation is divided into five chapters following this introduction chapter. In Chapter 2, we discuss the experimental fabrication and characterization techniques used in this work. Chapter 3 discusses in-depth spectroscopic studies performed on geological bulk crystals of MoS_2, the implications of which highlight the need to use grown TMDC channels for devices. Chapter 4 is a discussion of experimental work on TMDC-on-dielectric structures, where we demonstrate direct integration of TMDCs onto oxide films, and we study how the TMDC growth conditions affect the properties of ferroelectric and dielectric oxide substrates. Chapter 5 will cover our studies of dielectric-on-TMDC stacks. In the first part of Chapter 5, we study the thermal stability of dielectric-on-TMDC interfaces, and in the second part, we report on a technique to functionalize the TMDC surface for improved ALD of oxides. Finally, in Chapter 6, we summarize our general conclusions from this collection of studies and present directions for future work.

1.5 Chapter 1 References

[1] G. Technology Working, "The International Roadmap for Devices and Systems: 2020," Executive Summary. Technical report, Institute of Electrical and Electronics …, 2020.

[2] D. Kahng and S. M. Sze, "A floating gate and its application to memory devices," *The Bell System Technical Journal,* vol. 46, no. 6, pp. 1288-1295, 1967, doi: 10.1002/j.1538-7305.1967.tb01738.x.

[3] S. Najmaei, A. L. Glasmann, M. A. Schroeder, W. L. Sarney, M. L. Chin, and D. M. Potrepka, "Advancements in materials, devices, and integration schemes for a new generation of neuromorphic computers," *Materials Today,* vol. 59, pp. 80-106, 2022/10/01/ 2022, doi: https://doi.org/10.1016/j.mattod.2022.08.017.

[4] R. Micheloni and L. Crippa, "3 - Multi-bit NAND Flash memories for ultra high density storage devices," in *Advances in Non-volatile Memory and Storage Technology*, Y. Nishi Ed.: Woodhead Publishing, 2014, pp. 75-119.

[5] J. S. Meena, S. M. Sze, U. Chand, and T.-Y. Tseng, "Overview of emerging nonvolatile memory technologies," *Nanoscale Research Letters,* vol. 9, no. 1, p. 526, 2014/09/25 2014, doi: 10.1186/1556-276X-9-526.

[6] W. Banerjee, "Challenges and Applications of Emerging Nonvolatile Memory Devices," *Electronics*, vol. 9, no. 6*,* doi: 10.3390/electronics9061029.

[7] S. Majumdar, "Back-End CMOS Compatible and Flexible Ferroelectric Memories for Neuromorphic Computing and Adaptive Sensing," *Advanced Intelligent Systems,* https://doi.org/10.1002/aisy.202100175 vol. 4, no. 4, p. 2100175, 2022/04/01 2022, doi: https://doi.org/10.1002/aisy.202100175.

[8] N. T. "What is Internal Memory in Computer Architecture? Types - Binary Terms." Binary Terms. https://binaryterms.com/internal-memory-in-computer-architecture.html (accessed 2023).

[9] C. Hu, *Modern Semiconductor Devices for Integrated Circuits*. Prentice Hall, 2010.

[10] G. D. Wilk, R. M. Wallace, and J. M. Anthony, "High-κ gate dielectrics: Current status and materials properties considerations," *Journal of Applied Physics,* vol. 89, no. 10, pp. 5243-5275, 2001, doi: 10.1063/1.1361065.

[11] H. Chakraborty and D. Misra, "Characterization of high-k gate dielectrics using MOS capacitors," *International Journal of Scientific and Research Publications,* vol. 3, no. 12, 2013.

[12] S. Mohsenifar and M. Shahrokhabadi, "Gate stack high-κ materials for Si-based MOSFETs past, present, and futures," *Microelectron. Solid State Electron.,* vol. 2, p. 5, 2015.

[13] S. H. Lo, D. A. Buchanan, Y. Taur, and W. Wang, "Quantum-mechanical modeling of electron tunneling current from the inversion layer of ultra-thin-oxide nMOSFET's," *IEEE Electron Device Letters,* vol. 18, no. 5, pp. 209-211, 1997, doi: 10.1109/55.568766.

[14] J. Robertson and R. M. Wallace, "High-K materials and metal gates for CMOS applications," *Materials Science and Engineering: R: Reports,* vol. 88, pp. 1-41, 2015/02/01/ 2015, doi: https://doi.org/10.1016/j.mser.2014.11.001.

[15] M. J. Kumar *et al.*, *Tunnel Field-effect Transistors (TFET): Modelling and Simulations*. Hoboken: Wiley (in English), 2016.

[16] K. Mistry *et al.*, "A 45nm Logic Technology with High-k+Metal Gate Transistors, Strained Silicon, 9 Cu Interconnect Layers, 193nm Dry Patterning, and 100% Pb-free Packaging," in *2007 IEEE International Electron Devices Meeting*, 10-12 Dec. 2007 2007, pp. 247-250, doi: 10.1109/IEDM.2007.4418914.

[17] D. G. Schlom, S. Guha, and S. Datta, "Gate Oxides Beyond SiO2," *MRS Bulletin,* vol. 33, no. 11, pp. 1017-1025, 2008, doi: 10.1557/mrs2008.221.

[18] H.-L. Lu and D. W. Zhang, "Issues in High-k Gate Dielectrics and its Stack Interfaces," in *High-k Gate Dielectrics for CMOS Technology*, 2012, pp. 31-59.

[19] A. Delabie *et al.*, "Scaling to Sub- 1 nm Equivalent Oxide Thickness with Hafnium Oxide Deposited by Atomic Layer Deposition," *Journal of The Electrochemical Society,* vol. 153, no. 8, p. F180, 2006/06/15 2006, doi: 10.1149/1.2209568.

[20] T. S. Böscke, J. Müller, D. Bräuhaus, U. Schröder, and U. Böttger, "Ferroelectricity in hafnium oxide thin films," *Applied Physics Letters,* vol. 99, no. 10, p. 102903, 2011/09/05 2011, doi: 10.1063/1.3634052.

[21] R. Waser, *Nanoelectronics and information technology: advanced electronic materials and novel devices*. John Wiley & Sons, 2012.

[22] J. F. Ihlefeld, "Chapter 1 - Fundamentals of Ferroelectric and Piezoelectric Properties," in *Ferroelectricity in Doped Hafnium Oxide: Materials, Properties and Devices*, U. Schroeder, C. S. Hwang, and H. Funakubo Eds.: Woodhead Publishing, 2019, pp. 1-24.

[23] M. H. Park *et al.*, "A comprehensive study on the structural evolution of HfO_2 thin films doped with various dopants," *Journal of Materials Chemistry C,* 10.1039/C7TC01200D vol. 5, no. 19, pp. 4677-4690, 2017, doi: 10.1039/C7TC01200D.

[24] H. J. Kim *et al.*, "Grain size engineering for ferroelectric $Hf_{0.5}Zr_{0.5}O_2$ films by an insertion of Al_2O_3 interlayer," *Applied Physics Letters,* vol. 105, no. 19, p. 192903, 2014/11/10 2014, doi: 10.1063/1.4902072.

[25] C. Künneth, R. Materlik, and A. Kersch, "Modeling ferroelectric film properties and size effects from tetragonal interlayer in $Hf_{1-x}Zr_xO_2$ grains," *Journal of Applied Physics,* vol. 121, no. 20, p. 205304, 2017/05/28 2017, doi: 10.1063/1.4983811.

[26] T. Shiraishi *et al.*, "Impact of mechanical stress on ferroelectricity in $(Hf_{0.5}Zr_{0.5})O_2$ thin films," *Applied Physics Letters,* vol. 108, no. 26, p. 262904, 2016/06/27 2016, doi: 10.1063/1.4954942.

[27] S. J. Kim *et al.*, "Large ferroelectric polarization of TiN/$Hf_{0.5}Zr_{0.5}O_2$/TiN capacitors due to stress-induced crystallization at low thermal budget," *Applied Physics Letters,* vol. 111, no. 24, p. 242901, 2017/12/11 2017, doi: 10.1063/1.4995619.

[28] S. J. Kim *et al.*, "Stress-Induced Crystallization of Thin $Hf_{1-X}Zr_XO_2$ Films: The Origin of Enhanced Energy Density with Minimized Energy Loss for Lead-Free Electrostatic Energy Storage Applications," *ACS Applied Materials & Interfaces,* vol. 11, no. 5, pp. 5208-5214, 2019/02/06 2019, doi: 10.1021/acsami.8b17211.

[29] E. D. Grimley *et al.*, "Structural Changes Underlying Field-Cycling Phenomena in Ferroelectric HfO_2 Thin Films," *Advanced Electronic Materials,* vol. 2, no. 9, p. 1600173, 2016/09/01 2016, doi: 10.1002/aelm.201600173.

[30] S. Starschich, S. Menzel, and U. Böttger, "Pulse wake-up and breakdown investigation of ferroelectric yttrium doped HfO_2," *Journal of Applied Physics,* vol. 121, no. 15, p. 154102, 2017/04/21 2017, doi: 10.1063/1.4981893.

[31] S. Mueller *et al.*, "Incipient Ferroelectricity in Al-Doped HfO_2 Thin Films," *Advanced Functional Materials,* vol. 22, no. 11, pp. 2412-2417, 2012/06/06 2012, doi: 10.1002/adfm.201103119.

[32] J. Müller *et al.*, "Ferroelectricity in yttrium-doped hafnium oxide," *Journal of Applied Physics,* vol. 110, no. 11, p. 114113, 2011/12/01 2011, doi: 10.1063/1.3667205.

[33] S. Mueller, C. Adelmann, A. Singh, S. Van Elshocht, U. Schroeder, and T. Mikolajick, "Ferroelectricity in Gd-Doped HfO_2 Thin Films," *ECS Journal of Solid State Science and Technology,* vol. 1, no. 6, pp. N123-N126, 2012, doi: 10.1149/2.002301jss.

[34] J. Müller *et al.*, "Ferroelectricity in Simple Binary ZrO_2 and HfO_2," *Nano Letters,* vol. 12, no. 8, pp. 4318-4323, 2012/08/08 2012, doi: 10.1021/nl302049k.

[35] M. Hyuk Park, H. Joon Kim, Y. Jin Kim, W. Lee, H. Kyeom Kim, and C. Seong Hwang, "Effect of forming gas annealing on the ferroelectric properties of $Hf_{0.5}Zr_{0.5}O_2$ thin films with and without Pt electrodes," *Applied Physics Letters,* vol. 102, no. 11, p. 112914, 2013/03/18 2013, doi: 10.1063/1.4798265.

[36] H. Yu *et al.*, "Flexible Inorganic Ferroelectric Thin Films for Nonvolatile Memory Devices," *Advanced Functional Materials,* vol. 27, no. 21, p. 1700461, 2017/06/01 2017, doi: 10.1002/adfm.201700461.

[37] Y. C. Jung *et al.*, "A Novel Combinatorial Approach to the Ferroelectric Properties in $Hf_xZr_{1-x}O_2$ Deposited by Atomic Layer Deposition," *physica status solidi (RRL) – Rapid Research Letters,* https://doi.org/10.1002/pssr.202100053 vol. 15, no. 5, p. 2100053, 2021/05/01 2021, doi: https://doi.org/10.1002/pssr.202100053.

[38] J. Hur, Y. C. Luo, N. Tasneem, A. I. Khan, and S. Yu, "Ferroelectric Hafnium Zirconium Oxide Compatible With Back-End-of-Line Process," *IEEE Transactions on Electron Devices,* vol. 68, no. 7, pp. 3176-3180, 2021, doi: 10.1109/TED.2021.3072610.

[39] K. S. Novoselov *et al.*, "Electric field effect in atomically thin carbon films," *Science (New York, N.Y.),* vol. 306, no. 5696, pp. 666-9, 2004, doi: 10.1126/science.1102896.

[40] A. Geim and K. Novoselov, "The nobel prize in physics 2010," *Nature Physics,* vol. 6, p. 836, 2010.

[41] Y. Liu, X. Duan, Y. Huang, and X. Duan, "Two-dimensional transistors beyond graphene and TMDCs," *Chemical Society Reviews,* 10.1039/C8CS00318A vol. 47, no. 16, pp. 6388-6409, 2018, doi: 10.1039/C8CS00318A.

[42] S. Zeng, Z. Tang, C. Liu, and P. Zhou, "Electronics based on two-dimensional materials: Status and outlook," *Nano Research,* vol. 14, no. 6, pp. 1752-1767, 2021/06/01 2021, doi: 10.1007/s12274-020-2945-z.

[43] Q. H. Wang, K. Kalantar-Zadeh, A. Kis, J. N. Coleman, and M. S. Strano, "Electronics and optoelectronics of two-dimensional transition metal dichalcogenides," *Nature Nanotechnology,* vol. 7, no. 11, pp. 699-712, 2012/11/01 2012, doi: 10.1038/nnano.2012.193.

[44] X. Duan, C. Wang, A. Pan, R. Yu, and X. Duan, "Two-dimensional transition metal dichalcogenides as atomically thin semiconductors: opportunities and challenges," *Chemical Society Reviews,* vol. 44, no. 24, pp. 8859-8876, 2015, doi: 10.1039/C5CS00507H.

[45] V. Podzorov, M. E. Gershenson, C. Kloc, R. Zeis, and E. Bucher, "High-mobility field-effect transistors based on transition metal dichalcogenides," *Applied Physics Letters,* vol. 84, no. 17, pp. 3301-3303, 2004/04/26 2004, doi: 10.1063/1.1723695.

[46] A. Ayari, E. Cobas, O. Ogundadegbe, and M. S. Fuhrer, "Realization and electrical characterization of ultrathin crystals of layered transition-metal dichalcogenides," *Journal of Applied Physics,* vol. 101, no. 1, p. 014507, 2007/01/01 2007, doi: 10.1063/1.2407388.

[47] B. Radisavljevic, A. Radenovic, J. Brivio, V. Giacometti, and A. Kis, "Single-layer MoS_2 transistors," *Nat. Nanotechnol.,* vol. 6, no. 3, pp. 147-150, Mar 2011, doi: 10.1038/nnano.2010.279.

[48] P. Joensen, R. F. Frindt, and S. R. Morrison, "Single-layer MoS_2," *Materials Research Bulletin,* vol. 21, no. 4, pp. 457-461, 1986/04/01/ 1986, doi: https://doi.org/10.1016/0025-5408(86)90011-5.

[49] K. S. Novoselov *et al.*, "Two-dimensional atomic crystals," *Proceedings of the National Academy of Sciences,* vol. 102, no. 30, pp. 10451-10453, 2005/07/26 2005, doi: 10.1073/pnas.0502848102.

[50] H. Fang, S. Chuang, T. C. Chang, K. Takei, T. Takahashi, and A. Javey, "High-Performance Single Layered WSe_2 p-FETs with Chemically Doped Contacts," *Nano Lett.,* vol. 12, no. 7, pp. 3788-3792, Jul 2012, doi: 10.1021/nl301702r.

[51] H. Ishiwara, "Current status and prospects of FET-type ferroelectric memories," *Journal of Semiconductor Technology and Science,* vol. 1, no. 1, pp. 1-14, 2001, doi: 10.1109/IEDM.2001.979615.

[52] I. P. Batra, P. Wurfel, and B. D. Silverman, "Depolarization Field and Stability Considerations in Thin Ferroelectric Films," *Journal of Vacuum Science and Technology,* vol. 10, no. 5, pp. 687-692, 1973/09/01 1973, doi: 10.1116/1.1318414.

[53] H. Ishiwara, "Recent progress of FET-type ferroelectric memories," *Integrated Ferroelectrics,* vol. 34, no. 1-4, pp. 11-20, 2001/02/01 2001, doi: 10.1080/10584580108012869.

[54] H. S. Lee *et al.*, "MoS_2 Nanosheets for Top-Gate Nonvolatile Memory Transistor Channel," *Small,* vol. 8, no. 20, pp. 3111-3115, 2012/10/22 2012, doi: 10.1002/smll.201200752.

[55] X. W. Zhang *et al.*, "MoS_2 Field-Effect Transistors With Lead Zirconate-Titanate Ferroelectric Gating," *IEEE Electron Device Letters,* vol. 36, no. 8, pp. 784-786, 2015, doi: 10.1109/LED.2015.2440249.

[56] A. Lipatov, P. Sharma, A. Gruverman, and A. Sinitskii, "Optoelectrical Molybdenum Disulfide (MoS_2)—Ferroelectric Memories," *ACS Nano,* vol. 9, no. 8, pp. 8089-8098, 2015/08/25 2015, doi: 10.1021/acsnano.5b02078.

[57] X. Wang *et al.*, "Ultrasensitive and Broadband MoS_2 Photodetector Driven by Ferroelectrics," *Advanced Materials,* https://doi.org/10.1002/adma.201503340 vol. 27, no. 42, pp. 6575-6581, 2015/11/01 2015, doi: https://doi.org/10.1002/adma.201503340.

[58] C. Ko *et al.*, "Ferroelectrically Gated Atomically Thin Transition-Metal Dichalcogenides as Nonvolatile Memory," *Advanced Materials,* https://doi.org/10.1002/adma.201504779 vol. 28, no. 15, pp. 2923-2930, 2016/04/01 2016, doi: https://doi.org/10.1002/adma.201504779.

[59] T. Kobayashi, N. Hori, T. Nakajima, and T. Kawae, "Electrical characteristics of MoS_2 field-effect transistor with ferroelectric vinylidene fluoride-trifluoroethylene copolymer gate structure," *Applied Physics Letters,* vol. 108, no. 13, p. 132903, 2016/03/28 2016, doi: 10.1063/1.4945327.

[60] D. S. Macintyre, O. Ignatova, S. Thoms, and I. G. Thayne, "Resist residues and transistor gate fabrication," *Journal of Vacuum Science & Technology B: Microelectronics and Nanometer Structures Processing, Measurement, and Phenomena,* vol. 27, no. 6, pp. 2597-2601, 2009/11/01 2009, doi: 10.1116/1.3243176.

[61] A. Pirkle *et al.*, "The effect of chemical residues on the physical and electrical properties of chemical vapor deposited graphene transferred to SiO_2," (in English), *Appl. Phys. Lett.,* vol. 99, no. 12, p. 122108, Sep 19 2011, doi: Artn 122108 Doi 10.1063/1.3643444.

[62] Y.-C. Lin, C.-C. Lu, C.-H. Yeh, C. Jin, K. Suenaga, and P.-W. Chiu, "Graphene Annealing: How Clean Can It Be?," *Nano Letters,* vol. 12, no. 1, pp. 414-419, 2012/01/11 2012, doi: 10.1021/nl203733r.

[63] R. Li *et al.*, "Determination of PMMA Residues on a Chemical-Vapor-Deposited Monolayer of Graphene by Neutron Reflection and Atomic Force Microscopy," *Langmuir,* vol. 34, no. 5, pp. 1827-1833, 2018/02/06 2018, doi: 10.1021/acs.langmuir.7b03117.

[64] K. M. Freedy *et al.*, "MoS_2 cleaning by acetone and UV-ozone: Geological and synthetic material," *Applied Surface Science,* vol. 478, pp. 183-188, 2019, doi: 10.1016/J.APSUSC.2019.01.222.

2 Experimental Methods

2.1 Fabrication

2.1.1 Atomic Layer Deposition (ALD)

Atomic layer deposition (ALD) is a cyclical, self-terminating chemical vapor deposition (CVD) process that we use in this work to deposit dielectric oxide thin films. We alternate pulses of metal-organic (reactant A) and oxidant (reactant B) precursors that react with each other to form the intended oxide film. Upon introduction into the ALD chamber, these precursors saturate the substrate surface, and it is important to note that reactions only take place on the substrate surface. To ensure self-limiting reactions, i.e., a predictable growth rate per cycle (GPC), a purge with an inert gas is performed following each precursor and each oxidant pulse. This purge step is intended to remove any excess reactants and volatile reaction products from the vicinity of the growth substrate. Each pulse A – purge – pulse B – purge cycle is repeated until the desired film thickness is grown based on the GPC. This process is schematically represented in Figure 2.1.

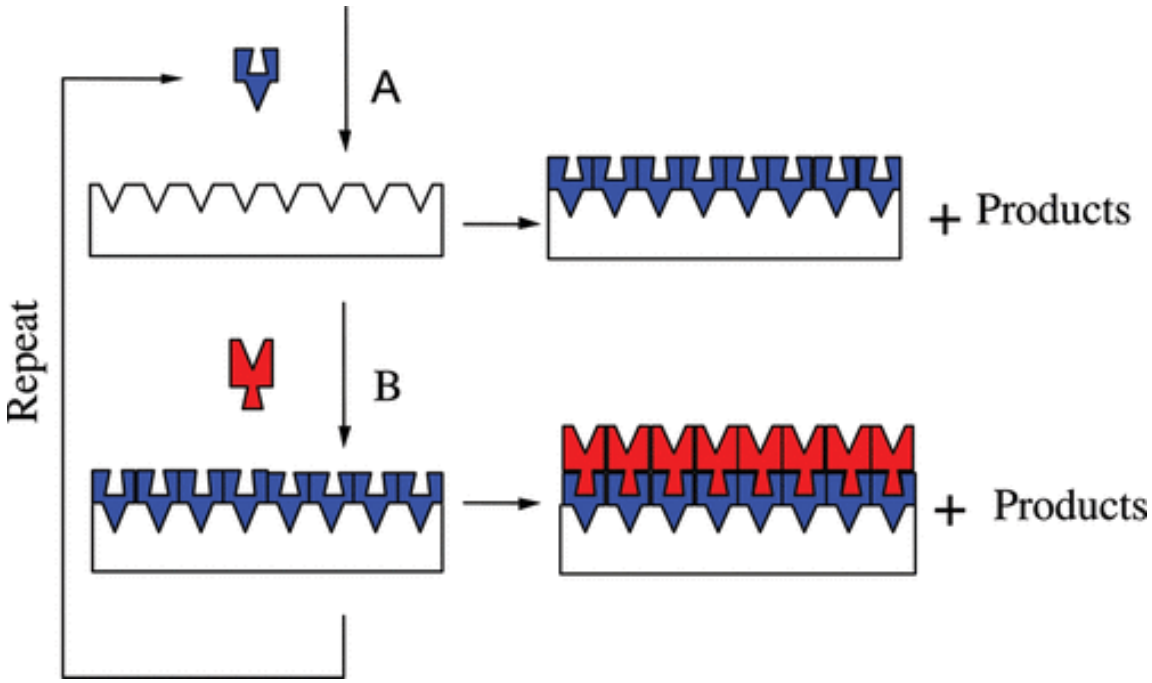

Figure 2.1. General schematic representation of the ALD process [1, 2].

In this work, ALD of films was performed in collaboration with other groups. The hafnium zirconium oxide (HZO) films used in Chapter 4 were deposited through ALD by collaborators at Sandia National Laboratories using a Cambridge Nanotech Savanah 100 flow through style reactor. In Chapter 5.1, HZO ALD was performed in collaboration with the Ihlefeld research group using an Oxford FlexAL II ALD. ALD of HfO_2 thin films in Chapters 4.2 and 5.2 was carried out using a Kurt J. Lesker ALD 150LX at the Army Research Laboratory (ARL).

While the cyclical process of ALD that we describe above is well-studied for a wide range of precursors, the initial nucleation requires reactions with the substrate. As such, there are unique challenges associated with ALD on 2D materials. Due to their 2D nature, the basal plane of an ideal transition metal dichalcogenide (TMDC) is absent of dangling bonds and does not provide reaction sites for the precursors. Instead, precursors nucleate on step edges and point defects which results in a non-uniform film. There are different ways to circumvent this issue of non-uniform ALD on 2D materials, such as the use of buffer layers [3-5], plasma-enhanced ALD (PEALD) [6, 7], surface treatment with O_2 plasma [8, 9], and functionalization with ultraviolet-ozone (UV-O_3) [10, 11]. In this work, we use the UV-O_3 functionalization technique to pre-treat our TMDC substrates before performing ALD.

2.1.2 Ultraviolet-Ozone (UV-O_3) Functionalization

UV-O_3 functionalization of TMDCs was initially demonstrated and replicated for MoS_2 [10-12]. It was found to be an effective route to producing more uniform ALD oxide films on MoS_2 (see Figure 2.2) because it induces adsorbed oxygen on the surface (i.e., S-O_{ads}) which serve as reaction sites for the ALD precursors on the otherwise unreactive surface. In inducing this adsorbed oxygen state, the Mo-S bonds are not broken, as evidenced by spectroscopic characterization. While well-studied and replicated on MoS_2, this functionalization technique is less trivial for other TMDCs such as WSe_2.

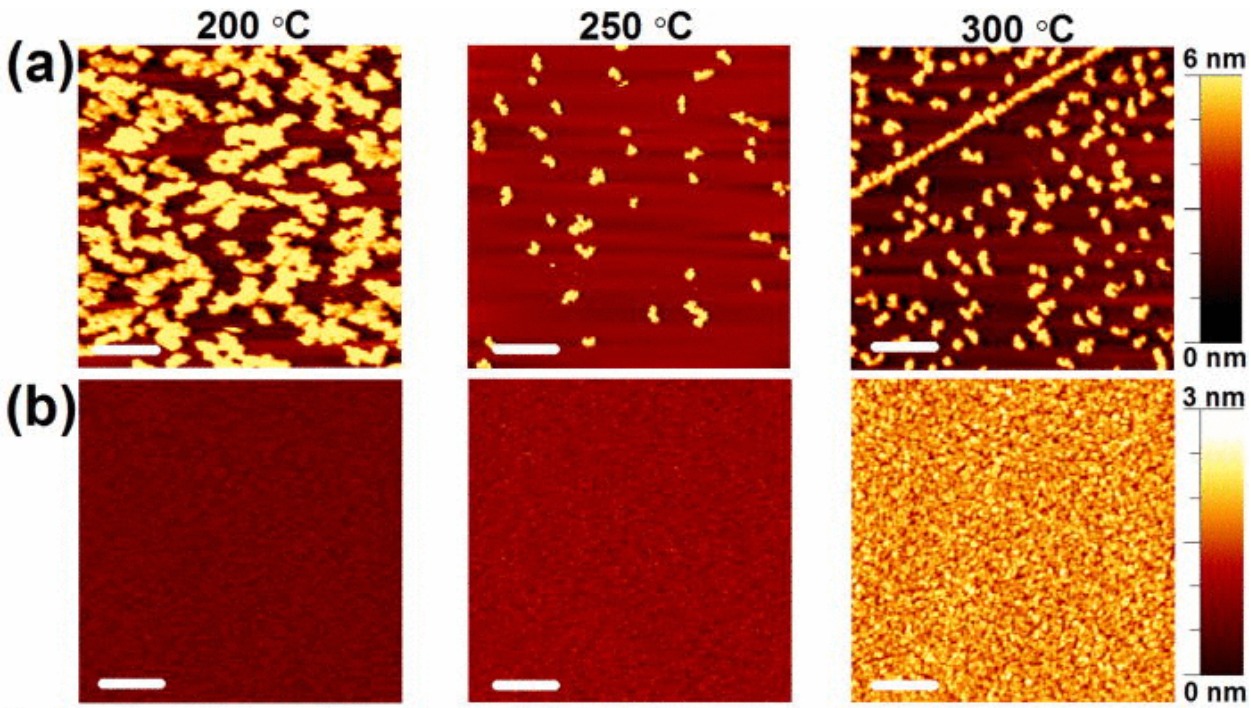

Figure 2.2. Atomic force microscopy (AFM) images of Al_2O_3 on (a) as-exfoliated/untreated MoS_2, and (b) UV-O_3 functionalized MoS_2. Temperatures denote the deposition temperature during Al_2O_3 ALD. [10]

Because WSe_2 has a higher reactivity towards oxidation compared to MoS_2 [13], the same UV-O_3 functionalization process that worked to induce S-O_{ads} on MoS_2 (6-min exposure in ultra-high vacuum (UHV)) has been previously found to break W-Se bonds and induce WO_x, SeO_x, and WSe_xO_y species on the WSe_2 surface [11]. Additionally, after subsequent ALD of HfO_2 on this oxidized WSe_2 surface, Azcatl et al. [11] observed that the deposited HfO_2 was comprised of triangular islands. This quasi-ordered triangular cluster growth mechanism was attributed to a partial etching of the WSe_2 surface because of "self-cleaning" [14] reduction reactions during ALD. In this self-cleaning process, the oxides on the WSe_2 surface are reduced or eliminated by reacting with the ALD precursor/s and then forming a volatile compound, leaving behind triangular hole-like structures for HfO_2 to preferentially nucleate on and form triangular islands. Azcatl et al. showed that a milder UV-O_3 exposure induced the Se-O_{ads} state on WSe_2, as evidenced by spectroscopic results. However, the morphology of a deposited oxide on this WSe_2 surface that underwent mild UV-O_3 exposure was not shown.

In the current work, we show that the UV-O_3 functionalization of TMDCs, as performed by Azcatl et al. in a UHV environment, can be adapted to a tabletop UV lamp in atmosphere. Additionally, we perform UV-O_3 functionalization of MoS_2 and WSe_2 surfaces.

2.1.3 Molecular Beam Epitaxy (MBE)

A molecular beam epitaxy (MBE) chamber is used in this work for deposition and growth of semiconducting 2D TMDCs, mainly WSe_2. WSe_2 is grown by co-depositing elemental W and Se sources onto a substrate that is heated to a specific growth temperature, monitored using a pyrometer, which is discussed in detail below. The Se:W flux ratio is controlled for each growth, with the individual fluxes measured by a beam flux monitor. This beam flux monitor is an ionization gauge positioned in line-of-sight of the sources before actual growth, and the beam equivalent pressure of each source (once heated to the specific source temperature required for evaporation) is taken to be the difference in the pressure reading of the beam flux monitor before and after opening the source shutter. After measurement of the beam equivalent pressures and once the desired Se:W flux ratio is achieved, the beam flux monitor is withdrawn so that the sample or growth substrate is in direct line-of-sight of the sources for growth. We use an electron beam evaporator for our W source and an effusion cell for our Se source. MBE is performed in a UHV environment which minimizes contaminants and provides a clear path for the source material to travel onto the growth substrate.

Because of this UHV environment, we need a non-contact measurement technique to determine the temperature of our sample surface during growth, so we use a Fluke E2RL pyrometer in 2-color mode. The pyrometer settings were calibrated by using the known surface desorption temperature of a thermally grown oxide on GaAs. We heated a GaAs wafer in our UHV system by increasing the manipulator heater current until the thermally grown oxide layer was desorbed, as monitored by in-situ reflective high energy electron diffraction (RHEED). At the point of desorption, the pyrometer slope was adjusted to match 582 °C, which is the known thermal oxide desorption temperature [15]. We used this same GaAs calibration sample to correlate the pyrometer temperature reading to the manipulator current.

The Scienta Omicron UHV system that houses our MBE tool is shown in Figure 2.3. Since this system is all in-vacuo with the analysis module attached to the MBE module, we have the capability of directly analyzing our MBE-grown samples without atmospheric exposure.

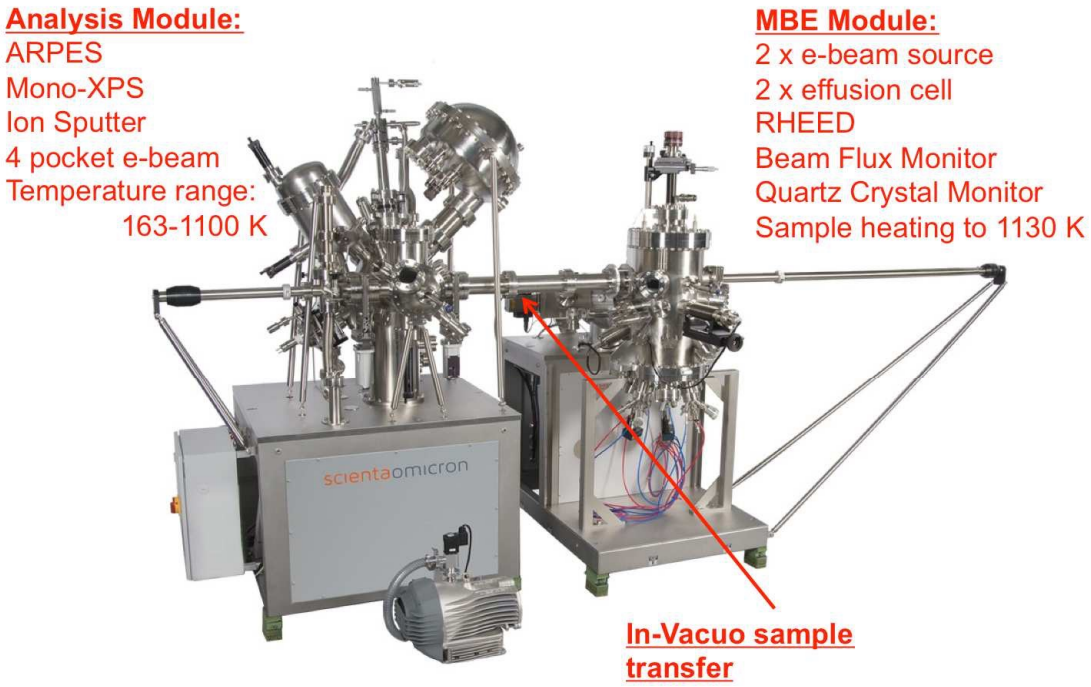

Figure 2.3. UHV system from Scienta Omicron [16].

2.1.3.1 Traditional Epitaxy

In traditional MBE, the growth process relies on primary bonds forming between the substrate and the film being grown. Epitaxy, in the traditional sense, pertains to the grown film adopting the crystal structure, lattice constant, and orientation of the substrate it is grown on. If the intrinsic lattice constant of the thin film material does not match the substrate's, strain develops in the film as it grows, which eventually leads to the formation of defects, specifically misfit dislocations, in the grown film. For applications of these materials wherein such defects can negatively impact its properties, i.e., for electronic conduction, lattice matching between the film and substrate is a requirement for traditional MBE. [17]

2.1.3.2 Van der Waals Epitaxy (VDWE)

As discussed in our introduction (Chapter 1), 2D van der Waals materials, such as TMDCs, do not have surface dangling bonds. The absence of dangling bonds on an ideal TMDC surface means that it cannot form primary bonds with the substrate it is being grown on; however, van der Waals epitaxy (VDWE) still allows epitaxial growth without the need for chemical bonding with the substrate. VDWE refers to the growth of dissimilar 2D materials on top of each other [18]. In VDWE, a van der Waals gap exists between the grown film and the substrate, with the film and substrate being held together by van der Waals interactions, rather than chemical bonding. Despite the absence of primary bonding, interlayer interactions allow the substrate to dictate the in-plane rotational alignment of the grown film [19, 20]. The advantage of VDWE over traditional epitaxy is that the lattice matching requirement between the film and substrate is greatly relaxed, as VDWE does not rely on atom-by-atom bonding at the interface. [18] This relaxed lattice constraint makes VDWE a highly adaptable and versatile growth technique for 2D material integration. In this dissertation, the MBE-WSe_2 samples discussed in Chapter 5.1 were grown by VDWE.

2.1.3.3 Physical Vapor Deposition (PVD)

For the MBE studies presented in this dissertation (Chapter 4: TMDC-on-Dielectric), we note that the crystal structure of our grown TMDC films does not have registry with our dielectric/ferroelectric growth substrates, which are either amorphous or polycrystalline in nature. As such, the mechanism of this growth can be described as a general physical vapor deposition (PVD) process, in which the source materials are heated to evaporation, and because of a pressure gradient, the vapor is transported from the source to a heated growth substrate, onto which it condenses into a thin film solid [21]. The crystal structure of our resulting TMDC thin film is not aligned with the atomic arrangement of the substrate it is grown on, i.e., in our case, a dielectric oxide. However, despite the lack of in-plane epitaxy with the dielectric substrate, we note that the c-axis of our grown TMDC film is always oriented perpendicular to the substrate surface, which is expected based on the kinetics of TMDC growth [22, 23].

Throughout this dissertation, regardless of the physical mechanism of the growth process (traditional epitaxy, VDWE, or PVD), all growths performed in our MBE chamber will be referred to as "MBE" for simplicity of the discussions.

2.2 Characterization

2.2.1 Photoelectron Spectroscopy

Photoelectron spectroscopy is a characterization technique that uses the photoelectric effect to obtain chemical information on a material. The photoelectric effect works by irradiating a sample with photons of known energy, and when a photon interacts with an atom in the sample, an electron is ejected from the material, now called a photoelectron. Upon removal from the solid, these photoelectrons arrive at a detector, which then counts the number of photoelectrons as a function of kinetic energy. The conservation of energy equation shown in Eq. 1 gives the relation of the photoelectron kinetic energy, KE, to the energy of the incident photon, $h\nu$ (Planck's constant × photon frequency), the photoelectron binding energy, BE, and the sample work function, ϕ_{sample}.

$$KE = h\nu - BE - \phi_{sample} \quad (1)$$

In practical photoelectron spectroscopy measurements, the measured kinetic energy, $KE_{measured}$, is affected by the difference between the spectrometer and sample work functions, ϕ_{spec} and ϕ_{sample}, respectively. This relation is given by Eq. 2.

$$KE_{measured} = KE - (\phi_{spec} - \phi_{sample}) \quad (2)$$

Combining Eq. 1 and 2 gives us Eq. 3, which relates $KE_{measured}$ to the incident photon energy, photoelectron binding energy, and spectrometer work function.

$$KE_{measured} = h\nu - BE - \phi_{spec} \quad (3)$$

In our X-ray photoelectron spectroscopy (XPS) tool (part of the analysis module in Figure 2.3), a monochromated Al Kα X-ray source, which has an energy of 1486.7 eV, is used as the incident photon probing the sample. We note that our Scienta Omicron XPS (Figure 2.3) has a ~1 mm spot size. For some parts of this work which require analysis of small areas, a PHI VersaProbe

III XPS is used, which has variable X-ray beam spot sizes ranging from 9 to 200 μm. The PHI VersaProbe system also makes use of a monochromated Al Kα X-ray source.

XPS is typically used for detection of core level electrons. Based on quantum mechanics, each core level electron has a designated set of quantum numbers, describing its position and energy in the atom – the principal, orbital angular momentum, magnetic, and electron spin quantum numbers. The principal quantum number is an integer ($n = 1, 2, 3 \ldots$) that denotes the electron energy level or shell. The orbital angular momentum ($\ell = 0, 1, 2, \ldots, n-1$) is referred to as the electron subshell. Each orbital angular momentum 0, 1, 2, and 3, is typically denoted as *s*, *p*, *d*, and *f*, respectively. Magnetic quantum numbers denote the orbital within the specific subshell, and the fourth quantum number, the electron spin, denotes an electron being either "spin up" (+1/2) or "spin down" (-1/2). The coupling between the orbital angular momentum and the spin leads to spin-orbit splitting, or the splitting of the *p*, *d*, and *f* levels into two distinct sub-states with distinct energies. Because *s* orbitals have an orbital angular momentum of zero, it does not exhibit spin-orbit splitting. In XPS spectra, this means that photoelectrons coming from *s* orbitals are seen as a single peak, while photoelectrons coming from all *p*, *d*, and *f* orbitals result in doublet peaks with specific peak area ratios, as dictated by the degeneracy of each sub-state, i.e., each doublet component. The notation for each doublet component is a subscript after the orbital, which indicates the total electron angular momentum, $j = \ell \pm s$, such that $p_{1/2}$ and $p_{3/2}$, $d_{3/2}$ and $d_{5/2}$, and $f_{5/2}$ and $f_{7/2}$ peaks are observed for *p*, *d*, and *f* core levels, respectively. Each of these split subshells can hold $2j + 1$ electrons, leading to peak area ratios of 1:2 for *p* levels, 2:3 for *d* levels, and 3:4 for *f* levels. In general, the magnitude of the spin-orbit splitting, or the energy separation between each component of the doublet, increases with atomic number. [24] We use XPS databases to reference the spin-orbit separation for our elemental core levels of interest [25].

XPS results are conventionally represented as a plot of intensity vs. binding energy. Because each element has a specific set of distinct electron energy levels, the XPS spectrum of each element is composed of a set of peaks at specific binding energies, with each set of binding energies being unique to each element. Thus, XPS provides a unique spectrum for each element, making it a useful technique for elemental identification of species present in the sample being analyzed. The observed photoelectron binding energies obtained from a sample also provide information on the material chemistry. This is because the interatomic interaction due to bonding between atoms causes some shift in their electron orbitals, resulting in slightly shifted energy

levels. XPS can detect small shifts in binding energy and is therefore particularly powerful in differentiating various chemical bonding environments of the elements present in the sample.

For an example analysis of XPS core level peaks, shown in Figure 2.4 is the W 4*f* core level spectrum collected from a sample of WSe_2. As mentioned previously, small shifts in binding energy that are indicative of changes in the chemical bonding environment of the atom can be detected with XPS. In Figure 2.4, we see this through the presence of the W 4*f* doublet corresponding to the W-Se bond (WSe_2) and another doublet at higher binding energy corresponding to the W-O bond; this indicates that the WSe_2 material being analyzed is partially oxidized. The chemical shift seen with W 4*f* is also reflected in the other W core levels, as evident with the W $5p_{3/2}$ peak also shown in the same binding energy window.

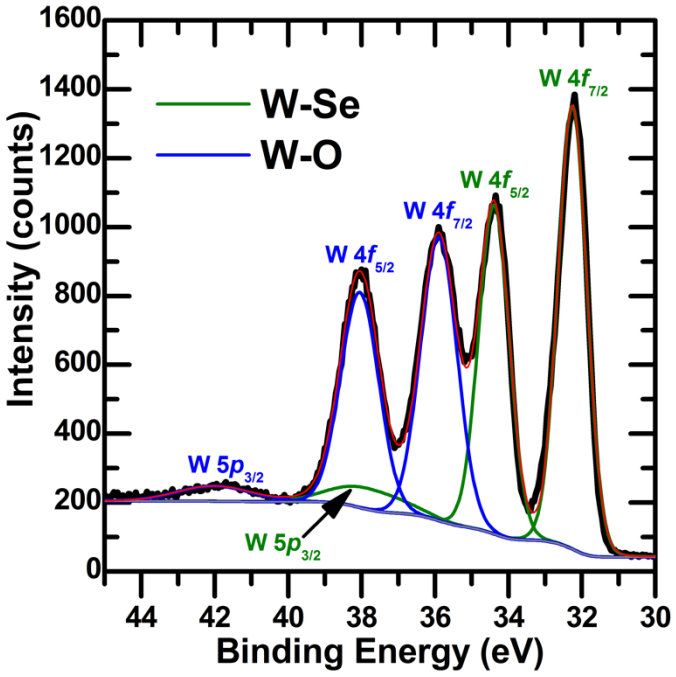

Figure 2.4. Deconvoluted W 4f spectrum of WSe_2 showing the shift of the core level peaks due to partial oxidation of the WSe_2 material.

To deconvolute XPS spectra, such as that shown in Figure 2.4, we fit the features using kolXPD software [26], which allows us to consider the background and peak shapes. Unless stated otherwise, in this work, we use a Shirley background [27] to fit our XPS spectra. This accounts for

inelastically scattered electrons during the photoemission process that contribute to the asymmetric shape of the background seen in XPS. In the discussion of results in later chapters, the background is typically subtracted from the fitted spectra for visual clarity.

For metallic species, an asymmetric Doniach-Sunjic lineshape [28] convoluted with a Gaussian is used to fit the core level peak, while for non-metals, we use a symmetric Voigt function. In our fitting software, the Lorentzian and Gaussian components of the peak width are separated. The Lorentzian width is a property of the photoemission process, as it comes from the lifetime of the core hole left behind by the emitted photoelectron. The Gaussian width is due to other factors extrinsic to the nature of the photoemission process, such as instrumental broadening, temperature, and disorder in the material being measured.

2.2.1.1 Quantitative Analysis Using XPS

For quantification of elemental composition using XPS, we use the core level peak intensity obtained through peak fitting. The intensity (I) generated from photoemission comes from several factors, as shown in Eq. 4 [29-31].

$$I = nF\sigma\phi yT\lambda \qquad (4)$$

Here, n is the number of atoms participating in photoemission per unit volume (atoms/cm^3), F is the incident X-ray flux (photons/cm^2), σ is the partial photoionization cross-section of the measured core level [32], ϕ is an angular distribution term, y is the fraction of σ retained in the measured peak, T is the transmission function, or efficiency of detection, of the detector used (varies with photoelectron KE) [33], and λ is the inelastic mean free path (IMFP) of the measured core level electrons.

When using XPS peak intensities to quantify the relative composition of different elements in a sample, all of the factors contributing to the intensity must be considered. The term $\sigma\phi yT\lambda$ is referred to as the relative sensitivity factor (RSF) of the measured core level. To obtain the atomic concentration (n) of each element measured based on their respective XPS peak intensities, we normalize the measured intensity, I, of each core level peak by their respective RSF. Given a constant X-ray flux, F, for spectra acquired successively using the same XPS instrument and scan settings, RSF-normalized peak intensities allow us to compare the atomic concentration of

different elements measured from our sample and calculate % composition. In this work, we use RSFs that are specific to the XPS instrument used for any given spectra.

2.2.1.1.1 Single-Material Overlayer Thickness Calculation

XPS can also be used to estimate the thickness of a layer over a given underlying substrate material by using measured intensities of the overlayer and substrate. This is because any overlayer that electrons have to travel through before escaping the material will attenuate the measured XPS signal. In the presence of an overlayer with thickness d, the intensity of the overlayer ($I_{overlayer}$) and substrate ($I_{substrate}$) are given by Eq. 5 and 6, respectively [34].

$$I_{overlayer} = I^{\infty}_{overlayer}[1 - \exp\left(\frac{-d}{\ell_{overlayer\ CL}cos\theta}\right)] \quad (5)$$

$$I_{substrate} = I^{\infty}_{substrate}[\exp\left(\frac{-d}{\ell_{substrate\ CL}cos\theta}\right)] \quad (6)$$

In these equations, $I^{\infty}_{overlayer}$ and $I^{\infty}_{substrate}$ are intensities of pure bulk samples of the overlayer and substrate, respectively, $\ell_{overlayer\ CL}$ and $\ell_{substrate\ CL}$ are the effective attenuation lengths (EAL) of electrons coming from the overlayer and substrate core level (CL), respectively, traveling through the overlayer material, and θ is the photoelectron take-off angle with respect to the surface normal. We note that EAL (ℓ) is used in place of IMFP (λ) in these calculations because it corrects for elastic scattering effects and takes into account instrument configuration [35]. In our calculations, we use the National Institute of Standards and Technology (NIST) EAL database [36, 37] to find the appropriate EALs for the different overlayer/substrate systems we study at the specific geometry of the XPS instrument used.

2.2.1.1.2 Partial Coverage by Island Overlayers

The above overlayer/substrate intensity equations assume a fully continuous and flat overlayer film with a constant thickness. However, this is not always the case, and some overlayers we analyze with XPS exist as islands or clusters on the surface rather than a uniform film. Assuming that the fraction of the substrate area covered by clusters is x, we modify the overlayer and substrate intensity equations (from Eq. 5 and 6), as shown in Eq. 7 and 8. [38]

$$I_{overlayer} = (x)I^{\infty}_{overlayer}\left[1 - \exp\left(\frac{-d}{\ell_{overlayer\ CL}cos\theta}\right)\right] \quad (7)$$

$$I_{substrate} = (x)I^{\infty}_{substrate}\left[\exp\left(\frac{-d}{\ell_{substrate\ CL}cos\theta}\right)\right] + (1-x)(I^{\infty}_{substrate}) \quad (8)$$

In Eq. 7 (overlayer), the right-hand side of the equation is simply multiplied by the fraction x because all of the overlayer signal comes from the clusters. In Eq. 8 (substrate), the first term corresponds to substrate signal buried under clusters, and the second term comes from exposed areas of the substrate not covered by clusters. These equations can be used to estimate surface coverage using measured XPS intensities by rearranging and solving for x, or they can also be used to predict the expected XPS intensity given a specific fraction of the surface covered by islands.

However, note that Eq. 7 and 8 assume that all of the clusters/islands have a uniform thickness, d, which is not a fully accurate assumption. We use these partial coverage equations for clustered HfO_2 on MoS_2 in Chapter 5.1, and as seen with microscopy data of the same samples, island/cluster heights are greatly varied. Therefore, discrepancies may arise between the actual and predicted surface coverages or intensities. These equations should be used for semi-quantitative estimation rather than for determination of absolute values.

2.2.1.1.3 Compound Overlayer Thickness Calculation

In cases where the substrate intensity is attenuated by more than one material component as the overlayer, and each component is composed of different elements such that their core level peaks are at different binding energy ranges, we modify the above overlayer/substrate intensity equations. Given a compound of species A and B (each with their individual core level peaks) that are assumed to be homogeneously mixed as one overlayer, the attenuation due to both A and B have to be incorporated in the equations. We take the ratio of the overlayer intensity to the substrate intensity for A and B individually, as shown in Eq. 9 and 10, respectively. [39]

$$\frac{I_A}{I_{substrate}} = \frac{I^{\infty}_A}{I^{\infty}_{substrate}}\left[\frac{1-\exp\left(\frac{-d_A}{(\ell_{A\ CL\ in\ A})(cos\theta)}\right)}{\exp\left(\frac{-d_A}{(\ell_{substrate\ CL\ in\ A})(cos\theta)}+\frac{-d_B}{(\ell_{substrate\ CL\ in\ B})(cos\theta)}\right)}\right] \quad (9)$$

$$\frac{I_B}{I_{substrate}} = \frac{I^{\infty}_B}{I^{\infty}_{substrate}}\left[\frac{1-\exp\left(\frac{-d_B}{(\ell_{B\ CL\ in\ B})(cos\theta)}\right)}{\exp\left(\frac{-d_B}{(\ell_{substrate\ CL\ in\ B})(cos\theta)}+\frac{-d_A}{(\ell_{substrate\ CL\ in\ A})(cos\theta)}\right)}\right] \quad (10)$$

To calculate the thickness of a compound overlayer composed of A and B, we use Eq. 9 and 10 to iteratively calculate the effective thickness of each component, d_A and d_B. We do this by starting with an educated guess for d_B to use in Eq. 9 and an educated guess for d_A to use in Eq. 10. We then solve for d_A and d_B in Eq. 9 and 10, respectively, and use those calculated effective thicknesses as a new educated guess for the other equation. This process is repeated until the effective thickness values for A and B are consistent between both equations. Finally, the compound overlayer thickness, d, is taken to be the sum of the individual effective thicknesses: $d = d_A + d_B$. [39]

In performing these thickness calculations, if pure bulk samples of either the overlayer or substrate material are not available for experimental determination of the I^{∞} values, the ratio $\frac{I^{\infty}_{overlayer}}{I^{\infty}_{substrate}}$, also referred to as R_o, can be theoretically determined as described by Seah and Spencer [40]. As shown in Eq. 11, R_o depends on the bulk density of the overlayer/substrate (ρ), the molecular mass of the overlayer/substrate material (M), and the EAL of the specific core level electron as it travels through the overlayer/substrate (ℓ).

$$R_o = \frac{I^{\infty}_{overlayer}}{I^{\infty}_{substrate}} = \frac{\rho_{overlayer} M_{overlayer} \ell_{overlayer\ CL\ in\ overlayer}}{\rho_{substrate} M_{substrate} \ell_{substrate\ CL\ in\ substrate}} \qquad (11)$$

These compound overlayer thickness equations are used in Chapter 5.2 to estimate the thickness of a compound WO_3-SeO_2 layer on top of WSe_2.

2.2.1.2 Electronic Characterization Using XPS

Other than measuring chemical composition, interfacial chemistry, and overlayer thicknesses, this work will also use XPS to investigate the electronic character of our material. For compounds, we discuss the difference between XPS peak shifts due to changes in material chemistry and peak shifts due to a Fermi level shift. Chemical shifts are brought about by atomic bonding. Because of differences in electronegativity of the atoms participating in a bond, their core level electrons may be more tightly or loosely bound to the nucleus, resulting in shifts in the core level binding energies as seen with XPS. Given a compound composed of two elements, chemical shifts are observed as shifts of their core level peaks in opposite directions; bonding with a more electronegative atom increases the binding energy, and bonding with a less electronegative atom shifts the peaks to lower binding energy.

Conversely, with a non-metal compound, the peaks of the elements in the compound may also shift in the same direction. Note that the binding energy scale is referenced such that the Fermi energy of the material is at 0 eV. Equal shifts in the same direction of all of the core level peaks corresponding to that compound (regardless of the element being measured) are evidence of a shift in the compound's Fermi level. If the peaks uniformly shift to lower binding energy, the core levels are closer to the Fermi level (0 eV), indicating more p-type behavior. If the peaks uniformly shift to higher binding energy, they are further from the Fermi level at 0 eV, indicating the material is more n-type in nature.

We demonstrate a chemical vs. a Fermi level shift for the same material in Figure 2.5. The shifts of the O 1*s* and Zr 3*d* core level peaks of $Hf_{0.36}Zr_{0.64}O_2$ (HZO) samples are shown. The Hf core level peaks are not plotted in this figure, but note that the direction of the Hf core level peak shifts mimic that of Zr's. To simplify the discussion, we focus on the Zr 3*d* and O 1*s* peaks.

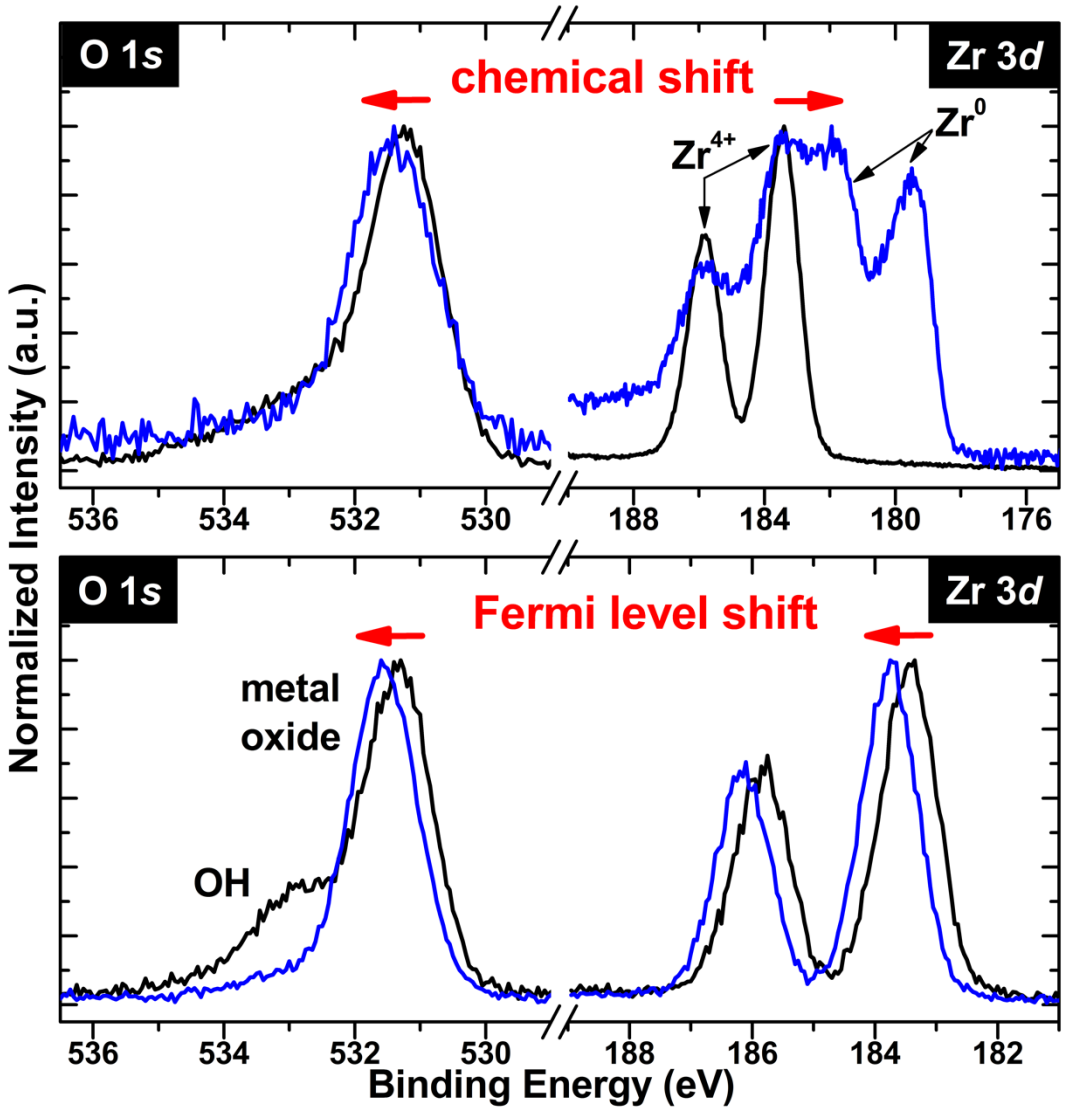

Figure 2.5. O 1s and Zr 3d spectra of HZO showing opposite peak shifts due to chemical changes (top), and uniform peak shifts due to a change in the Fermi level (bottom).

In the top panel, the HZO was reduced through in-situ Ar^+ sputtering. As seen in the blue post-sputter spectra, the Zr 3*d* peaks have shifted to lower binding energy. This means that the Zr^{4+} from HZO has been partially converted to metallic Zr (Zr^0) and other sub-oxides (between Zr^0 and Zr^{4+}). With this reduction in the Zr oxidation state, an accompanying shift is observed in the O 1*s* peak in the opposite direction, to higher binding energy.

In the bottom panel, the HZO was annealed in UHV to induce the formation of oxygen vacancies, which serve as n-type dopants in HfO_2 [41, 42] and ZrO_2 [42]. The increase in n-type charge carriers in the HZO material is reflected in the XPS spectra as a uniform shift of the HZO features to higher binding energy, shown as the blue spectra in the bottom panel. This means these O and Zr (and Hf) core levels are now further from the Fermi level, 0 eV. For the O 1*s* region, the removal of the OH feature, which is likely to be from adventitious contamination, signifies desorption of these OH species during the in-situ UHV anneal. However, the feature due to the metal oxide bond (O atoms in HZO), is seen to shift to higher binding energy along with the Zr (and Hf) peaks.

To further demonstrate that these uniform core level shifts indicate Fermi level shifts, we show the core level and valence band (VB) spectra of a sample of WSe_2 before and after p-type doping. It is known that p-type doping is induced in WSe_2 when its top surface is oxidized [43-47]. The spectra in Figure 2.6 show the Se 3*d*, W 4*f*, and VB features of WSe_2 before (bottom) and after (top) oxidation of the top layer.

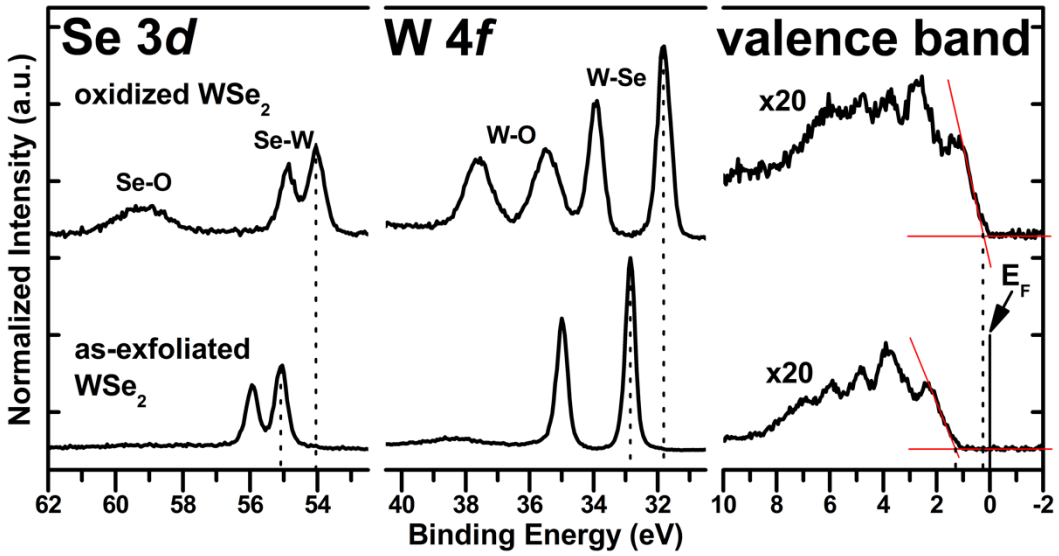

Figure 2.6. p-type shift of oxidized WSe_2 uniformly observed in the Se 3d and W 4f core level peaks and the extrapolated valence band maximum.

For the VB spectra, which are the features seen close to 0 eV, the valence band maximum (VBM) for non-metals is conventionally taken as the intersection of lines extrapolated from the linear region of the drop-off in counts (VB leading edge) and the noise level [48-50], shown in Figure 2.6 as red lines. For the bottom spectrum (as-exfoliated), the VB features seen are only for WSe_2, and for the top spectrum (oxidized), we see a superposition of the VB features of WSe_2 and WO_3/SeO_2. This is why the general shape of the VB spectrum is broader for oxidized WSe_2, but the same main peaks/features as in the as-exfoliated spectrum are evident, similar to a previous report showing VB spectra of oxidized WSe_2 [44]. WO_3 and SeO_2 both have larger band gaps and VBM-to-Fermi-level distances than WSe_2 [51, 52]. Thus, for the top spectrum in Figure 2.6, the drop-off in counts that we measure is attributed to the VBM of WSe_2, with the VBM of the WO_3-SeO_2 layer superimposed and hidden by the WSe_2 VB features. In this figure, the Fermi level (E_F) is marked by a solid drop line to 0 eV to illustrate the distance between the VBM and E_F.

The main core level peaks and VBM of WSe_2 are marked with dotted drop lines. It is clearly seen that after inducing p-type doping in the WSe_2 through oxidation, all of these features are uniformly shifted to lower binding energy by ~1 eV. Specifically, in the as-exfoliated material, the Fermi level is 1.24 eV away from the VBM, and after oxidation, the Fermi-level-to-VBM distance decreases to 0.25 eV. As shown in Figure 2.6, the W 4*f* and Se 3*d* core levels of WSe_2 reflect the same shift in the VBM position.

As discussed in our results in Chapters 4 and 5, we use uniform core level peak shifts to determine Fermi level shifts in our material. This allows us to eliminate errors arising from the low counts and low signal-to-noise of valence band spectra, as this leads to increased error and subjectivity in the linear extrapolation of the VBM.

2.2.2 X-ray Diffraction (XRD)

In this work, X-ray diffraction (XRD) is primarily used to assess the crystalline structure of our dielectric oxide films. The underlying principle of XRD follows Bragg's Law, $n\lambda = 2dsin\theta$. When X-rays arrive at a crystal at a certain θ angle, and the atomic plane spacing, d, of the set of crystallographic planes in the sample satisfy Bragg's Law (given the incident X-ray wavelength, λ), the interaction of the incident X-ray with the set of atomic planes produces

scattered waves that constructively interfere to produce a diffracted X-ray at angle θ with respect to the atomic plane. Note that n in Bragg's Law is simply an integer representing the diffraction order, which is due to the crystal's symmetry. In XRD measurements, the diffracted X-rays are collected by a diffractometer, and the θ angles at which there are diffracted X-ray signals detected are conventionally represented in an intensity vs. 2θ plot. Using knowledge of the sample and its expected possible crystal structures, the obtained peaks are indexed based on which atomic planes have the interplanar spacing that would satisfy Bragg's Law. Determining which planar reflections are responsible for the measured XRD peaks provides information on the sample's crystallographic orientation.

For the thin oxide films that we characterize using XRD in this work, we use an asymmetric XRD setup wherein the incident angle is fixed, and a range of 2θ angles are swept and measured. In our case where the samples are of thin film geometry, the incident X-ray is fixed at a very small angle, such that it does not penetrate deep into the bulk/substrate. The small angle of incidence allows more grains of the thin film to be illuminated, increasing the X-ray interaction volume with the material of interest. This maximizes the intensity of the thin film diffraction peaks and reduces the intensity of the substrate features. [53] In collaboration with the Ihlefeld group, XRD studies in Chapters 4.1 and 5.1 were performed using a Rigaku Smartlab X-ray diffractometer with Cu Kα radiation. In Chapter 4.2, an Empyrean X-ray diffractometer equipped with Cu Kα radiation was used for XRD studies.

2.2.3 Atomic Force Microscopy (AFM)

Atomic force microscopy (AFM) allows us to investigate the morphology of our deposited samples. It works by bringing a microscale tip, which is attached to a cantilever, in close proximity of a sample in order to scan the topography of its surface. The common modes of operation used for AFM measurements are: 1) contact mode, where the tip touches the sample and is dragged across its surface, 2) non-contact mode, where the tip is maintained at a height where it floats above the sample surface, and 3) tapping mode, in which the tip intermittently contacts the sample surface. For scanning under contact mode, the tip is maintained in contact with the sample under a constant force, and changes in the sample height cause deflections in the cantilever. For non-contact and tapping mode, the tip is deliberately vibrated at or close to the resonance frequency of

the cantilever, and as the oscillating tip is brought close to the sample, tip-sample interactions result in changes in the amplitude of the oscillations. [54-56] These deflections are measured using a laser reflected off of the back of the cantilever. The laser is reflected onto a photodiode array, and tip deflections caused by the sample topography result in a shift in the position of the laser on the photodiode array. A height profile of the scanned area on the surface is produced, providing us with information on the uniformity of our deposited films.

In this work, a Bruker Dimension Icon AFM at James Madison University and a Hitachi AFM 5300 at ARL were employed for the AFM studies in Chapter 5. Gwyddion software [57] was used for analysis of AFM micrographs. This analysis software allows us to quantify the roughness of a surface measured with AFM, provide line profiles across an AFM micrograph area, and statistically characterize areas (i.e., measure surface coverage) by thresholding with the use of suitable image masking, among other features.

2.2.4 Transmission Electron Microscopy (TEM)

Transmission electron microscopy (TEM) relies on transmission of electrons through an electron transparent sample ($\leq$ 100 nm thick) to project an image of the atoms in the material onto a screen. A series of electromagnetic lenses are used to bend, focus, and direct the electron beam in vacuum towards the sample being imaged. As the electron beam is transmitted through the sample, if the sample is a crystalline material, the ordered structure of the atoms in space produces a diffraction pattern due to its interaction with the electron beam. Obtaining sharp diffraction spots requires ensuring that the crystal is flat with respect to the beam, having knowledge of the sample orientation, and aligning the sample to the electron beam by tilting appropriately. Features in a TEM image can originate from “diffraction contrast” or “mass-thickness contrast”, among others. Depending on the aperture set-up, a bright-field image (from transmitted electrons) or a dark-field image (only from specific diffracted electrons) can be generated, providing diffraction contrast in crystalline materials. On the other hand, mass-thickness contrast does not require an objective aperture selecting only specific transmitted or diffracted electrons. Instead, mass-thickness contrast arises from differences in atomic number and material thickness, due to elastic scattering of the incident electrons from individual atoms. [58]

In Chapters 4.1 and 5.2, TEM sample preparation (thinning to electron transparency) and TEM characterization were performed by collaborators at ARL. To analyze the interfaces in the material stacks we fabricate in this work, samples were cross-sectioned and thinned by mechanical polishing and ion milling using a ThermoFisher Helios G4 UX dual beam focused ion beam-scanning electron microscope (FIB-SEM). TEM analysis was then performed using a JEOL ARM 200F instrument.

2.2.5 Measurement of Ferroelectric Properties

For Chapter 4, where we work with ferroelectric 20 nm films of hafnium zirconium oxide (HZO), the ferroelectricity of the HZO is assessed by measuring its polarization response as a function of applied electric field (P-E). We performed P-E measurements on HZO films that were deposited on a TaN bottom electrode by ALD. Top electrodes (Pd) were sputter deposited onto these samples prior to electrical measurements. Ferroelectric materials are characterized by bi-stable and reversible macroscopic polarization states at a zero applied electric field, called the remanent polarization. The signature of a ferroelectric is a hysteretic P-E loop, as shown in Figure 2.7. To measure this hysteresis cycle, a sufficiently strong electric field is applied across the ferroelectric to switch the polarization from P to $-P$. The applied electric field is typically swept until the saturation polarization is reached in both the positive and negative directions.

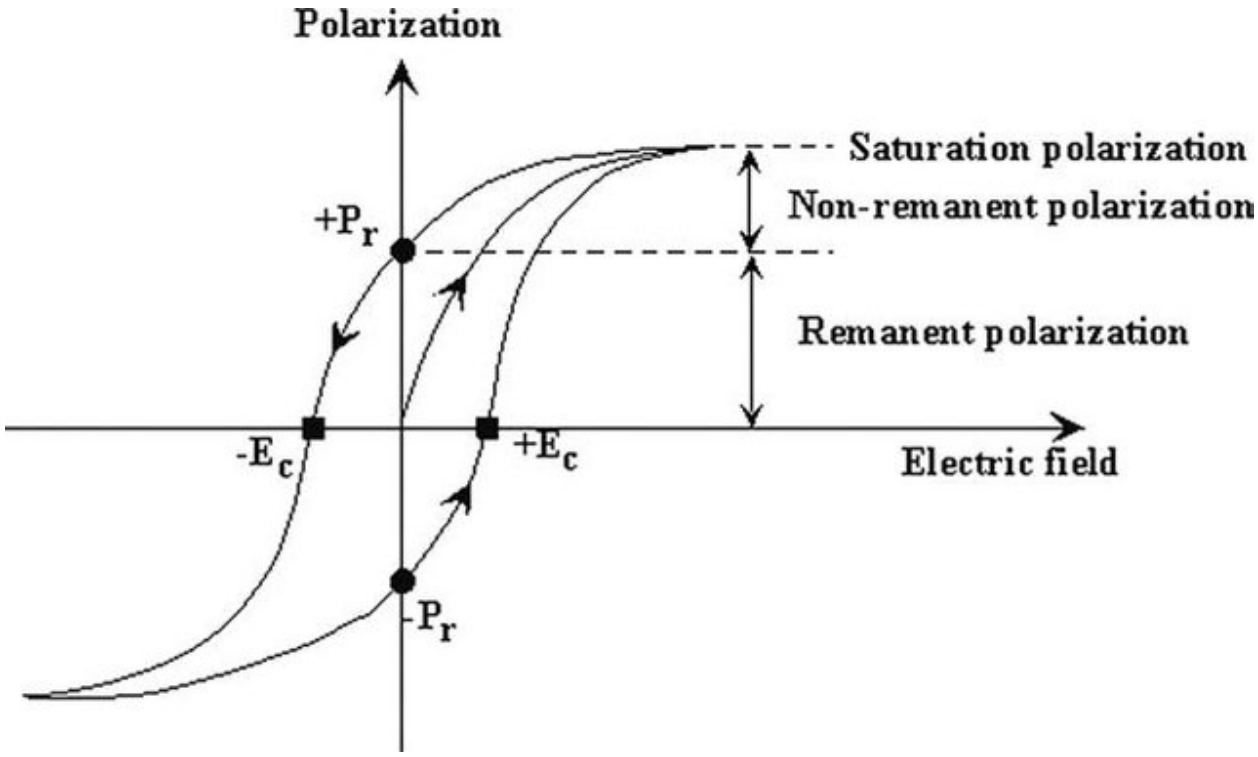

Figure 2.7. Typical polarization vs. electric field (P-E) loop of ferroelectrics [59].

Positive up negative down (PUND) measurements are useful for distinguishing ferroelectric switching from artifacts (i.e., grain boundaries, defects, tunneling through the thin film) that cause leakage through the dielectric, which superimposes curvature in the hysteresis loop that can result in an overestimation of the actual polarization [60]. In PUND measurements, a series of voltage pulses, or a pulse train, is applied to the sample. First, pulse 0 is applied, which is an applied voltage enough to polarize the sample to a definite polarization state. The next pulse, pulse 1, is an applied voltage in the opposite direction to switch the polarization. Then, pulse 2 is applied in the same direction as pulse 1 and should not switch the sample. Pulse 3 is then applied in the opposite direction, switching the polarization back, and finally, pulse 4 is applied in the same direction as pulse 3. A constant time delay between each pulse is set for a given PUND measurement. As shown in Figure 2.8, pulses that result in polarization switching (pulse 1 and 3) due to the opposite direction of the applied voltage, result in a spike in the measured current as a function of time. If a sample is leaky, currents are measured outside of the designated switching pulses. [61]

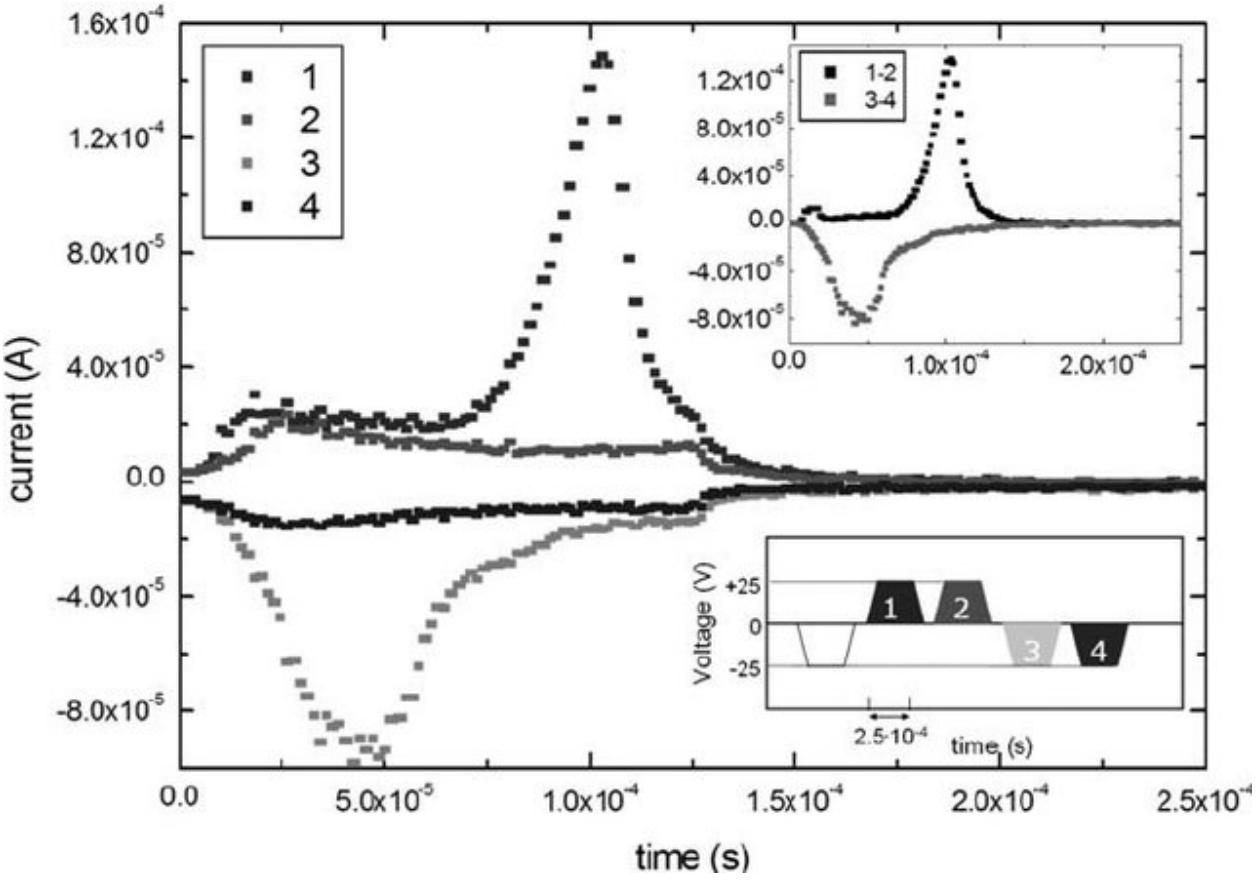

Figure 2.8. Example PUND measurement taken from a sample of ferroelectric $PbTiO_3/SrTiO_3$. Lower inset shows a diagram of the pulse train. Upper inset shows the difference in measured current between the switching and non-switching pulse. [61]

The measured current for the non-switching pulse is subtracted from the switching pulse ($pulse\ 2 - pulse\ 1$ and $pulse\ 4 - pulse\ 3$), as shown in the upper inset of Figure 2.8, and this corresponds to the charge that is switched upon reversal of the polarization state in the ferroelectric material. The integral of this switching current curve is taken to be the polarization. [61]

Ferroelectric measurements such as those described herein can be found in Chapter 4 of this work and were performed by the Ihlefeld group using a Radiant Technologies Precision LC II Ferroelectric Tester.

2.2.6 Field-Effect Transistor Measurements

To electrically characterize our deposited dielectric-on-TMDC stacks in Chapter 5, field-effect transistor devices were fabricated in collaboration with a team at ARL. Devices were tested

in a Lake Shore vacuum probe station using a Keithley 4200-SCS. A diagram of an FET structure similar to the devices we tested is shown in Figure 2.9(a), where “S”, “D”, and “G” are the source, drain, and gate metal contacts, respectively, “ch” is the semiconducting channel, shown in blue, and in gray (“ins”) are gate dielectrics interfaced with the channel. Figure 2.9(a) also highlights important structural parameters/dimensions of the FET components that affect its performance.

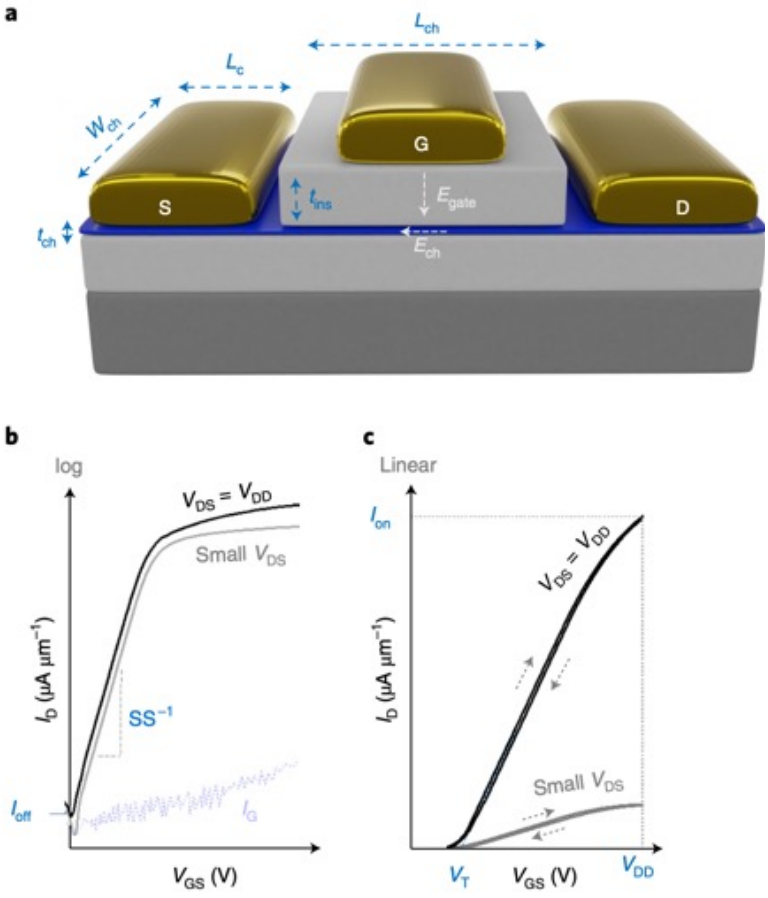

Figure 2.9. (a) FET device structure diagram. (b) Example subthreshold characteristics (off-state). (c) Example transfer characteristics (on-state). [62]

The transfer characteristics of the device are examined by measuring the drain-source current as a function of the gate-source voltage (I_{DS} vs. V_{GS}), at a constant drain-source voltage (V_{DS}). A common performance metric for the switching behavior of FETs is the on/off ratio, or the ratio of the on-current (I_{ON}) to the off-current (I_{OFF}). I_{ON} and I_{OFF} are I_{DS} values measured at a

V_{GS} that is higher and lower, respectively, than the threshold voltage (V_T). As shown in Figure 2.9(c), V_T is determined by extrapolating the region of maximum slope in the linear scale (on-state) transfer curve to $I_{DS} = 0$. In addition, as noted in the figure, a recommended I_{ON} metric, though not always reported in literature, is taking the I_{DS} at V_{DD}, which is the target maximum operation voltage for both V_{GS} and V_{DS}. V_{DD} is defined as the positive supply voltage connected to the drain terminal of the FET. [62, 63]

In the subthreshold region ($V_{GS} < V_T$), the off-state behavior of the FET can be characterized by plotting I_{DS} vs. V_{GS} in the logarithmic scale, as shown in Figure 2.9(b). From this log plot, the subthreshold swing (SS) is obtained by taking the inverse of the slope of the linear region. The SS is an important parameter in certain devices such as analog circuits and low-voltage applications [64].

The gate leakage current (I_G) is also simultaneously measured as V_{GS} is swept. High gate leakage values are caused by conduction through the supposedly insulating gate dielectric, so this allows us to determine the voltage range on the gate that the FET can withstand.

Lastly, we also measure the output curves of our FETs, which are the drain-source current as a function of the drain-source voltage (I_{DS} vs. V_{DS}) at a given constant V_{GS}. Figure 2.10 shows an example I_{DS}-V_{DS} output curve. In the low V_{DS} range, I_{DS} increases linearly with V_{DS} (and V_{GS}). Past a certain drain-source voltage (i.e., $V_{GS} - V_T$ for n-channel FETs), the I_{DS} saturates and is independent of V_{DS}. Note that in the low V_{DS} or linear region, nonlinear/exponential output characteristics can sometimes be observed, as some of our results in Chapter 5.2 show. Such output behavior is attributed to poor carrier injection due to a large Schottky barrier at the metal/semiconductor interface. [62, 65]

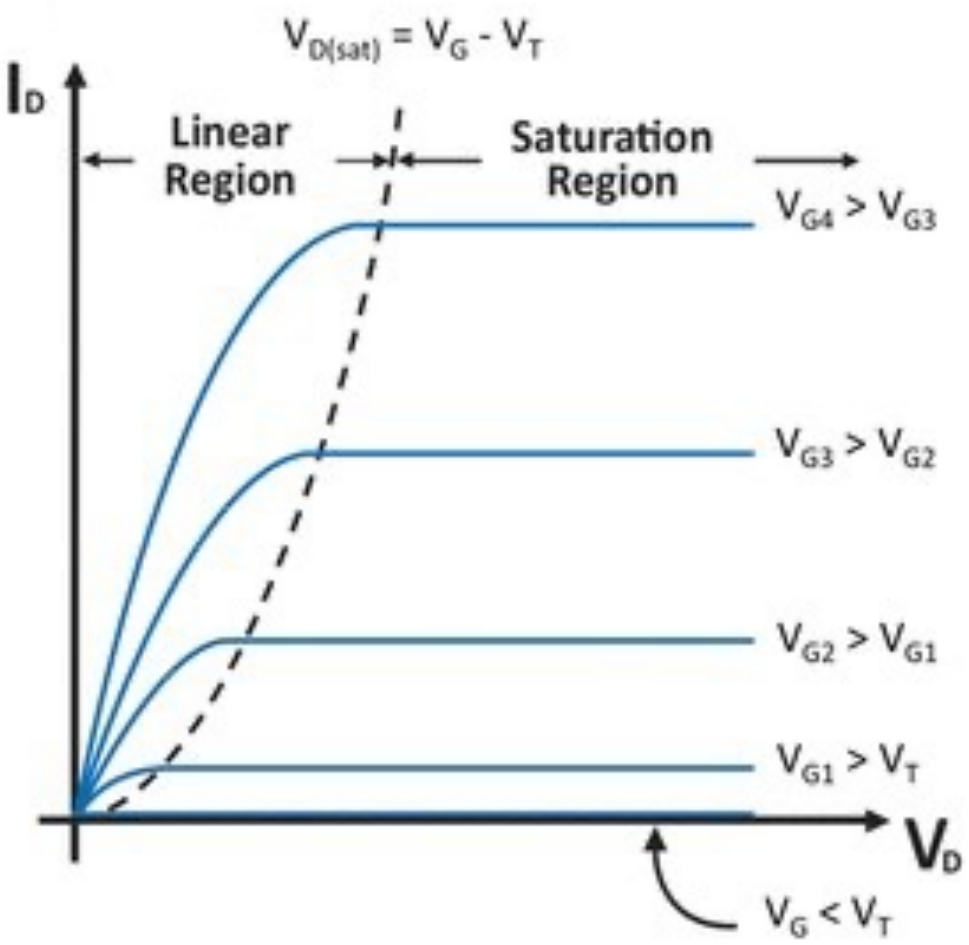

Figure 2.10. Example FET output characteristics [66].

By convention, the positive transfer and output characteristics shown in Figure 2.9 and Figure 2.10 are for n-channel FETs, in which the conducting charge carriers in the channel are electrons. For p-channel FETs, wherein holes are the charge carriers in the channel, the applied voltages would be in the opposite direction, i.e., plotted on the negative x-axis.

2.3 Chapter 2 References

[1] S. M. George, A. W. Ott, and J. W. Klaus, "Surface Chemistry for Atomic Layer Growth," *The Journal of Physical Chemistry,* vol. 100, no. 31, pp. 13121-13131, 1996/01/01 1996, doi: 10.1021/jp9536763.

[2] S. M. George, "Atomic Layer Deposition: An Overview," *Chemical Reviews,* vol. 110, no. 1, pp. 111-131, 2010/01/13 2010, doi: 10.1021/cr900056b.

[3] J. H. Park *et al.*, "Atomic Layer Deposition of Al_2O_3 on WSe_2 Functionalized by Titanyl Phthalocyanine," *ACS Nano,* vol. 10, no. 7, pp. 6888-6896, 2016/07/26 2016, doi: 10.1021/acsnano.6b02648.

[4] W. J. Woo *et al.*, "Bi-layer high-k dielectrics of Al_2O_3/ZrO_2 to reduce damage to MoS_2 channel layers during atomic layer deposition," *2D Materials,* vol. 6, no. 1, p. 015019, 2018/11/22 2018, doi: 10.1088/2053-1583/aaef1e.

[5] W. Li *et al.*, "Uniform and ultrathin high-κ gate dielectrics for two-dimensional electronic devices," *Nature Electronics,* vol. 2, no. 12, pp. 563-571, 2019/12/01 2019, doi: 10.1038/s41928-019-0334-y.

[6] K. M. Price, K. E. Schauble, F. A. McGuire, D. B. Farmer, and A. D. Franklin, "Uniform Growth of Sub-5-Nanometer High-κ Dielectrics on MoS_2 Using Plasma-Enhanced Atomic Layer Deposition," *ACS Applied Materials & Interfaces,* vol. 9, no. 27, pp. 23072-23080, 2017/07/12 2017, doi: 10.1021/acsami.7b00538.

[7] K. M. Price, S. Najmaei, C. E. Ekuma, R. A. Burke, M. Dubey, and A. D. Franklin, "Plasma-Enhanced Atomic Layer Deposition of HfO_2 on Monolayer, Bilayer, and Trilayer MoS_2 for the Integration of High-κ Dielectrics in Two-Dimensional Devices," *ACS Applied Nano Materials,* vol. 2, no. 7, pp. 4085-4094, 2019/07/26 2019, doi: 10.1021/acsanm.9b00505.

[8] J. Yang *et al.*, "Improved Growth Behavior of Atomic-Layer-Deposited High-k Dielectrics on Multilayer MoS_2 by Oxygen Plasma Pretreatment," *ACS Applied Materials & Interfaces,* vol. 5, no. 11, pp. 4739-4744, 2013/06/12 2013, doi: 10.1021/am303261c.

[9] W. Yang *et al.*, "The Integration of Sub-10 nm Gate Oxide on MoS_2 with Ultra Low Leakage and Enhanced Mobility," *Scientific Reports,* vol. 5, no. 1, p. 11921, 2015/07/06 2015, doi: 10.1038/srep11921.

[10] A. Azcatl *et al.*, "MoS_2 functionalization for ultra-thin atomic layer deposited dielectrics," *Applied Physics Letters,* vol. 104, no. 11, p. 111601, 2014/03/17 2014, doi: 10.1063/1.4869149.

[11] A. Azcatl *et al.*, "HfO_2 on $UV–O_3$ exposed transition metal dichalcogenides: interfacial reactions study," *2D Materials,* vol. 2, no. 1, p. 014004, 2015/01/13 2015, doi: 10.1088/2053-1583/2/1/014004.

[12] M. G. Sales, S. T. Jaszewski, S. S. Fields, P. M. Litwin, J. F. Ihlefeld, and S. J. McDonnell, "Thermal stability of hafnium zirconium oxide on transition metal dichalcogenides," *Applied Surface Science,* vol. 546, p. 149058, 2021/04/30/ 2021, doi: https://doi.org/10.1016/j.apsusc.2021.149058.

[13] W. Jaegermann and D. Schmeisser, "Reactivity of layer type transition metal chalcogenides towards oxidation," *Surface Science,* vol. 165, no. 1, pp. 143-160, 1986/01/01/ 1986, doi: https://doi.org/10.1016/0039-6028(86)90666-7.

[14] C. L. Hinkle *et al.*, "GaAs interfacial self-cleaning by atomic layer deposition," *Applied Physics Letters,* vol. 92, no. 7, p. 071901, 2008/02/18 2008, doi: 10.1063/1.2883956.

[15] A. J. SpringThorpe, S. J. Ingrey, B. Emmerstorfer, P. Mandeville, and W. T. Moore, "Measurement of GaAs surface oxide desorption temperatures," *Applied Physics Letters,* vol. 50, no. 2, pp. 77-79, 1987, doi: 10.1063/1.97824.

[16] K. M. Freedy, P. M. Litwin, and S. J. McDonnell, "(Invited) In-Vacuo Studies of Transition Metal Dichalcogenide Synthesis and Layered Material Integration," (in en), *ECS Transactions,* vol. 77, no. 8, pp. 11-25, 2017-05-03 2017, doi: 10.1149/07708.0011ecst.

[17] J. R. Arthur, "Molecular beam epitaxy," *Surface Science,* vol. 500, no. 1, pp. 189-217, 2002/03/10/ 2002, doi: https://doi.org/10.1016/S0039-6028(01)01525-4.

[18] A. Koma, K. Sunouchi, and T. Miyajima, "Fabrication and characterization of heterostructures with subnanometer thickness," *Microelectronic Engineering,* vol. 2, no. 1, pp. 129-136, 1984/10/01/ 1984, doi: https://doi.org/10.1016/0167-9317(84)90057-1.

[19] D. Tsoutsou *et al.*, "Epitaxial 2D $MoSe_2$ ($HfSe_2$) Semiconductor/2D $TaSe_2$ Metal van der Waals Heterostructures," *ACS Applied Materials & Interfaces,* vol. 8, no. 3, pp. 1836-1841, 2016/01/27 2016, doi: 10.1021/acsami.5b09743.

[20] L. A. Walsh *et al.*, "WTe_2 thin films grown by beam-interrupted molecular beam epitaxy," *2D Materials,* vol. 4, no. 2, p. 025044, 2017/03/08 2017, doi: 10.1088/2053-1583/aa61e1.

[21] A. V. Rane, K. Kanny, V. K. Abitha, and S. Thomas, "Chapter 5 - Methods for Synthesis of Nanoparticles and Fabrication of Nanocomposites," in *Synthesis of Inorganic Nanomaterials*, S. Mohan Bhagyaraj, O. S. Oluwafemi, N. Kalarikkal, and S. Thomas Eds.: Woodhead Publishing, 2018, pp. 121-139.

[22] Y. Nie *et al.*, "First principles kinetic Monte Carlo study on the growth patterns of WSe_2 monolayer," *2D Materials,* vol. 3, no. 2, p. 025029, 2016/05/19 2016, doi: 10.1088/2053-1583/3/2/025029.

[23] Y. Nie, C. Liang, P.-R. Cha, L. Colombo, R. M. Wallace, and K. Cho, "A kinetic Monte Carlo simulation method of van der Waals epitaxy for atomistic nucleation-growth processes of transition metal dichalcogenides," *Scientific Reports,* vol. 7, no. 1, p. 2977, 2017/06/07 2017, doi: 10.1038/s41598-017-02919-2.

[24] M. C. Burrell, "Chemical Analysis, Electron Spectroscopy," in *Encyclopedia of Materials: Science and Technology*, K. H. J. Buschow *et al.* Eds. Oxford: Elsevier, 2001, pp. 1142-1149.

[25] J. Chastain and J. F. Moulder, *Handbook of X-ray Photoelectron Spectroscopy: A Reference Book of Standard Spectra for Identification and Interpretation of XPS Data*. ULVAC-PHI, Incorporated, 1995.

[26] "Kolibrik.net, s.r.o. - Custom develompent of electronics and software." http://www.kolibrik.net/ (accessed.

[27] D. A. Shirley, "High-Resolution X-Ray Photoemission Spectrum of the Valence Bands of Gold," *Physical Review B,* vol. 5, no. 12, pp. 4709-4714, 06/15/ 1972, doi: 10.1103/PhysRevB.5.4709.

[28] S. Doniach and M. Sunjic, "Many-electron singularity in X-ray photoemission and X-ray line spectra from metals," (in en), *Journal of Physics C: Solid State Physics,* Text vol. 3, no. 2, 1 February 1970 1970, doi: doi:10.1088/0022-3719/3/2/010.

[29] C. D. Wagner, L. E. Davis, M. V. Zeller, J. A. Taylor, R. H. Raymond, and L. H. Gale, "Empirical atomic sensitivity factors for quantitative analysis by electron spectroscopy for chemical analysis," *Surface and Interface Analysis,* https://doi.org/10.1002/sia.740030506 vol. 3, no. 5, pp. 211-225, 1981/10/01 1981, doi: https://doi.org/10.1002/sia.740030506.

[30] C. R. Brundle and B. V. Crist, "X-ray photoelectron spectroscopy: A perspective on quantitation accuracy for composition analysis of homogeneous materials," *Journal of Vacuum Science & Technology A,* vol. 38, no. 4, p. 041001, 2020/07/01 2020, doi: 10.1116/1.5143897.

[31] C. R. Brundle, B. V. Crist, and P. S. Bagus, "Accuracy limitations for composition analysis by XPS using relative peak intensities: LiF as an example," *Journal of Vacuum Science & Technology A,* vol. 39, no. 1, p. 013202, 2021/01/01 2020, doi: 10.1116/6.0000674.

[32] J. H. Scofield, "Hartree-Slater subshell photoionization cross-sections at 1254 and 1487 eV," *Journal of Electron Spectroscopy and Related Phenomena,* vol. 8, no. 2, pp. 129-137, 1976/01/01/ 1976, doi: https://doi.org/10.1016/0368-2048(76)80015-1.

[33] G. Drera *et al.*, "Transmission function calibration of an angular resolved analyzer for X-ray photoemission spectroscopy: Theory vs experiment," *Journal of Electron Spectroscopy and Related Phenomena,* vol. 195, pp. 109-116, 2014/08/01/ 2014, doi: https://doi.org/10.1016/j.elspec.2014.06.010.

[34] F. J. Himpsel, F. R. McFeely, A. Taleb-Ibrahimi, and J. A. Yarmoff, "Microscopic structure of the SiO_2/Si interface," *Physical Review B,* vol. 38, no. 9, pp. 6084-6096, 1988.

[35] C. J. Powell, "Practical guide for inelastic mean free paths, effective attenuation lengths, mean escape depths, and information depths in x-ray photoelectron spectroscopy," *Journal of Vacuum Science & Technology A,* vol. 38, no. 2, p. 023209, 2020/03/01 2020, doi: 10.1116/1.5141079.

[36] A. Jablonski and C. J. Powell, "The electron attenuation length revisited," *Surface Science Reports,* vol. 47, no. 2, pp. 33-91, 2002/06/01/ 2002, doi: https://doi.org/10.1016/S0167-5729(02)00031-6.

[37] A. Jablonski, "NIST Electron Effective-Attenuation-Length Database," 2011.

[38] S. McDonnell *et al.*, "Controlling the Atomic Layer Deposition of Titanium Dioxide on Silicon: Dependence on Surface Termination," *The Journal of Physical Chemistry C,* vol. 117, no. 39, pp. 20250-20259, 2013/10/03 2013, doi: 10.1021/jp4060022.

[39] S. McDonnell, "Spectroscopic characterisation of high dielectric constant materials on semiconducting surfaces," PhD NonPeerReviewed, National Centre for Sensor Research (NCSR), Dublin City University, 2355, 2009. [Online]. Available: https://doras.dcu.ie/2355/

[40] M. P. Seah and S. J. Spencer, "Ultrathin SiO2 on Si II. Issues in quantification of the oxide thickness," *Surface and Interface Analysis: An International Journal devoted to the development and application of techniques for the analysis of surfaces, interfaces and thin films,* vol. 33, no. 8, pp. 640-652, 2002.

[41] K. Xiong, J. Robertson, M. C. Gibson, and S. J. Clark, "Defect energy levels in HfO_2 high-dielectric-constant gate oxide," *Applied Physics Letters,* vol. 87, no. 18, p. 183505, 2005/10/31 2005, doi: 10.1063/1.2119425.

[42] J. Robertson, K. Xiong, and S. J. Clark, "Band gaps and defect levels in functional oxides," *Thin Solid Films,* vol. 496, no. 1, pp. 1-7, 2006/02/01/ 2006, doi: https://doi.org/10.1016/j.tsf.2005.08.175.

[43] M. Yamamoto *et al.*, "Self-Limiting Layer-by-Layer Oxidation of Atomically Thin WSe_2," *Nano Letters,* vol. 15, no. 3, pp. 2067-2073, 2015/03/11 2015, doi: 10.1021/nl5049753.

[44] R. Addou *et al.*, "One dimensional metallic edges in atomically thin WSe_2 induced by air exposure," *2D Materials,* vol. 5, no. 2, p. 025017, 2018/03/09 2018, doi: 10.1088/2053-1583/aab0cd.

[45] A. N. Hoffman *et al.*, "Tuning the electrical properties of WSe_2 via O_2 plasma oxidation: towards lateral homojunctions," *2D Materials,* vol. 6, no. 4, p. 045024, 2019/07/24 2019, doi: 10.1088/2053-1583/ab2fa7.

[46] Y. C. Lin *et al.*, "Modification of the Electronic Transport in Atomically Thin WSe_2 by Oxidation," *Advanced Materials Interfaces,* vol. 7, no. 18, p. 2000422, 2020.

[47] A. Nipane *et al.*, "Damage-Free Atomic Layer Etch of WSe_2: A Platform for Fabricating Clean Two-Dimensional Devices," *ACS Applied Materials & Interfaces,* vol. 13, no. 1, pp. 1930-1942, 2021/01/13 2021, doi: 10.1021/acsami.0c18390.

[48] V. A. Gritsenko, A. V. Shaposhnikov, W. M. Kwok, H. Wong, and G. M. Jidomirov, "Valence band offset at silicon/silicon nitride and silicon nitride/silicon oxide interfaces," *Thin Solid Films,* vol. 437, no. 1, pp. 135-139, 2003/08/01/ 2003, doi: https://doi.org/10.1016/S0040-6090(03)00601-1.

[49] S. W. King *et al.*, "Valence and conduction band offsets at amorphous hexagonal boron nitride interfaces with silicon network dielectrics," *Applied Physics Letters,* vol. 104, no. 10, p. 102901, 2014/03/10 2014, doi: 10.1063/1.4867890.

[50] J. DiStefano *et al.*, "Band Alignment at Molybdenum Disulphide/Boron Nitride/Aluminum Oxide Interfaces," *Journal of Electronic Materials,* vol. 45, no. 2, pp. 983-988, 2016/02/01 2016, doi: 10.1007/s11664-015-4255-x.

[51] S. S. Kalanur, Y.-G. Noh, and H. Seo, "Engineering band edge properties of WO_3 with respect to photoelectrochemical water splitting potentials via a generalized doping protocol of first-row transition metal ions," *Applied Surface Science,* vol. 509, p. 145253, 2020/04/15/ 2020, doi: https://doi.org/10.1016/j.apsusc.2020.145253.

[52] N. M. Khusayfan, H. K. Khanfar, and S. R. Alharbi, "Design and characterization of Ge/SeO_2 heterojunctions as tunneling thin film transistors," *Optik,* vol. 265, p. 169520, 2022/09/01/ 2022, doi: https://doi.org/10.1016/j.ijleo.2022.169520.

[53] G. Cappuccio and M. L. Terranova, "Thin film characterisation by advanced X-ray diffraction techniques," Italy, 1996-09-01 1996, Istituto Nazionale di Fisica Nucleare, Frascati (Italy). Lab. Nazionale di Frascati. [Online]. Available: https://www.osti.gov/etdeweb/servlets/purl/465281

[54] Y. Martin, C. C. Williams, and H. K. Wickramasinghe, "Atomic force microscope–force mapping and profiling on a sub 100-Å scale," *Journal of Applied Physics,* vol. 61, no. 10, pp. 4723-4729, 1987, doi: 10.1063/1.338807.

[55] D. Leadley. "Atomic Force Microscopy (AFM)." The University of Warwick Department of Physics. https://warwick.ac.uk/fac/sci/physics/current/postgraduate/regs/mpagswarwick/ex5/techniques/structural/afm/ (accessed.

[56] H. Zhang *et al.*, "Atomic force microscopy for two-dimensional materials: A tutorial review," *Optics Communications,* vol. 406, pp. 3-17, 2018/01/01/ 2018, doi: https://doi.org/10.1016/j.optcom.2017.05.015.

[57] D. Nečas and P. Klapetek. "Gwyddion – Free SPM (AFM, SNOM/NSOM, STM, MFM, …) data analysis software." http://gwyddion.net (accessed.

[58] B. Fultz and J. M. Howe, *Transmission Electron Microscopy and Diffractometry of Materials* (Graduate Texts in Physics). Springer Berlin Heidelberg, 2012.

[59] N. Izyumskaya, Y. I. Alivov, S. J. Cho, H. Morkoç, H. Lee, and Y. S. Kang, "Processing, Structure, Properties, and Applications of PZT Thin Films," *Critical Reviews in Solid State and Materials Sciences,* vol. 32, no. 3-4, pp. 111-202, 2007/12/07 2007, doi: 10.1080/10408430701707347.

[60] J. F. Scott, "Ferroelectrics go bananas," *Journal of Physics: Condensed Matter,* vol. 20, no. 2, p. 021001, 2007/12/13 2008, doi: 10.1088/0953-8984/20/02/021001.

[61] K. M. Rabe, M. Dawber, C. Lichtensteiger, C. H. Ahn, and J.-M. Triscone, *Modern physics of ferroelectrics: Essential background*. Springer, 2007.

[62] Z. Cheng *et al.*, "How to report and benchmark emerging field-effect transistors," *Nature Electronics,* vol. 5, no. 7, pp. 416-423, 2022/07/01 2022, doi: 10.1038/s41928-022-00798-8.

[63] C. Hu, *Modern Semiconductor Devices for Integrated Circuits*. Prentice Hall, 2010.

[64] E. P. Vandamme, P. Jansen, and L. Deferm, "Modeling the subthreshold swing in MOSFET's," *IEEE Electron Device Letters,* vol. 18, no. 8, pp. 369-371, 1997, doi: 10.1109/55.605442.

[65] A. Borah, A. Nipane, M. S. Choi, J. Hone, and J. T. Teherani, "Low-Resistance p-Type Ohmic Contacts to Ultrathin WSe_2 by Using a Monolayer Dopant," *ACS Applied Electronic Materials,* vol. 3, no. 7, pp. 2941-2947, 2021/07/27 2021, doi: 10.1021/acsaelm.1c00225.

[66] M. H. Boratto, "Semiconducting and Insulating oxides applied to electronic devices," 2018.

3 Spectroscopic Studies of Impurities in Geological MoS_2 Crystals

This chapter discusses X-ray photoelectron spectroscopy (XPS) investigations of geological crystals of MoS_2, which naturally occur on the surface of the earth as molybdenite minerals. Geological MoS_2 crystals are commercially available from different vendors, and because of the ease of acquiring them, these crystals are typically used by the 2D materials research community for studying the electronic properties of MoS_2 and fabricating various MoS_2-based device architectures. Single- or few-layer MoS_2 can be isolated from a geological piece by mechanical exfoliation with scotch tape, subsequently followed by transfer to a suitable device stack for testing. However, because these crystals are mined from the earth, they are known to possess a number of unintentional intrinsic defects, which include structural and chemical inhomogeneities, variable doping, and the presence of various impurity elements, as previously reported in literature by other groups. Our work discussed in this chapter specifically highlights the presence of large bismuth impurity clusters found in geological MoS_2. Such clustered impurities raise important concerns about the difficulty of obtaining large-area MoS_2 with uniform properties, which is a critical requirement if MoS_2 were to be widely integrated in commercial electronic devices in the future. The work presented in this chapter emphasizes and motivates the need for controlled growth methods for MoS_2 and other transition metal dichalcogenides (TMDCs) in order to achieve uniform and large-area 2D materials with high purity, avoiding the many limitations currently provided by geological material.

3.1 Abstract

Molybdenum disulfide (MoS_2) is the most widely studied transition metal dichalcogenide (TMDC) material, in part because it is a natural crystal present in the earth, thus making it abundant and easily accessible. Geological MoS_2 has been used in various studies that look at incorporating MoS_2 into devices for nanoelectronics and optoelectronics. However, variations in the electronic properties of a single MoS_2 surface are known to exist due to defects that are intrinsic to natural MoS_2. This work reports the presence of bismuth impurities in MoS_2 with concentrations high enough to be detected by X-ray photoelectron spectroscopy (XPS). These concentrations are further corroborated with inductively coupled plasma optical emission spectroscopy (ICP-OES). Localization of these bismuth clusters is shown using XPS mapping, and the cluster size is determined to be on the order of tens of microns. This work provides important insights into the nature of impurities that are known to exist in MoS_2. The presence of bismuth clusters in geological MoS_2 material highlights the difficulty of obtaining large-area uniform and pristine MoS_2 in geological crystals.

3.2 Introduction

Since the demonstration of the unique electronic properties of isolated graphene [1], there has been renewed interest in similarly structured 2D materials for new applications in next-generation electronics. Of note are the transition metal dichalcogenides (TMDCs), which, for specific metal and chalcogen combinations, can be semiconducting materials whose band gaps are tunable with thickness, making them a versatile material with a wide range of possible applications. By far the most widely studied TMDC is molybdenum disulfide or MoS_2. Like graphene/graphite, MoS_2 is easily accessible because it is a naturally occurring compound and is commercially available. Several studies have reported the use of geological MoS_2 flakes in devices for applications in nanoelectronics [2-4], optoelectronics [5-7], batteries [8], biosensors [9, 10], and hydrogen production [11-13], among others.

Geological MoS_2 is known to have various intrinsic defects which have been explored for several years. A known issue with geological MoS_2 material is its variability in doping across at least tens of nanometers of spatial resolution, which is attributed to defects in the MoS_2 crystal

[14]. Variability in the doping and electronic properties of the starting MoS_2 is attributed to structural and chemical non-uniformities that are a characteristic of geological material. Such variations may greatly affect the properties of any device into which the material is integrated. A prior study observed a correlation between n-type regions and S vacancies or metallic Mo-like clusters, while p-type regions were correlated with regions of high structural defect density in the crystal [14]. Related to this doping variability, ring-like structures a few nanometers in diameter have been found in scanning tunneling microscopy (STM) studies of geological MoS_2, and these have been attributed to the electronic effect of the presence of impurity point defects acting as dopants in MoS_2 [15, 16]. A separate study [17] reported the various defects experimentally observed on the surface of geological MoS_2 with STM, and these include pits, step edges, voids underneath the top surface, local surface reconstructions, and point defects like vacancies and impurities.

Similarly structured defects have been found in WSe_2 materials obtained from different sources or synthesis methods, such as chemical vapor deposition (CVD) [18], molecular beam epitaxy (MBE) [19], and commercially available single-crystal pieces [20] (which are commonly grown by chemical vapor transport (CVT) or flux zone growth [21, 22]). A study by Ding et al. [23] compared the quantity of point defects from these three sources for WSe_2 (CVD-grown, MBE-grown, and commercial), and they reported that CVD-grown WSe_2 had the highest concentration and most varied types of point defects, with the MBE and commercial single-crystal samples having comparable point defect characteristics and quantities. Chapter 4 of this dissertation focuses on an MBE WSe_2 growth method used as a technique for direct integration onto devices.

For commercially available WSe_2, which can be purchased from the same vendors that offer geological MoS_2 crystals, our group has found that some of these WSe_2 samples may contain contaminants. The contaminant elements that we found likely come from other CVT- or flux-zone-grown TMDCs sold commercially, especially if the same growth chamber is used for different TMDCs sold by the company. Figure 3.1 shows X-ray photoelectron spectroscopy (XPS) measurements of a WSe_2 crystal, purchased from SPI Supplies [21], that we found to be contaminated with some iodine and tellurium. Iodine is a common transport agent for CVT crystal growth [24], and tellurium is another chalcogen atom also used in TMDC compounds.

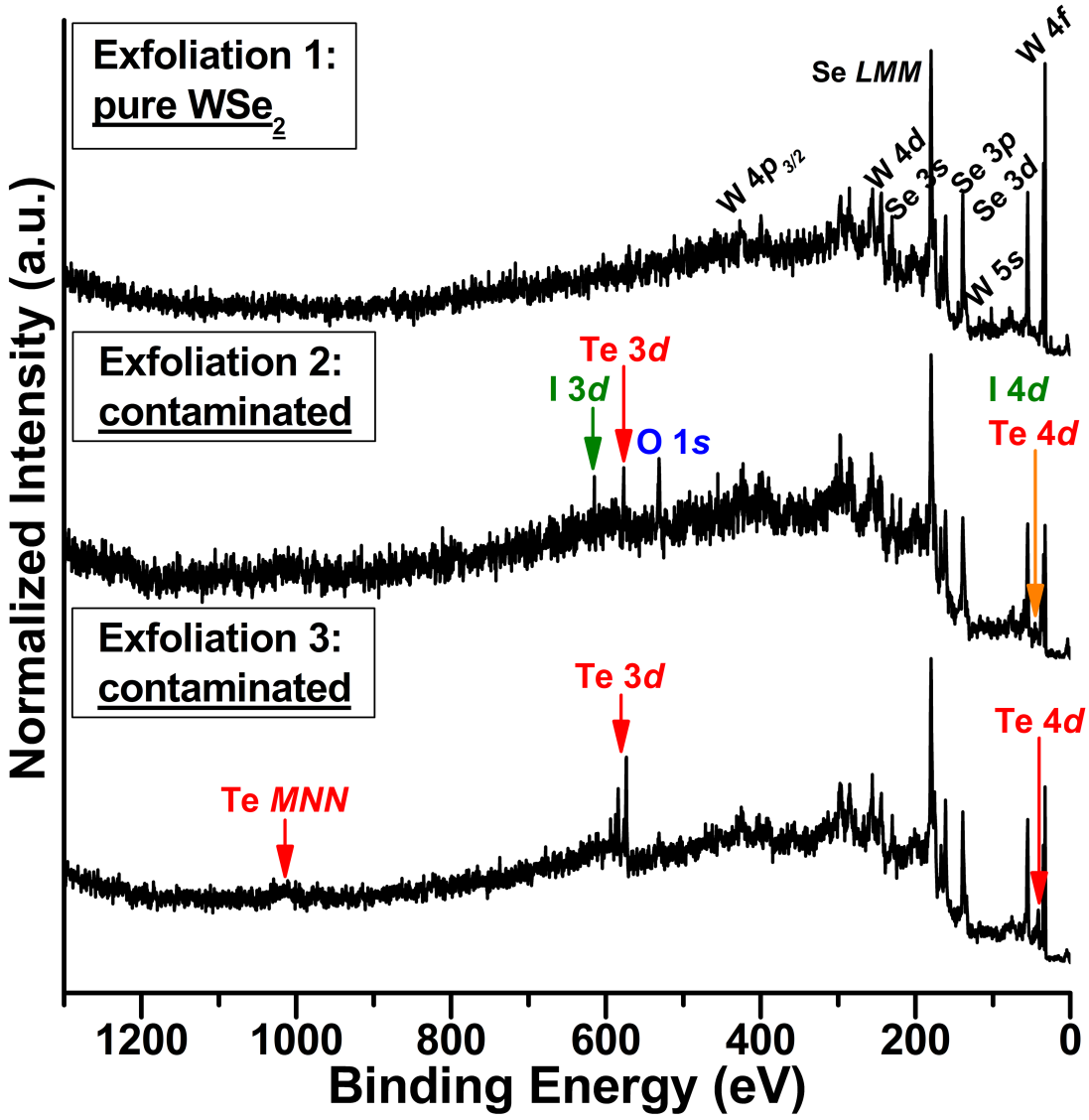

Figure 3.1. XPS survey spectra taken from the same WSe_2 crystal that was mechanically exfoliated three times. Exfoliations 2 and 3 revealed the presence of impurity elements in the sample. The extra survey peaks from impurity elements are labeled in the figure with colored arrows.

TMDC materials that are not grown synthetically can also contain impurities. In natural/geological MoS_2 material, the presence of impurity elements has been shown through various mass spectroscopy techniques [15-17, 25]. Addou et al. report bismuth to be the most abundant trace element in natural MoS_2, at ~20 parts per million by weight (ppmw) [25]. In the present study, it is reported that Bi is sometimes observed in geological MoS_2 with XPS, indicating

that there are localized regions in which the Bi concentrations are higher than ~0.1%, which is the typical detection limit of XPS [26]. The chemical state of these Bi impurities is determined. Estimates of the impurity size and distribution across the MoS_2 surface are also reported.

3.3 Material and Methods

Geological MoS_2 crystals (Graphene Supermarket [27]) were cleaned by mechanical exfoliation with scotch tape which removed the top most layers of MoS_2, leaving a freshly exposed crystal surface. These samples were then loaded into ultra-high vacuum (UHV) for X-ray photoelectron spectroscopy (XPS) in less than 30 min. XPS spectra were acquired using monochromated Al Kα X-rays (1486.7 eV) at a pass energy of 26 eV in a PHI VersaProbe III system. This XPS tool is also equipped with a scanning X-ray induced (SXI) secondary electron imaging feature for accurate point selection in the micrometer range, and a variety of X-ray spot sizes ranging from 9 to 200 μm. Spectra of geological MoS_2 from another vendor (SPI Supplies [21]) are shown in Figure 3.2 to confirm that Bi is detected from more than one material source, but all XPS analyses shown in the Results and Discussion section are of MoS_2 from Graphene Supermarket.

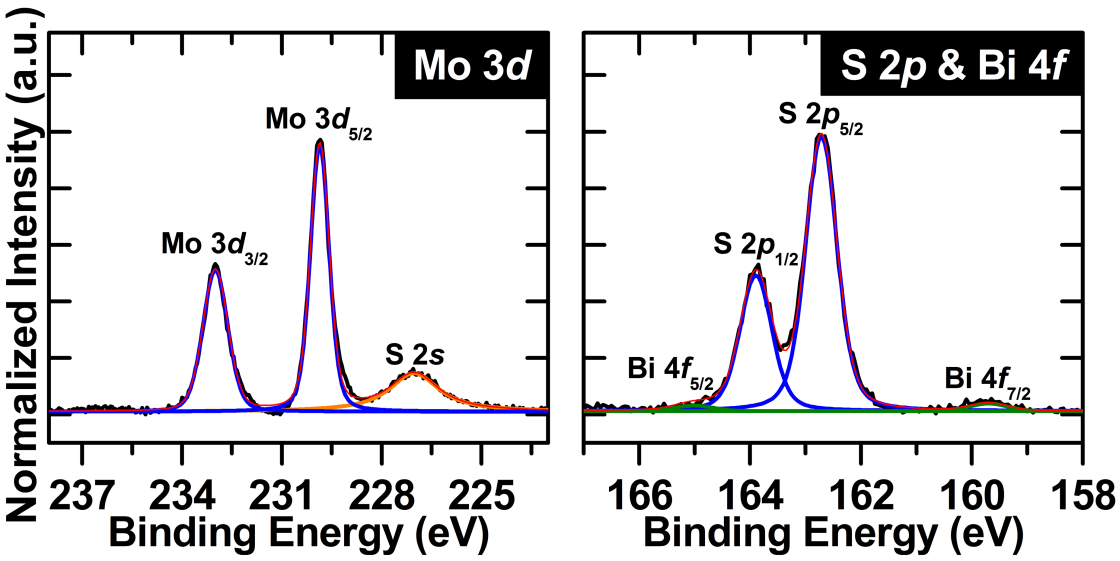

Figure 3.2. Representative XPS spectra of geological MoS_2 from SPI Supplies showing the presence of Bi impurities.

XPS mapping was performed by selecting a random area of the crystal and through the SXI imaging mode, setting up an array of points that are 100 μm apart horizontally and vertically. The Mo 3*d* and S 2*p* spectra were taken at each of these points using an X-ray beam spot size of 100 μm. The points analyzed were within an 800 μm x 800 μm area, for a total of 81 spots checked. These spectra were batch processed using the PHI MultiPak software in order to identify which of the 81 points had Bi peaks present from XPS.

A particle/cluster size check of the bismuth impurities was achieved by centering the X-ray spot on a Bi impurity, and without moving the sample, using different X-ray beam spot sizes: 9 μm, 15 μm, 20 μm, 50 μm, 100 μm, and 200 μm. This changes the size of the area that is scanned without changing the central spot (approximated center of the Bi impurity). The given X-ray beam spot sizes correspond to an analysis spot of roughly the same area on the sample. All XPS peak fitting in this work to obtain areas of the Mo 3*d*, S 2*p*, and Bi 4*f* features was carried out using kolXPD software [28]. All peaks were fit with Voigt lineshapes.

Inductively coupled plasma optical emission spectroscopy (ICP-OES) measurements were collected by the Opila research group to support the XPS measurements. A 7 mg geological MoS_2 flake (SPI Supplies) was placed inside a high-purity polypropylene centrifuge (VWR International) tube filled with a 13 mL H_2O and 2 mL HNO_3 acid containing solution. Digestion of MoS_2 was performed for several days in a 40 °C water bath with intermittent sonication. Upon completion of digestion, 3-4 emission lines each from Bi, W, Ag, Cd, Fe Re and Ca were detected using ICP-OES (Duo Spectrometer iCAP 6200, ThermoFisher Scientific). The reported concentrations (in ppmw) are averages from all emission lines for a given element.

3.4 Results and Discussion

3.4.1 XPS of MoS_2 with Bismuth

Shown in Figure 3.3 is a typical XPS spectra of MoS_2 with the additional peaks corresponding to Bi impurities in the geological crystal. Using a 100 μm X-ray beam spot, peaks that are not attributed to MoS_2 were sporadically found at approximately 159.5 eV and 164.8 eV, which correspond to Bi $4f_{7/2}$ and Bi $4f_{5/2}$, respectively. Elemental Bi 4*f* peaks are expected at around

157 eV and 162 eV, which are more than 2 eV lower. This suggests that the Bi impurities that have been known to exist in geological MoS_2, as demonstrated in previous studies [25], are not metallic Bi impurities. Based on the peak positions in our XPS analyses, it can be confirmed that these Bi impurities exist in the MoS_2 as bismuth oxide or bismuth sulfate.

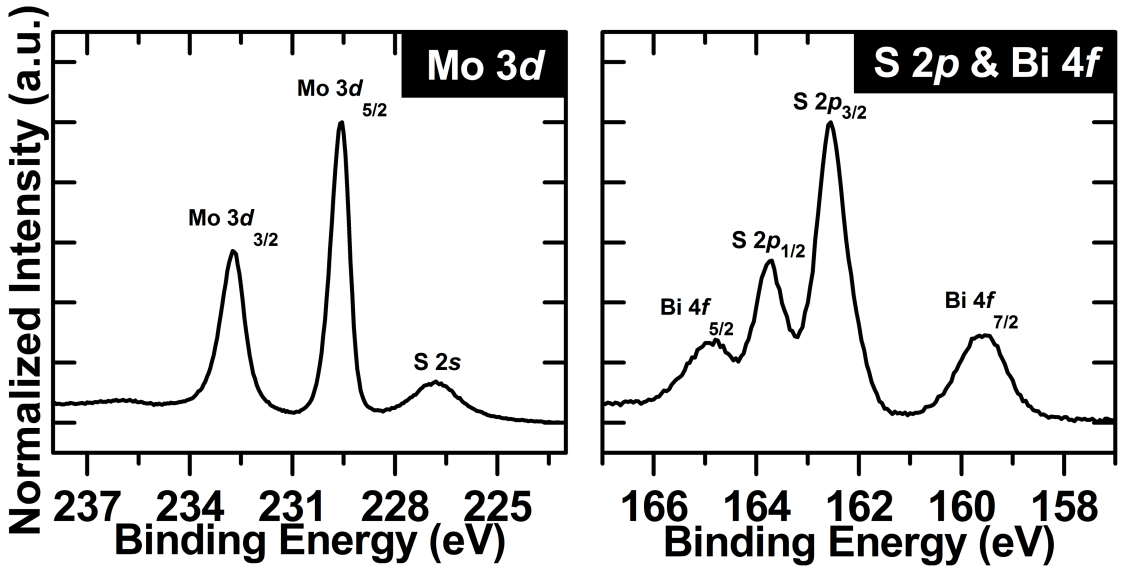

Figure 3.3. Mo 3d and S 2p regions of a geological MoS_2 crystal showing additional peaks corresponding to Bi. Spectra taken with a 100 μm X-ray beam spot size.

3.4.2 XPS Mapping

The Mo 3*d* and S 2*p* regions were taken at 81 spots in an 800 μm x 800 μm XPS map set up, as presented in Figure 3.4(a). The results from this 800 μm x 800 μm area is assumed to be representative of the entire MoS_2 crystal because this area was chosen at random in the middle of a region where the MoS_2 appeared to be smooth. The distribution of bismuth found through XPS mapping reveals that these Bi impurity compounds are present at random localized spots of the bulk geological MoS_2 crystal. A map of Bi $4f_{7/2}$ intensities normalized to the S $2p_{3/2}$ peak found through XPS is shown in Figure 3.4(b), which clearly exhibits how localized these Bi impurities are. Out of the 81 analyzed spots, 12 were seen to have a Bi 4*f* feature, the majority of which are

localized in regions which are a few hundred microns across. The normalized spectra of the 12 points with detectable Bi presence are shown in Figure 3.4(c). It can be seen that their Mo 3*d* spectra are almost the same except for some peak shifting which is likely due to variable doping [14]. However, major differences are evident in the S 2*p* & Bi 4*f* region because of varying intensities of the Bi 4*f* features. The spectrum with the highest Bi feature relative to S 2*p* is shown as the blue curve, while the one with the lowest non-zero Bi 4*f* peak area is shown as the red curve. Normalized to the maximum of the S 2*p* peak (as in Figure 3.4(c)), the Bi intensity of the blue curve is almost 50 times greater than that of the red curve.

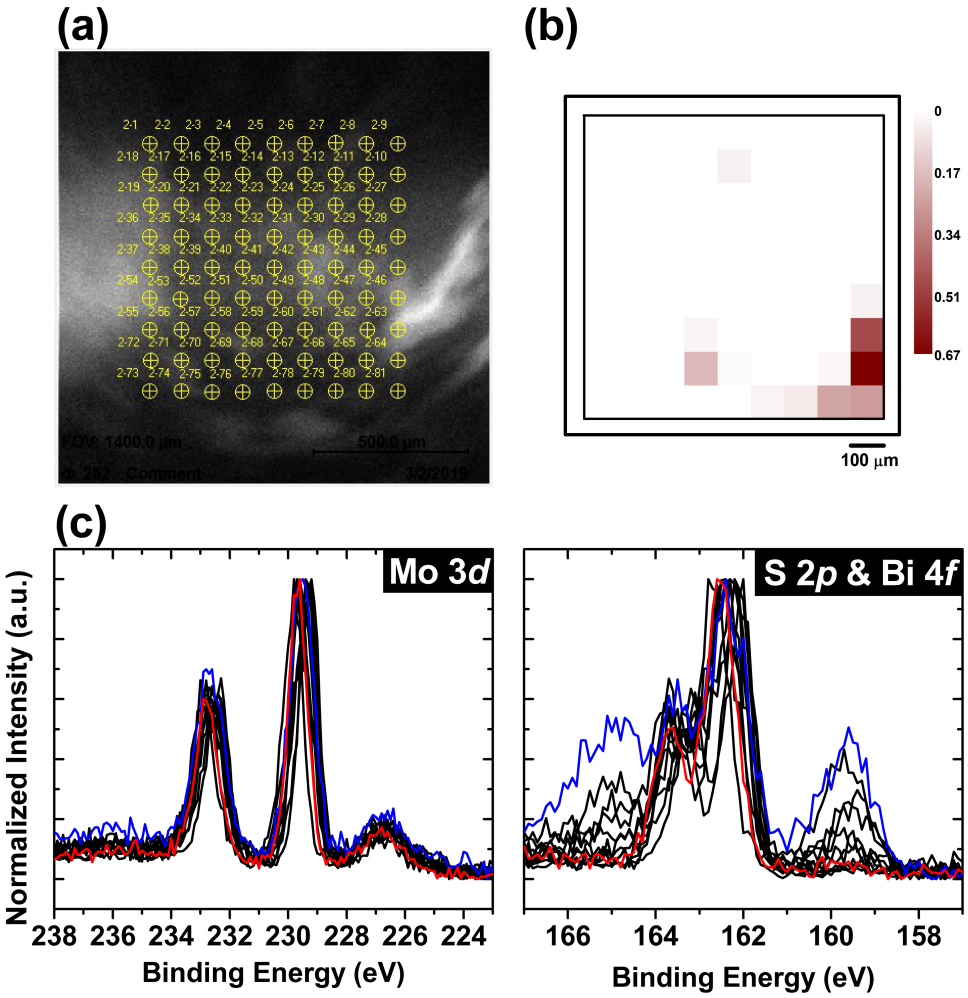

Figure 3.4. (a) Set-up of the array of 81 points spaced 100 µm apart for XPS mapping on an 800 µm x 800 µm surface of geological MoS_2. (b) Map of normalized Bi intensities obtained through XPS mapping. (c) Normalized spectra of the 12 analysis spots that were found to have some amount of Bi.

It is worth noting that concentrations calculated using relative sensitivity factors (RSFs) assume a homogenous distribution. As will be discussed later, it is likely that all of the Bi clusters observed in this work are actually covered with layers of MoS_2, therefore their intensities are attenuated. Simply averaging all intensities and applying sensitivity factors would result in a gross underestimation of the Bi concentration. However, concentrations calculated from each individual spot in the XPS map can still give a sense of the amount of Bi detected in the area analyzed.

The Bi concentration in each of the 12 spots that showed Bi presence in the XPS map (Figure 3.4) can be calculated based on the following equation, assuming only Mo, S, and Bi are detected in each spot:

$$Bi\ concentration\ (\%) = \frac{\frac{I_{Bi\ 4f}}{Bi\ 4f\ RSF}}{\frac{I_{Mo\ 3d}}{Mo\ 3d\ RSF}+\frac{I_{S\ 2p}}{S\ 2p\ RSF}+\frac{I_{Bi\ 4f}}{Bi\ 4f\ RSF}} \times 100 \qquad (1)$$

where I_X is the intensity of the X core level peak, and the PHI-recommended RSFs, corrected for the geometry of the PHI VersaProbe III system used, are as follows:

Mo 3*d* RSF = 87.535; S 2*p* RSF = 17.497; Bi 4*f* RSF = 244.962

Table 3.1. Calculated Bi concentrations in the 12 spots with Bi presence (shown in Figure 3.4) using Mo 3d, S 2p, and Bi 4f peak intensities and RSFs.

Spot Number (based on Figure 3.4(a))	$I_{Mo\ 3d}$	$I_{S\ 2p}$	$I_{Bi\ 4f}$	$\frac{I_{Mo\ 3d}}{Mo\ 3d\ RSF}$	$\frac{I_{S\ 2p}}{S\ 2p\ RSF}$	$\frac{I_{Bi\ 4f}}{Bi\ 4f\ RSF}$	**Bi concentration (%)**
2-14	2666	1095	55	30.5	62.6	0.2	**0.24**
2-46	9251	3703	237	105.7	211.6	1.0	**0.30**
2-58	5359	2109	81	61.2	120.5	0.3	**0.18**
2-63	3521	1238	1061	40.2	70.8	4.3	**3.76**
2-64	2890	1246	1096	33.0	71.2	4.5	**4.11**
2-65	4795	1953	42	54.8	111.6	0.2	**0.10**
2-68	3396	1393	27	38.8	79.6	0.1	**0.09**

2-69	2982	1240	287	34.1	70.9	1.2	**1.10**
2-78	2711	1025	44	31.0	58.6	0.2	**0.20**
2-79	2372	935	71	27.1	53.4	0.3	**0.36**
2-80	1728	665	220	19.7	38.0	0.9	**1.53**
2-81	2110	768	269	24.1	43.9	1.1	**1.59**

Averaging the last column over 81, which is the total number of spots analyzed in the XPS map, the estimated Bi concentration in the 800 μm x 800 μm area analyzed is approximately 0.17%. Note that the Bi concentration in all other spots not included in Table 3.1 were assumed to be 0%. The average concentration of 0.17% over the entire area in Figure 3.4(b) is close to the typical limit of detection of XPS, ~0.1% [26]. This would explain why Bi is not typically detected in studies which show XPS spectra of geological MoS_2 [5, 9, 12, 14, 17, 25, 29, 30], specifically when using conventional spot sizes in the millimeter range, which would average over a larger area on the sample surface compared to what we use in this work.

3.4.3 Cluster Size Determination

It was found that regions with Bi in geological MoS_2 are on the order of hundreds of microns, however we note that this does not necessarily mean that this is the size of a single impurity. This region could be composed of clusters of Bi impurity particles which would be indistinguishable from a single large inclusion from our measurements. We are able to estimate the size of the clusters by focusing on the Bi cluster and varying X-ray beam spot sizes from 200 to 9 μm. By doing so, we are able to scan the same central spot on the sample but change the radius of the area around it that is scanned with XPS. As we vary the spot size from large to small, we expect to see changes in the Bi:S ratio as the percentage of the area being dominated by Bi changes. We expect one of three possible changes in this ratio. 1) The Bi:S ratio increases to a point where the S signal becomes zero. This would be interpreted as a Bi cluster on top of MoS_2. The cluster size in this case would be bigger than the X-ray spot size at the point when the MoS_2 signal dropped to zero. Therefore, the cluster size would be estimated to be between that of the X-ray beam spot sizes that could detect and could not detect S. 2) The Bi:S ratio increases to a point and plateaus. This would be interpreted as a Bi cluster that is bigger than the spot size at the point when the ratio

plateaus, but with the cluster being below some layers of MoS_2 (hence the Mo and S signals never decay to zero). 3) No change in the Bi:S ratio. This would be determined as a cluster that is bigger than 200 µm, but still below MoS_2 layers.

The normalized Mo 3*d* and S 2*p* spectra of two different spots in the MoS_2 that have Bi impurities are shown in Figure 3.5. It is evident in Figure 3.5(a) that the Bi 4*f* features at small spot sizes have comparable intensities, and above a critical spot size, the peak intensity of the Bi 4*f* feature drops relative to the S 2*p* peak.

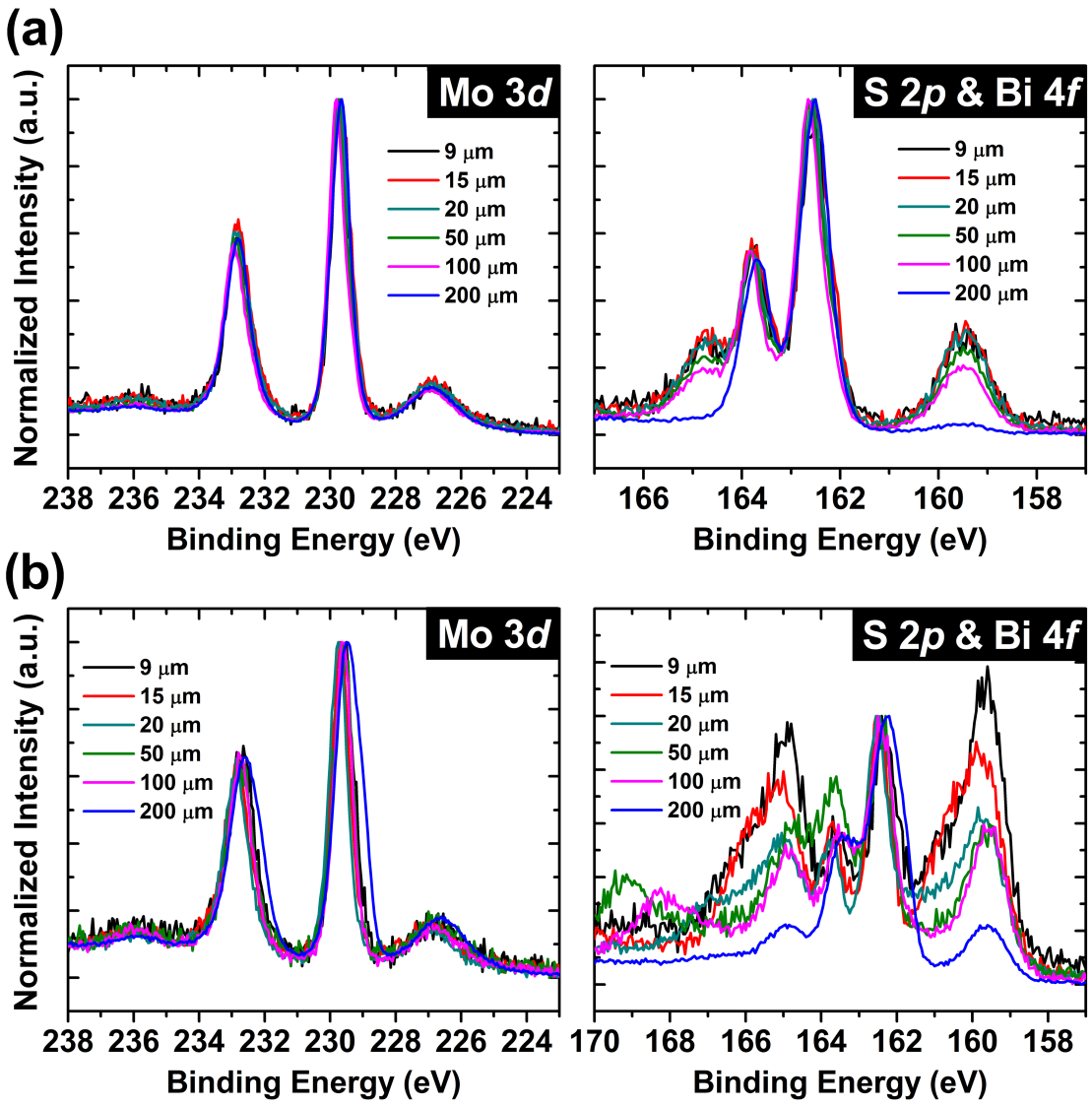

Figure 3.5. Normalized spectra of (a) analysis spot 1 and (b) analysis spot 2, taken with varying X-ray spot sizes.

For Figure 3.5(b), which is a second analysis spot, the Bi feature is composed of two chemical states, one of the typical Bi 4*f* peak positions present in MoS_2 as shown in Figure 3.3, and a second bismuth peak at higher binding energy. A deconvolution of the spectrum taken with the 9 μm X-ray beam spot is shown in Figure 3.6, wherein the presence of two Bi oxidation states, Bi^{3+} and Bi^{5+}, is exhibited. The peaks for Bi^{3+} are at 159.6 eV and 164.9 eV, while the Bi^{5+} peaks are at 160.9 eV and 166.2 eV, which agree with peak assignments of bismuth oxidation states in other reports [31, 32]. Bi_2O_3 (Bi^{3+}) is the most thermodynamically stable form of bismuth oxide, but Bi_2O_5 (Bi^{5+}) and other oxidation states, Bi^{2+} and Bi^{4+}, can form from the stable Bi_2O_3 phase when it is heated to 1100-1300 K [33]. Some of the spectra in the S 2*p* region of Figure 3.5(b) also show extra features at around 168 to 169 eV, which indicates the presence of some sulfate. Because Bi_2O_3 and $Bi_2(SO_4)_3$ both have an oxidation state of Bi^{3+}, their Bi peaks would appear at similar binding energies [34]. The presence of sulfate peaks in some of our spectra indicate the possibility that some of the bismuth impurities may exist as $Bi_2(SO_4)_3$ compounds. However, it is important to note that XPS only provides information from the surface (5-10 nm) of the clusters, and so the chemical state of the Bi within the core of the clusters remains unknown.

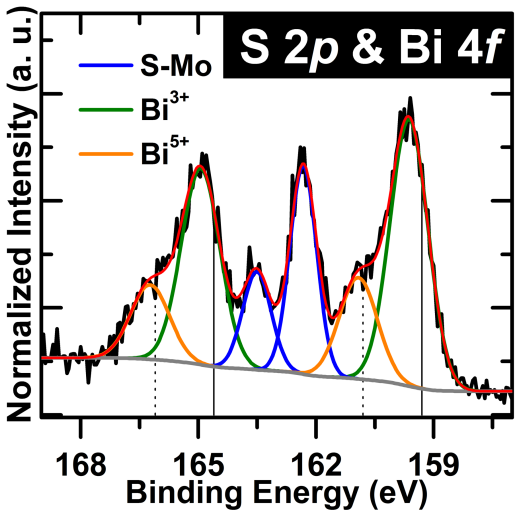

Figure 3.6. Deconvolution of the S 2p region at analysis spot 2 taken with a 9 μm X-ray beam spot. The solid lines represent the binding energies of the Bi^{3+} peaks found from ref. [32]. The dotted lines represent the binding energies of the Bi^{5+} peaks found from ref. [31, 35].

Table 3.2 shows the Bi intensities, normalized to the maximum S 2*p* intensity of each spectrum, at these different spot sizes, which are also plotted in Figure 3.7. The Bi intensities for analysis spot 1 are the normalized intensity of the single Bi peak corresponding to Bi^{3+}, while for analysis spot 2, the reported Bi intensities are the sum of the normalized intensities of the Bi^{3+} and Bi^{5+} states. We assume that the Bi^{5+} was chemically transformed from Bi^{3+}, and thus assign both oxidation states to be part of the same impurity cluster. Table 3.2 and Figure 3.7 clearly show that the Bi signal stays about the same at the smaller spot sizes. At these spot sizes where the normalized Bi intensities are approximately equal, the X-ray beam spot size must be smaller than the impurity cluster size. As the spot size gets bigger, the area that is probed is bigger, and at a critical spot size this area probed becomes bigger than the impurity cluster size. This is seen as a drop in the normalized Bi intensity because there is more MoS_2 that contributes to the signal. For analysis spot 1, the first significant drop in the Bi signal is between 20 and 50 μm, while for analysis spot 2 the first significant drop is between 15 and 20 μm. From this, it can be implied that the size of the impurity analyzed in spot 1 is somewhere between 20 and 50 μm. For analysis spot 2, the impurity size is somewhere between 15 and 20 μm.

Table 3.2. Normalized Bi intensities found using different X-ray beam spot sizes at analysis spots 1 and 2.

X-ray Beam Spot Size	**Normalized Bi Intensity**	
	Analysis Spot 1	**Analysis Spot 2**
9 μm	0.27	1.67
15 μm	0.31	1.67
20 μm	0.30	1.25
50 μm	0.24	0.82
100 μm	0.20	0.86
200 μm	0.02	0.32

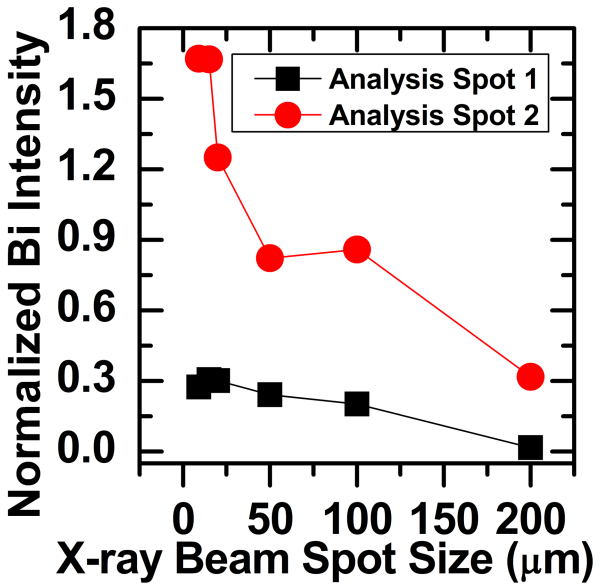

Figure 3.7. Normalized Bi intensities of analysis spots 1 and 2 plotted against X-ray beam spot size.

A key point is that at low spot sizes, while the Bi intensity has increased and plateaued, the detection of MoS_2 has never dropped to zero. Assuming approximately spherical clusters, the > 10 μm diameter can be estimated to imply a > 10 μm depth. This is >> the ~10 nm sampling depth of XPS, and so the MoS_2 would easily be entirely attenuated by a cluster that was on top of the MoS_2. Therefore, we speculate that the observed clusters are actually under at least a few layers of MoS_2. We note that the extreme surface sensitivity of XPS means that clusters underneath anything more than ~10 layers of MoS_2 are likely not detected at all.

It is possible to estimate the thickness of the MoS_2 covering the Bi cluster. This was achieved by comparing the Mo $3d_{5/2}$ intensities of analysis spots 1 and 2 with the same core level intensities for pure geological MoS_2 (i.e., no Bi) scanned using the same XPS settings. The integrated XPS intensity, I, of a layer of certain thickness d is given by Eq. 2 [36].

$$I = I_\infty[1 - \exp\left(-\frac{d}{\ell cos\theta}\right)] \quad (2)$$

In this equation, I is the measured intensity of the overlayer, I_∞ is the intensity of a pure, clean, bulk sample of the same material as the overlayer, d is the overlayer thickness, ℓ is the effective attenuation length of a photoelectron traveling through the overlayer, and θ is the photoelectron

take-off angle measured with respect to the surface normal. Manipulating Eq. 2, the thickness of the overlayer, d, is given by Eq. 3. [36]

$$d = -\ell \cos\theta \ln\left(\frac{I_\infty - I}{I_\infty}\right) \qquad (3)$$

For our purposes, the core level that we use for these equations is Mo $3d_{5/2}$. The effective attenuation length, ℓ, of Mo $3d_{5/2}$ in MoS_2, which is our overlayer, is taken to be 23.815 Å [37]. The photoelectron take-off angle, θ, is 45°, as given by the geometry of the XPS system used. The I_∞ used was the Mo $3d_{5/2}$ peak intensity from pure MoS_2, while I was the Mo $3d_{5/2}$ peak intensity at analysis spot 1 or 2. The peak intensity at analysis spot 1 or 2 is assumed to be the intensity of the overlayer whose thickness we are calculating. The intensities that we used for our calculations were the intensities at 9 μm, which is the smallest X-ray spot size, in order to ensure that the X-ray spot is not bigger than the Bi impurity. This is important so that it is safe to assume that all of the Mo and S signals are from some thickness, d, of MoS_2 on top of the Bi impurity. The calculated MoS_2 overlayer thickness was 3.17 nm for analysis spot 1, and 0.85 nm for analysis spot 2. The thicker overlayer for analysis spot 1 would explain the lower Bi signal, despite it having a bigger Bi impurity based on the spot size analysis.

These findings obtained from varying the spot size at analysis spots 1 and 2 are summarized and represented schematically in Figure 3.8. We show that the size of the X-ray beam spot can help estimate the bismuth cluster size. A drop in the Bi:S intensity ratio indicates that the X-ray spot size used must be greater than the Bi cluster size, and at X-ray spot sizes where the Bi:S ratio is plateaued, the beam spot must be fully within the Bi cluster. We also show that the thickness of the MoS_2 above a detected Bi impurity can be estimated with XPS. Furthermore, by considering this thickness, we can explain why the Bi:S ratio is higher for analysis spot 2 despite the impurity being smaller than that in analysis spot 1.

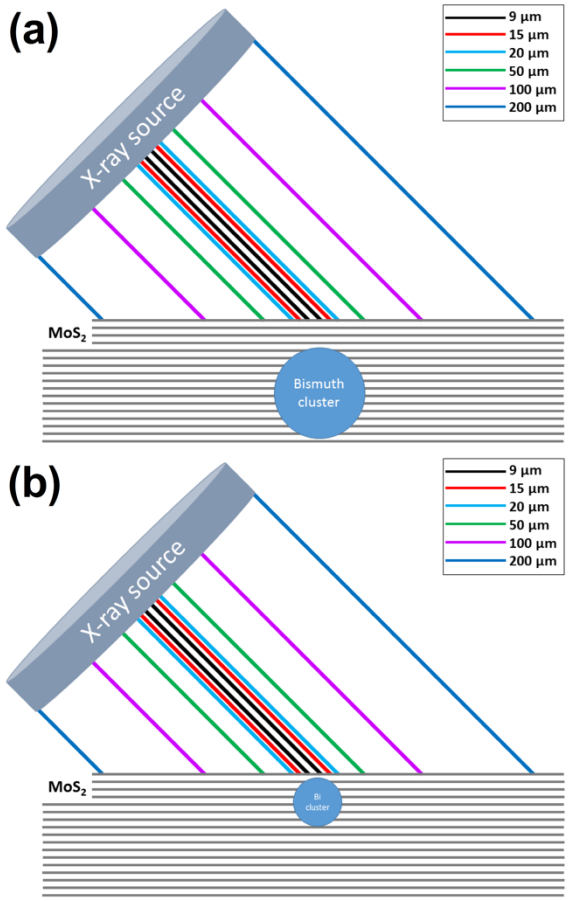

Figure 3.8. Diagrams representing the cluster size and MoS_2 overlayer thickness determined at (a) analysis spot 1 and (b) analysis spot 2.

3.4.4 Impurity Concentrations

The concentration of bismuth in an entire geological MoS_2 sample can be estimated based on our findings from spatially resolved XPS. Taking the area scanned for XPS mapping, 12 out of 81 laterally arranged spots were found to have Bi presence; that is, about 15% of that area contained some form of Bi impurities. Taking that area to be representative of a chunk of geological MoS_2, we can assume that an entire natural MoS_2 crystal is composed of up to 15% Bi. Given that the Bi impurities are not homogenously distributed throughout the material, estimates from XPS are anticipated to be unreliable. Therefore, we performed ICP-OES to determine the

actual concentration of Bi. The concentration of each element measured with ICP-OES is summarized in Table 3.3.

Table 3.3. Results from ICP-OES measurements.

Element	Bi	Mo	Re	S	Sb	W
ppmw	102.04	173.32	1.51	19.18	1.38	0.23
Weight (mg)	1.5305	2.5999	0.0227	0.2876	0.0208	0.0034
Wt%	21.87%	37.14%	0.32%	4.11%	0.30%	0.05%

We note that the sum of the weights obtained in the second row of Table 3.3 does not amount to 7 mg, which was the initial weight of the geological MoS_2 flake digested for ICP-OES (see Material and Methods). We speculate two possible reasons for this. First, the aqueous solution used for digestion could have reacted with the sample, possibly resulting in volatile species that escaped as gaseous products or the formation of precipitates that settled at the bottom of the solution. Second, the ICP-MS study conducted by Addou et al. showed other elemental impurities in geological MoS_2, thus it is possible that other impurities present in the MoS_2 were not measured in our ICP-OES analysis. Aside from Bi, Mo, Re, S, Sb, and W, as shown in Table 3.3, we also checked for the presence of Ag, Ca, Cd, and Fe. We did not detect any Ag, Ca, Cd, and Fe through ICP-OES.

Our ICP-OES composition measurements revealed Bi impurity levels to be ~100 ppmw. The entire specimen was dissolved in a 15 mL solution, indicating that ~20 wt% of the geological MoS_2 crystal was Bi. It can be seen that there is only a small difference between the ICP-OES measurement of ~20% Bi and the XPS estimate (from the XPS map) of ~15% Bi, indicating that the Bi content in the flakes analyzed were likely within this range. We note that ~100 ppmw is five times greater than that reported by Addou et al. [25] (~20 ppmw), however this is likely an indication of sample to sample variability which is to be expected from geological samples.

3.4.5 Implications

These bismuth impurity compounds have consequences on the properties of the MoS_2. It would change the chemical bonding environment and electronic properties in its vicinity. However, since devices made using exfoliated flakes of MoS_2 are typically carried out after visual inspection focused on finding 'clean' flakes, it is likely that these micron-sized clusters of Bi are avoided. This is especially important when micrometer-sized contacts are used with MoS_2, which is typical in recent studies [2-4, 6, 38-47]. Because we know, through our spot size analysis, that the size of these bismuth impurities in MoS_2 is in the micrometer range, they could potentially dominate the properties of the MoS_2 if proper visual inspection and selection of good flakes is not performed. The presence of these micron-sized Bi clusters also highlights the difficulty of achieving large-area pristine MoS_2 without variability when using geological material.

We also know that these defects are present in clusters rather than uniform distributions, suggesting that the substitutional impurity concentration may be significantly lower than worst case estimates based on ICP-OES and ICP-MS [25] concentrations. The concentrations of substitutional Bi and smaller Bi clusters however, remain an unknown quantity that may be partly responsible for the atomic scale defects observed by Addou et al. and may therefore have a significant impact on device properties.

3.5 Conclusions

In this work, Bi impurities in geological MoS_2 have been spatially resolved with XPS mapping. We show that these impurities are localized in certain regions of the bulk MoS_2 crystal. Majority of the surface is chemically pristine MoS_2 as verified by XPS, but as shown in the concentration map, there are bismuth-rich areas. It was observed that the size of these impurities is in the order of tens of microns. Specific selected points indicate impurity sizes of somewhere between 15 to 50 μm. XPS also suggests that any Bi detected in MoS_2 are bismuth oxide or sulfate compounds (Bi_2O_3/Bi_2O_5/$Bi_2(SO_4)_3$), although these Bi chemical states can only be confirmed for the near surface and cannot be determined for the bulk of the clusters. Bi impurities have also been confirmed using ICP-OES. The presence of these impurity clusters in geological MoS_2 highlights the difficulty of obtaining large areas of geological flakes without variation. The abundance of

these impurities in geological MoS_2 brings to light the importance of developing controlled synthesis and growth methods for MoS_2 as well as other TMDCs before they can be widely integrated into various device applications.

3.6 Chapter 3 References

[1] K. S. Novoselov *et al.*, "Electric field effect in atomically thin carbon films," *Science (New York, N.Y.),* vol. 306, no. 5696, pp. 666-9, 2004, doi: 10.1126/science.1102896.

[2] H. Nam *et al.*, "MoS_2 Transistors Fabricated via Plasma-Assisted Nanoprinting of Few-Layer MoS_2 Flakes into Large-Area Arrays," *ACS Nano,* vol. 7, no. 7, pp. 5870-5881, 2013, doi: 10.1021/nn401093u.

[3] Y. Zhang, J. Ye, Y. Matsuhashi, and Y. Iwasa, "Ambipolar MoS_2 Thin Flake Transistors," *Nano Letters,* vol. 12, no. 3, pp. 1136-1140, 2012, doi: 10.1021/nl2021575.

[4] S. Das, H.-Y. Chen, A. V. Penumatcha, and J. Appenzeller, "High Performance Multilayer MoS_2 Transistors with Scandium Contacts," *Nano Letters,* vol. 13, no. 1, pp. 100-105, 2013, doi: 10.1021/nl303583v.

[5] A. Capasso *et al.*, "Few-Layer MoS_2 Flakes as Active Buffer Layer for Stable Perovskite Solar Cells," *Advanced Energy Materials,* vol. 6, no. 16, pp. 1600920-1600920, 2016, doi: 10.1002/aenm.201600920.

[6] S. Bertolazzi, D. Krasnozhon, and A. Kis, "Nonvolatile Memory Cells Based on MoS_2 /Graphene Heterostructures," *ACS Nano,* vol. 7, no. 4, pp. 3246-3252, 2013, doi: 10.1021/nn3059136.

[7] M.-L. Tsai *et al.*, "Monolayer MoS_2 Heterojunction Solar Cells," *ACS Nano,* vol. 8, no. 8, pp. 8317-8322, 2014, doi: 10.1021/nn502776h.

[8] J. Xiao, D. Choi, L. Cosimbescu, P. Koech, J. Liu, and J. P. Lemmon, "Exfoliated MoS_2 Nanocomposite as an Anode Material for Lithium Ion Batteries," *Chem. Mater,* vol. 22, pp. 4522-4524, 2010, doi: 10.1021/cm101254j.

[9] S. S. Chou *et al.*, "Chemically Exfoliated MoS_2 as Near-Infrared Photothermal Agents," *Angewandte Chemie International Edition,* vol. 52, no. 15, pp. 4160-4164, 2013, doi: 10.1002/anie.201209229.

[10] D. Sarkar, W. Liu, X. Xie, A. C. Anselmo, S. Mitragotri, and K. Banerjee, "MoS_2 Field-Effect Transistor for Next-Generation Label-Free Biosensors," *ACS Nano,* vol. 8, no. 4, pp. 3992-4003, 2014, doi: 10.1021/nn5009148.

[11] M. A. Lukowski, A. S. Daniel, F. Meng, A. Forticaux, L. Li, and S. Jin, "Enhanced Hydrogen Evolution Catalysis from Chemically Exfoliated Metallic MoS_2 Nanosheets," *J. Am. Chem. Soc,* vol. 135, 2013, doi: 10.1021/ja404523s.

[12] Q. Xiang, J. Yu, and M. Jaroniec, "Synergetic effect of MoS_2 and graphene as cocatalysts for enhanced photocatalytic H_2 production activity of TiO_2 nanoparticles," *J. Am. Chem. Soc.,* vol. 134, no. 15, pp. 6575-6578, 2012.

[13] C. Ataca and S. Ciraci, "Dissociation of H_2O at the vacancies of single-layer MoS_2," *Physical Review B,* vol. 85, no. 19, pp. 195410-195410, 2012, doi: 10.1103/PhysRevB.85.195410.

[14] S. McDonnell, R. Addou, C. Buie, R. M. Wallace, and C. L. Hinkle, "Defect-Dominated Doping and Contact Resistance in MoS_2," *ACS Nano,* vol. 8, no. 3, pp. 2880-2888, 2014, doi: 10.1021/nn500044q.

[15] W. M. Heckl, F. Ohnesorge, G. Binnig, M. Specht, and M. Hashmi, "Ring structures on natural molybdenum disulfide investigated by scanning tunneling and scanning force microscopy," *Citation: Journal of Vacuum Science & Technology B: Microelectronics and Nanometer Structures Processing,* vol. 9, pp. 1072-1072, 1991, doi: 10.1116/1.585263.

[16] J. S. Ha, H.-S. Roh, S.-J. Park, J.-Y. Yi, and E.-H. Lee, "Scanning tunneling microscopy investigation of the surface structures of natural MoS_2," *Surf. Sci.,* vol. 315, no. 1, pp. 62-68, 1994.

[17] R. Addou, L. Colombo, and R. M. Wallace, "Surface Defects on Natural MoS_2," *ACS Applied Materials and Interfaces,* vol. 7, no. 22, pp. 11921-11929, 2015, doi: 10.1021/acsami.5b01778.

[18] Y. J. Zheng *et al.*, "Point Defects and Localized Excitons in 2D WSe_2," *ACS Nano,* vol. 13, no. 5, pp. 6050-6059, 2019/05/28 2019, doi: 10.1021/acsnano.9b02316.

[19] W. H. Blades, N. J. Frady, P. M. Litwin, S. J. McDonnell, and P. Reinke, "Thermally Induced Defects on WSe_2," *The Journal of Physical Chemistry C,* vol. 124, no. 28, pp. 15337-15346, 2020/07/16 2020, doi: 10.1021/acs.jpcc.0c04440.

[20] R. Leiter, Y. Li, and U. Kaiser, "In-situ formation and evolution of atomic defects in monolayer WSe_2 under electron irradiation," *Nanotechnology,* vol. 31, no. 49, p. 495704, 2020/09/22 2020, doi: 10.1088/1361-6528/abb335.

[21] "SPI Supplies." https://www.2spi.com/ (accessed.

[22] "2D Semiconductors." https://www.2dsemiconductors.com (accessed.

[23] S. Ding, F. Lin, and C. Jin, "Quantify point defects in monolayer tungsten diselenide," *Nanotechnology,* vol. 32, no. 25, p. 255701, 2021/03/31 2021, doi: 10.1088/1361-6528/abeeb2.

[24] P. Schmidt, M. Binnewies, R. Glaum, and M. Schmidt, "Chemical Vapor Transport Reactions–Methods, Materials, Modeling," in *Advanced Topics on Crystal Growth*, F. Sukarno Olavo Ed. Rijeka: IntechOpen, 2013, p. Ch. 9.

[25] R. Addou *et al.*, "Impurities and Electronic Property Variations of Natural MoS_2 Crystal Surfaces," *ACS Nano,* vol. 9, no. 9, pp. 9124-9133, 2015/09/22 2015, doi: 10.1021/acsnano.5b03309.

[26] J. C. Vickerman and I. S. Gilmore, *Surface analysis : the principal techniques*. John Wiley & Sons, 2009.

[27] "Graphene Supermarket." https://graphene-supermarket.com/ (accessed.

[28] "Kolibrik.net, s.r.o. - Custom develompent of electronics and software." http://www.kolibrik.net/ (accessed.

[29] J. Suh *et al.*, "Doping against the native propensity of MoS_2 : Degenerate hole doping by cation substitution," *Nano Letters,* vol. 14, no. 12, pp. 6976-6982, 2014, doi: 10.1021/nl503251h.

[30] M. G. Stanford *et al.*, "Lithographically patterned metallic conduction in single-layer MoS_2 via plasma processing," *npj 2D Materials and Applications,* vol. 3, no. 1, pp. 13-13, 2019, doi: 10.1038/s41699-019-0095-5.

[31] M. Ciszewski, A. Mianowski, P. Szatkowski, G. Nawrat, and J. Adamek, "Reduced graphene oxide–bismuth oxide composite as electrode material for supercapacitors," *Ionics,* vol. 21, no. 2, pp. 557-563, 2015, doi: 10.1007/s11581-014-1182-4.

[32] W. Zuo *et al.*, "Bismuth oxide: a versatile high-capacity electrode material for rechargeable aqueous metal-ion batteries," *Energy & Environmental Science,* 10.1039/C6EE01871H vol. 9, no. 9, pp. 2881-2891, 2016, doi: 10.1039/C6EE01871H.

[33] G. K. Moiseev and A. L. Ivanovskii, "The numerical modeling of the composition and state of aggregation of the condensed medium formed in heating the Bi_2O_3 oxide in argon," *Russian Journal of Physical Chemistry,* vol. 80, no. 12, pp. 1887-1890, 2006, doi: 10.1134/S0036024406120028.

[34] R. Malakooti, L. Cademartiri, Y. Akçakir, S. Petrov, A. Migliori, and G. A. Ozin, "Shape-Controlled Bi2S3 Nanocrystals and Their Plasma Polymerization into Flexible Films," *Advanced Materials,* vol. 18, no. 16, pp. 2189-2194, 2006/08/18 2006, doi: 10.1002/adma.200600460.

[35] R. Ahmed, Y. Xu, M. G. Sales, Q. Lin, S. McDonnell, and G. Zangari, "Synthesis and Material Properties of Bi_2Se_3 Nanostructures Deposited by SILAR," *The Journal of Physical Chemistry C,* vol. 122, no. 22, pp. 12052-12060, 2018, doi: 10.1021/acs.jpcc.8b01692.

[36] F. J. Himpsel, F. R. McFeely, A. Taleb-Ibrahimi, and J. A. Yarmoff, "Microscopic structure of the SiO_2/Si interface," *Physical Review B,* vol. 38, no. 9, pp. 6084-6096, 1988.

[37] A. Jablonski, "NIST Electron Effective-Attenuation-Length Database," 2011.

[38] B. Radisavljevic, A. Radenovic, J. Brivio, V. Giacometti, and A. Kis, "Single-layer MoS_2 transistors," *Nat. Nanotechnol.,* vol. 6, no. 3, pp. 147-150, Mar 2011, doi: 10.1038/nnano.2010.279.

[39] H. B. Michaelson, "The work function of the elements and its periodicity," *Journal of Applied Physics,* vol. 48, no. 11, pp. 4729-4733, 1977, doi: 10.1063/1.323539.

[40] A. T. Neal, H. Liu, J. J. Gu, and P. D. Ye, "Metal contacts to MoS_2: A two-dimensional semiconductor," in *70th Device Research Conference*, 18-20 June 2012 2012, pp. 65-66, doi: 10.1109/DRC.2012.6256928.

[41] H. Liu, A. T. Neal, and P. D. Ye, "Channel Length Scaling of MoS_2 MOSFETs," *ACS Nano,* vol. 6, no. 10, pp. 8563-8569, 2012, doi: 10.1021/nn303513c.

[42] H. Wang *et al.*, "Integrated Circuits Based on Bilayer MoS_2 Transistors," *Nano Lett.,* vol. 12, no. 9, pp. 4674-4680, Sep 2012, doi: 10.1021/nl302015v.

[43] B. W. H. Baugher, H. O. H. Churchill, Y. Yang, and P. Jarillo-Herrero, "Intrinsic Electronic Transport Properties of High-Quality Monolayer and Bilayer MoS_2," *Nano Letters,* vol. 13, no. 9, pp. 4212-4216, 2013, doi: 10.1021/nl401916s.

[44] Z. Yin *et al.*, "Single-Layer MoS_2 Phototransistors," *ACS Nano,* vol. 6, no. 1, pp. 74-80, 2012, doi: 10.1021/nn2024557.

[45] H. Li *et al.*, "Fabrication of Single- and Multilayer MoS_2 Film-Based Field-Effect Transistors for Sensing NO at Room Temperature," *Small,* vol. 8, no. 1, pp. 63-67, 2012, doi: 10.1002/smll.201101016.

[46] S. Kim *et al.*, "High-mobility and low-power thin-film transistors based on multilayer MoS_2 crystals," *Nature Communications,* vol. 3, no. 1, pp. 1011-1011, 2012, doi: 10.1038/ncomms2018.

[47] M. Fontana *et al.*, "Electron-hole transport and photovoltaic effect in gated MoS_2 Schottky junctions," *Scientific Reports,* vol. 3, no. 1, pp. 1634-1634, 2013, doi: 10.1038/srep01634.

4 TMDC-on-Dielectric by Molecular Beam Epitaxy

The main objective of the work in this chapter is to use our group's established transition metal dichalcogenide (TMDC) growth technique via molecular beam epitaxy (MBE), and apply it to various dielectric and ferroelectric oxide substrates. This allows us to examine the feasibility of depositing semiconducting TMDC channels directly onto dielectric oxides for device fabrication. Successful direct TMDC integration through MBE would provide large-area TMDC channels and avoid residual contaminants from various polymer-assisted transfer process commonly used for "pick and place" device fabrication. Specifically, in this chapter we focus on our prototypical growth technique for WSe_2 [1]. WSe_2 is an attractive channel candidate for next-generation field-effect transistors (FETs) and low power memory devices [2, 3], in part due to its dominant hole conduction properties and enhanced spin-orbit coupling compared to other TMDCs [4-6].

In the first part of this chapter, we demonstrate the WSe_2 MBE growth process and its effects on ferroelectric hafnium zirconium oxide (HZO). This section is geared towards using these WSe_2/HZO stacks for ferroelectric FET device applications. The second part of this chapter is a more general approach, in which we investigate various considerations for using our MBE growth technique directly onto device-relevant substrates, such as HZO, SiO_2, and HfO_2 dielectrics. We also highlight growth of our WSe_2 material at back-end-of-the-line (BEOL) compatible temperatures, as this would provide a route for device fabrication and testing immediately after TMDC channel growth, without needing any intermediate transfer steps. We present a process for direct semiconductor integration through low temperature MBE, as opposed to the conventional "pick and place" method for fabricating device stacks.

4.1 WSe_2 Growth on Hafnium Zirconium Oxide by Molecular Beam Epitaxy: The Effect of the WSe_2 Growth Conditions on the Ferroelectric Properties of HZO

4.1.1 Abstract

Direct integration of transition metal dichalcogenides (TMDCs) on a ferroelectric such as hafnium zirconium oxide (HZO) using an industrially scalable technique is important for realizing various ferroelectric-based device architectures. The interface formed due to the processing conditions during direct deposition is the focus of the current study. In this work, molecular beam epitaxy (MBE) is used to directly deposit WSe_2 on HZO substrates, and the effects of the MBE growth conditions, specifically high temperature and a high Se flux, are examined. Anneals of HZO under a Se flux, which serve to replicate the conditions during actual WSe_2 deposition, result in the crystallization of amorphous as-deposited HZO substrates and incorporation of Se into the HZO. The crystallinity and composition of the HZO substrates affect the degree of Se incorporation. Some of the Se found in the HZO is an adsorbed layer that can be thermally desorbed, but it also has a chemisorbed component fully incorporated within the HZO lattice. Measurement of the electrical properties of the HZO films did not provide evidence that the incorporated Se was detrimental to the functionality of the HZO as a ferroelectric layer.

4.1.2 Introduction

Ferroelectric field effect transistors (FeFETs) offer a promising route toward more scalable and compatible memory devices. Compared to traditional resistive random-access memory (RRAM), FeFETs allow operation with an enhanced number of memory states and require fewer

accessory circuit elements for integration. In FeFETs, the ferroelectric layer essentially acts as the gate dielectric, and its polarization state dictates the device's threshold voltage and current. [7] A key component of an FeFET device is the interface between the ferroelectric and semiconductor materials. [8]

Ferroelectricity in HfO_2 thin films was recently discovered and found to originate from the non-centrosymmetric orthorhombic phase of HfO_2 [9]. This ferroelectric orthorhombic phase can be stabilized in a variety of different ways, such as doping. Some example dopant atoms that have been reported previously are Si, Al, Y, Gd, and Zr [10-15]. HfO_2 doped with Zr to form $Hf_{1-x}Zr_xO_2$, hafnium zirconium oxide (HZO) offers several advantages, such as a large composition space allowing orthorhombic phase formation and low crystallization temperatures [14, 16-20]. In the thin film geometry, pure HfO_2 crystallizes into the monoclinic phase, while pure ZrO_2 crystallizes into the tetragonal phase upon heating. Alloying HfO_2 with ZrO_2 provides a tetragonal to orthorhombic phase transition pathway during cooling, thus resulting in the presence of the ferroelectric orthorhombic phase in HZO alloys. [14]

HfO_2-based FeFETs have been realized with the use of transition metal dichalcogenides (TMDCs) as the semiconducting channel [21-24]. The choice of TMDCs as the semiconductor in FeFETs is gaining interest because of their unique electronic properties that are versatile and tunable [25]. TMDCs have a band gap that changes with layer thickness, which offers the potential for band gap engineering depending on the specific device application [26-28]. The 2D nature of TMDCs, in which the surface is essentially absent of dangling bonds, allows a theoretically sharp interface with other materials, leading to improved interface quality and stability compared to traditional channel materials such as silicon [29-32].

Reports of TMDCs interfaced with a ferroelectric for FeFETs typically make use of exfoliated or chemical vapor deposited (CVD) TMDCs [21-24, 33]. Exfoliated TMDC flakes from geological crystals are known to have a variety of defects, leading to non-uniform properties [34-37], and CVD growth methods for TMDCs require high growth temperatures, i.e., 650-800 °C [38-40], that are not compatible with industrially relevant back-end-of-the-line (BEOL) processes [41]. Additionally, exfoliated flakes and CVD-grown material require transfer of the TMDC onto the suitable device substrate, and such transfer processes introduce residual contaminants that result in interfaces that are not pristine and modified electrical behavior of the device [42-46]. Direct integration of dielectric oxides on TMDCs has been previously demonstrated through

atomic layer deposition (ALD) directly on van der Waals surfaces, and a relatively sharp interface between the two materials with no intermixing of constituents has been shown [47-52]. Furthermore, the thermal stability of the interface of ALD HZO on MoS_2 and WSe_2 has been shown up to 700 °C [53]. Our present work is focused on the reverse structure – TMDC-on-HZO. In this work, we aim to directly integrate TMDCs, specifically WSe_2, onto ferroelectric HZO substrates using molecular beam epitaxy (MBE). Direct growth of WSe_2 films on HZO is demonstrated, and the effects of the MBE growth process on the HZO substrates are investigated.

4.1.3 Methodology

Amorphous HZO thin films, 20 nm thick, were deposited by ALD in a Cambridge Nanotech Savanah 100 flow through style reactor at 150 °C in a nitrogen ambient. Tetrkis(dimethylamino) zirconium (TDMA-Zr, 75 °C, STREM) and tetrakis(dimethylamino) hafnium (TDMA-Hf, 75 °C, STREM) were used as reactants for ZrO_2 and HfO_2, respectively. Water (~30 °C) was used as an oxidant. The composition was controlled by changing the relative number of ZrO_2:HfO_2 cycles in a 10 cycle supercycle. Two HZO compositions were fabricated – $Hf_{0.58}Zr_{0.42}O_2$ (58:42 HZO) and $Hf_{0.36}Zr_{0.64}O_2$ (36:64 HZO). Due to the slightly higher growth rate per cycle of HfO_2, films tended to be Hf-rich with respect to the intended 50:50 and 30:70 compositions [54]. The HZO thin films were deposited on 20 nm of pulsed DC sputtered TaN onto a (001)-oriented Si wafer.

MBE was used to grow different thicknesses of WSe_2 on HZO. The MBE growth chamber is part of an ultra-high vacuum (UHV) system described elsewhere [55]. During growth, the HZO substrates were maintained at 500 °C, and the Se:W flux ratio was maintained at ~6000:1. WSe_2 growth occurred by exposing the HZO substrates to the W and Se fluxes simultaneously. The growth continued uninterrupted with a deposition rate of approximately one WSe_2 monolayer every 30 minutes. This growth rate was estimated based on the known growth rate of WSe_2 on a highly ordered pyrolytic graphite (HOPG) substrate, monitored through in-situ reflective high energy electron diffraction (RHEED). At the end of the growth, the sample was cooled in a Se flux until it reached 275 °C, at which the Se flux was turned off. The sample was allowed to further cool down to room temperature.

To investigate the effects of exposure of the HZO films to the MBE growth conditions (specifically high temperature and Se flux), an annealing experiment simulating WSe_2 growth was performed. This involved annealing the HZO to 500 °C in the MBE chamber for approximately 3 h while exposed to a Se flux of approximately 2×10^{-6} mbar, which is measured with a beam flux monitor in the position of the sample prior to exposure. The 3 h anneal time is chosen to be comparable to a multilayer WSe_2 growth time. Exposure to a Se flux while heating in the MBE chamber is important for simulating the growth conditions because Se is in excess during WSe_2 growth. The typical cooling process during growth, wherein the sample is cooled down in a Se flux until a temperature of 275 °C, was performed for these anneals. Each anneal was conducted with the two compositions of HZO substrates (58:42 HZO and 36:64 HZO) side-by-side, thus ensuring that they were exposed to the exact same conditions for the same annealing experiment.

In-situ X-ray photoelectron spectroscopy (XPS) was performed on all the samples in the same UHV system described previously [55]. XPS spectra were acquired using a monochromated Al Kα X-ray source at 300 W and a Scienta Omicron R3000 analyzer at a pass energy of 50 eV. Peak fitting of the collected XPS spectra was performed using kolXPD software [56]. All peaks were fit with Voigt lineshapes. The structural and chemical morphology of the WSe_2 layers and HZO substrates (before and after MBE growth) were also examined with a JEOL ARM 200F transmission electron microscope (TEM) equipped with an Oxford energy dispersive spectroscope (EDS). The cross-sectional samples were mechanically thinned with a tripod polished to $\sim<$ 20 μm and then ion milled to electron transparency on a liquid nitrogen cooled stage. X-ray diffraction (XRD) was performed to further investigate structural changes in the HZO after exposure to the MBE growth conditions using a Rigaku Smartlab diffractometer equipped with Cu Kα radiation in a grazing incidence geometry with ω angle fixed at 0.7°. For electrical characterization, Pd top electrodes were deposited on the samples. We sputtered 50 nm of Pd through a shadow mask, using 67 W DC power on a 2" Pd target. Hysteresis loops, measured out to a field of 2.5 MV/cm with a period of 1 ms, and positive up negative down (PUND) measurements, made at 2.5 MV/cm with a 1 ms pulse width and a 1000 ms pulse delay, were carried out utilizing a Radiant Technologies Precision LC II Tester.

4.1.4 Results and Discussion

4.1.4.1 WSe_2 Growth on HZO

WSe_2 growth was performed on both types of HZO substrates – 58:42 HZO and 36:64 HZO. The MBE growth on both substrates produced WSe_2 as verified by the XPS spectra in Figure 4.1.1, which shows the Se 3*d* and W 4*f* regions. It is noticeable that the peak shapes are similar for both 58:42 and 36:64 HZO substrates, indicating consistency in the grown WSe_2 films regardless of the composition of the HZO substrate used. The binding energy positions of the observed peaks, which are further discussed below, correspond to the WSe_2 chemical state. Therefore, the grown species were chemically verified by XPS, and the WSe_2 growth process was successful for both 58:42 and 36:64 HZO.

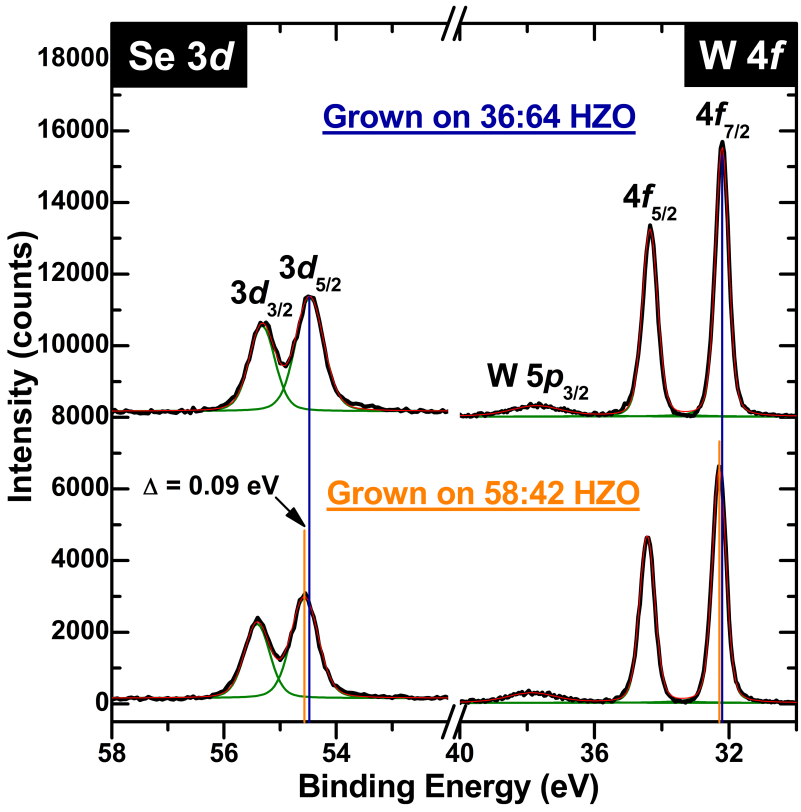

Figure 4.1.1. Se 3d and W 4f spectra of approximately 5 layers of WSe_2 grown on 36:64 and 58:42 HZO.

The fitting parameters used for the W 4*f* and Se 3*d* spectra in Figure 4.1.1 are tabulated in Table 4.1.1 to quantitatively show the similarity in the XPS lineshapes and peak positions of the WSe_2 films grown on the two HZO substrates.

Table 4.1.1. Fitting parameters used for W 4f and Se 3d spectra of the ~5-layer grown WSe2 films shown in Figure 4.1.1.

		Lorentzian width	**Gaussian width**	**Amplitude (counts)**	**Position (eV)**
W $4f_{7/2}$	36:64 Hf:Zr	0.12	0.41	4194	32.21
	58:42 Hf:Zr	0.12	0.41	3739	32.30
W $4f_{5/2}$	36:64 Hf:Zr	0.12	0.48	3313	34.35
	58:42 Hf:Zr	0.12	0.47	2954	34.44
Se $3d_{5/2}$	36:64 Hf:Zr	0.12	0.53	2180	54.47
	58:42 Hf:Zr	0.12	0.51	1883	54.56
Se $3d_{3/2}$	36:64 Hf:Zr	0.12	0.47	1504	55.32
	58:42 Hf:Zr	0.12	0.47	1299	55.41

Note that the ratio of the total Se 3*d* amplitude to the total W 4*f* amplitude is **0.49** for the 36:64 Hf:Zr substrate and **0.48** for the 58:42 Hf:Zr substrate, which quantitatively shows that we produce WSe_2 with similar relative amounts of Se/W for both HZO substrates. Accounting for relative sensitivity factors of each core level [57], these amplitude ratios correspond to calculated Se/W stoichiometries of **2.09** and **2.03** for 36:64 and 58:42 Hf:Zr HZO substrates, respectively, which tells us that the material grown was WSe_2 with close to the desired 2:1 (Se:W) stoichiometry. As a reference sample, we measured a CVT-grown WSe_2 crystal (from SPI Supplies [58]) with our XPS, and the calculated Se:W stoichiometry using the same relative sensitivity factors was 2.24.

We observe that the W 4*f* and Se 3*d* peaks have a constant 0.09 eV shift between our two growth substrates, noted by vertical marker lines in Figure 4.1.1. This constant Δ in the W and Se core level binding energies provides us with further evidence that the chemistry of the WSe_2 material grown on both substrates is the same. The 0.09 eV difference could be easily explained by either partial grounding of the WSe_2 layer via the mounting clips, or shifts in the Fermi level of

the HZO depending on the Hf:Zr composition, which would cause differences in band bending at the WSe_2/HZO interface. After WSe_2 growth, the Hf 4*f* peak positions are 17.58 eV for 36:64 HZO and 18.12 eV for 58:42 HZO.

TEM was performed on the same 5-layer film whose XPS spectra are shown in Figure 4.1.1. The TEM micrographs, shown in Figure 4.1.2, reveal crystallized domains in the underlying HZO substrate, which is likely a result of the high substrate temperature required for WSe_2 growth. The crystalline phases present in the HZO are discussed later. The WSe_2 film has undulations, which appear to be conformal to the surface of the HZO substrate. The roughness of the HZO surface may be attributed to the crystallization process, as previously noted in prior reports [59-62]. Also, the HZO layer may be following the roughness of the underlying TaN layer; TEM analysis revealed a diffuse interface between the HZO and the underlying TaN (shown in Figure 4.1.3).

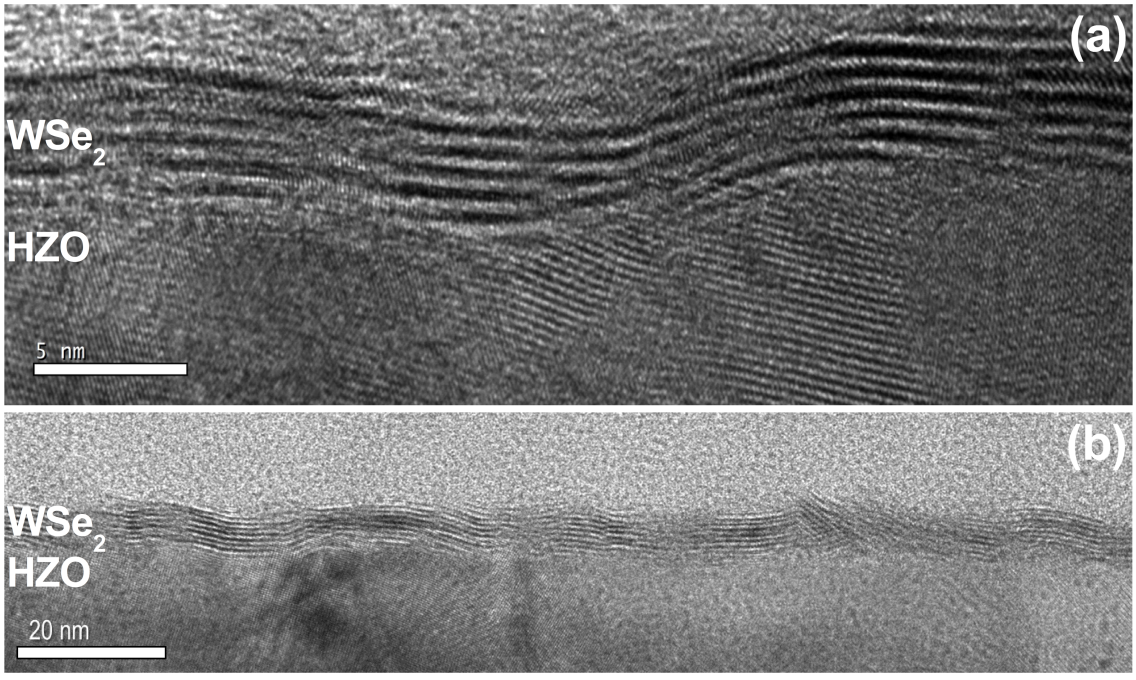

Figure 4.1.2. TEM micrographs of 5-layer WSe_2 directly MBE-grown on HZO. (a) Crystallized domains of HZO and undulations of the HZO and WSe_2 are clearly visible. (b) Large-area micrograph showing a continuous WSe_2 film across more than 100 nm.

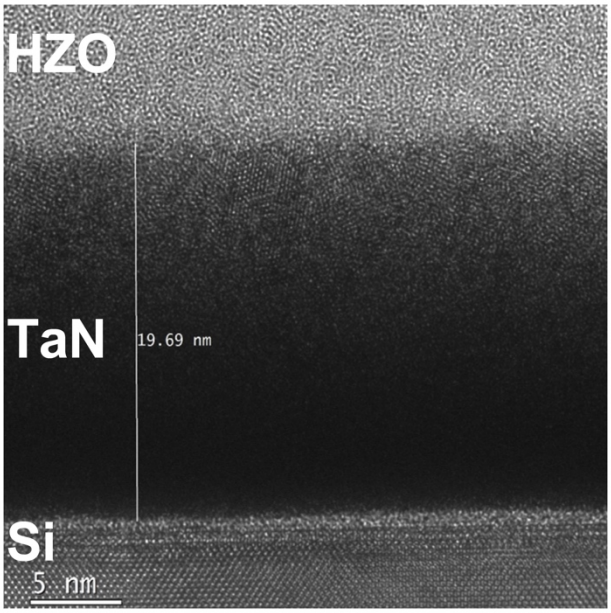

Figure 4.1.3. TEM micrograph of the interface between as-deposited HZO and TaN. The as-deposited HZO layer is amorphous, and as shown, it does not have a sharp interface with the TaN underlayer.

We report that our directly grown WSe_2 film on HZO is continuous across a large area, and is composed of large grains on the order of hundreds of nm, as evidenced by the micrographs shown. We show that our MBE growth process on HZO produces repeatable high-quality WSe_2 in terms of chemistry and film morphology, regardless of the WSe_2 film thickness. The XPS and TEM results of a thinner WSe_2 sample (approximately 3-4 layers) are shown in Figure 4.1.4.

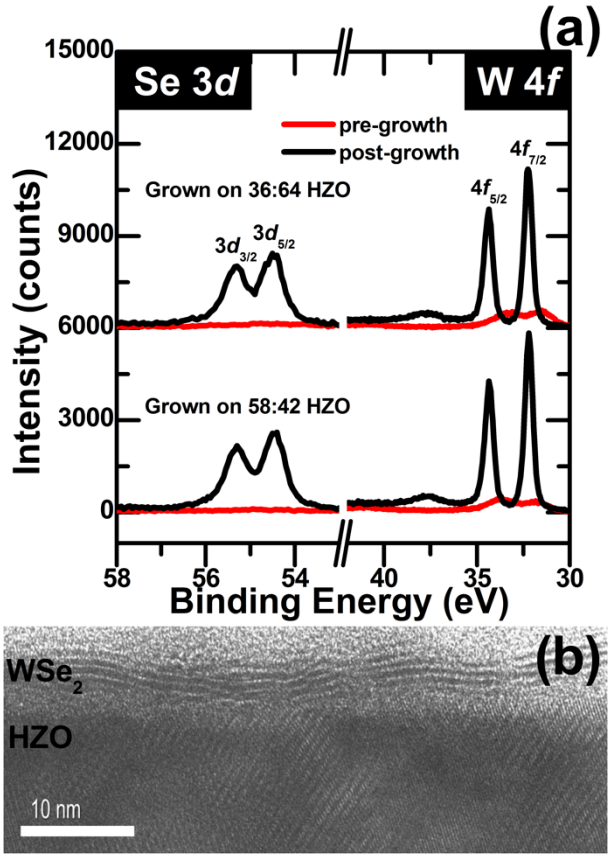

Figure 4.1.4. (a) Se 3d and W 4f spectra before and after growth of approximately 3-4 layers of WSe_2 on 36:64 and 58:42 HZO. (b) TEM micrograph of the same WSe_2 film on 58:42 HZO.

Figure 4.1.5 shows the polarization-electric field (P-E) loops measured from a 58:42 HZO substrate that had similarly grown WSe_2 on top of it. As can be seen in this figure, the initial response appears dielectric, and with field cycling, the response becomes more ferroelectric. This wake-up phenomenon, where the polarization increases with field cycling, is typical of HfO_2-based ferroelectrics. Both the general shape of the P-E loop and the increase in polarization with wake-up are evidence that the device is ferroelectric. Nested hysteresis loops are shown in Figure 4.1.6.

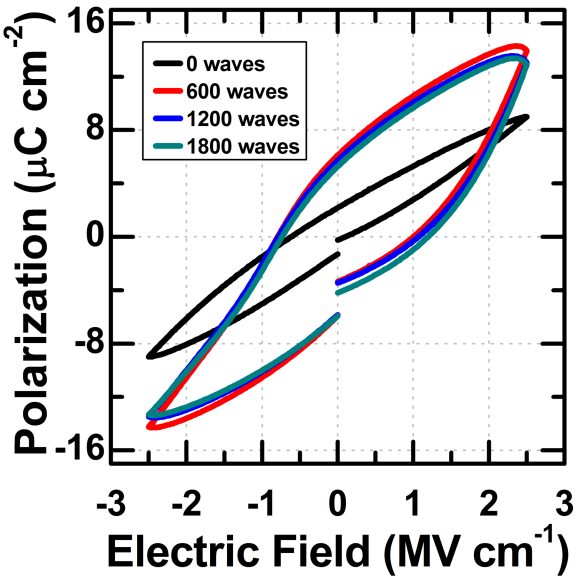

Figure 4.1.5. P-E loops measured from 58:42 HZO with MBE-grown WSe_2 on top.

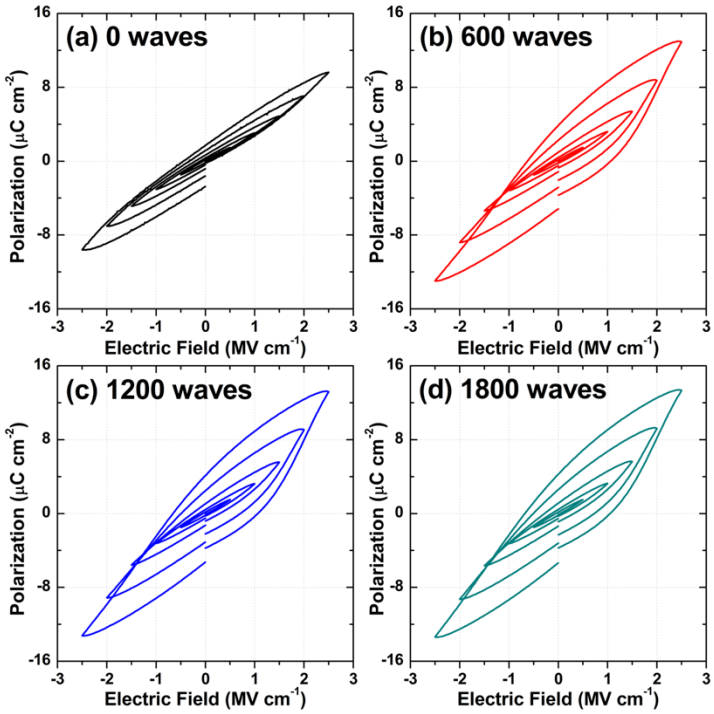

Figure 4.1.6. Nested hysteresis loop measurements made on 58:42 HZO with MBE-grown WSe_2 on top (same device as Figure 4.1.5).

The results of current-voltage (I-V) measurements performed on this device are shown in Figure 4.1.7, and we report higher leakage currents measured on the WSe_2/HZO device compared to blank HZO substrates. We speculate that oxygen vacancies in the HZO layer may be facilitating leakage in this WSe_2/HZO device.

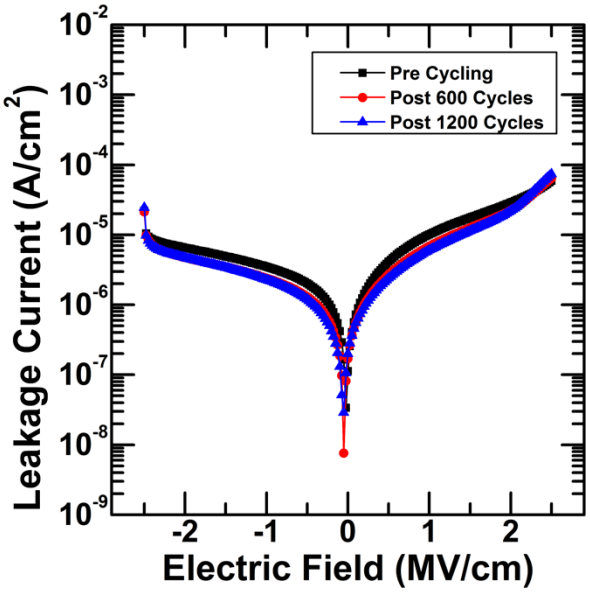

Figure 4.1.7. I-V curves of the same MBE-WSe_2 on HZO device as Figure 4.1.5 and Figure 4.1.6. The leakage current values shown here appear higher than those shown for blank HZO substrates without WSe_2 grown on top (Figure 4.1.14).

EDS measurements shown in Figure 4.1.8 reveal that after MBE growth of WSe_2, the oxygen concentration in the HZO layer decreases. While we cannot use EDS to accurately quantify oxygen concentration, we can use it as a qualitative measure to look at trends of how the amount of oxygen changes. It is seen here that the O signal relative to Hf and Zr in the HZO layer is lower in Figure 4.1.8(b) compared to Figure 4.1.8(a). This decrease in the oxygen concentration after MBE provides qualitative evidence of removal of some oxygen in the HZO film, likely leading to the formation of more oxygen vacancies that facilitate leakage through the HZO after WSe_2 deposition.

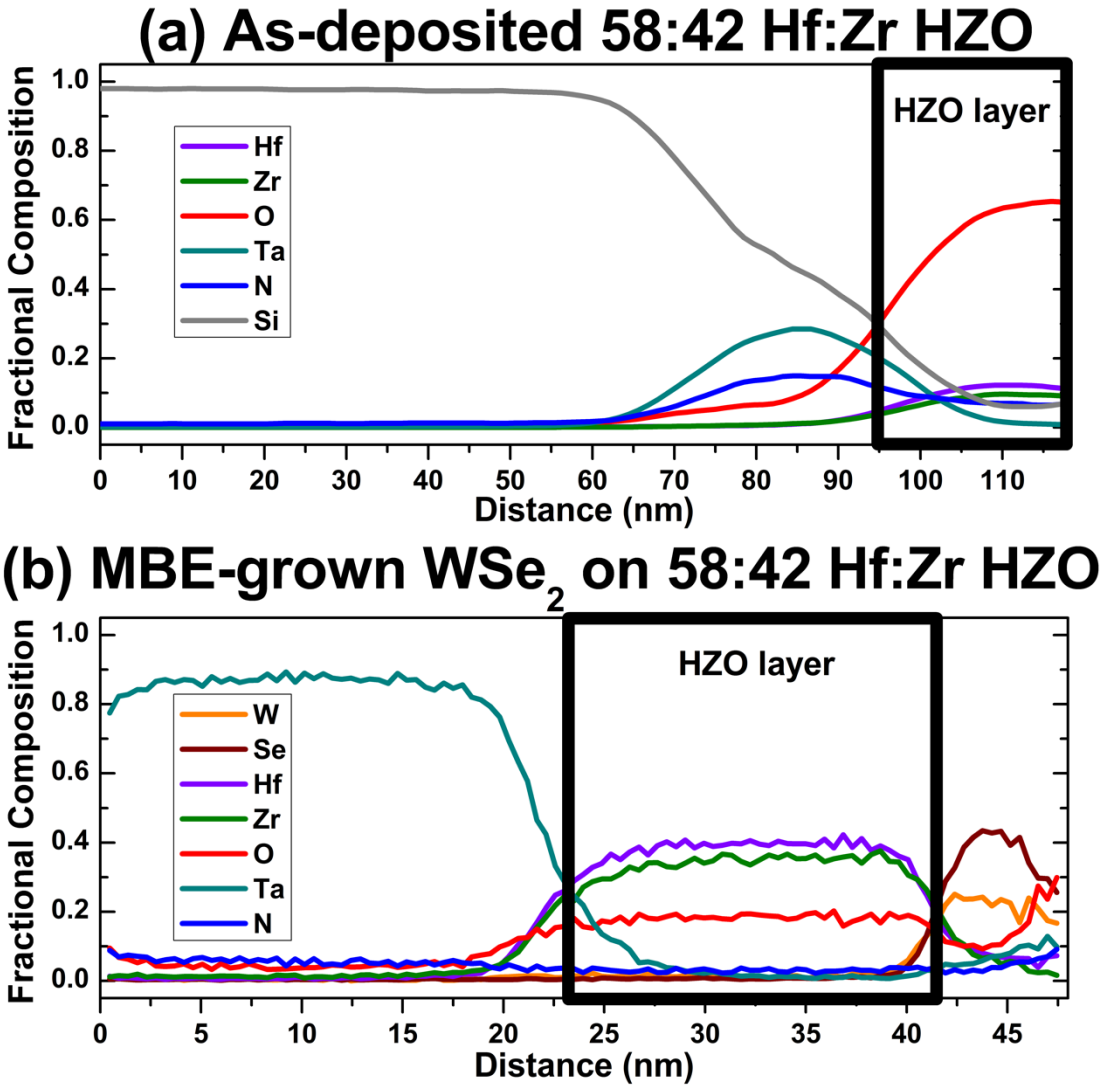

Figure 4.1.8. EDS results of (a) as-deposited amorphous 58:42 HZO and (b) MBE-grown WSe_2 on 58:42 HZO.

However, fully understanding the reasons for the high leakage we observe in our MBE-WSe_2/HZO devices requires further investigation. In the current work, the main focus is the effect of processing conditions on the properties of the WSe_2/HZO interface, and altering the process to produce better electrical devices will be the focus of future work.

4.1.4.2 Impact of the MBE Growth Conditions

Direct growth of TMDCs onto dielectrics avoids the introduction of transfer residues, as noted above. However, it introduces the potential for the growth process to modify the interface that is formed between the two materials. In the specific case of WSe_2 deposition on HZO there is potential W or Se incorporation into the dielectric layer. Since we see no evidence of W-O bonds in our XPS analysis, we acknowledge that any W intermixing with the HZO layer is below our limit of detection. It is also less likely to be incorporated in the HZO substrate than Se because the W flux used during WSe_2 deposition is three orders of magnitude lower than the Se flux. Therefore, we focus on potential Se incorporation into the HZO layer as well as the impact of MBE growth temperatures on the HZO film. To do this, we performed a 3 h anneal on the HZO at 500 °C, while exposed to the same Se flux that is used during actual growth (~2×10^{-6} mbar). These annealing conditions replicate the conditions during MBE growth of WSe_2. The structural, chemical, and electrical properties of the samples were investigated.

Structurally, the substrate annealing conditions required for growth of WSe_2, i.e., 500 °C in UHV for ~3 hours, allow crystallization of the as-deposited amorphous HZO films. We note that prior to this 3-h 500 °C anneal, the HZO substrates were amorphous and would not have produced a diffraction pattern, as previously shown [53]. After annealing, a mixed phase assemblage composed of the monoclinic, orthorhombic, and tetragonal phases of HZO is observed through XRD, as shown in Figure 4.1.9. This provides clear evidence of the WSe_2 growth conditions crystallizing the HZO substrates into the same three phases, regardless of their composition. Based upon peak intensity ratios, the 36:64 HZO composition likely contains more non-ferroelectric monoclinic phase than the 58:42 HZO composition. The crystalline HZO phases revealed by XRD are in agreement with the appearance of crystallized HZO domains evident in the TEM micrographs in Figure 4.1.2.

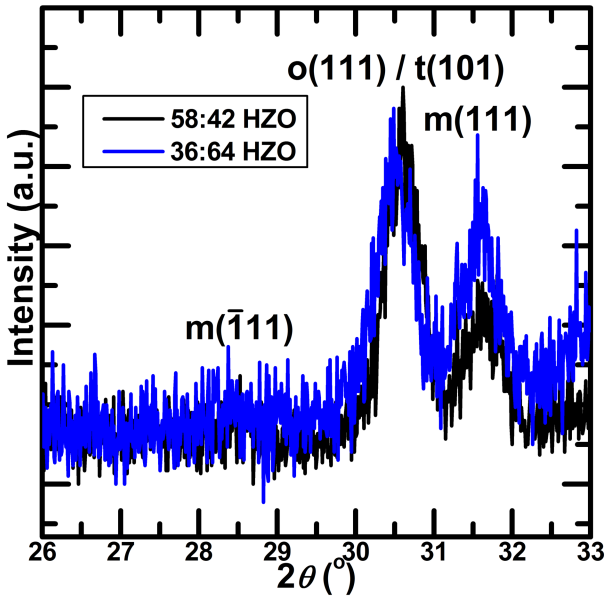

Figure 4.1.9. XRD patterns of 58:42 HZO and 36:64 HZO after annealing at 500 °C for 3 h under a ~2 × 10^{-6} mbar Se flux. Reflections of the monoclinic, orthorhombic, and tetragonal phases are labeled. These XRD measurements were performed with a fixed incident X-ray angle of 0.7 °C.

Chemically, we observed that this same anneal in Se flux led to incorporation of Se into the HZO films, which was determined by analyzing the Se 3*d* core level peaks. We note that the Zr 4*s* signal overlaps with Se 3*d*, and the raw data prior to Zr 4*s* subtraction is shown in Figure 4.1.10. The same binding energy region was scanned prior to each anneal in Se flux (shown as thinner lines) in order to measure the Zr 4*s* peak on its own. After annealing in a Se flux, the position and area of the Zr 4*s* feature were referenced to the Zr 3*d* peak of each sample and subtracted from the raw spectra, shown as thicker lines in Figure 4.1.10. The result of this data subtraction is plotted in Figure 4.1.11.

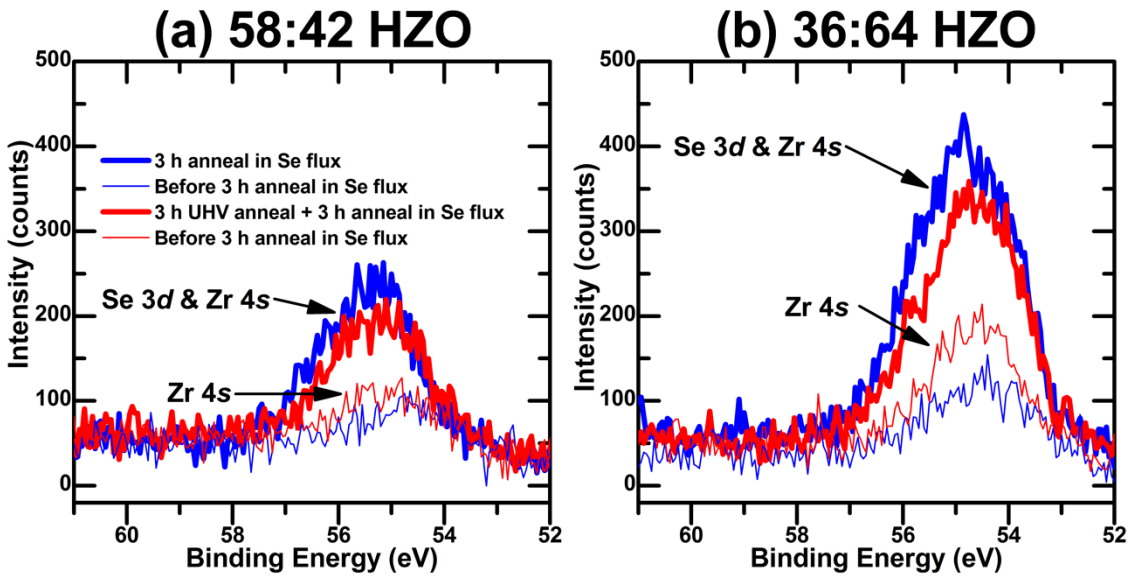

Figure 4.1.10. Raw data corresponding to the binding energy range where the Se 3d peaks are expected; (a) 58:42 HZO and (b) 36:64 HZO.

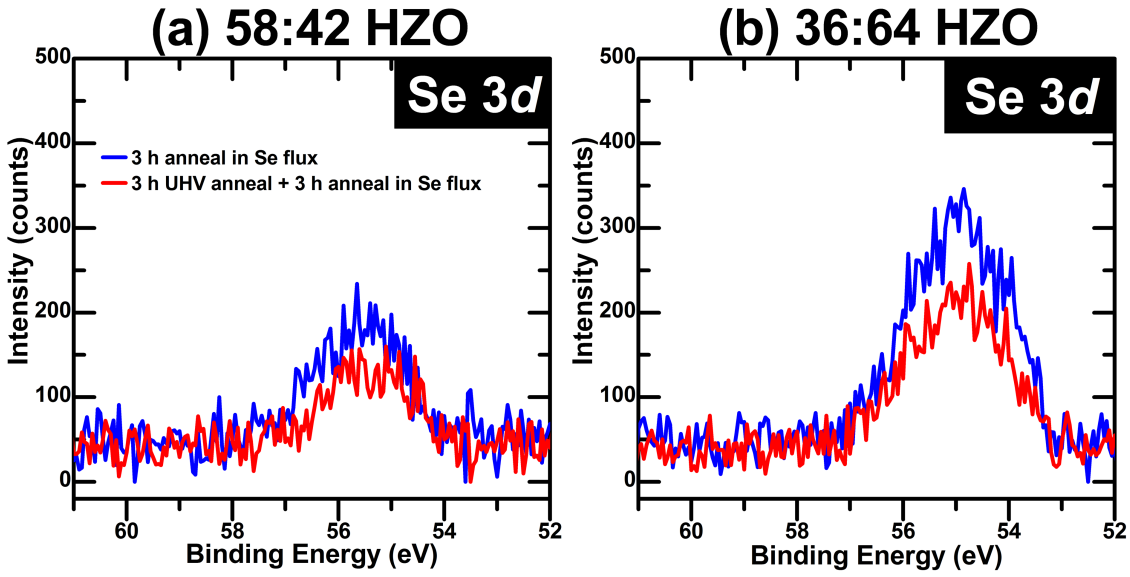

Figure 4.1.11. Se 3d spectra of (a) 58:42 HZO and (b) 36:64 HZO after exposure to various annealing conditions.

In Figure 4.1.11, the blue spectra represent as-deposited HZO that were exposed to the MBE conditions, meaning that these were amorphous films prior to the Se flux anneal. The red curves represent HZO that underwent pre-annealing in UHV before annealing in a Se flux. We know from our XRD results (Figure 4.1.9) that its pre-annealing condition, 3 h at 550 °C in UHV, is sufficient for HZO crystallization prior to the anneal in Se flux. It can be seen that the amorphous HZO (blue spectra) is more susceptible to Se incorporation, agreeing with reports of more open diffusion paths and higher diffusivities in analogous amorphous SiO_2 compared to crystalline silica phases [63-66].

From Figure 4.1.11, it is also noticeable that HZO with a higher Zr content (36:64 HZO) is more susceptible to Se adsorption and incorporation than the lower Zr content HZO sample (58:42 HZO). The integrated area of the Se 3*d* peaks for 36:64 HZO are higher, by a factor of ~2.1, than that for 58:42 HZO that underwent the same annealing conditions, indicating a higher amount of Se present. We attribute this to a higher number of available sites for Se in 36:64 HZO than in 58:42 HZO. Assuming that Se, having the same valence as oxygen, occupies oxygen sites in the HZO lattice, the oxygen vacancy (V_O) concentration is a good indicator of the amount of Se that could be incorporated into HZO. It should be noted that thermodynamically, ZrO_2 has a lower V_O formation energy, and thus is expected to have a higher V_O concentration at a given temperature, than HfO_2 [67, 68]. Therefore, since 36:64 HZO has a higher fraction of ZrO_2, it would have more oxygen vacancies compared to 58:42 HZO. This higher V_O concentration allows more Se incorporation into the HZO lattice, which explains our observation in Figure 4.1.11.

Changes in V_O concentration result in Fermi level shifts in the HZO. As such, we can use XPS binding energy positions as a quantitative measure of Fermi level shifts and an indirect qualitative measure of changes in vacancy concentrations. In our XPS tool, all binding energies are referenced to the Fermi level at 0 eV; therefore, uniform shifts of XPS peak positions to higher binding energies are indicative of the Fermi level shifting closer to the conduction band, i.e., increase in n-type charge carriers. Since oxygen vacancies are known to be n-type dopants in HfO_2 [69, 70] and ZrO_2 [70], we can qualitatively correlate Hf and Zr binding energy shifts to changes in V_O concentration. As shown in Figure 4.1.12, a 12-h UHV anneal at 500 °C shifts the Hf 4*f* and Zr 3*d* peaks to binding energies ~0.3 to 0.4 eV higher than the as-deposited spectra. Such identical shifts to higher binding energy of both the Hf and Zr peaks indicate an increase in n-type character

and is correlated with an increase in V_O [53, 69, 70], which is an expected consequence of annealing [71-73]. After this prolonged annealing to induce a high V_O concentration, this sample was annealed under a Se flux. We observe that the HZO peaks shift to binding energies ~0.3 eV lower after a 250 °C anneal in Se, and to even lower binding energies (~0.4 to 0.5 eV) after a 500 °C anneal in Se. Overall, these binding energy shifts indicate that the oxygen vacancies that were initially created during the 12-h UHV anneal were filled after the anneal under a Se flux, thus providing evidence that the detected incorporated Se is occupying oxygen sites in the HZO lattice. Therefore, it can be said that the susceptibility to Se incorporation is due to an interplay between the diffusivity of Se and the oxygen vacancy concentration of the HZO substrate, as gleaned from the results shown in Figure 4.1.11 and Figure 4.1.12.

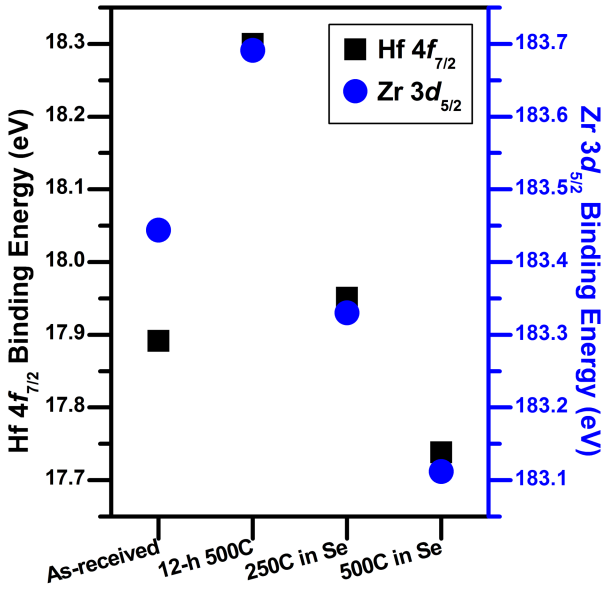

Figure 4.1.12. Measured positions of the Hf $4f_{7/2}$ and Zr $3d_{5/2}$ peaks of 36:64 HZO upon exposure to various annealing steps.

We further investigated the chemical state of this Se incorporated into the HZO. The XPS results revealed that the Se detected in the HZO films was composed of two components, as seen in Figure 4.1.13, which shows deconvoluted Se 3*d* spectra (with the overlapping Zr 4*s* feature removed). Based on the binding energies of the fitted peaks in these spectra, their chemical states

can be determined. The higher binding energy peaks at 55.4 and 56.2 eV are the Se $3d_{5/2}$ and $3d_{3/2}$, respectively, both corresponding to Se-Se bonds. The lower binding energy peaks at 54.3 and 55.2 eV are both similarly attributed to a metal selenide (M-Se) or Se-M-O species, wherein the metal can be either Hf or Zr from HZO. It is expected that any Se adsorbed on top of the HZO films can be thermally desorbed, so we performed an anneal under a Se flux on a 36:64 HZO sample, followed by sequential desorption anneals in UHV, without a Se background pressure, at 150-550 °C for 1 h at each temperature. As shown in Figure 4.1.13, the anneals in UHV progressively decreased the amount of the Se-Se component until it was completely removed, unlike the Se-M-O component, which was not thermally desorbed. We note that after the 550 °C desorption anneal, a 33% reduction in the intensity of the Se-M-O component (normalized to the Hf 4*f* intensity) is observed relative to the starting Se-M-O intensity post-anneal in Se flux. However, most of the Se-M-O signal remains in the sample even after relatively aggressive anneals in UHV. From these results, we can conclude that the Se-Se component is physisorbed, while the Se-M-O component is chemisorbed into the HZO. Because some of the Se present after annealing in a Se flux (Se-M-O component) is actually chemically bonded to the HZO, it is important to investigate if and how this affects the electrical properties and functionality of the ferroelectric HZO film.

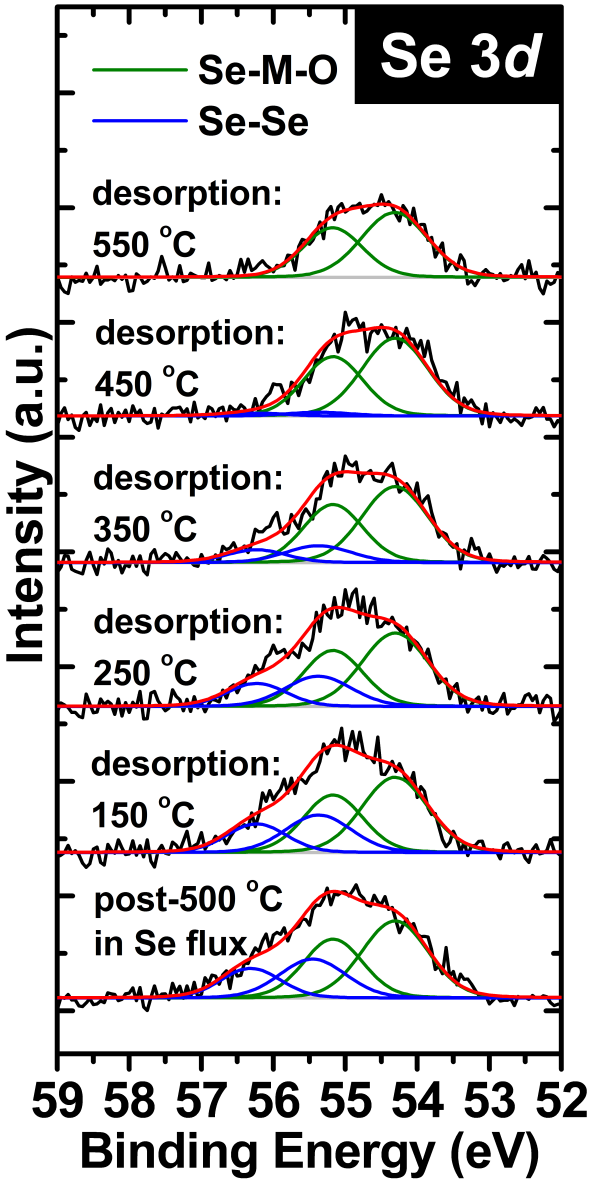

Figure 4.1.13. Deconvolution of the Se 3d spectra of a 36:64 HZO sample after an anneal in a Se flux and after sequential desorption anneals in UHV.

We measured and compared the electrical characteristics of the HZO samples after exposure to the various UHV pre-annealing and Se flux annealing conditions. Ferroelectricity was observed in these samples, as expected, knowing that all of these HZO films have some fraction

transformed into the ferroelectric orthorhombic phase due to crystallization through the anneals. Table 4.1.2 shows the remanent polarization (P_r) values of 58:42 HZO and 36:64 HZO after undergoing these different thermal treatments. The reported P_r values are taken from PUND measurements after field cycling. Note that all UHV anneals indicated in the table are performed without a Se background pressure, and all Se flux anneals were performed with the same Se flux used during WSe_2 growth, which is approximately 2×10^{-6} mbar. It was found that exposure to Se did not significantly affect P_r. This is evident when comparing the P_r of the UHV-annealed only samples and the Se flux-annealed only sample for the same HZO composition. The more significant factor affecting P_r was thermal history. It can be seen that UHV+Se flux anneals resulted in P_r values that are higher than the corresponding UHV only or Se flux only anneal. We note that the effect of thermal history on P_r is more pronounced for 36:64 HZO because of the general decrease in required thermal budget for crystallization and oxygen vacancy formation with increasing Zr content in HZO. This makes the more Zr-rich sample, i.e., 36:64 HZO, more sensitive to changes in annealing conditions.

Table 4.1.2. Remanent polarization (P_r) of 58:42 and 36:64 HZO with different thermal histories. (All values given in $\mu C/cm^2$.)

Thermal History	**58:42 HZO ($Hf_{0.58}Zr_{0.42}O_2$)**	**36:64 HZO ($Hf_{0.36}Zr_{0.64}O_2$)**
80-min UHV only (600 °C)	5.5	4.1
3-h UHV only (550 °C)	5.4	3.1
3-h Se flux only (500 °C)	5.1	2.9
80-min UHV (600 C°) + 3-h Se flux (500 °C)	6.6	6.7
3-h UHV (550 °C) + 3-h Se flux (500 °C)	6.4	5.7

Leakage current measurements of UHV-annealed vs. Se flux-annealed samples were acquired, and the I-V plots are shown in Figure 4.1.14. It is noticeable that the leakage current response of 36:64 HZO increases more with field cycling, which is an expected result of the ALD processing for more Zr-rich HZO compositions. However, for the same HZO composition, the Se flux anneal resulted in leakage currents that were up to an order of magnitude lower than the results for the UHV anneal. The lower leakage response of the Se flux-annealed samples may be due to

the fact that Se diffuses into oxygen vacancy sites, thereby limiting the contribution of oxygen vacancies to leakage.

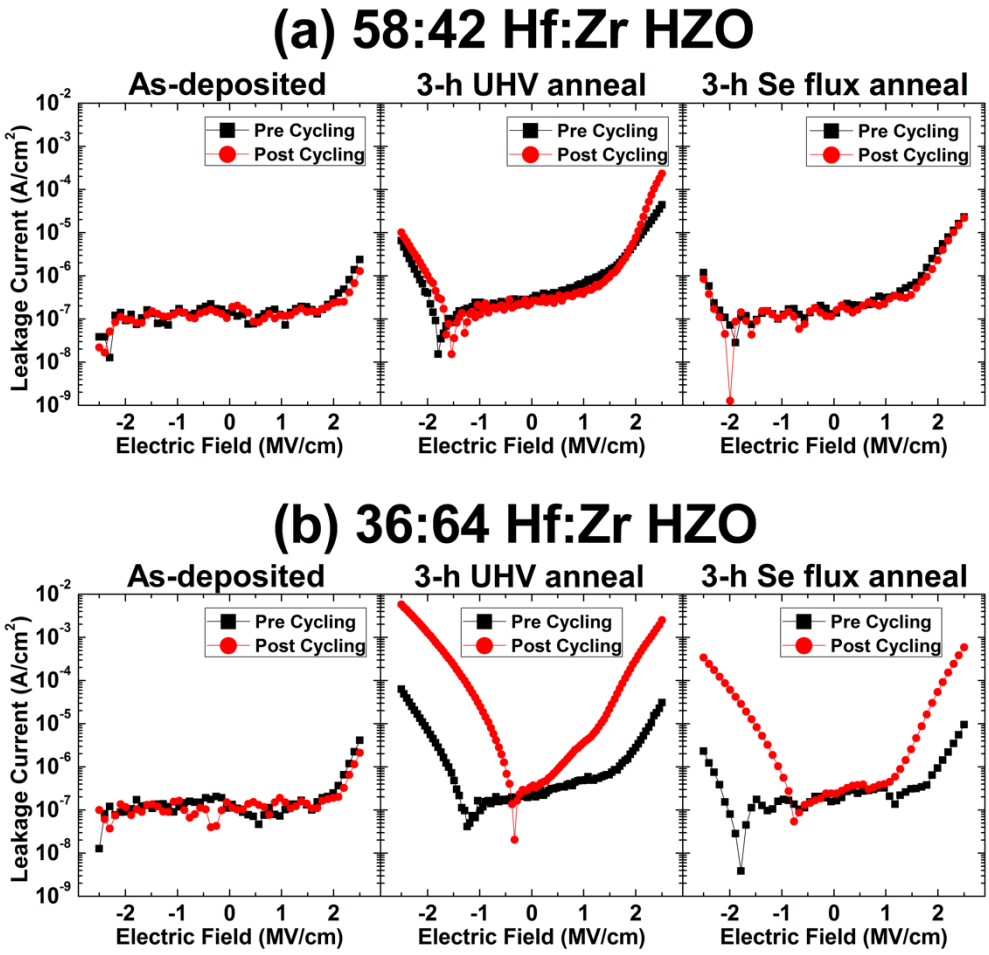

Figure 4.1.14. I-V curves of (a) 58:42 HZO and (b) 36:64 HZO before any processing (as-deposited), after a 3-h UHV only anneal at 550 °C, and after a 3-h Se flux only anneal at 500 °C.

The electrical results indicate that any incorporated Se in HZO due to the MBE growth process is not detrimental to its functionality as a ferroelectric layer. An HZO sample annealed in a Se flux exhibits the same P_r as a sample that was UHV-annealed without Se. This shows that in-situ crystallization of an amorphous HZO substrate during MBE growth presents a feasible approach for growing TMDCs on ferroelectric HZO. However, it is also important to note that an improved P_r is observed when the HZO is pre-crystallized prior to MBE growth, as demonstrated

by the P_r of the UHV+Se flux-annealed samples in Table 4.1.2. In general, our measurements show the viability of using HZO thin films, whether amorphous or crystalline, as substrates for TMDC growth in order to realize a TMDC-on-ferroelectric stacking configuration for FeFET devices.

4.1.5 Conclusions

In this work, we demonstrated successful MBE growth of chemically homogeneous WSe_2 on two different compositions of HZO substrates (58:42 Hf:Zr and 36:64 Hf:Zr). We showed that our MBE growth process is repeatable and produces continuous large-area WSe_2 films on HZO. The effects of the MBE growth conditions on the HZO substrates were investigated by performing anneals in the MBE chamber which replicate the WSe_2 growth process. Due to the high temperature required for MBE, the HZO substrates crystallized, forming the monoclinic, orthorhombic, and tetragonal phases. Chemically, we showed that Se incorporates into the HZO during MBE growth. In addition, the susceptibility to Se adsorption and incorporation varied with the pre-MBE crystalline state and the composition of the HZO. The amount of incorporated Se is attributed to effects of an interplay between Se diffusivity and oxygen vacancy concentration in HZO. The Se found in the HZO was composed of a physisorbed and a chemisorbed component. The remanent polarization of the HZO substrates annealed under a Se flux was equal to or greater than those crystallized under similar conditions but without exposure to Se. This indicates that exposure to the high Se fluxes employed during the direct MBE growth of WSe_2 does not negatively affect the functionality of HZO for use as a ferroelectric layer in FeFETs. While we do not observe a more significant impact of the Se on the 20 nm HZO films that we studied, we note that the small amount of Se incorporated during the MBE process may have more pronounced effects for thinner HZO films, and it remains to be determined whether or not Se plays a role in the stabilization of the ferroelectric orthorhombic phase.

4.2 WSe_2 Deposition on Other Dielectric Oxides: Opportunities and Challenges in Integrating Molecular Beam Epitaxy in Device Fabrication

4.2.1 Abstract

Presented in this chapter are further investigations of the effects of our molecular beam epitaxy (MBE) WSe_2 deposition process on a selection of different dielectric oxides. We first discuss the impact of the MBE growth conditions on these dielectric oxides by heating them in our MBE chamber under a Se flux, similar to the experiments discussed in section 4.1.4.2. We further investigate the nature of the incorporated Se in the same hafnium zirconium oxide (HZO) compositions as in Chapter 4.1. We study the temperature dependence of Se chemisorption/incorporation, penetration depth of the Se atoms into the HZO film thickness, and atmospheric stability of Se-incorporated HZO. We then present similar studies made on two other dielectric oxides, SiO_2 and HfO_2, and investigate impacts on their chemistry and crystallinity. Lastly, we demonstrate back-end-of-the-line (BEOL) compatible WSe_2 growths on SiO_2 and HfO_2.

4.2.2 Methodology

For part of this work, we used amorphous hafnium zirconium oxide (HZO) substrates that were deposited by atomic layer deposition (ALD) in a Cambridge Nanotech Savanah 100 flow through style reactor at 150 °C in a nitrogen ambient. Tetrkis(dimethylamino) zirconium (TDMA-Zr, 75 °C, STREM) and tetrakis(dimethylamino)hafnium (TDMA-Hf, 75 °C, STREM) were used as reactants for ZrO_2 and HfO_2, respectively. Water (~30 °C) was used as an oxidant. The composition was controlled by changing the relative number of ZrO_2:HfO_2 cycles in a 10 cycle supercycle. The HZO thin films were deposited on 20 nm of pulsed DC sputtered TaN onto a (001)-oriented Si wafer.

For section 4.2.3.1.1, the HZO substrates, $Hf_{0.58}Zr_{0.42}O_2$ (58:42 HZO) and $Hf_{0.36}Zr_{0.64}O_2$ (36:64 HZO) mounted adjacent to each other, were exposed to sequential anneals under a Se flux of ~2×10^{-6} mbar. They were sequentially annealed at 250 °C, 325 °C, 410 °C, and 500 °C for 3 h at each temperature. After each 3-hour anneal, in-situ X-ray photoelectron spectroscopy (XPS) measurements were collected using a monochromated Al Kα X-ray source at 300 W and a Scienta

Omicron R3000 analyzer at a pass energy of 50 eV. Peak fitting of all collected XPS spectra was performed using kolXPD software [56].

To determine how deep the incorporated Se diffused into the HZO layer, depth profiling was performed using an ex-situ PHI VersaProbe III XPS system, equipped with a 130 W moonochromated Al Kα X-ray source, 100 μm X-ray spot size, and 26 eV pass energy. For this depth profiling experiment, we used a 36:64 HZO sample that was Se-annealed at 500 °C in our MBE chamber and sputtered it in the PHI VersaProbe III system with a 3 kV Ar^+ ion sputter gun. XPS measurements were collected after every 1 min sputter cycle.

Apart from HZO, we also investigated SiO_2 and HfO_2 substrates in this work. We used 18 nm thermal SiO_2/Si from the National Institute of Standards and Technology (NIST) and 20 nm HfO_2 deposited by ALD on a 10 nm SiO_2/Si wafer. ALD of HfO_2 was performed using a Kurt J. Lesker ALD 150LX, with tetrakis(dimethylamido)hafnium (TDMA-Hf) as the Hf precursor and H_2O as the oxidant, at a substrate temperature of 200 °C. The growth rate per cycle (GPC) of the HfO_2 ALD recipe, calibrated on a bare silicon wafer, was 0.1 nm/cycle.

The main goal of the work on SiO_2 and HfO_2 was to investigate back-end-of-the-line (BEOL) compatible processing temperatures, which helps us determine the feasibility and limitations of integrating our TMDC MBE process into wafer-scale device fabrication. In addition, SiO_2 and HfO_2 are studied in this section because they are two of the most common state-of-the-art dielectric oxide materials currently in the market.

The SiO_2 and HfO_2 surfaces were cleaned by exposure to ultraviolet-ozone (UV-O_3) for 5 min, after which they were immediately loaded into ultra-high vacuum (UHV). To study the impact of the MBE growth conditions while maintaining BEOL temperatures, they were annealed to 400 °C under a Se flux of ~2×10^{-6} mbar for approximately 3 h. The chemistry of the substrates following this Se annealing experiment was investigated with ex-situ XPS using the same PHI VersaProbe III system described above. The atmospheric exposure time of these samples prior to XPS measurement was approximately 10 min. To assess changes in the structure of the HfO_2 substrate after annealing in the MBE chamber, X-ray diffraction (XRD) was performed using an Empyrean X-ray diffractometer equipped with Cu Kα radiation in a grazing incidence geometry, with ω angle fixed at 0.7°.

We also demonstrated direct WSe_2 growth on both SiO_2 and HfO_2. During WSe_2 growth, the substrate was maintained at 400 °C, and the Se:W flux ratio was maintained at ~5000:1.

Throughout the growth process, the substrate was continuously exposed to both the W and Se sources simultaneously. The growth was allowed to continue for 2 h and 30 min, which produced approximately 4 layers of WSe_2, based on thickness calculations using the attenuation of the substrate signal in XPS (i.e., Si 2*p* for SiO_2 or Hf 4*f* for HfO_2). At the end of the 2 h and 30 min growth, the sample was cooled in a Se flux until it reached 275 °C, at which point the Se flux was turned off. The sample was allowed to further cool down to room temperature.

4.2.3 Results and Discussion

4.2.3.1 Further Investigations of Se in HZO

4.2.3.1.1 Temperature Dependence of Se Incorporation

The same HZO compositions as those discussed in Chapter 4.1 were exposed to sequential Se flux anneals at increasing temperatures in order to see how much the degree of Se incorporation changed with increasing the substrate temperature. Shown in Figure 4.2.1 are the Se 3*d* spectra for the two HZO samples that we studied. As we discussed in Chapter 4.1, the Zr 4*s* peak overlaps with the binding energy range where the Se 3*d* peaks are expected, so to better quantify the Se 3*d* intensity, we subtract the Zr 4*s* contribution from the raw data.

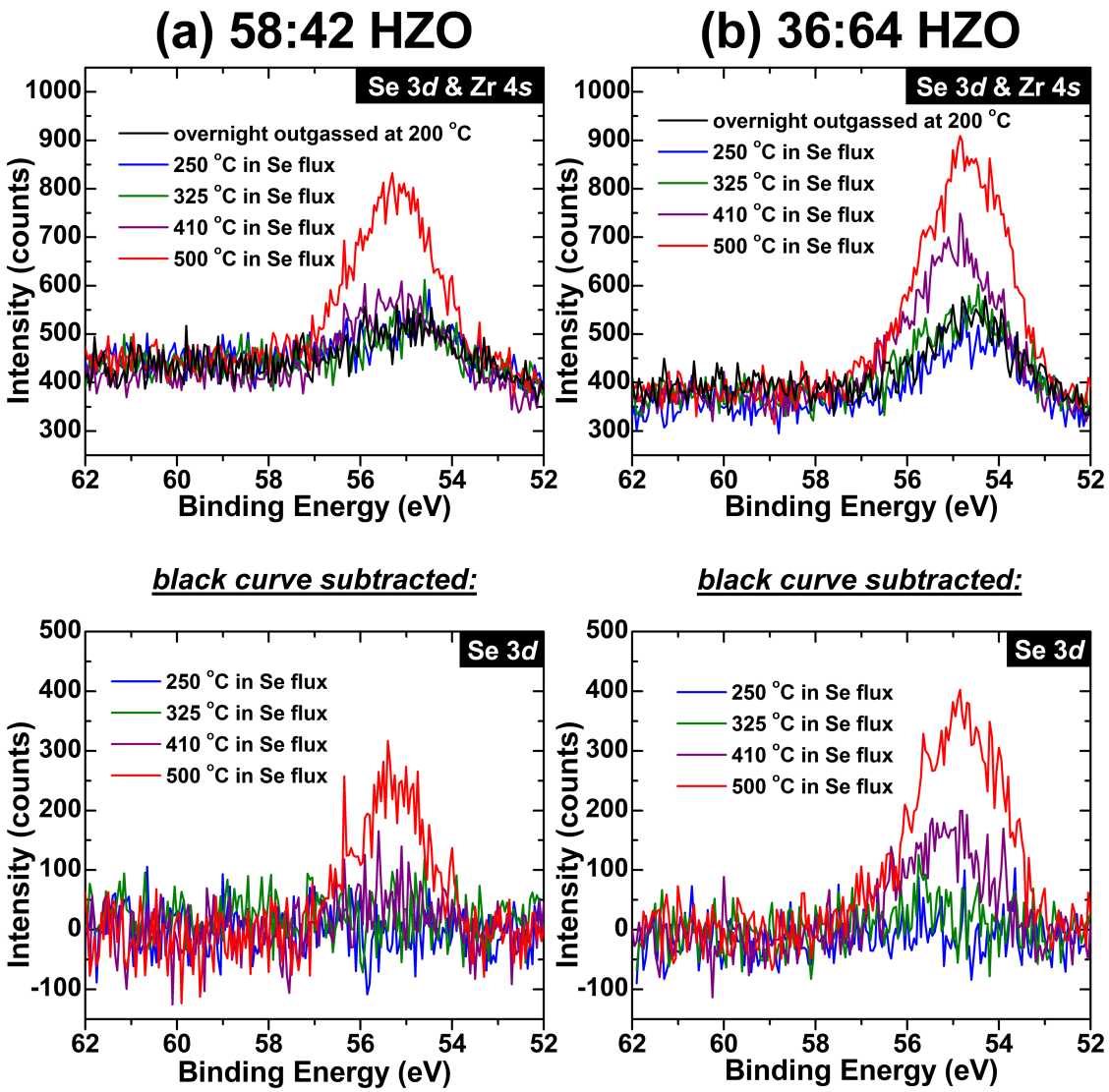

Figure 4.2.1. Measured Se 3d curves after each sequential anneal under a Se flux for (a) 58:42 HZO and (b) 36:64 HZO. The top panels have the Zr 4s contribution to each curve, and the bottom panels show the spectra after subtraction of the Zr 4s features.

In the top panels of Figure 4.2.1, we show the pre-Se anneal XPS spectra, which was collected after an overnight outgas of the samples at 200 °C in UHV. Because this measurement was taken before any exposure to Se in the MBE chamber, we can use the post-overnight outgas curves as a baseline for the Zr 4*s* feature of each sample (58:42 and 36:64 HZO). Their position and amplitude were referenced to the Zr 3*d* peak of each spectra, and was then subtracted from the measured curve at 52 to 62 eV binding energy after each Se annealing temperature. The results of

this curve subtraction, shown in the bottom panels of Figure 4.2.1, can be assumed to only represent the Se 3*d* features, as any contribution to that binding energy range coming from the HZO components, i.e., Zr 4*s*, have been accounted for and subtracted.

The components of the Se 3*d* peaks can be determined by fitting each resulting curve, and an example is shown in Figure 4.2.2. For both HZO compositions, as the annealing temperature is increased, the first Se feature that we detect is a doublet above 55 eV, which we assign to be a physisorbed Se-Se component. The position and width of the Se-Se peaks are fixed for each subsequent temperature. As the annealing temperature is increased, a second Se chemical state at lower binding energy (~54 eV for the Se $3d_{5/2}$ peak) is needed to fit the spectral feature. We attribute this lower binding energy chemical state to a chemisorbed Se-M-O component that is fully incorporated into the HZO lattice (in our Se-M-O notation, M is either hafnium or zirconium, and O is oxygen). The chemisorbed nature of this Se-M-O state was previously discussed in section 4.1.4.2.

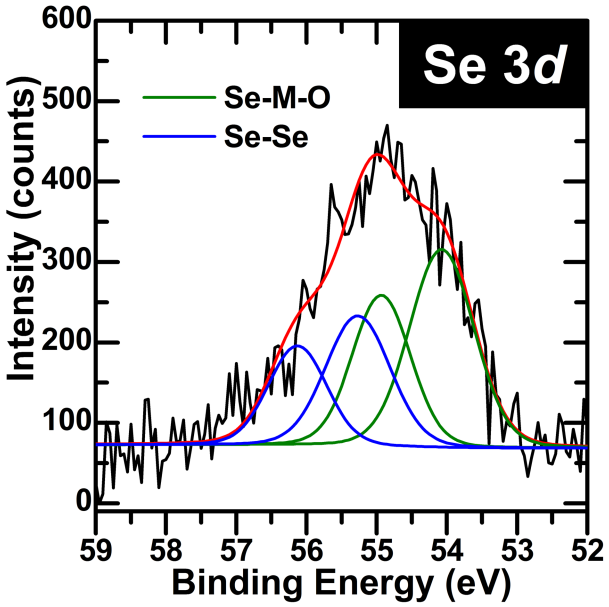

Figure 4.2.2. Example fitted Se 3d spectrum showing the Se-M-O doublet at 54.1 eV and 54.9 eV, and the Se-Se doublet at 55.3 eV and 56.1 eV. This fitted spectrum corresponds to the 500 °C curve in Figure 4.2.1 after Zr 4s subtraction.

The intensity of the Se $3d_{5/2}$ peak for each chemical state as a function of Se annealing temperature is plotted in Figure 4.2.3. In this figure, the data for the 58:42 HZO sample are shown as solid bars, and the data for the 36:64 HZO sample are shown as hashed bars. It can be seen that for both HZO compositions, the amount of incorporated Se increases with increasing substrate temperature. For both cases, the Se that is initially adsorbed at lower annealing temperatures is composed of only a physisorbed Se-Se state, and the chemisorbed Se component, Se-M-O, is only detected above a certain annealing temperature. For 58:42 HZO, this happens after the 500 °C anneal, but for the more Zr-rich sample, 36:64 HZO, Se incorporation (Se-M-O chemical state) is detected after a lower annealing temperature of 410 °C. This result is expected because ZrO_2 has a lower oxygen vacancy formation energy than HfO_2 [67, 68], which means the generation of oxygen vacancies requires a lower temperature for ZrO_2 than it does for HfO_2. Because of this, it is expected that after simultaneously annealing our HZO samples to the same temperature, the more Zr-rich HZO sample (36:64) would have more available oxygen vacancy sites for Se than the more Hf-rich sample (58:42), resulting in a higher amount of incorporated Se at every temperature step that we tested.

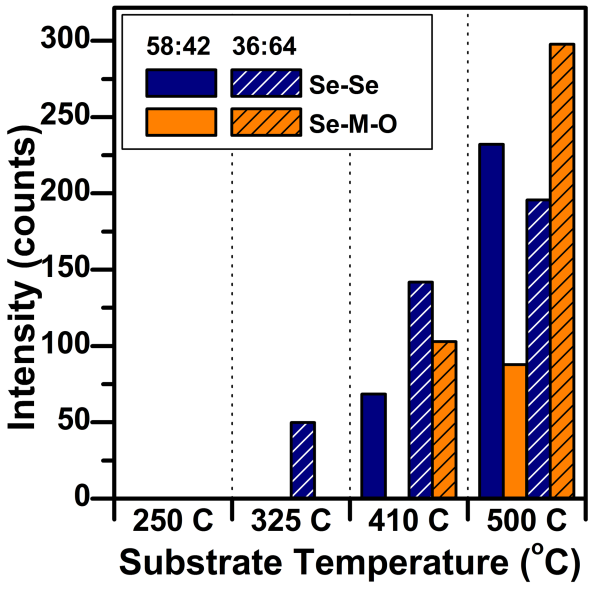

Figure 4.2.3. Plot of Se $3d_{5/2}$ intensity vs. annealing temperature under a Se flux for 58:42 and 36:64 HZO. The Se components (Se-Se and Se-M-O) are distinguished based on the color of the bar.

4.2.3.1.2 Depth Profiling of Se-Incorporated HZO

We performed Ar^+ sputter depth profiling of Se-incorporated 36:64 HZO to investigate how far into the 20 nm thick HZO film we can detect the incorporated Se atoms. Sputtering of thin films with Ar^+ ions is known to induce chemical changes, reduce cation oxidation states in an oxide film, displace lattice atoms, and disrupt the crystalline structure of films [74]. Because of these ion bombardment-induced effects that may change the chemistry and structure of the film, we caveat that the spatial location of different species determined through this sputter depth profiling technique should only be taken as an estimated, and not an absolute, location within the film.

Shown in Figure 4.2.4 is the Hf 4*f* region to illustrate how the chemistry of the Hf atoms changes as the HZO film is sputtered. The pre-sputter measurement shows the Hf 4*f* peaks at 18.0 eV and 19.7 eV, which correspond to Hf^{4+} in HZO. It is noticeable that with sputtering, these peaks get broader, and a low binding energy shoulder is observed. The development of this low binding energy state is indicative of a reduction in the Hf oxidation state to something closer to metallic Hf. This observed effect is due to the preferential sputtering of oxygen [74-76], which is a lighter and smaller atom compared to the transition metals it is bonded to, i.e., Hf and Zr.

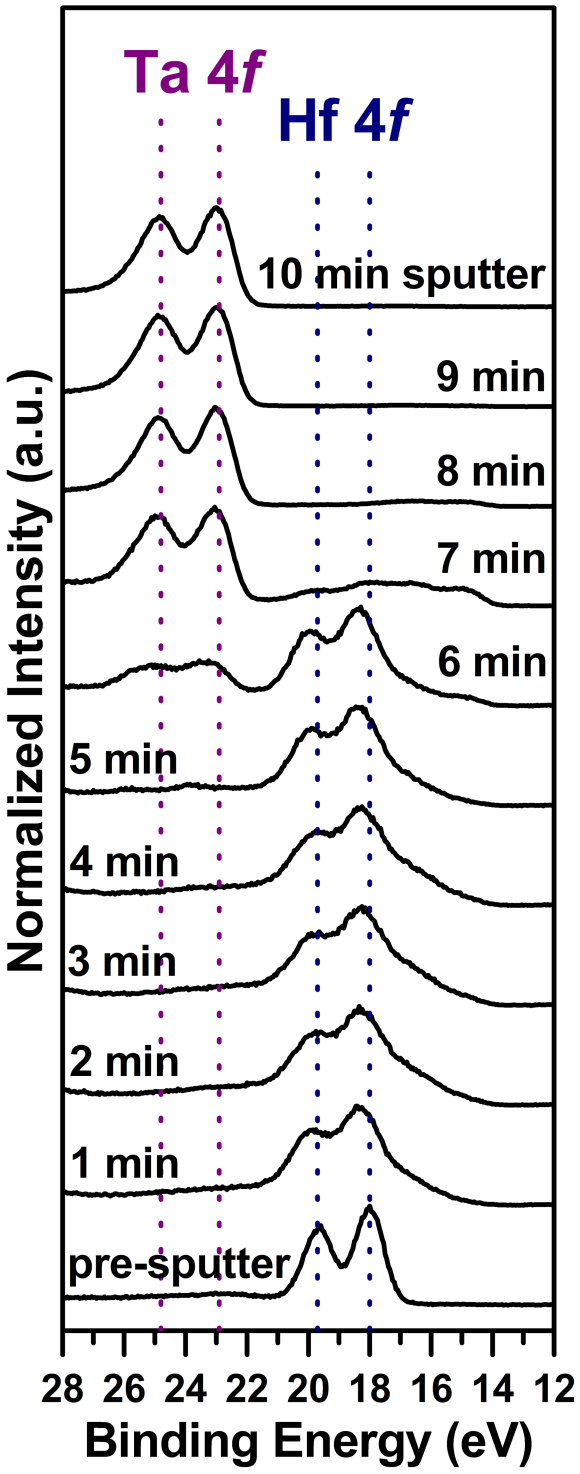

Figure 4.2.4. Hf 4f region of a 36:64 HZO film on TaN post-anneal in a Se flux, measured after incremental sputtering with 3 kV Ar^+ ions. We show the spectra as-received (pre-sputter) and after every 1-min sputtering increment.

Another noticeable result seen in Figure 4.2.4 is the emergence of new peaks on the high binding energy side of the Hf 4*f* peaks after roughly 5 min of total sputtering time. These doublet peaks at 22.9 eV and 24.8 eV are from the Ta 4*f* core level and correspond to the TaN layer underneath our HZO film. The emergence and development of the Ta 4*f* peaks after sputtering for > 5 min indicates that we are thinning the HZO material sufficiently to enable detection of the underlying TaN layer with increased sputter time. Because these Ta 4*f* peaks are close in binding energy to Hf 4*f*, the Hf 4*f* signal is difficult to distinguish at higher sputter times due to the tall Ta 4*f* features right next to it.

Therefore, we draw our attention to the Zr 3*d* core level, which is shown in Figure 4.2.5. In Figure 4.2.5(a), the spectra as-received (pre-sputter) and after each incremental 1-min sputtering step are overlaid on top of each other. We see that the maximum Zr 3*d* peak intensity is decreasing with increasing sputter time, again indicating that we are thinning our HZO material. We also see that as the HZO film is sputtered, the Zr 3*d* peaks are getting broader and shifting to lower binding energy, similar to the trend observed with the Hf 4*f* peaks. This shift to lower binding energy of the Zr 3*d* peaks is indicative of a reduction in the Zr oxidation state towards metallic Zr. After a sputtering time of ≥ 8 min, majority of the Zr signal is composed of metallic Zr, Zr^0.

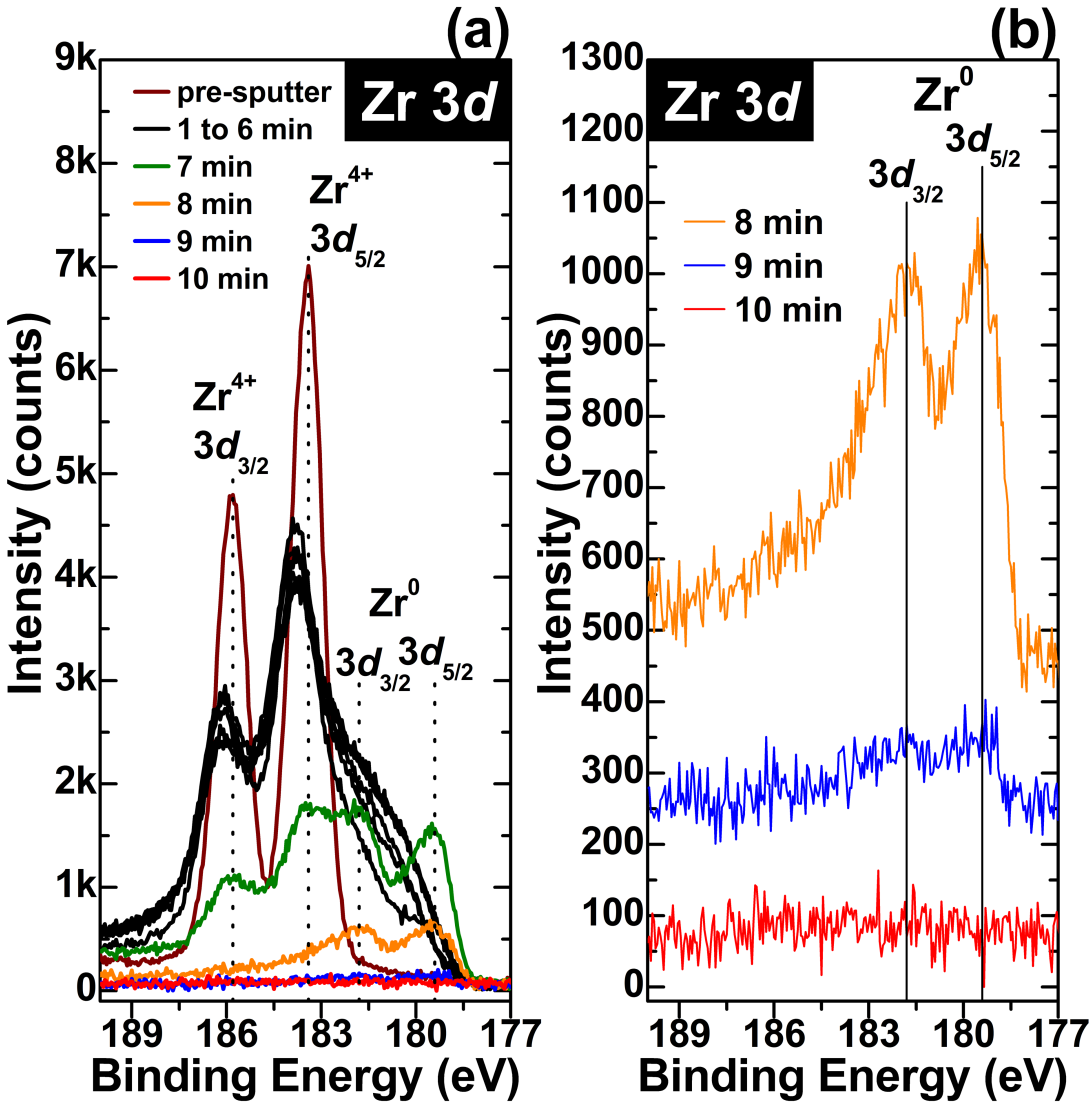

Figure 4.2.5. (a) Overlaid Zr 3d spectra of Se-annealed 36:64 HZO before and after incremental 1-min sputtering steps. (b) Same 8-, 9-, and 10-min post-sputter spectra as in (a), offset and with the y-axis rescaled for better clarity of the low intensity peaks.

In Figure 4.2.5(b), the Zr 3*d* region after 8, 9, and 10 min of sputtering are plotted offset from each other to show when the Zr 3*d* signal drops to the noise level. Features corresponding to Zr^0 are noticeable after 8 and 9 min of sputtering, but after a total sputter time of 10 min, we see no discernible Zr features in the Zr 3*d* window. Based on this, we assume that our 20 nm HZO

film was completely sputtered after 10 min of Ar^+ sputtering at the ion gun conditions that we used, which gives us an estimated HZO sputtering rate of approximately 2 nm per min.

We note that this sputtering rate is a slowest-case estimate, and does not account for the bombardment with Ar^+ ions possibly driving Zr atoms deeper into the bulk of the HZO film. However, we expect any error to be within tenths of a nanometer based on when we first start to see Ta features from the TaN substrate (Figure 4.2.4). The effective attenuation length (EAL) of Ta 4*f* electrons in a layer of HZO is 2.16 nm [77, 78], and the information depth of XPS is taken to be approximately 3× the EAL of the photoelectrons being measured. Based on this assumption, the Ta 4*f* electrons that we first detect after 6 min of sputtering are traveling through ~6.5 nm (three times the EAL of 2.16 nm) of the HZO film remaining. This means that of the 20 nm thick film, approximately 13.5 nm had been sputtered off after 6 min, which translates to an estimated sputtering rate of 2.25 nm per min.

We can use our assumed ~2 nm per min sputtering rate to determine where the Se atoms are located within the thickness of the HZO film. After each incremental sputtering step, we also measured the Se 3*d* binding energy window. Figure 4.2.6 shows the Se 3*d* core level before any sputtering step, overlaid with the curves after 1 to 6 min of sputtering (1-min increments). The spectra plotted in Figure 4.2.6 are after subtraction of the Zr 4*s* contribution. We see that all of the post-sputter curves overlap with each other at the noise level, and we are only able to measure a Se peak before any sputtering step. We do not detect any Se 3*d* signal in our sample after the first (and each subsequent) 1-min sputtering step, informing us that any incorporated Se lies close to the surface of the HZO film. Based on our sputtering rate of 2 nm / min, we can assume that within XPS detection limits, the incorporated Se atoms are approximately located at the top 2 nm of the HZO film.

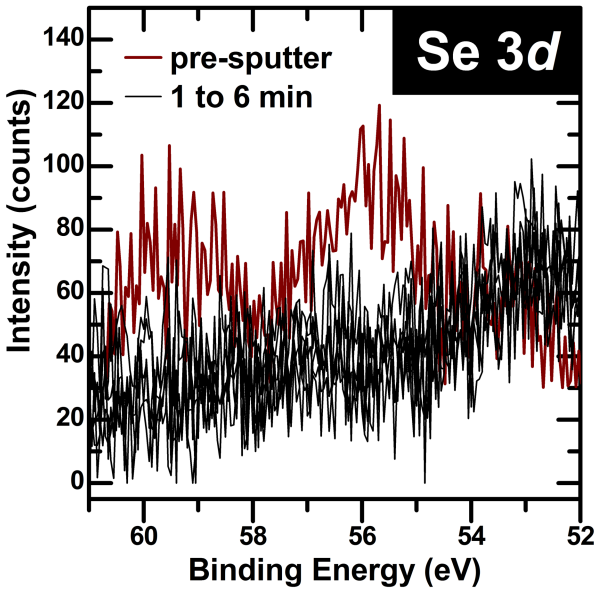

Figure 4.2.6. Se 3d core level of a 36:64 HZO sample annealed at 500 °C under a Se flux. We show the measured Se 3d curves before and after each incremental 1-min sputtering step, from 1 to 6 min total sputtering time. For clarity, the Zr 4s features have been subtracted from these spectra.

In Chapter 4.1, we discuss that the incorporated Se does not have significant effects on the properties of the HZO film; however, in our studies in this chapter, we use 20 nm thick HZO films. Ferroelectric HZO is highly scalable, with ferroelectricity being demonstrated in films as thin as 1 nm [79]. Given our result that incorporated Se is within the top ~2 nm of our HZO films, only 10% of the film has been modified. Incorporated Se atoms may have more significant electrical effects for applications using ultrathin HZO layers, where the Se-incorporated region will make up a greater fraction of the total film.

4.2.3.1.3 Stability of Incorporated Se

We also study the atmospheric stability of this incorporated Se, which is important to know in case ex-situ processing and/or ex-situ measurements are employed after a growth or annealing

step is performed in the MBE chamber. Since we know that the Se atoms are localized close to the surface, we expect them to be susceptible to atmospheric effects.

We first examine the stability of Se-incorporated 36:64 HZO, shown in Figure 4.2.7. With increasing air exposure, we see that the Se 3*d* peaks decrease in intensity, indicating loss or volatilization, and shift to higher binding energy, indicating Se oxidation. In this figure, vertical marker lines are drawn to show the binding energy position of the Se $3d_{5/2}$ peak for different Se chemical states: the chemisorbed component incorporated in the HZO film, Se-M-O, the physisorbed component, Se-Se, and the most stable oxide of Se, SeO_2.

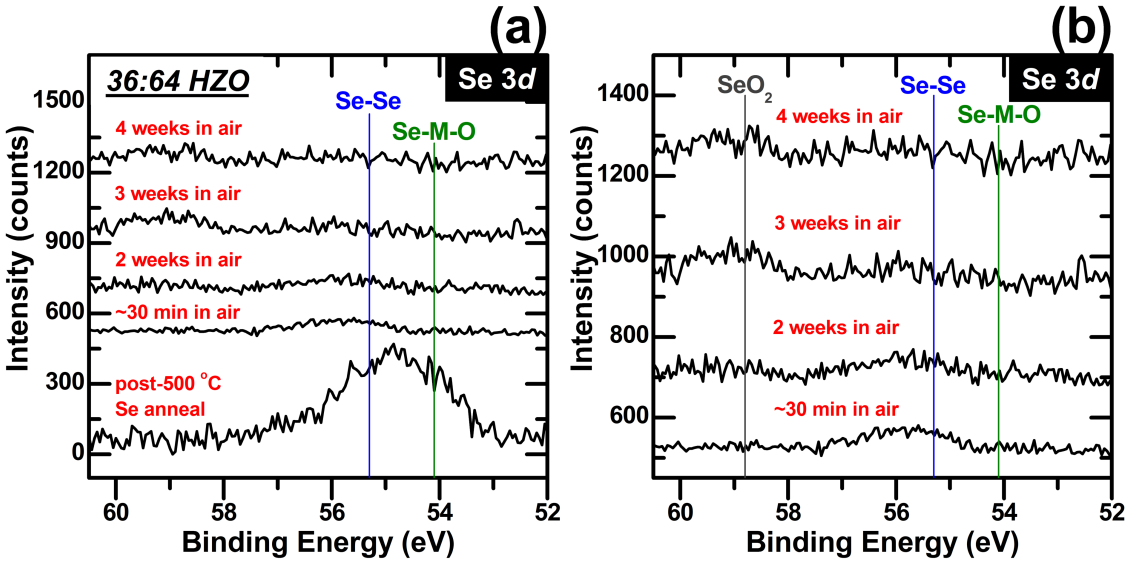

Figure 4.2.7. (a) Measured Se 3d spectra of Se-annealed 36:64 HZO after increasing amounts of time in atmosphere. (b) Same spectra as in (a), but with the y-axis rescaled to clearly show the low intensity peaks. All curves shown are post-subtraction of the overlapping Zr 4s features.

In Figure 4.2.7(b), the y-axis of the plot is rescaled to clearly show the differences in the post-air exposure Se 3*d* curves. After only 30 min in atmosphere, we do not detect the chemisorbed Se-M-O component, and the only Se chemical state that we detect is elemental Se-Se. With longer air exposures, we observe that the Se oxidizes, based on the appearance of the SeO_2 peak and the decreasing intensity of the Se-Se peak.

We report that there are several effects at play here. The rapid decrease in intensity of the Se 3*d* peaks within minutes of air exposure shows loss of some of the Se. Because Se is known to be highly volatile [80], it makes sense that our ultrathin physisorbed Se, estimated to be only ~1-2 Å thick based on the attenuation of the Hf, Zr, and O peaks, readily evaporates.

In addition, we also see that our incorporated Se (Se-M-O state) is not detected after minutes in air; after a 30-min air exposure, we only measure a peak corresponding to Se-Se. We have shown in section 4.1.4.2 that for the Se-M-O state, Se atoms fill oxygen vacancy sites in HZO, so they are bonded to either a Hf or Zr atom. Upon atmospheric exposure, these substitutional Se atoms are likely displaced by oxygen from atmosphere because the formation of Hf-O and Zr-O bonds, which results in local O-Hf-O and O-Zr-O bonding environments, is much more favorable than the Hf and Zr atoms being bonded to one Se and one O atom (i.e., Se-Hf-O or Se-Zr-O). This is supported by the bond energies and enthalpies of formation of selenides vs. oxides of Hf and Zr. Thermodynamic investigations show that the enthalpies of formation of HfO_2 and ZrO_2 are more negative (i.e., more thermodynamically favorable) than diatomic Hf and Zr selenide. [81, 82] Furthermore, it has also been shown that thermodynamically stable dichalcogenides of Hf and Zr, i.e., $HfSe_2$, $ZrSe_2$, rapidly oxidize in air [83-85], providing more evidence of the favorable formation of Hf-O and Zr-O bonds over Hf-Se and Zr-Se.

The discussed thermodynamic arguments and bond energetics provide a reason for the disappearance of the Se-M-O state in atmosphere, accompanied by the segregation of the remaining detectable Se atoms into an elemental Se-Se chemical state for 36:64 HZO. However, for 58:42 HZO, Se is completely absent based on XPS after 30 min in atmosphere, as shown in Figure 4.2.8. As discussed in sections 4.1.4.2 and 4.2.3.1.1, our lower Zr content HZO, 58:42, has less incorporated Se than 36:64 HZO. After a 500 °C anneal in a Se flux, based on our spectral fits, the Se-M-O peak intensity for 58:42 HZO is ~3.5× smaller than that for 36:64 HZO, as depicted visually in the bar graph shown in Figure 4.2.3. Since there is a smaller amount of incorporated Se atoms in 58:42 HZO, we expect that their segregation into elemental Se and subsequent oxidation and/or volatilization in air is a much faster process than what we observed for 36:64 HZO; based on our results in Figure 4.2.8, this occurs within 30 minutes in atmosphere. We note that Se can be volatilized from both the elemental Se state or the oxidized (SeO_2) state, as both species are known to have high vapor pressures [80, 86-88].

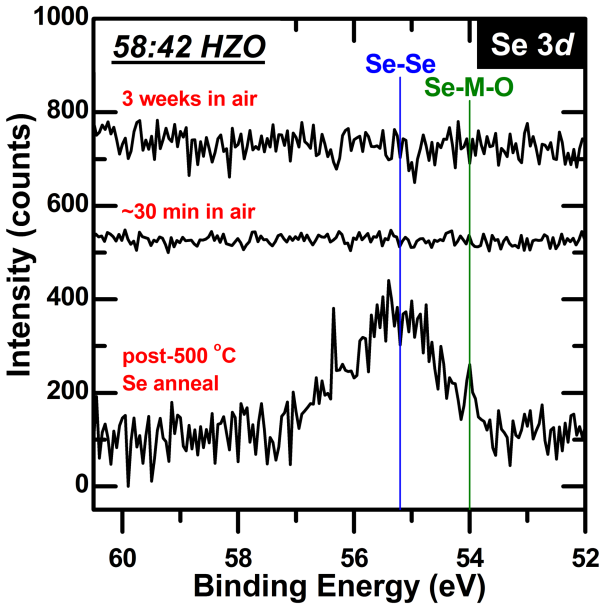

Figure 4.2.8. Measured Se 3d spectra of Se-annealed 58:42 HZO after increasing amounts of time in atmosphere. All curves shown are post-subtraction of the overlapping Zr 4s features.

For the following section on SiO_2 and HfO_2, all of the measurements post-annealing/post-MBE processing were performed ex-situ, so the lack of atmospheric stability of any incorporated Se, as discussed in this section, should be taken into account. We also note that for all of our studies where we only perform an anneal in the MBE chamber, i.e., no WSe_2 growth on the dielectric, we do not have a protective layer on top of our Se-incorporated dielectric/ferroelectric, making them susceptible to atmospheric effects. This issue of instability in air could be circumvented by implementing in-situ contact deposition for future electrical testing of bare Se-incorporated oxides. Additionally, for actual TMDC channel growth using MBE, the TMDC, i.e., WSe_2, grown on top of the dielectric will prevent the Se-incorporated oxide surface from chemically reacting with oxygen in air. This is expected to be true even for a thin WSe_2 barrier between the oxide surface and atmosphere, as oxidation of WSe_2 is self-limiting at the monolayer level, i.e., in ambient conditions, oxygen species have a high diffusion barrier across a layer of oxidized WSe_2 [89-92]. Chapter 5.2 of this dissertation presents studies where we investigate the mechanisms of deliberate oxidation of WSe_2.

4.2.3.2 Impact of the MBE Growth Conditions on SiO_2 and HfO_2

In addition to our work on interfaces between TMDCs and ferroelectrics, we have also investigated TMDCs interfaced with linear dielectrics, focusing specifically on SiO_2 and HfO_2. We limit these studies to BEOL-compatible temperatures because in order to properly assess the feasibility of integrating our MBE technique into the fabrication of real devices, we have to ensure that pre-fabricated stacks are not damaged by our process. To do this, we maintain processing temperatures of 400 °C, which is compatible with BEOL complementary metal-oxide-semiconductor (CMOS) fabrication [93], for all of the following sections.

Similar to the process used for earlier sections on HZO, we annealed our SiO_2 and HfO_2 samples at 400 °C for 3 h under a Se flux of 2×10^{-6} mbar, in order to replicate the substrate temperature and Se overpressure that these samples would undergo during actual WSe_2 growth. For this section, XPS measurements were performed ex-situ, and the Se-annealed SiO_2 and HfO_2 samples were in air for 10 min during transfer to the XPS analysis chamber.

4.2.3.2.1 Chemistry

For SiO_2, we show the Si 2*p* and O 1*s* XPS features in Figure 4.2.9. We see that the only observable change in these spectra is a slight shift of the peaks after surface cleaning with UV-O_3. After the anneal in Se flux, the peaks overlap with the peaks measured after the UV-O_3 surface cleaning step.

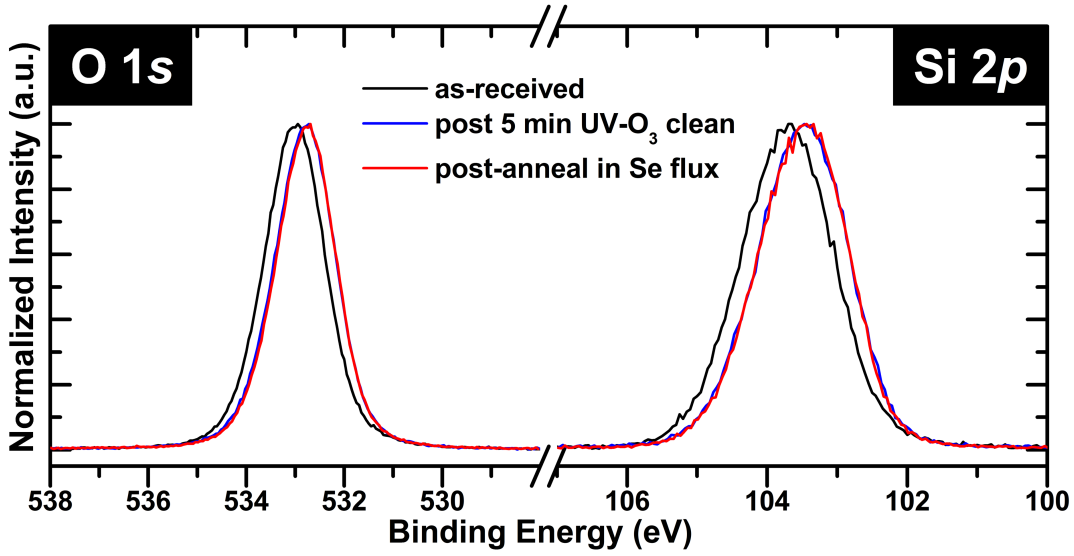

Figure 4.2.9. Si 2p and O 1s spectra of SiO_2 measured as-received, after surface cleaning with UV-O_3, and after annealing under a Se flux in the MBE chamber.

We also measured the Se 3*d* region, which is shown in Figure 4.2.10. It is evident from this figure that we do not detect any peaks corresponding to Se on the SiO_2 surface. The results shown in Figure 4.2.9 and Figure 4.2.10 indicate that within the limits of our ex-situ XPS measurements, SiO_2 is robust to the temperature and Se pressure used during WSe_2 growth. This means that the use of MBE for direct deposition of a 2D semiconducting channel, i.e., WSe_2, on SiO_2 is a promising route for transistor device fabrication that does not alter the properties and chemistry of the SiO_2 dielectric.

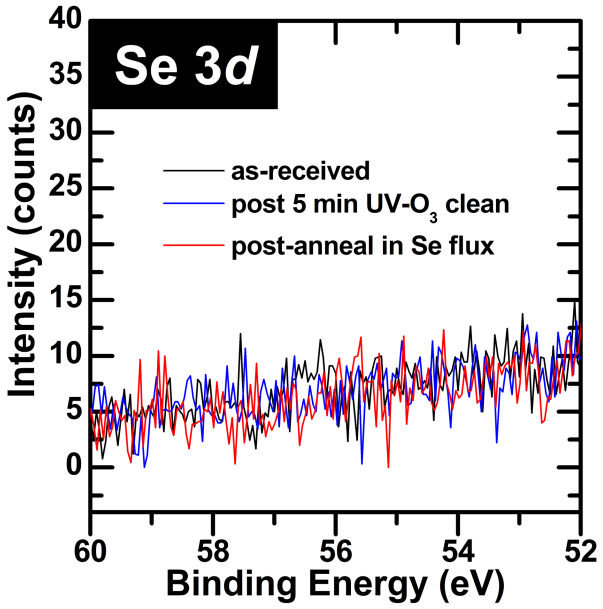

Figure 4.2.10. Se 3d binding energy region measured from SiO_2 as-received, after surface cleaning with UV-O_3, and after annealing under a Se flux in the MBE chamber.

We performed this same annealing experiment (400 °C, 3 h) in a Se flux on two HfO_2 samples: one that was not pre-cleaned (annealed as-received) and one that underwent the same surface cleaning procedure as SiO_2 (annealed post-5-min UV-O_3 cleaning). The Hf 4*f* and O 1*s* spectra of these samples are plotted in Figure 4.2.11. Based on the general shape and position of these peaks, we do not observe any extra chemical features that do not correspond to the Hf-O chemical bonding environment in HfO_2. We note that the high binding energy hump in the O 1*s* region is assigned to non-lattice oxygen [53, 94-96] present in the HfO_2 film.

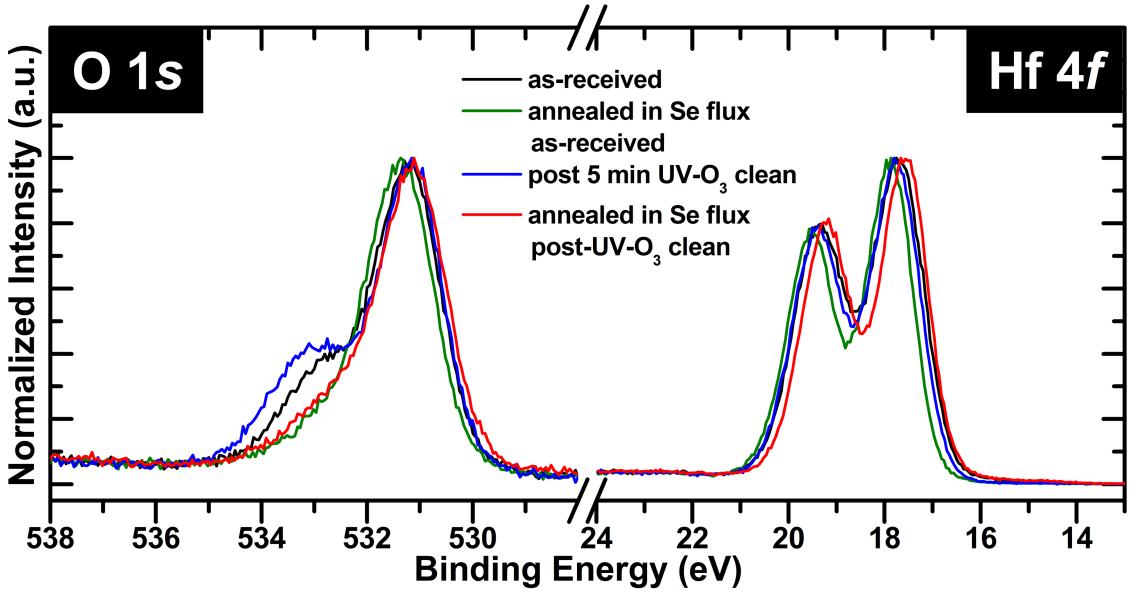

Figure 4.2.11. Hf 4f and O 1s spectra of HfO_2 before and after annealing under a Se flux in the MBE chamber.

As seen in Figure 4.2.11, there are subtle shifts in the peaks from sample to sample. We quantify these peak shifts by fitting each curve and plotting the binding energy positions of the Hf $4f_{7/2}$ and O 1*s* peaks. This is plotted in Figure 4.2.12, which shows that the peak shifts are mostly within the error of our measurement. The only shift that is bigger than our window of error is the uniform shift of both Hf and O peaks to higher binding energy after annealing as-received HfO_2 under a Se flux in our MBE chamber.

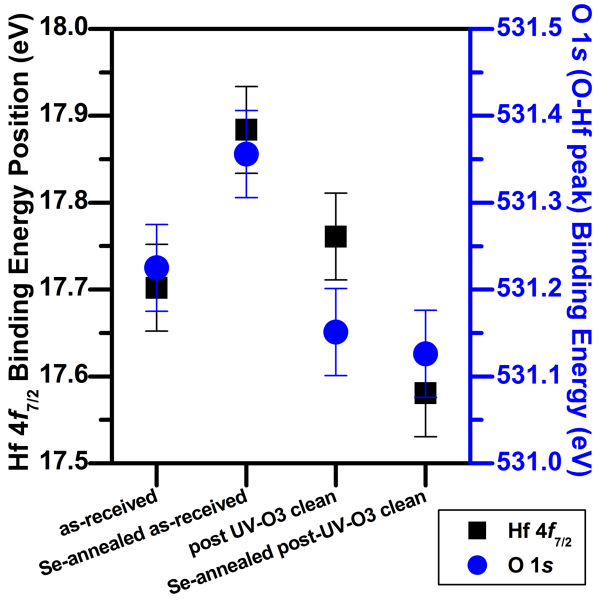

Figure 4.2.12. Plot of Hf $4f_{7/2}$ and O 1s binding energy positions for HfO_2 samples.

As discussed in Chapter 4.1, oxygen vacancies are n-type dopants in HfO_2 [69, 70], and in XPS core level spectra, n-type doping manifests as a uniform shift of the HfO_2 peaks to higher binding energy (further from the Fermi level at 0 eV). We demonstrated this in section 4.1.4.2 by deliberately creating oxygen vacancies in a film of HZO, after which we measured a uniform higher binding energy shift in the XPS core level peaks of Hf and Zr. The similar trend of the Se-annealed as-received HfO_2 sample shown in Figure 4.2.12 may be indicating that the anneal in a Se flux created oxygen vacancies in this film.

This increase in number of oxygen vacancies is the opposite of what we would expect if Se was being incorporated in HfO_2 through the anneal under a Se flux. Incorporated Se atoms would occupy oxygen vacancy sites, and therefore an increase in vacancy concentration would not be expected. However, in measuring the Se 3*d* region of our Se flux-annealed HfO_2 samples (both as-received and pre-cleaned), shown in Figure 4.2.13, we see no evidence of incorporated Se in the HfO_2 films. One caveat with this is that due to oxidation and volatilization in air, as discussed

in section 4.2.3.1.3, it is possible that any physisorbed/chemisorbed Se is outside the limit of detection of our ex-situ XPS measurements, as the samples were in air for 10 min during transfer to the XPS analysis chamber.

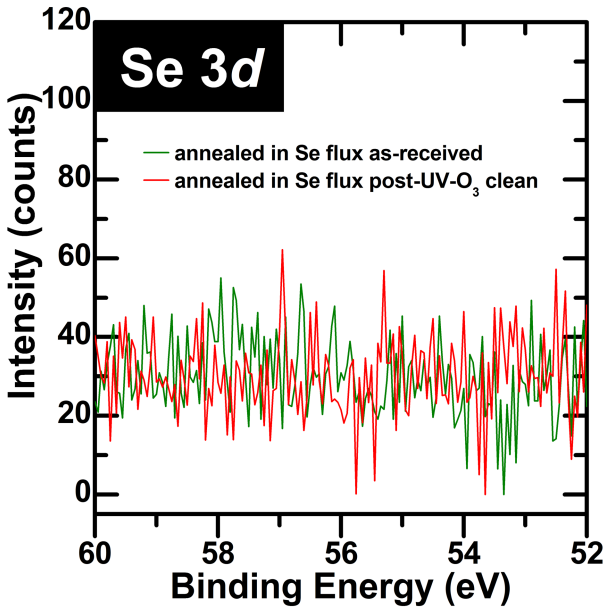

Figure 4.2.13. Measured Se 3d region of the Se-annealed HfO_2 samples (with and without a pre-clean).

The findings presented in Figure 4.2.12 and Figure 4.2.13 – the measured n-type shift of the HfO_2 film along with the lack of a detectable Se peak following an anneal in a Se flux – indicate that the Se flux anneal in our MBE chamber created oxygen vacancies in our as-received HfO_2 sample. This highlights that only the high temperature in a UHV environment had an effect on the HfO_2 film, and not the high Se flux that it was exposed to. Annealing to 400 °C in UHV reduced the HfO_2 film, thereby creating more oxygen vacancies. However, at this substrate temperature of 400 °C, which is deliberately lower than the temperatures used in Chapter 4.1 in order to maintain BEOL compatibility, the Se atoms impinging on the HfO_2 surface likely did not have enough energy to be chemisorbed or incorporated into the sample. Our results in section 4.2.3.1.1 support this argument; as shown in Figure 4.2.3, our Hf-rich HZO (58:42 HZO, the closer of the two HZO samples to HfO_2 stoichiometry) only resulted in a very small amount of physisorbed Se, and no

chemisorbed Se-M-O component, after annealing to ~400 °C under a Se flux. Our results on the HfO_2 samples indicate that HfO_2 behaves similarly with mild heating in Se.

4.2.3.2.2 Crystallinity

In a device, leakage through a dielectric layer is known to occur along the grain boundaries of a crystallized dielectric. We can potentially mitigate this problem by ensuring that during the MBE growth process, the substrate temperature is maintained to be below the crystallization temperature of the amorphous dielectric.

Amorphous SiO_2 crystallizes at temperatures > 1000 °C [97], so we know that for the Se flux anneal performed in our MBE chamber (400 °C for 3 h), we are well below the temperature required for forming grains of crystalline SiO_2. For HfO_2 thin films, crystallization is more nuanced. Various groups have shown that the crystallization temperature of HfO_2 can depend on several factors, such as its thickness, substrate, and deposition conditions, among others. Prior reports show a range of HfO_2 crystallization temperatures: 250-275 °C for HfO_2 deposited on a GaAs(100) substrate [98], 400 °C (with onset of crystallization observed at 300 °C) for HfO_2 deposited by plasma-enhanced ALD [99], 450-550 °C for rapid thermal annealing (RTA) in nitrogen [100], and 550-600 °C depending on the O/Hf ratio of the HfO_2 film [101].

For our annealing experiments under a Se flux, our 20 nm HfO_2 films were heated to 400 °C for 3 h in a UHV environment. We observe that after this anneal, the Hf 4*f* peaks that we measure with XPS are narrower than the peaks measured before heating the sample. This is evident in Figure 4.2.14, where the Hf 4*f* peaks of a HfO_2 sample as-received and after annealing in a Se flux are normalized and aligned. From this plot, it can be seen that at around 18.5 eV, the valley between the Hf 4*f* doublet dips lower for the Se-annealed sample compared to the as-received sample. This is a visual indicator that its full width at half maximum (FWHM) is smaller, i.e., its peaks are narrower. Narrowing of XPS peaks, as observed here, can be indicative of several phenomena, such as inducing a more uniform Hf-O bonding environment with desorption of adventitious species (i.e., OH), or inducing a higher degree of atomic order in the HfO_2 film. In Chapter 5, we have similar XPS observations and further experiments that show that such narrowing of core level peaks can indicate at least an onset of crystallization (nucleation of grains) in the sample.

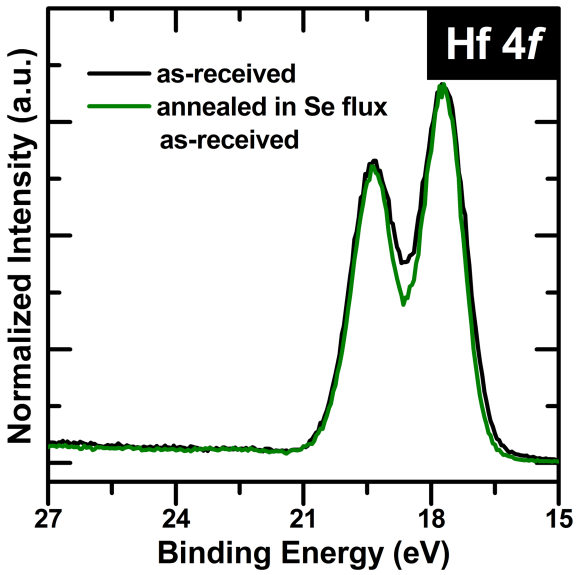

Figure 4.2.14. Normalized and aligned Hf 4f spectra of HfO_2 measured as-received and post-anneal in a Se flux.

To differentiate between nucleation of grains vs. full crystallization, we carried out grazing incidence XRD (GIXRD) on the same Se-annealed sample as in Figure 4.2.14. The result of that measurement is shown in Figure 4.2.15, where we did not detect any diffraction peaks from the orthorhombic (111), tetragonal (101), monoclinic ($\bar{1}11$), or monoclinic (111) reflections of HfO_2. The marker lines drawn on the plot indicate the 2θ angles at which the reflections resulting from these phases would have been expected.

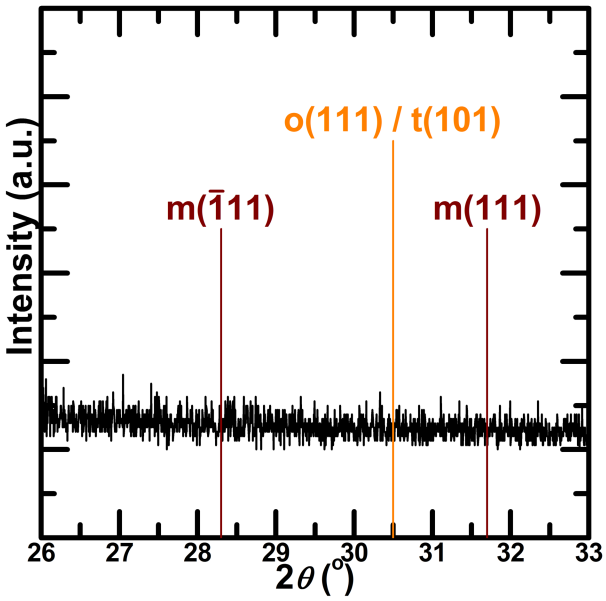

Figure 4.2.15. GIXRD pattern of a 20 nm HfO_2 thin film that was annealed for 3 h at 400 °C under a Se flux.

The absence of any diffraction peaks provides evidence that our 3-h 400 °C Se flux anneal does not result in large grains in our HfO_2 dielectric. While we may be inducing some amount of short-range order based on our XPS measurements (Figure 4.2.14), the lack of a diffraction pattern through GIXRD suggests that any increased order in the film is likely from very small nuclei, possibly from early onset of crystallization. However, we did not fully crystallize our HfO_2 sample.

The lack of large crystalline grains in our HfO_2 thin film provides promising implications for the applicability of our BEOL-compatible MBE growth technique. Because we have shown that the dielectric HfO_2 layer is not crystallized in-situ, we expect to avoid grain boundary contributions to dielectric leakage; however, this hypothesis remains to be tested in a real fabricated device.

4.2.3.3 BEOL-Compatible WSe_2 Growths on SiO_2 and HfO_2

In this section, we demonstrate that we are able to grow WSe_2 on SiO_2 and HfO_2 at a substrate temperature of 400 °C. We performed the same growth process and deposited approximately 4 layers of WSe_2 on both dielectric substrates. The W 4*f* and Se 3*d* spectra of these MBE-grown samples are shown in Figure 4.2.16.

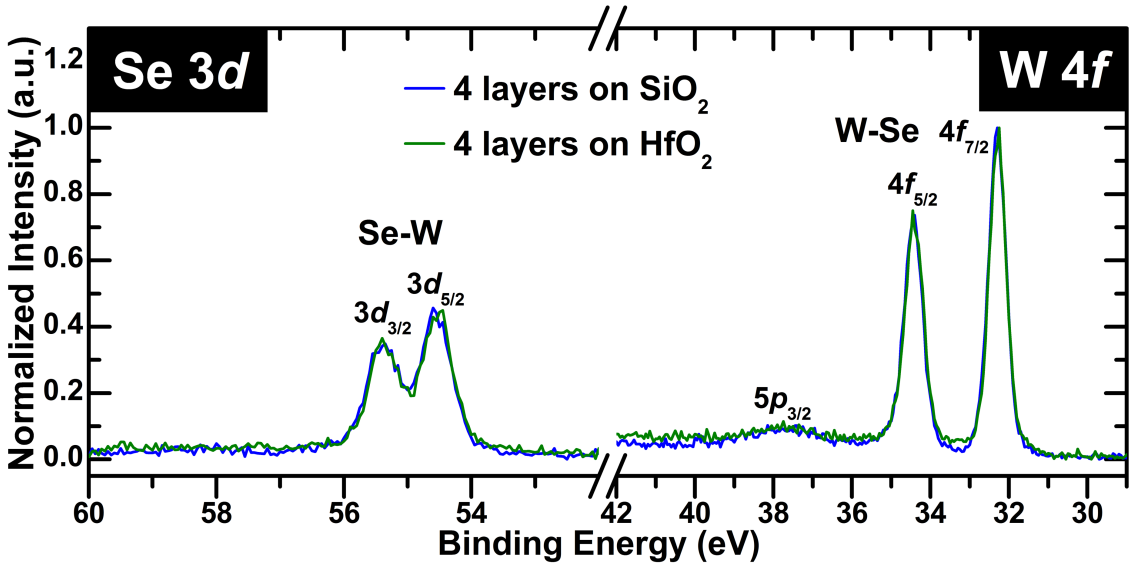

Figure 4.2.16. W 4f and Se 3d spectra of 4-layer WSe_2 films directly deposited on SiO_2 and HfO_2 at a substrate temperature of 400 °C.

We can see that the measured W 4*f* and Se 3*d* peaks match what we would expect for stoichiometric and chemically homogeneous WSe_2. We do not observe the presence of any additional chemical states, suggesting that the 400 °C substrate temperature maintained for these growths is sufficiently within the "Goldilocks zone" of temperatures that produces stoichiometric semiconducting WSe_2, as we have previously described in another report [1].

We note that at 400 °C, we are close to or at the lower limit of temperatures that allows the growth of the stable semiconducting WSe_2 phase. WSe_2 has a metastable phase, called 1T', that is metallic in nature. Our group has demonstrated growth of this metallic 1T' phase at a substrate temperature of 375 °C during MBE [1]. Other reports have shown that 1T' WSe_2 undergoes a phase transition into a more stable phase at 400 °C [102, 103]. Therefore, by maintaining our substrate temperature at 400 °C throughout the whole growth process, we are able to avoid the formation of the 1T' phase in our WSe_2 films, while staying within BEOL temperature limits for device fabrication.

While we have demonstrated successful BEOL-compatible growths of WSe_2 and directly deposited them onto dielectric substrates that are relevant to transistor device structures, the

electrical properties and device performance of our directly grown WSe_2 channels have yet to be studied. This will be the subject of suggested future work, as discussed in Chapter 6.

4.2.4 Conclusions

In this section, we reported on our investigations of different considerations needed to integrate our MBE WSe_2 growth process as a step in device fabrication. We studied the temperature dependence of Se incorporation in HZO and quantified the amount of physisorbed vs. chemisorbed Se in our HZO substrates as a function of temperature. We found that anneals in a Se flux carried out at lower temperatures did not result in incorporated/chemisorbed Se atoms in HZO, and the temperature limit that prevents Se chemisorption varied depending on the HZO alloy composition. We report that incorporated Se atoms reside in the top ~2 nm of the HZO film, and because of their proximity to the surface, the chemisorbed Se state is not stable in atmosphere.

We demonstrated the effects of our MBE growth conditions on two state-of-the-art dielectric oxides, SiO_2 and HfO_2. For these studies on SiO_2 and HfO_2, we specifically maintained BEOL compatibility of our substrate temperatures during MBE processing. We show that the SiO_2 and HfO_2 chemistries are not affected by the substrate temperature and Se flux used during growth. We also did not observe in-situ crystallization of either substrate in the MBE. Finally, we demonstrated successful direct WSe_2 growth on these dielectric substrates at a BEOL-compatible growth temperature of 400 °C, as we have shown with measurements of the surface and interface chemistry. Overall, these studies highlight the feasibility of using this MBE technique to deposit TMDC channels directly onto a device.

4.3 Chapter 4 References

[1] P. M. Litwin, M. G. Sales, V. Nilsson, P. V. Balachandran, C. Constantin, and S. McDonnell, *The effect of growth temperature and metal-to-chalcogen on the growth of WSe2 by molecular beam epitaxy* (SPIE Nanoscience + Engineering). SPIE, 2019.

[2] A. Eftekhari, "Tungsten dichalcogenides (WS_2, WSe_2, and WTe_2): materials chemistry and applications," *Journal of Materials Chemistry A,* 10.1039/C7TA04268J vol. 5, no. 35, pp. 18299-18325, 2017, doi: 10.1039/C7TA04268J.

[3] Q. Cheng *et al.*, "WSe_2 2D p-type semiconductor-based electronic devices for information technology: Design, preparation, and applications," *InfoMat,* https://doi.org/10.1002/inf2.12093 vol. 2, no. 4, pp. 656-697, 2020/07/01 2020, doi: https://doi.org/10.1002/inf2.12093.

[4] D. Xiao, G.-B. Liu, W. Feng, X. Xu, and W. Yao, "Coupled Spin and Valley Physics in Monolayers of MoS_2 and Other Group-VI Dichalcogenides," *Physical Review Letters,* vol. 108, no. 19, p. 196802, 05/07/ 2012, doi: 10.1103/PhysRevLett.108.196802.

[5] H. Yuan *et al.*, "Zeeman-type spin splitting controlled by an electric field," *Nature Physics,* vol. 9, no. 9, pp. 563-569, 2013/09/01 2013, doi: 10.1038/nphys2691.

[6] F. Withers *et al.*, "WSe_2 Light-Emitting Tunneling Transistors with Enhanced Brightness at Room Temperature," *Nano Letters,* vol. 15, no. 12, pp. 8223-8228, 2015/12/09 2015, doi: 10.1021/acs.nanolett.5b03740.

[7] T. Mikolajick, "Ferroelectric Nonvolatile Memories," in *Reference Module in Materials Science and Materials Engineering*: Elsevier, 2016.

[8] A. I. Khan, A. Keshavarzi, and S. Datta, "The future of ferroelectric field-effect transistor technology," *Nature Electronics,* vol. 3, no. 10, pp. 588-597, 2020/10/01 2020, doi: 10.1038/s41928-020-00492-7.

[9] X. Sang, E. D. Grimley, T. Schenk, U. Schroeder, and J. M. LeBeau, "On the structural origins of ferroelectricity in HfO_2 thin films," *Applied Physics Letters,* vol. 106, no. 16, p. 162905, 2015/04/20 2015, doi: 10.1063/1.4919135.

[10] T. S. Böscke, J. Müller, D. Bräuhaus, U. Schröder, and U. Böttger, "Ferroelectricity in hafnium oxide thin films," *Applied Physics Letters,* vol. 99, no. 10, p. 102903, 2011/09/05 2011, doi: 10.1063/1.3634052.

[11] S. Mueller *et al.*, "Incipient Ferroelectricity in Al-Doped HfO_2 Thin Films," *Advanced Functional Materials,* vol. 22, no. 11, pp. 2412-2417, 2012/06/06 2012, doi: 10.1002/adfm.201103119.

[12] J. Müller *et al.*, "Ferroelectricity in yttrium-doped hafnium oxide," *Journal of Applied Physics,* vol. 110, no. 11, p. 114113, 2011/12/01 2011, doi: 10.1063/1.3667205.

[13] S. Mueller, C. Adelmann, A. Singh, S. Van Elshocht, U. Schroeder, and T. Mikolajick, "Ferroelectricity in Gd-Doped HfO_2 Thin Films," *ECS Journal of Solid State Science and Technology,* vol. 1, no. 6, pp. N123-N126, 2012, doi: 10.1149/2.002301jss.

[14] J. Müller *et al.*, "Ferroelectricity in Simple Binary ZrO_2 and HfO_2," *Nano Letters,* vol. 12, no. 8, pp. 4318-4323, 2012/08/08 2012, doi: 10.1021/nl302049k.

[15] M. H. Park *et al.*, "A comprehensive study on the structural evolution of HfO_2 thin films doped with various dopants," *Journal of Materials Chemistry C,* 10.1039/C7TC01200D vol. 5, no. 19, pp. 4677-4690, 2017, doi: 10.1039/C7TC01200D.

[16] M. Hyuk Park, H. Joon Kim, Y. Jin Kim, W. Lee, H. Kyeom Kim, and C. Seong Hwang, "Effect of forming gas annealing on the ferroelectric properties of $Hf_{0.5}Zr_{0.5}O_2$ thin films with and without Pt electrodes," *Applied Physics Letters,* vol. 102, no. 11, p. 112914, 2013/03/18 2013, doi: 10.1063/1.4798265.

[17] H. Yu *et al.*, "Flexible Inorganic Ferroelectric Thin Films for Nonvolatile Memory Devices," *Advanced Functional Materials,* vol. 27, no. 21, p. 1700461, 2017/06/01 2017, doi: 10.1002/adfm.201700461.

[18] S. J. Kim *et al.*, "Large ferroelectric polarization of TiN/$Hf_{0.5}Zr_{0.5}O_2$/TiN capacitors due to stress-induced crystallization at low thermal budget," *Applied Physics Letters,* vol. 111, no. 24, p. 242901, 2017/12/11 2017, doi: 10.1063/1.4995619.

[19] Y. C. Jung *et al.*, "A Novel Combinatorial Approach to the Ferroelectric Properties in $Hf_xZr_{1-x}O_2$ Deposited by Atomic Layer Deposition," *physica status solidi (RRL) – Rapid Research Letters,* https://doi.org/10.1002/pssr.202100053 vol. 15, no. 5, p. 2100053, 2021/05/01 2021, doi: https://doi.org/10.1002/pssr.202100053.

[20] J. Hur, Y. C. Luo, N. Tasneem, A. I. Khan, and S. Yu, "Ferroelectric Hafnium Zirconium Oxide Compatible With Back-End-of-Line Process," *IEEE Transactions on Electron Devices,* vol. 68, no. 7, pp. 3176-3180, 2021, doi: 10.1109/TED.2021.3072610.

[21] P.-C. Shen, C. Lin, H. Wang, K. H. Teo, and J. Kong, "Ferroelectric memory field-effect transistors using CVD monolayer MoS_2 as resistive switching channel," *Applied Physics Letters,* vol. 116, no. 3, p. 033501, 2020/01/21 2020, doi: 10.1063/1.5129963.

[22] S. Zhang *et al.*, "Low Voltage Operating 2D MoS_2 Ferroelectric Memory Transistor with $Hf_{1-x}Zr_xO_2$ Gate Structure," *Nanoscale Research Letters,* vol. 15, no. 1, p. 157, 2020/08/02 2020, doi: 10.1186/s11671-020-03384-z.

[23] M.-Y. Cha *et al.*, "MoS_2-based ferroelectric field-effect transistor with atomic layer deposited $Hf_{0.5}Zr_{0.5}O_2$ films toward memory applications," *AIP Advances,* vol. 10, no. 6, p. 065107, 2020/06/01 2020, doi: 10.1063/5.0010829.

[24] K. Huang *et al.*, "$Hf_{0.5}Zr_{0.5}O_2$ Ferroelectric Embedded Dual-Gate MoS_2 Field Effect Transistors for Memory Merged Logic Applications," *IEEE Electron Device Letters,* vol. 41, no. 10, pp. 1600-1603, 2020, doi: 10.1109/LED.2020.3019681.

[25] X. Liu *et al.*, "Post-CMOS Compatible Aluminum Scandium Nitride/2D Channel Ferroelectric Field-Effect-Transistor Memory," *Nano Letters,* vol. 21, no. 9, pp. 3753-3761, 2021/05/12 2021, doi: 10.1021/acs.nanolett.0c05051.

[26] A. D. Franklin, "Nanomaterials in transistors: From high-performance to thin-film applications," *Science,* vol. 349, no. 6249, p. aab2750, 2015, doi: 10.1126/science.aab2750.

[27] X. Duan, C. Wang, A. Pan, R. Yu, and X. Duan, "Two-dimensional transition metal dichalcogenides as atomically thin semiconductors: opportunities and challenges," *Chemical Society Reviews,* vol. 44, no. 24, pp. 8859-8876, 2015, doi: 10.1039/C5CS00507H.

[28] A. Chaves *et al.*, "Bandgap engineering of two-dimensional semiconductor materials," *npj 2D Materials and Applications,* vol. 4, no. 1, p. 29, 2020/08/24 2020, doi: 10.1038/s41699-020-00162-4.

[29] I. P. Batra, P. Wurfel, and B. D. Silverman, "Depolarization Field and Stability Considerations in Thin Ferroelectric Films," *Journal of Vacuum Science and Technology,* vol. 10, no. 5, pp. 687-692, 1973/09/01 1973, doi: 10.1116/1.1318414.

[30] H. Ishiwara, "Recent progress of FET-type ferroelectric memories," *Integrated Ferroelectrics,* vol. 34, no. 1-4, pp. 11-20, 2001/02/01 2001, doi: 10.1080/10584580108012869.

[31] H. Ishiwara, "Current status and prospects of FET-type ferroelectric memories," *Journal of Semiconductor Technology and Science,* vol. 1, no. 1, pp. 1-14, 2001, doi: 10.1109/IEDM.2001.979615.

[32] N. Tasneem *et al.*, "The Impacts of Ferroelectric and Interfacial Layer Thicknesses on Ferroelectric FET Design," *IEEE Electron Device Letters,* vol. 42, no. 8, pp. 1156-1159, 2021, doi: 10.1109/LED.2021.3088388.

[33] C. Zhou and Y. Chai, "Ferroelectric-Gated Two-Dimensional-Material-Based Electron Devices," *Advanced Electronic Materials,* vol. 3, no. 4, p. 1600400, 2017/04/01 2017, doi: 10.1002/aelm.201600400.

[34] S. McDonnell, R. Addou, C. Buie, R. M. Wallace, and C. L. Hinkle, "Defect-Dominated Doping and Contact Resistance in MoS_2," *ACS Nano,* vol. 8, no. 3, pp. 2880-2888, 2014, doi: 10.1021/nn500044q.

[35] R. Addou, L. Colombo, and R. M. Wallace, "Surface Defects on Natural MoS_2," *ACS Applied Materials and Interfaces,* vol. 7, no. 22, pp. 11921-11929, 2015, doi: 10.1021/acsami.5b01778.

[36] R. Addou *et al.*, "Impurities and Electronic Property Variations of Natural MoS_2 Crystal Surfaces," *ACS Nano,* vol. 9, no. 9, pp. 9124-9133, 2015, doi: 10.1021/acsnano.5b03309.

[37] M. G. Sales, L. Herweyer, E. Opila, and S. McDonnell, "MoS_2 impurities: Chemical identification and spatial resolution of bismuth impurities in geological material," *Applied Surface Science,* vol. 508, p. 145256, 2020/04/01/ 2020, doi: https://doi.org/10.1016/j.apsusc.2020.145256.

[38] L. Xu *et al.*, "Ferroelectric-Modulated MoS_2 Field-Effect Transistors as Multilevel Nonvolatile Memory," *ACS Applied Materials & Interfaces,* vol. 12, no. 40, pp. 44902-44911, 2020/10/07 2020, doi: 10.1021/acsami.0c09951.

[39] K.-W. Chen *et al.*, "Pulse-Mediated Electronic Tuning of the MoS_2–Perovskite Ferroelectric Field Effect Transistors," *ACS Applied Electronic Materials,* vol. 2, no. 12, pp. 3843-3852, 2020/12/22 2020, doi: 10.1021/acsaelm.0c00676.

[40] S. K. Pandey, H. Alsalman, J. G. Azadani, N. Izquierdo, T. Low, and S. A. Campbell, "Controlled p-type substitutional doping in large-area monolayer WSe_2 crystals grown by chemical vapor deposition," *Nanoscale,* 10.1039/C8NR07070A vol. 10, no. 45, pp. 21374-21385, 2018, doi: 10.1039/C8NR07070A.

[41] H. Abuzaid, N. X. Williams, and A. D. Franklin, "How good are 2D transistors? An application-specific benchmarking study," *Applied Physics Letters,* vol. 118, no. 3, p. 030501, 2021/01/18 2021, doi: 10.1063/5.0029712.

[42] D. S. Macintyre, O. Ignatova, S. Thoms, and I. G. Thayne, "Resist residues and transistor gate fabrication," *Journal of Vacuum Science & Technology B: Microelectronics and Nanometer Structures Processing, Measurement, and Phenomena,* vol. 27, no. 6, pp. 2597-2601, 2009/11/01 2009, doi: 10.1116/1.3243176.

[43] A. Pirkle *et al.*, "The effect of chemical residues on the physical and electrical properties of chemical vapor deposited graphene transferred to SiO_2," *Applied Physics Letters,* vol. 99, no. 12, p. 122108, 2011/09/19 2011, doi: 10.1063/1.3643444.

[44] Y.-C. Lin, C.-C. Lu, C.-H. Yeh, C. Jin, K. Suenaga, and P.-W. Chiu, "Graphene Annealing: How Clean Can It Be?," *Nano Letters,* vol. 12, no. 1, pp. 414-419, 2012/01/11 2012, doi: 10.1021/nl203733r.

[45] R. Li *et al.*, "Determination of PMMA Residues on a Chemical-Vapor-Deposited Monolayer of Graphene by Neutron Reflection and Atomic Force Microscopy," *Langmuir,* vol. 34, no. 5, pp. 1827-1833, 2018/02/06 2018, doi: 10.1021/acs.langmuir.7b03117.

[46] K. M. Freedy *et al.*, "MoS_2 cleaning by acetone and UV-ozone: Geological and synthetic material," *Applied Surface Science,* vol. 478, pp. 183-188, 2019, doi: 10.1016/J.APSUSC.2019.01.222.

[47] S. McDonnell *et al.*, "HfO_2 on MoS_2 by Atomic Layer Deposition: Adsorption Mechanisms and Thickness Scalability," *ACS Nano,* vol. 7, no. 11, pp. 10354-10361, 2013/11/26 2013, doi: 10.1021/nn404775u.

[48] A. Azcatl *et al.*, "MoS_2 functionalization for ultra-thin atomic layer deposited dielectrics," *Applied Physics Letters,* vol. 104, no. 11, p. 111601, 2014/03/17 2014, doi: 10.1063/1.4869149.

[49] A. Azcatl *et al.*, "HfO_2 on UV–O_3 exposed transition metal dichalcogenides: interfacial reactions study," *2D Materials,* vol. 2, no. 1, p. 014004, 2015/01/13 2015, doi: 10.1088/2053-1583/2/1/014004.

[50] V. V. Afanas'ev *et al.*, "Band alignment at interfaces of few-monolayer MoS_2 with SiO_2 and HfO_2," *Microelectronic Engineering,* vol. 147, pp. 294-297, 2015/11/01/ 2015, doi: https://doi.org/10.1016/j.mee.2015.04.106.

[51] S. K. Pradhan, B. Xiao, and A. K. Pradhan, "Energy band alignment of high-k oxide heterostructures at MoS_2/Al_2O_3 and MoS_2/ZrO_2 interfaces," *Journal of Applied Physics,* vol. 120, no. 12, p. 125305, 2016/09/28 2016, doi: 10.1063/1.4963289.

[52] K. M. Price and A. D. Franklin, "Integration of 3.4 nm HfO_2 into the gate stack of MoS_2 and WSe_2 top-gate field-effect transistors," in *2017 75th Annual Device Research Conference (DRC)*, 25-28 June 2017 2017, pp. 1-2, doi: 10.1109/DRC.2017.7999405.

[53] M. G. Sales, S. T. Jaszewski, S. S. Fields, P. M. Litwin, J. F. Ihlefeld, and S. J. McDonnell, "Thermal stability of hafnium zirconium oxide on transition metal dichalcogenides," *Applied Surface Science,* vol. 546, p. 149058, 2021/04/30/ 2021, doi: https://doi.org/10.1016/j.apsusc.2021.149058.

[54] S. W. Smith, A. R. Kitahara, M. A. Rodriguez, M. D. Henry, M. T. Brumbach, and J. F. Ihlefeld, "Pyroelectric response in crystalline hafnium zirconium oxide ($Hf_{1-x}Zr_xO_2$) thin films," *Applied Physics Letters,* vol. 110, no. 7, p. 072901, 2017/02/13 2017, doi: 10.1063/1.4976519.

[55] K. M. Freedy, P. M. Litwin, and S. J. McDonnell, "(Invited) In-Vacuo Studies of Transition Metal Dichalcogenide Synthesis and Layered Material Integration," (in en), *ECS Transactions,* vol. 77, no. 8, pp. 11-25, 2017-05-03 2017, doi: 10.1149/07708.0011ecst.

[56] "Kolibrik.net, s.r.o. - Custom develompent of electronics and software." http://www.kolibrik.net/ (accessed.

[57] J. H. Scofield, "Hartree-Slater subshell photoionization cross-sections at 1254 and 1487 eV," *Journal of Electron Spectroscopy and Related Phenomena,* vol. 8, no. 2, pp. 129-137, 1976/01/01/ 1976, doi: https://doi.org/10.1016/0368-2048(76)80015-1.

[58] "SPI Supplies." https://www.2spi.com/ (accessed.

[59] D. M. Hausmann, E. Kim, J. Becker, and R. G. Gordon, "Atomic Layer Deposition of Hafnium and Zirconium Oxides Using Metal Amide Precursors," *Chemistry of Materials,* vol. 14, no. 10, pp. 4350-4358, 2002/10/01 2002, doi: 10.1021/cm020357x.

[60] D. M. Hausmann and R. G. Gordon, "Surface morphology and crystallinity control in the atomic layer deposition (ALD) of hafnium and zirconium oxide thin films," *Journal of Crystal Growth,* vol. 249, no. 1, pp. 251-261, 2003/02/01/ 2003, doi: https://doi.org/10.1016/S0022-0248(02)02133-4.

[61] W. Weinreich *et al.*, "Structural properties of as deposited and annealed ZrO_2 influenced by atomic layer deposition, substrate, and doping," *Journal of Vacuum Science & Technology A,* vol. 31, no. 1, p. 01A119, 2013/01/01 2012, doi: 10.1116/1.4765047.

[62] K. M. Price, K. E. Schauble, F. A. McGuire, D. B. Farmer, and A. D. Franklin, "Uniform Growth of Sub-5-Nanometer High-κ Dielectrics on MoS_2 Using Plasma-Enhanced Atomic Layer Deposition," *ACS Applied Materials & Interfaces,* vol. 9, no. 27, pp. 23072-23080, 2017/07/12 2017, doi: 10.1021/acsami.7b00538.

[63] J. Rodríguez-Viejo, F. Sibieude, M. T. Clavaguera-Mora, and C. Monty, "^{18}O diffusion through amorphous SiO_2 and cristobalite," *Applied Physics Letters,* vol. 63, no. 14, pp. 1906-1908, 1993/10/04 1993, doi: 10.1063/1.110644.

[64] G. Roma, Y. Limoge, and S. Baroni, "Oxygen Self-Diffusion in α -Quartz," *Physical Review Letters,* vol. 86, no. 20, pp. 4564-4567, 05/14/ 2001, doi: 10.1103/PhysRevLett.86.4564.

[65] J. Q. He *et al.*, "Microstructure and interfaces of HfO_2 thin films grown on silicon substrates," *Journal of Crystal Growth,* vol. 262, no. 1, pp. 295-303, 2004/02/15/ 2004, doi: https://doi.org/10.1016/j.jcrysgro.2003.10.026.

[66] K. Kajihara *et al.*, "Diffusion and reactions of interstitial oxygen species in amorphous SiO_2: A review," *Journal of Non-Crystalline Solids,* vol. 354, no. 2, pp. 224-232, 2008/01/15/ 2008, doi: https://doi.org/10.1016/j.jnoncrysol.2007.07.038.

[67] J. X. Zheng, G. Ceder, T. Maxisch, W. K. Chim, and W. K. Choi, "First-principles study of native point defects in hafnia and zirconia," *Physical Review B,* vol. 75, no. 10, p. 104112, 03/14/ 2007, doi: 10.1103/PhysRevB.75.104112.

[68] J. L. Lyons, A. Janotti, and C. G. Van de Walle, "The role of oxygen-related defects and hydrogen impurities in HfO_2 and ZrO_2," *Microelectronic Engineering,* vol. 88, no. 7, pp. 1452-1456, 2011/07/01/ 2011, doi: https://doi.org/10.1016/j.mee.2011.03.099.

[69] K. Xiong, J. Robertson, M. C. Gibson, and S. J. Clark, "Defect energy levels in HfO_2 high-dielectric-constant gate oxide," *Applied Physics Letters,* vol. 87, no. 18, p. 183505, 2005/10/31 2005, doi: 10.1063/1.2119425.

[70] J. Robertson, K. Xiong, and S. J. Clark, "Band gaps and defect levels in functional oxides," *Thin Solid Films,* vol. 496, no. 1, pp. 1-7, 2006/02/01/ 2006, doi: https://doi.org/10.1016/j.tsf.2005.08.175.

[71] C. C. Fulton, G. Lucovsky, and R. J. Nemanich, "Process-dependent band structure changes of transition-metal (Ti,Zr,Hf) oxides on Si (100)," *Applied Physics Letters,* vol. 84, no. 4, pp. 580-582, 2004/01/26 2004, doi: 10.1063/1.1639944.

[72] C. C. Fulton, T. E. Cook, G. Lucovsky, and R. J. Nemanich, "Interface instabilities and electronic properties of ZrO_2 on silicon (100)," *Journal of Applied Physics,* vol. 96, no. 5, pp. 2665-2673, 2004/09/01 2004, doi: 10.1063/1.1776313.

[73] D. Lim and R. Haight, "Temperature dependent defect formation and charging in hafnium oxides and silicates," *Journal of Vacuum Science & Technology B: Microelectronics and Nanometer Structures Processing, Measurement, and Phenomena,* vol. 23, no. 1, pp. 201-205, 2005/01/01 2005, doi: 10.1116/1.1850105.

[74] J.-N. Kim, K.-S. Shin, D.-H. Kim, B.-O. Park, N.-K. Kim, and S.-H. Cho, "Changes in chemical behavior of thin film lead zirconate titanate during Ar^+-ion bombardment using XPS," *Applied Surface Science,* vol. 206, no. 1, pp. 119-128, 2003/02/15/ 2003, doi: https://doi.org/10.1016/S0169-4332(02)01229-1.

[75] Y. Lebedinskii and A. Zenkevich, "Silicide formation at HfO_2–Si and ZrO_2–Si interfaces induced by Ar^+ ion bombardment," *Journal of Vacuum Science & Technology A,* vol. 22, no. 6, pp. 2261-2264, 2004, doi: 10.1116/1.1795823.

[76] P. K. Hurley, K. Cherkaoui, S. McDonnell, G. Hughes, and A. W. Groenland, "Characterisation and passivation of interface defects in (100)-Si/SiO_2/HfO_2/TiN gate stacks," *Microelectronics Reliability,* vol. 47, no. 8, pp. 1195-1201, 2007/08/01/ 2007, doi: https://doi.org/10.1016/j.microrel.2006.09.030.

[77] A. Jablonski and C. J. Powell, "The electron attenuation length revisited," *Surface Science Reports,* vol. 47, no. 2, pp. 33-91, 2002/06/01/ 2002, doi: https://doi.org/10.1016/S0167-5729(02)00031-6.

[78] A. Jablonski, "NIST Electron Effective-Attenuation-Length Database," 2011.

[79] S. S. Cheema *et al.*, "Enhanced ferroelectricity in ultrathin films grown directly on silicon," *Nature,* vol. 580, no. 7804, pp. 478-482, 2020/04/01 2020, doi: 10.1038/s41586-020-2208-x.

[80] Z. K. Heiba, "X-ray quantitative analysis of the phases developed upon air annealing of ZnSe, CdSe, and CdS semiconductors," *Powder Diffraction,* vol. 17, no. 3, pp. 191-195, 2002, doi: 10.1154/1.1487862.

[81] E. J. Huber and C. E. Holley, "Enthalpy of formation of hafnium dioxide," *Journal of Chemical & Engineering Data,* vol. 13, no. 2, pp. 252-253, 1968/04/01 1968, doi: 10.1021/je60037a034.

[82] J. J. Sorensen, T. D. Persinger, A. Sevy, J. A. Franchina, E. L. Johnson, and M. D. Morse, "Bond dissociation energies of diatomic transition metal selenides: TiSe, ZrSe, HfSe, VSe, NbSe, and TaSe," *The Journal of Chemical Physics,* vol. 145, no. 21, p. 214308, 2016, doi: 10.1063/1.4968601.

[83] M. J. Mleczko *et al.*, "$HfSe_2$ and $ZrSe_2$: Two-dimensional semiconductors with native high-κ oxides," *Science Advances,* vol. 3, no. 8, pp. e1700481-e1700481, 2017, doi: 10.1126/sciadv.1700481.

[84] Q. Yao, L. Zhang, P. Bampoulis, and H. J. W. Zandvliet, "Nanoscale Investigation of Defects and Oxidation of $HfSe_2$," *The Journal of Physical Chemistry C,* vol. 122, no. 44, pp. 25498-25505, 2018/11/08 2018, doi: 10.1021/acs.jpcc.8b08713.

[85] S. S. Jo *et al.*, "Growth Kinetics and Atomistic Mechanisms of Native Oxidation of ZrS_xSe_{2-x} and MoS_2 Crystals," *Nano Letters,* vol. 20, no. 12, pp. 8592-8599, 2020/12/09 2020, doi: 10.1021/acs.nanolett.0c03263.

[86] E. B. Dismukes, "Trace element control in electrostatic precipitators and fabric filters," *Fuel Processing Technology,* vol. 39, no. 1, pp. 403-416, 1994/08/01/ 1994, doi: https://doi.org/10.1016/0378-3820(94)90195-3.

[87] L. Marsal, H. Mariette, Y. Samson, J. L. Rouvière, and E. Picard, "Nanoscale surface clustering on CdTe epilayers," *Applied Physics Letters,* vol. 73, no. 20, pp. 2974-2976, 1998, doi: 10.1063/1.122648.

[88] W. Xu, Q. Song, G. Song, and Q. Yao, "The vapor pressure of Se and SeO_2 measurement using thermogravimetric analysis," *Thermochimica Acta,* vol. 683, p. 178480, 2020/01/01/ 2020, doi: https://doi.org/10.1016/j.tca.2019.178480.

[89] M. Yamamoto *et al.*, "Self-Limiting Layer-by-Layer Oxidation of Atomically Thin WSe_2," *Nano Letters,* vol. 15, no. 3, pp. 2067-2073, 2015/03/11 2015, doi: 10.1021/nl5049753.

[90] Y. C. Lin *et al.*, "Modification of the Electronic Transport in Atomically Thin WSe_2 by Oxidation," *Advanced Materials Interfaces,* vol. 7, no. 18, p. 2000422, 2020.

[91] A. Nipane *et al.*, "Damage-Free Atomic Layer Etch of WSe_2: A Platform for Fabricating Clean Two-Dimensional Devices," *ACS Applied Materials & Interfaces,* vol. 13, no. 1, pp. 1930-1942, 2021/01/13 2021, doi: 10.1021/acsami.0c18390.

[92] Z. Li *et al.*, "Layer Control of WSe_2 via Selective Surface Layer Oxidation," *ACS Nano,* vol. 10, no. 7, pp. 6836-6842, 2016/07/26 2016, doi: 10.1021/acsnano.6b02488.

[93] S. Datta, S. Dutta, B. Grisafe, J. Smith, S. Srinivasa, and H. Ye, "Back-End-of-Line Compatible Transistors for Monolithic 3-D Integration," *IEEE Micro,* vol. 39, no. 6, pp. 8-15, 2019, doi: 10.1109/MM.2019.2942978.

[94] M. K. Yang, G. H. Kim, H. Ju, J.-K. Lee, and H.-C. Ryu, "An analysis of "non-lattice" oxygen concentration effect on electrical endurance characteristic in resistive switching MnO_x thin film," *Applied Physics Letters,* vol. 106, no. 5, p. 053504, 2015/02/02 2015, doi: 10.1063/1.4907704.

[95] M. K. Yang, J.-W. Park, T. K. Ko, and J.-K. Lee, "Bipolar resistive switching behavior in Ti/MnO_2/Pt structure for nonvolatile memory devices," *Applied Physics Letters,* vol. 95, no. 4, p. 042105, 2009/07/27 2009, doi: 10.1063/1.3191674.

[96] M. Sowinska *et al.*, "Hard x-ray photoelectron spectroscopy study of the electroforming in Ti/HfO_2-based resistive switching structures," *Applied Physics Letters,* vol. 100, no. 23, p. 233509, 2012/06/04 2012, doi: 10.1063/1.4728118.

[97] L. Zhao *et al.*, "Crystallization of Amorphous SiO_2 Microtubes Catalyzed by Lithium," *Advanced Functional Materials,* https://doi.org/10.1002/adfm.200601104 vol. 17, no. 12, pp. 1952-1957, 2007/08/13 2007, doi: https://doi.org/10.1002/adfm.200601104.

[98] T. Gougousi, "Low-Temperature Dopant-Assisted Crystallization of HfO_2 Thin Films," *Crystal Growth & Design,* vol. 21, no. 11, pp. 6411-6416, 2021/11/03 2021, doi: 10.1021/acs.cgd.1c00875.

[99] X.-Y. Zhang *et al.*, "Crystallinity Effect on Electrical Properties of PEALD-HfO_2 Thin Films Prepared by Different Substrate Temperatures," *Nanomaterials*, vol. 12, no. 21, doi: 10.3390/nano12213890.

[100] X.-Y. Zhang *et al.*, "Temperature-Dependent HfO_2/Si Interface Structural Evolution and its Mechanism," *Nanoscale Research Letters,* vol. 14, no. 1, p. 83, 2019/03/07 2019, doi: 10.1186/s11671-019-2915-0.

[101] D. Biswas, M. N. Singh, A. K. Sinha, S. Bhattacharyya, and S. Chakraborty, "Effect of excess hafnium on HfO_2 crystallization temperature and leakage current behavior of HfO_2/Si metal-oxide-semiconductor devices," *Journal of Vacuum Science & Technology B,* vol. 34, no. 2, p. 022201, 2016, doi: 10.1116/1.4941247.

[102] W. Chen *et al.*, "Growth and Thermo-driven Crystalline Phase Transition of Metastable Monolayer 1T′-WSe_2 Thin Film," *Scientific Reports,* vol. 9, no. 1, p. 2685, 2019/02/25 2019, doi: 10.1038/s41598-019-39238-7.

[103] M. S. Sokolikova, P. C. Sherrell, P. Palczynski, V. L. Bemmer, and C. Mattevi, "Direct solution-phase synthesis of 1T' WSe_2 nanosheets," *Nature Communications,* vol. 10, no. 1, p. 712, 2019/02/12 2019, doi: 10.1038/s41467-019-08594-3.

5 Dielectric-on-TMDC by Atomic Layer Deposition

In this chapter, we present studies involving the direct deposition of dielectric/ferroelectric oxides on transition metal dichalcogenides (TMDCs) by atomic layer deposition (ALD). The dielectric-on-TMDC stack is of particular relevance for top-gated metal-oxide-semiconductor field-effect transistor (MOSFET) device design, in which the gate oxide is on top of the TMDC channel. Additionally, even in cases where the device structure is not a top-gated MOSFET, TMDC channels are still sometimes encapsulated with a dielectric layer for protection from atmospheric degradation, especially during device operation [1-4]. Thus, achieving high-quality dielectric-on-TMDC interfaces is important for TMDC-based devices, regardless of the FET gating scheme. However, the direct deposition of oxides on TMDCs and subsequent processing for the specific device application presents some challenges in terms of achieving uniform and ultrathin dielectric films and ensuring stability of the dielectric/TMDC interface during processing and device operation.

We aim to address some of these challenges in this chapter, which is divided into two sections. The first part of Chapter 5 will discuss the interface between ferroelectric hafnium zirconium oxide (HZO) and TMDCs – MoS_2 and WSe_2. We report on the thermal stability of these HZO/TMDC interfaces at temperatures relevant for crystallization of HZO, which is a critical fabrication step to form the ferroelectric phase of HZO and make it applicable in ferroelectric FETs. The second part of Chapter 5 focuses on challenges associated with direct ALD on TMDCs, specifically WSe_2. In this section, we explore the technique of ultraviolet-ozone (UV-O_3) functionalization of WSe_2 in order to improve the nucleation of HfO_2 on the WSe_2 surface and result in smooth and uniform thin HfO_2 films deposited by ALD.

5.1 Thermal Stability of Hafnium Zirconium Oxide on Transition Metal Dichalcogenides

The following section is adapted from M.G. Sales, S.T. Jaszewski, S.S. Fields, P.M. Litwin, J.F. Ihlefeld, S.J. McDonnell; Thermal stability of hafnium zirconium oxide on transition metal dichalcogenides; Applied Surface Science, Volume 546, 149058; Published 19 January 2021; https://doi.org/10.1016/j.apsusc.2021.149058.

5.1.1 Abstract

Ferroelectric oxides interfaced with transition metal dichalcogenides (TMDCs) offer a promising route toward ferroelectric-based devices due to lack of dangling bonds on the TMDC surface leading to a high-quality and abrupt ferroelectric/TMDC interface. In this work, the thermal stability of this interface is explored by first depositing hafnium zirconium oxide (HZO) directly on geological MoS_2 and as-grown WSe_2, followed by sequential annealing in ultra-high vacuum (UHV) over a range of temperatures (400-800 °C), and examining the interface through X-ray photoelectron spectroscopy (XPS). We show that the nucleation and stability of HZO grown through atomic layer deposition (ALD) varied depending on functionalization of the TMDC, and the deposition conditions can cause tungsten oxidation in WSe_2. It was observed that HZO deposited on non-functionalized MoS_2 was unstable and volatile upon annealing, while HZO on functionalized MoS_2 was stable in the 400-800 °C range. The HZO/WSe_2 interface was stable until 700 °C, after which Se began to evolve from the WSe_2. In addition, there is evidence of oxygen vacancies in the HZO film being passivated at high temperatures. Lastly, X-ray diffraction (XRD) was used to confirm crystallization of the HZO within the temperature range studied.

5.1.2 Introduction

Ferroelectrics have been utilized in non-volatile memory devices owing to their bi-stable and reversible polarization states and low power consumption [5]. The most common ferroelectrics in such devices, such as lead zirconate titanate, however, suffer from size scaling effects [6] that

limit the accessible technology node to 130 nm [7]. The relatively recent discovery of ferroelectricity in sub-20 nm thick, crystalline silicon-doped HfO_2 [8] offers a potential pathway toward continued device scaling [9] and development of new devices utilizing the switchable polarization. Such devices include ferroelectric field effect transistors (FeFETs) [10, 11] and negative differential capacitance FETs [12, 13]. The ferroelectric response in HfO_2-based materials has been attributed to a metastable non-centrosymmetric orthorhombic phase, with space group $Pca2_1$ [14]. This orthorhombic phase may be stabilized over the equilibrium centrosymmetric monoclinic phase through reduced film thickness and/or constrained grain size [15, 16], biaxial stress [17-19], oxygen vacancies [20, 21], and dopants, such as Si, Al, Y, Gd, and Zr [8, 22-25]. Zr substitution for Hf to form hafnia zirconia alloys is particularly promising for device applications, as these alloys exhibit low crystallization temperatures [26], possess ferroelectric properties that are resistant to degradation with annealing [27], and demonstrate a large composition space that enable ferroelectric phase formation [23].

Some of the potential ferroelectric-based memory devices, such as FeFETs, require contact between the ferroelectric oxide, acting as a gate dielectric, and a semiconducting channel [28-32]. A poor interface between ferroelectric materials and silicon presents a challenge in integration with traditional semiconductor technology. Some issues include interdiffusion of constituents across the interface, and the presence of an interfacial dielectric layer (SiO_2) between the ferroelectric and silicon [33, 34]. Thus, a potential alternative would be to use transition metal dichalcogenides (TMDCs) as the semiconducting material in FeFETs. Due to their 2D van der Waals nature, TMDCs have strong in-plane covalent bonds with no out-of-plane dangling bonds, thus providing high in-plane chemical stability, leading to an improved interface quality with the ferroelectric without intermixing or interfacial chemical species [35]. In this work, we consider the thermal stability of this interface, which is important for identifying potential processing limitations.

Hafnium zirconium oxide (HZO) films deposited by atomic layer deposition (ALD) are typically amorphous and require annealing at temperatures ranging from 400-800 °C for crystallization [18, 19, 36]. Thus, the ferroelectric/TMDC heterostructure must be able to withstand these temperature excursions. Exposing ferroelectric/TMDC heterostructures to high temperatures in the fabrication of ferroelectric-based devices has been shown in previous work

[30], with the focus being mainly on the device fabrication and not on the interface itself. The present study is limited to the direct interface between the ferroelectric and the TMDC.

In this study, we explore HZO as our ferroelectric, and examine its interface with semiconducting TMDCs, MoS_2 and WSe_2. While it is conventional to prepare HZO on an electrode (e.g. TiN) [23], doing so would require transfer of the TMDC onto the HZO after the HZO is prepared. It is known that transfer processes introduce contaminants by leaving behind residues that could affect the interface and device properties [37-41]. Thus, in this work, we directly grow HZO on TMDCs through ALD, and show differences in the efficacy of the ALD process depending on the TMDC and its functionalization. The focus of this work is to study how the interface changes at anneal temperatures that are conventional to crystallizing HZO films (i.e., 400-800 °C).

5.1.3 Methodology

Two types of geological MoS_2 (SPI Supplies [42]) substrates were used – untreated and ultraviolet-ozone (UV-O_3) treated. The untreated sample was mechanically exfoliated with Scotch tape in order to remove the topmost layers of MoS_2 and expose a clean surface. The UV-O_3 treated sample was a similarly exfoliated sample that underwent UV-O_3 treatment in air for 30 s using a UV grid lamp connected to a 3 kV, 0.03 A power supply (BHK, Inc.). Prior work has shown that UV-O_3 enhances ALD nucleation on MoS_2 and leads to more uniform growth of Al_2O_3 and HfO_2 [43, 44]. Previous reports have used UV-O_3 treated MoS_2 in transistors [45, 46], and have shown that this UV-O_3 functionalization of MoS_2 allowed deposition of a continuous HfO_2 dielectric layer with low leakage [47].

WSe_2 was grown on a 1 x 1 cm square of highly ordered pyrolytic graphite (HOPG) from SPI Supplies [42] using molecular beam epitaxy (MBE) in an ultra-high vacuum (UHV) system described elsewhere [48]. The HOPG crystal was outgassed for approximately 12 h in the MBE chamber at 250 °C. The WSe_2 growth was performed at 550 °C with a Se:W flux ratio of 7500:1. An initial ripening step was carried out wherein the sample was periodically exposed to the W flux for 30 s in 90 s intervals while the Se flux was kept constant. This interrupted growth technique is adapted from literature [49, 50]. Additionally, the use of a ripening step has also been demonstrated in other reports [51, 52]. The ripening step was conducted for a total of 38 min, after which the

sample was cooled in a Se flux until it reached 375 °C. At this temperature, the Se flux was terminated, and the sample was continuously cooled to below 100 °C. The sample was then reheated to growth temperature. An uninterrupted growth followed, in which the W and Se fluxes were kept constant for 2 h 40 min. The growth rate was monitored through in-situ reflective high energy electron diffraction (RHEED), and the growth was ended when approximately 4 layers of WSe_2 were formed on the substrate. At the end of the growth, the sample was cooled to 275 °C in a Se flux to minimize chalcogen vacancies. At 275 °C the Se flux was turned off to avoid Se adsorption on the surface, and the sample was further cooled to room temperature. This employed MBE growth procedure results in repeatable WSe_2 chemistry as has been characterized in a number of publications [53-55].

The untreated MoS_2, UV-O_3 treated MoS_2, and as-grown WSe_2 were all loaded side-by-side into an Oxford FlexAL II ALD instrument for deposition of HZO. ALD was conducted at 150 °C utilizing Tetrakis(ethylmethylamido)hafnium (TEMA-Hf) and tetrakis(ethylmethylamido)zirconium (TEMA-Zr) precursors in a 1:1 dose ratio with H_2O as an oxidant and argon as a carrier gas. The precursor temperatures were 70 °C for TEMA-Hf and 85 °C for TEMA-Zr. For HZO deposition, unless otherwise stated, the deposition sequence was such that the TEMA-Hf precursor was introduced first, followed by oxidant, and then the TEMA-Zr precursor, followed by oxidant. The pulse and purge times were 1 s and 3 s, respectively, for TEMA-Hf, and 1.5 s and 6 s, respectively, for TEMA-Zr. Following each precursor dose, the H_2O oxidant was pulsed for 20 ms and evacuated for 16 s. The growth rates per cycle for HfO_2 and ZrO_2, calibrated on bare silicon substrates, were approximately 1.2 Å/cycle and 1.4 Å/cycle, respectively. In addition, we note that these ALD conditions are optimized for uniformity across a 100 mm wafer, and the three samples loaded were all placed within this 100 mm diameter. A film thickness of approximately 1 nm (4 total Hf and Zr cycles) was targeted for samples for interface chemistry studies using X-ray photoelectron spectroscopy (XPS). The 1 nm film thickness allows measurement of the XPS core levels of both the underlying TMDC substrate as well as the HZO film on the surface.

Sequential heating and XPS were performed on the HZO/TMDC samples in the same UHV chamber described previously [48]. XPS spectra were taken using a monochromated Al Kα X-ray source at 300 W with a Scienta Omicron R3000 analyzer at a pass energy of 50 eV. XPS binding energy calibration was performed by aligning the Au 4*f* peak of a clean reference gold sample to

83.96 eV [56]. XPS measurements were acquired after HZO deposition, after annealing in UHV for 20 min at 400 °C, and after annealing in UHV for 40 min each at 500 °C, 600 °C, 700 °C, and 800 °C. The anneals at each temperature were performed on all three samples simultaneously, meaning that the three samples were maintained at the same temperature for the same amount of time for each annealing step. Spectral analysis of XPS results was carried out using kolXPD software [57]. All peaks were fit with Voigt lineshapes.

In addition to the samples for XPS studies, two separate samples with thicker layers of HZO were prepared for X-ray diffraction (XRD) measurements to assess crystallization. Approximately 10 layers of WSe_2 was MBE-grown on an AlN/Si (111) substrate using the same method described for the WSe_2 growth on HOPG. After MBE growth, ~20 nm thick HZO (83 total Hf and Zr cycles) was deposited on the WSe_2 by ALD under the same conditions as described above. Note that for these samples for XRD, AlN/Si (111) was used as the substrate instead of HOPG because the (002) peak of HOPG at 26.6° in 2θ would interfere with the signal of HZO, whose peaks of interest are within the 2θ range of 26-33°. A Rigaku Smartlab X-ray Diffractometer using Cu Kα radiation in a parallel beam configuration with a fixed incident angle of 0.7° (greater than the critical angle for total external reflection) was used for grazing-incidence X-ray diffraction (GIXRD) measurements to assess crystallinity and phase assemblage. GIXRD measurements were performed in the 2θ range of 26-33° as this region possesses reflections of the possible polymorphs: the monoclinic $P2_1/c1$ phase, tetragonal $P4_2/nmc$ phase, and orthorhombic $Pca2_1$ phase.

5.1.4 Results and Discussion

5.1.4.1 HZO Atomic Layer Deposition Efficacy

Figure 5.1.1 shows the XPS spectra of the TMDC substrates immediately following HZO deposition. The detected features correspond to the expected peaks based on the chemical bonding environment of MoS_2 and WSe_2 (Mo-S and W-Se bonds, respectively). We note that for the WSe_2 sample, oxidation of W (W-O bonds) from the ALD process was evident, and this is discussed further in section 5.1.4.3. No additional features were observed after ALD on MoS_2. A non-covalent interface between the TMDCs and HZO film is expected, as a smooth interface without

intermixing between TMDCs and oxides such as HfO_2 [44, 58-60], ZrO_2 [61], and Al_2O_3 [43, 60, 61] have been observed through photoemission spectroscopy and electron microscopy techniques in previous reports.

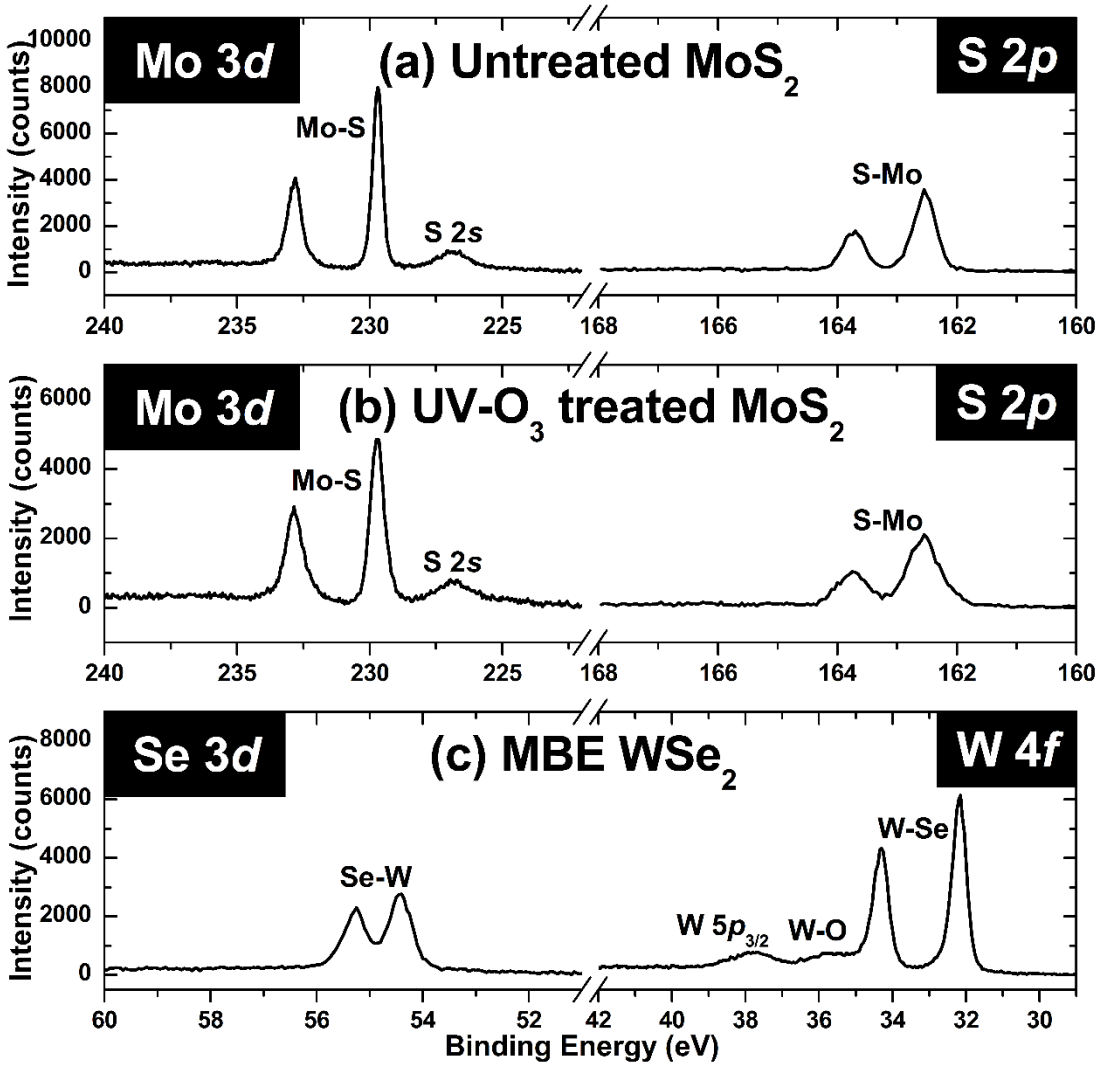

Figure 5.1.1. XPS spectra of the TMDC substrates after HZO deposition: (a) untreated MoS_2, (b) UV-O_3 treated MoS_2, and (c) WSe_2 grown via MBE. The different core levels and chemical states are labeled.

Shown in Figure 5.1.2 is the Hf 4*f* region for all three samples after HZO deposition. The peak intensities are related to the amount of HZO deposited on each sample. It should be noted

that the ALD conditions used were optimized for uniformity across a 100 mm wafer, indicating that any differences in thickness are not attributable to ALD processing nonuniformities. Since HZO deposition was performed with all three samples in parallel, and all were exposed to air for the same amount of time between the ALD process and XPS characterization, the differences in peak intensities can be confidently assumed to indicate differences in the efficacy of the same HZO deposition process on these different TMDC substrates.

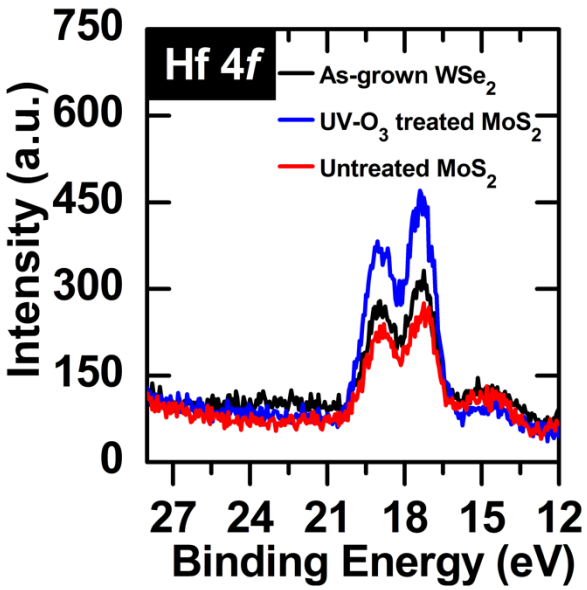

Figure 5.1.2. Hf 4f spectra after ALD of HZO on as-grown WSe_2, UV-O_3 treated MoS_2, and untreated MoS_2.

The untreated MoS_2 sample resulted in the lowest Hf 4*f* peak intensity after HZO deposition. It is likely that the HZO deposited on untreated MoS_2 is composed of islands, rather than a uniform HZO film. A poor ALD oxide film morphology on a non-functionalized MoS_2 surface has been shown previously in other works [43, 58].

The UV-O_3 treated MoS_2 sample resulted in the highest Hf 4*f* peak intensity. Prior research has shown that UV-O_3 treated MoS_2 results in a functionalization of the surface that increases the number of nucleation sites for ALD of oxides on MoS_2, which leads to uniform film deposition [43]. The functionalization of the MoS_2 surface through UV-O_3 exposure, as reported by Azcatl et al. [43], is achieved by forming bonds between sulfur and oxygen atoms adsorbed on the surface, without breaking the Mo-S bonds. The oxygen-terminated surface provides ideal nucleation sites

for ALD, leading to good film morphology and uniformity. However, long exposures of MoS_2 to UV-O_3 have also been found to oxidize the Mo, which compromises the MoS_2 [41, 62]. In this work, the process developed by Azcatl et al. has been found to be transferrable to a bench-top UV lamp, with 30 s of UV-O_3 exposure in air. XPS results showing the differences between as-exfoliated (untreated) MoS_2 and UV-O_3 treated MoS_2 can be found in Figure 5.1.3. XPS shows that a 30 s UV-O_3 treatment provided S-O_{ads} bonds without breaking Mo-S and forming Mo-O.

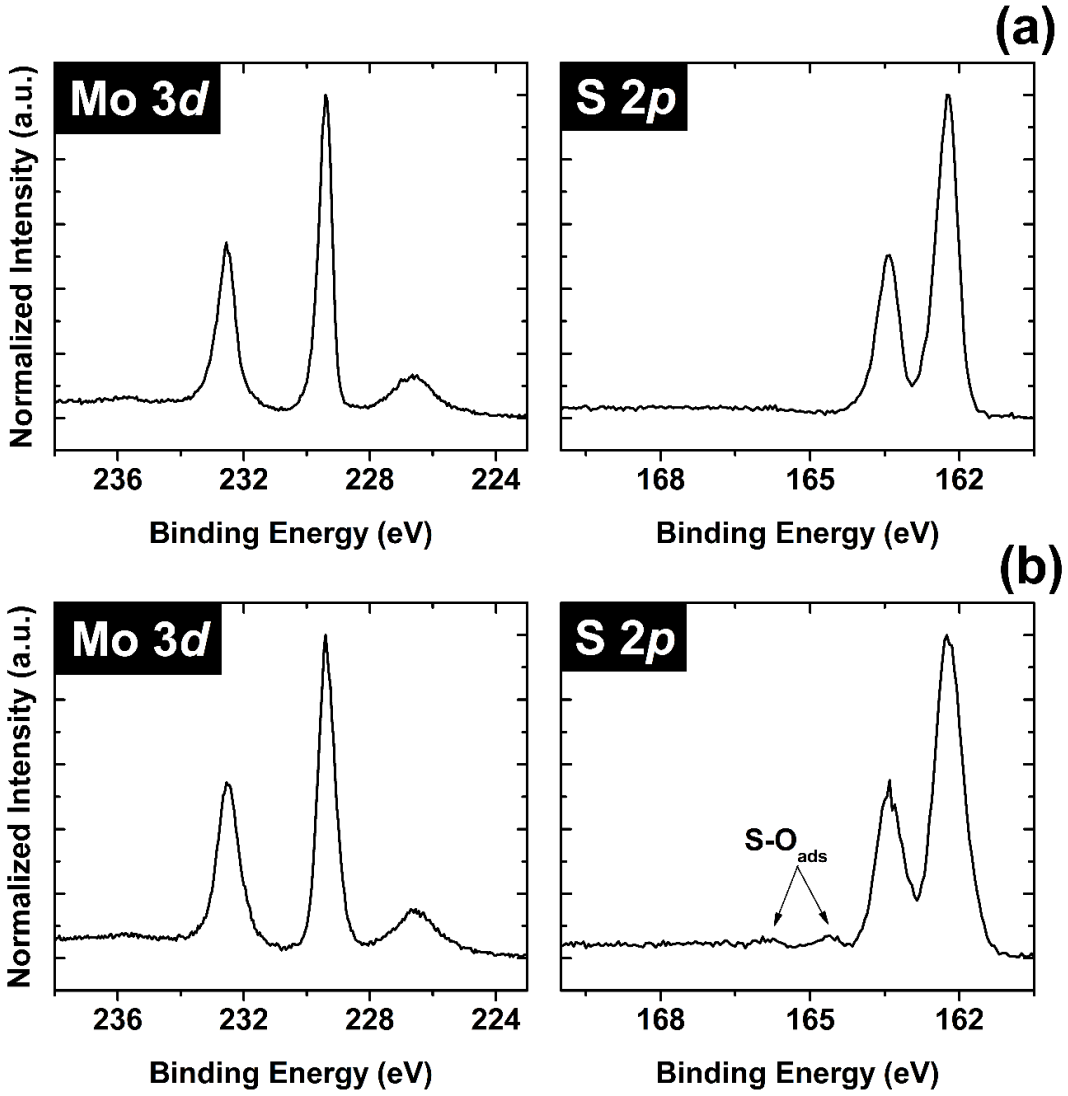

Figure 5.1.3. Mo 3d and S 2p spectra of MoS_2: (a) as-exfoliated/untreated, and (b) after UV-O_3 exposure in air for 30 s. Through UV-O_3 treatment, the MoS_2 is functionalized by adsorbed oxygen atoms on the surface, forming S-O_{ads} bonds that are confirmed with XPS.

As shown in Figure 5.1.2, this functionalization allowed improved nucleation and growth of HZO by ALD, as evidenced by the increased Hf 4*f* peak intensity for the UV-O_3 treated sample. The ALD was found to be most optimal for UV-O_3 treated MoS_2, and least optimal for untreated MoS_2. The intensities of the Hf 4*f* peaks for the as-grown WSe_2 and untreated MoS_2 samples are similar, but it will be shown later that the HZO film on untreated MoS_2 is highly unstable at elevated temperatures, whereas the HZO film on as-grown WSe_2 is comparatively stable. Furthermore, it was shown previously that UV-O_3 treatments of WSe_2 can lead to etching of the WSe_2 [44], so this was not employed here.

5.1.4.2 HZO Thermal Stability on MoS_2

To demonstrate the difference in the thermal stability of HZO on non-functionalized (untreated) vs. functionalized (UV-O_3 treated) MoS_2, Figure 5.1.4 shows the evolution of the Hf 4*f* spectra on both types of MoS_2 at varying anneal temperatures, conducted under UHV conditions.

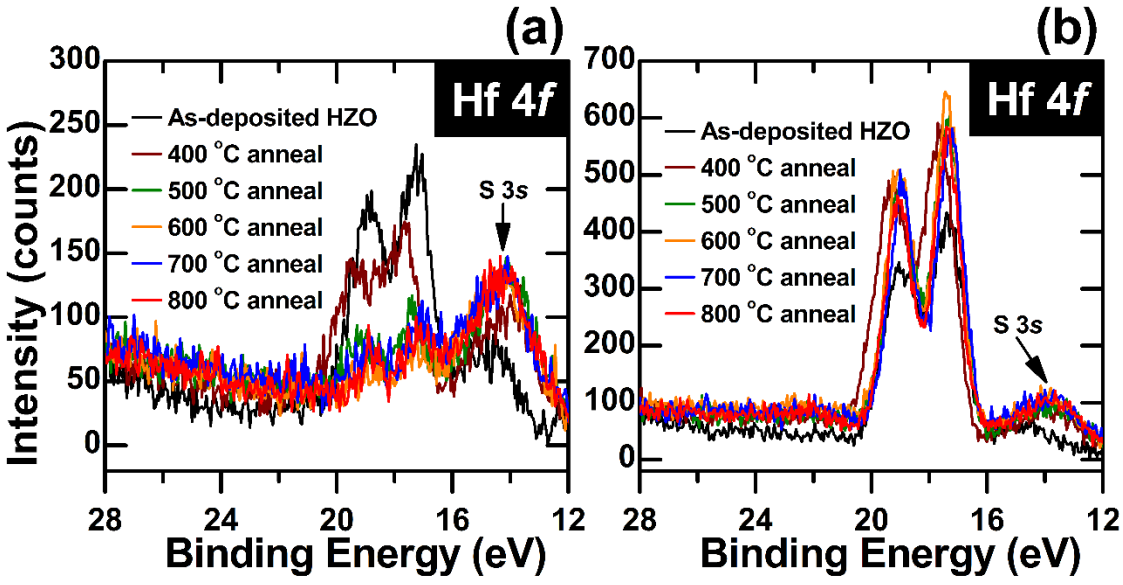

Figure 5.1.4. Hf 4f spectra of HZO deposited on (a) untreated MoS_2 and (b) UV-O_3 treated MoS_2 after ALD and after each annealing step.

For the non-functionalized MoS_2 sample as shown in Figure 5.1.4(a), the Hf 4*f* features at approximately 17 eV and 19 eV decrease in intensity after the 400 °C anneal. At the higher temperature anneals, the Hf 4*f* peak intensities decrease further. This suggests that the HZO film is removed with heating the untreated MoS_2 sample. We acknowledge that a decrease in XPS peak intensity could be interpreted as diffusion of the HZO components into the bulk, but this is unlikely when decreasing peak intensities are not observed for the parallel sample (UV-O_3 treated MoS_2). The decreasing trend can also be observed with the Zr 3*d* spectra of the untreated MoS_2 sample (shown in Figure 5.1.5(a)), and there are no discernable Zr 3*d* peaks for anneal temperatures higher than 400 °C, further elucidating the removal of the HZO film on untreated MoS_2 at high temperatures.

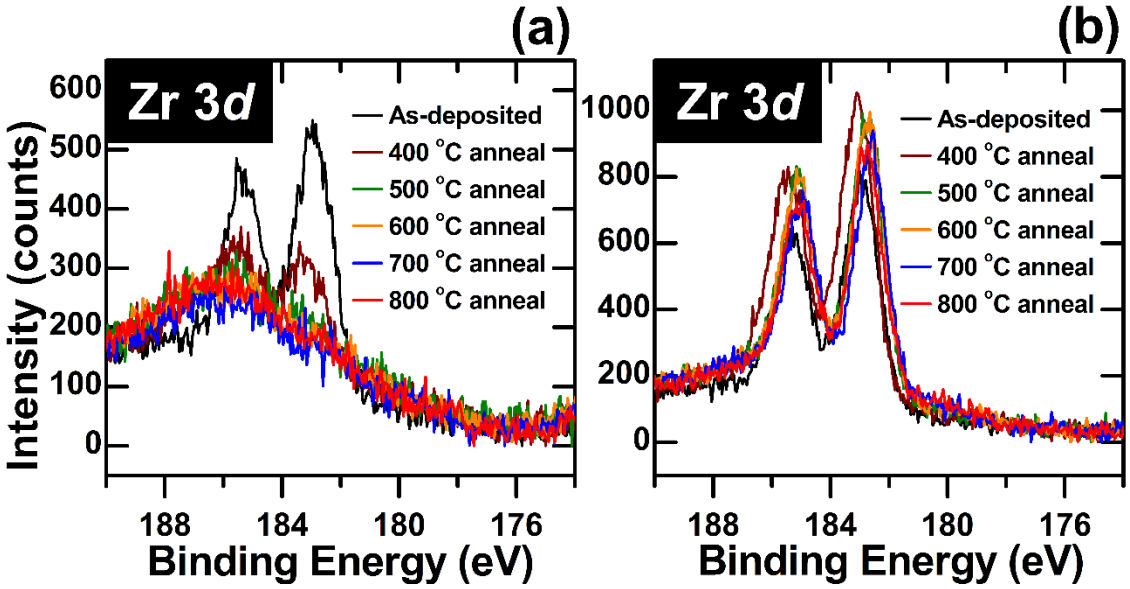

Figure 5.1.5. Zr 3d spectra of HZO deposited on (a) untreated MoS_2 and (b) UV-O_3 treated MoS_2, after ALD and after each annealing step. For untreated MoS_2, the Zr 3d peaks significantly decrease in intensity after annealing, and are no longer discernable after annealing to 500 °C and higher. For the spectra of both samples, note that the peaks for the 400 °C anneal curves (maroon) are shifted to higher binding energy (~0.3 eV higher), exhibiting a similar trend as the Hf 4f spectra. This shift to higher binding energy after the first annealing step is attributed to a loss os oxygen in the HZO with initial heating.

Because there are no detectable Zr 3*d* features remaining at anneal temperatures of 500 °C and higher, while small Hf 4*f* peaks are still detected, this suggests that the Zr species are desorbed before the Hf species. To verify that this is not an effect of the order in which the ALD precursors were deposited, a separate HZO on untreated MoS_2 sample was prepared wherein the deposition order of the precursors was reversed, i.e., TEMA-Zr was the first precursor introduced to the growth chamber followed by oxidant and then TEMA-Hf. The results for this additional sample are shown in Figure 5.1.6 and reveal the same behavior of near complete reduction of Zr 3*d* signals and significant reduction of Hf 4*f* peaks.

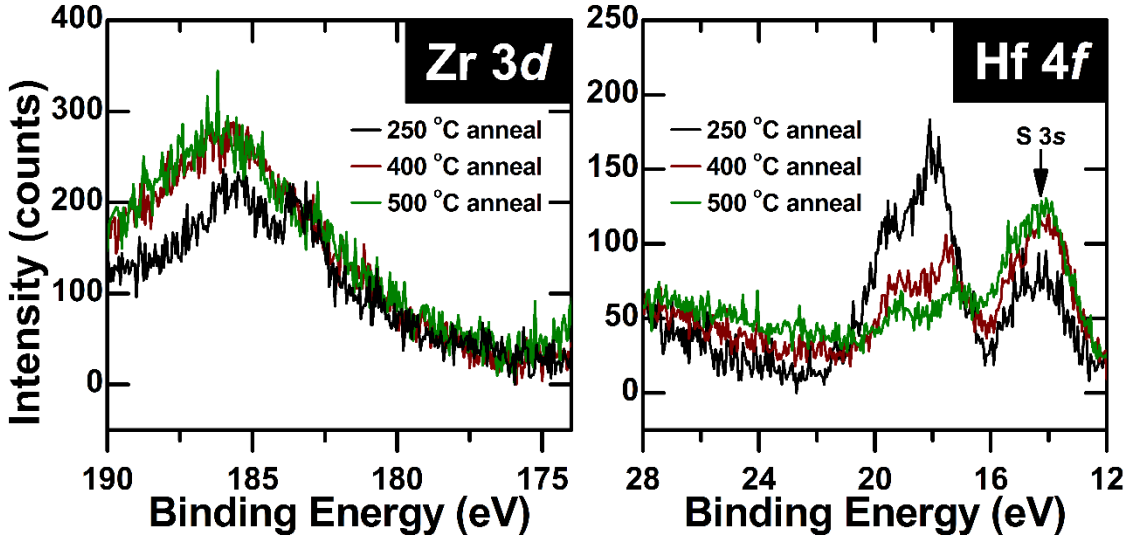

Figure 5.1.6. Zr 3d and Hf 4f spectra of an additional HZO on untreated MoS_2 sample. For this sample, the Zr precursor was deposited before the Hf precursor, which is the opposite deposition order for the other HZO samples discussed in this chapter. It can be seen that even with the order of the precursors reversed, the Hf species are still retained on the sample surface better than the Zr species. The Zr 3d doublet (seen at ~183 eV and ~186 eV in the black curve) is not present after the 400 ℃ anneal, indicating loss of the Zr species, but detectable peaks are still evident in the Hf 4f spectra (~17 eV and ~19 eV), which are indicative of Hf species remaining on the sample.

Reasons for preferred sticking of HfO_2 over ZrO_2 on MoS_2 are not clear at this time and will require further investigation. Atomic force microscopy (AFM) characterization, as shown in Figure 5.1.7, reveals no major difference in the film morphology of HZO on untreated MoS_2 post-annealing, regardless of the order of HZO precursor deposition. An analysis describing the

correlation of the surface coverage in these AFM micrographs and the measured HfO_2 XPS peak intensities is presented in Appendix A.

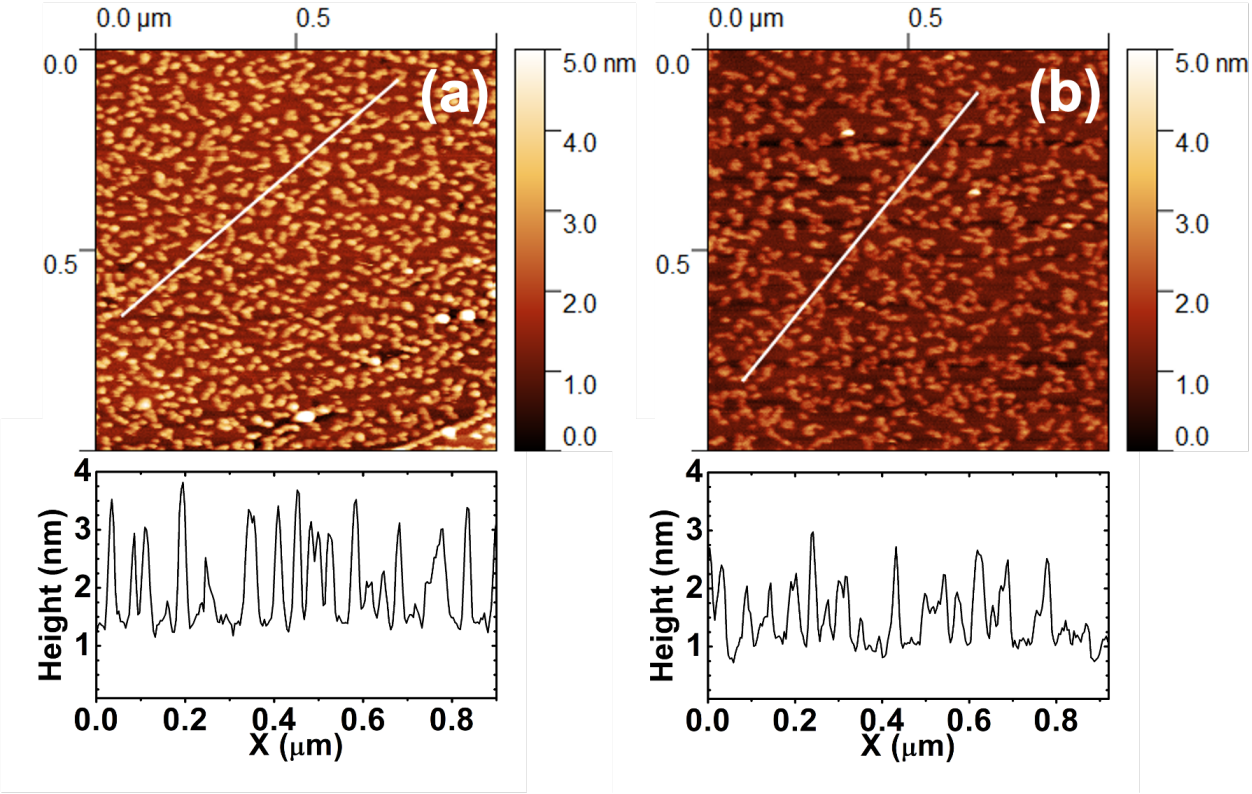

Figure 5.1.7. AFM micrographs and line profiles of HZO on untreated MoS_2 samples after annealing. For (a), TEMA-Hf precursor was deposited first, and for (b), TEMA-Zr precursor was first during ALD of HZO. These micrographs indicate no major differences in the film morphology regardless of the order of precursor deposition during ALD. It is known from XPS that the remaining material after annealing of HZO on untreated MoS_2 is HfO_2. These HfO_2 clusters seen in AFM are estimated to be ~1.4 nm tall based on the average peak height from the line profiles.

The removal of HZO from the untreated MoS_2 surface at temperatures > 400 °C is consistent with the model for ALD on MoS_2 proposed in earlier work [58]. In that work, it was suggested that depositions on MoS_2 did not occur through reactions with the substrate, but instead relied on reactions between the precursors in physisorbed states on the substrate surface. The reaction products were assumed to be less volatile than the unreacted precursors at the deposition temperature of 200 °C, and it was still assumed to be lacking covalent bonds to the surface as evidenced by the lack of observable changes in the XPS core level spectra of the Mo or S features. This assumption of weakly bonded species that were less volatile than individual precursors would

seem to be consistent with our present observations of thermal desorption at higher temperature; however, it cannot exclude that the presence of Zr in the present study may also play a role in the instability.

HZO on a functionalized MoS_2 substrate, as shown in Figure 5.1.4(b), exhibits a different trend. The initial 400 °C anneal shows an increase in Hf 4*f* intensity compared to the as-deposited curve. This is consistent with adventitious carbon or hydroxide species being desorbed with heating, thus reducing attenuation effects and increasing the signal coming from the HZO film. Note that the desorption of adventitious contaminants also occurs for the non-functionalized MoS_2 sample, but the removal of the HZO film dominates over the effects of removing contaminants, with the overall result being the decrease in the Hf 4*f* intensity. It is observed that with increasing the anneal temperature, the Hf 4*f* intensity in Figure 5.1.4(b) stays consistent, indicating that most, or all adsorbates on top of the HZO film were likely removed from the initial 400 °C anneal. Further, by comparing the relative intensities of Hf 4*f* in Figure 5.1.4(b) with those of Zr 3*d* in Figure 5.1.5(b), we observe no clear trend. The ratio of the Hf 4*f* to Zr 3*d* intensities are plotted in Figure 5.1.8 to illustrate this.

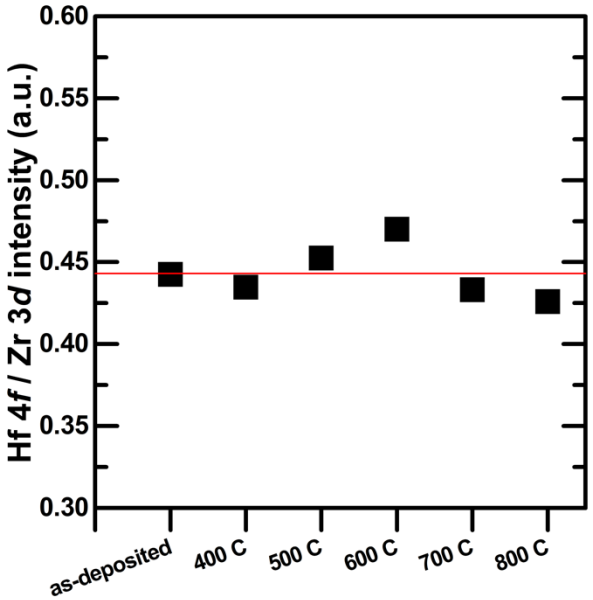

Figure 5.1.8. Plot of intensity ratio of Hf 4f (from Figure 5.1.4(b)) to Zr 3d (from Figure 5.1.5(b)) at the different annealing steps for HZO deposited on UV-O_3 treated MoS_2. The red line denotes the average of the six data points.

Fluctuations ≤ 6% of the average value are observed and are attributed to fitting errors which are enhanced by the S 2*p* loss feature that overlaps with the Zr 3*d* region. This indicates that the amount of HZO is not reduced with high temperature anneals, suggesting that the HZO on functionalized MoS_2 is thermally stable for the full temperature range used in this study. AFM micrographs of as-deposited and annealed HZO on functionalized MoS_2, shown in Figure 5.1.9, highlight this as well.

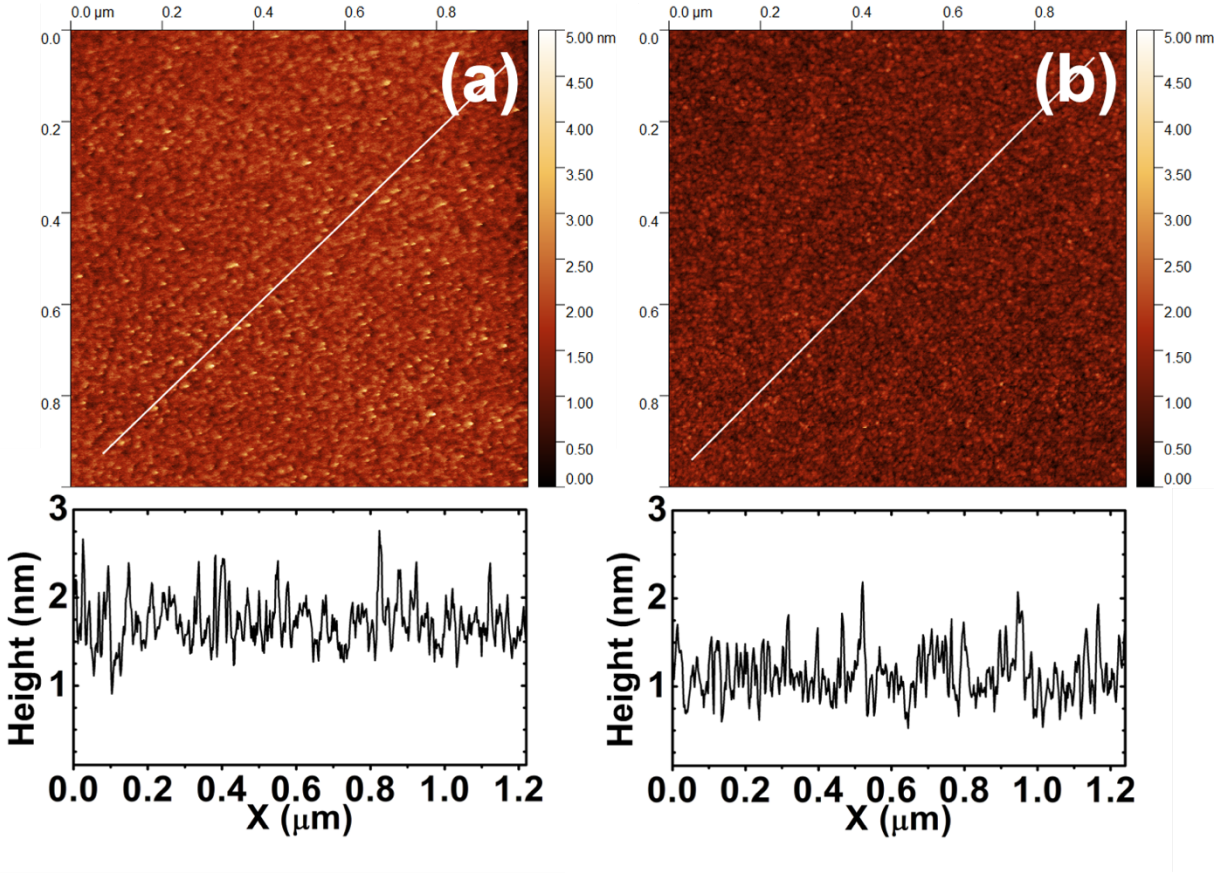

Figure 5.1.9. AFM micrographs of HZO on UV-O_3 treated MoS_2: (a) as-deposited, and (b) after 400-800 °C anneals in UHV.

Figure 5.1.9 shows AFM micrographs and line profiles of 5 nm HZO films, which are of comparable thickness to the work of Azcatl et al. [43]. We show uniform HZO deposition on functionalized MoS_2 and highlight the thermal stability of the deposited material, as shown by the unchanging general film morphology pre- and post-annealing. Furthermore, we demonstrate repeatability of the effects of MoS_2 functionalization from previous work [43], in which conformal growth and full coverage, based on the absence of 5 nm pinholes, are achieved.

This emphasizes the importance of functionalization for oxide growth on MoS_2. As well as exhibiting low coverage, island growth, and a non-ideal interface, as shown previously [43, 58], this present study also demonstrates that ALD of an oxide on a non-functionalized MoS_2 surface will produce a thermally unstable film. Other than changes in intensity, it is also notable that the 400 °C curve in Figure 5.1.4(a) and (b) are shifted to higher binding energy. These peak shifts will be discussed in section 5.1.4.4.

5.1.4.3 HZO Thermal Stability on WSe_2

To examine the thermal stability of the HZO film deposited on MBE-grown WSe_2, the evolution of the Hf 4*f* curves after ALD of HZO and after sequential annealing is shown in Figure 5.1.10. The intensities of the Hf features do not change significantly within the temperature range studied. When compared to MoS_2, these results demonstrate that HZO deposited on non-functionalized WSe_2 has superior thermal stability over a non-functionalized MoS_2 substrate.

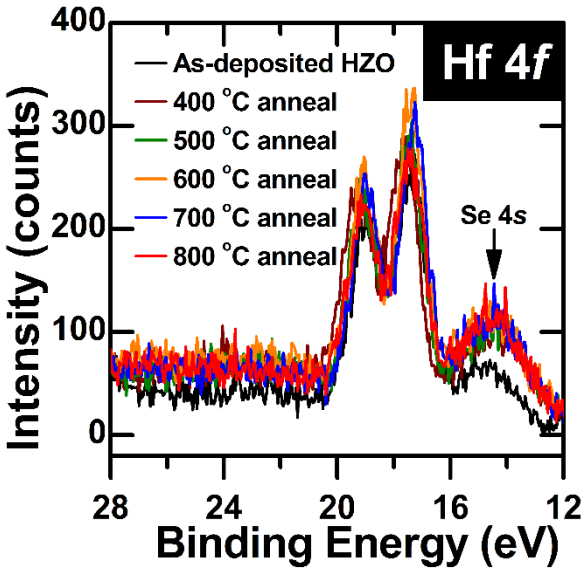

Figure 5.1.10. Hf 4f spectra of HZO deposited on as-grown WSe_2 after ALD and after each annealing step.

We now turn our attention to changes in the WSe_2 itself at the different annealing temperatures. The normalized W 4*f* spectra after ALD and after each anneal are plotted in Figure

5.1.11(a). It is evident that following ALD of HZO, the W is partially oxidized, based on the presence of high binding energy peaks corresponding to WO_3 (~35.6 and 37.8 eV). The WO_3 peaks are observed to decrease in intensity with increasing anneal temperature, as discussed in section 5.1.4.4. The presence of this oxide indicates that excess oxygen in the ALD process, i.e., water vapor and impurities in the carrier gas, have oxidized the tungsten. A higher density of defects such as step edges in the as-grown WSe_2 sample makes it more susceptible to reaction with oxygen sources in the ALD chamber, thus forming WO_3. It is important to note that atmospheric exposure was minimized in transferring this WSe_2 sample between the ALD and analysis chambers, so oxidation of the underlying WSe_2 film due to a few minutes of atmospheric exposure pre- and post-HZO deposition is unlikely. The W 4*f* spectra of a similarly grown WSe_2 sample before and after 20 minutes of atmospheric exposure is shown in Appendix B. It is noted that this brief exposure to atmosphere did not lead to the emergence of any significant tungsten oxide peaks, which is consistent with a previous report showing similar WSe_2 exposure data [63].

Another noteworthy observation from the normalized W 4*f* spectra is the emergence of a sub-stoichiometric (WSe_{2-x}) state after the 800 °C anneal. This state is seen as an asymmetry at the low binding energy side for the 800 °C curve, which has also been observed for MBE growths of WSe_2 using low Se:W flux ratios [55]. The spectral deconvolution of the post-800 °C anneal W 4*f* spectrum is shown in Figure 5.1.11(b). In this figure, the low intensity portion of the spectrum is enlarged and emphasized, in order to clearly depict the WSe_{2-x} peaks. The main WSe_2 peaks are present at 32.2 eV and 34.4 eV (green peak fits), while the sub-stoichiometric peaks are at 31.5 eV and 33.7 eV (magenta peak fits). The appearance of the sub-stoichiometric state, WSe_{2-x}, shows that annealing to temperatures as high as 800 °C volatilizes some of the Se in the WSe_2 film, which makes it selenium-deficient and thus may affect its properties. This result shows that our as-grown WSe_2 is not thermally stable beyond 700 °C. Similar decomposition of MBE-grown WSe_2 above 700 °C has been shown in other work [64]. For the annealing time used in this experiment (20-40 min), we report a thermal budget of 700 °C for the HZO/WSe_2 interface. At 700 °C and below, both the HZO and the WSe_2 appear to be thermally stable. After annealing this sample to 800 °C, decomposition was observed in the TMDC. Some Se was driven off of the WSe_2, leaving behind a sub-stoichiometric component in the film as shown in Figure 5.1.11.

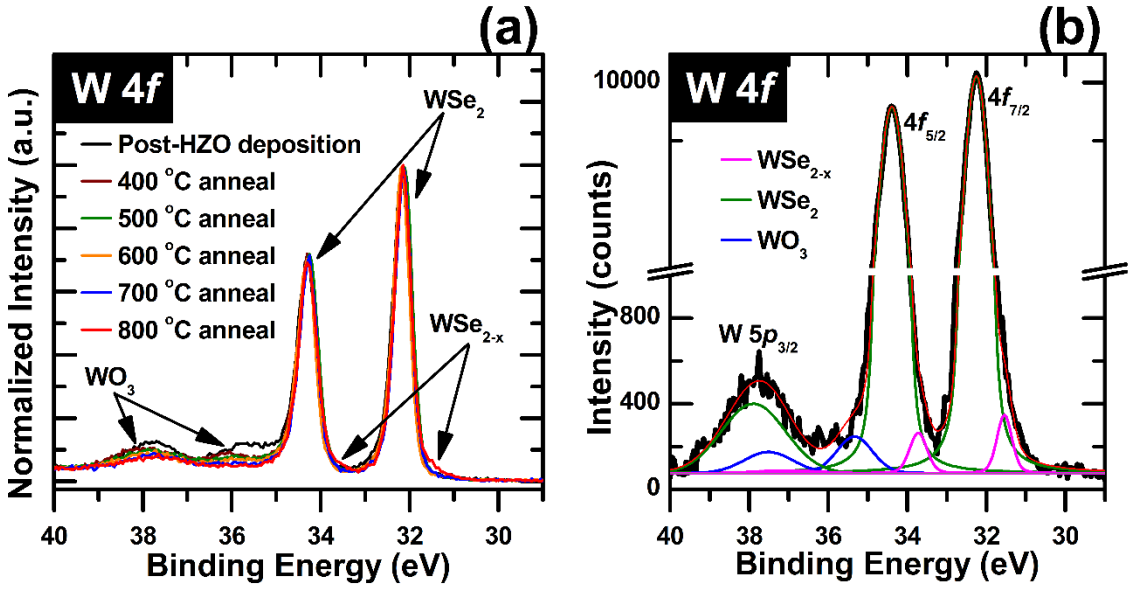

Figure 5.1.11. (a) Normalized W 4f spectra after ALD of HZO and after each annealing step. (b) Spectral deconvolution of 800 °C W 4f spectrum (red curve in (a)). Three chemical states are present: WO_3, WSe_2, and WSe_{2-x}. Note that the WSe_2 and WSe_{2-x} peaks have similar peak widths. The WO_3 features are broader because the oxide state is expected to be more disordered.

We also utilized Raman spectroscopy after each process performed on the TMDCs to further characterize any changes caused by our HZO deposition and annealing conditions. Raman spectra for WSe_2 and MoS_2 as-grown and as-received, respectively, after ALD of HZO, and after annealing treatments in UHV, are shown in Figure 5.1.12. In the Raman spectra, no major changes are observed in the peak positions and relative intensities between the as-grown/as-received material, post-ALD, and post-annealing (500 °C) steps.

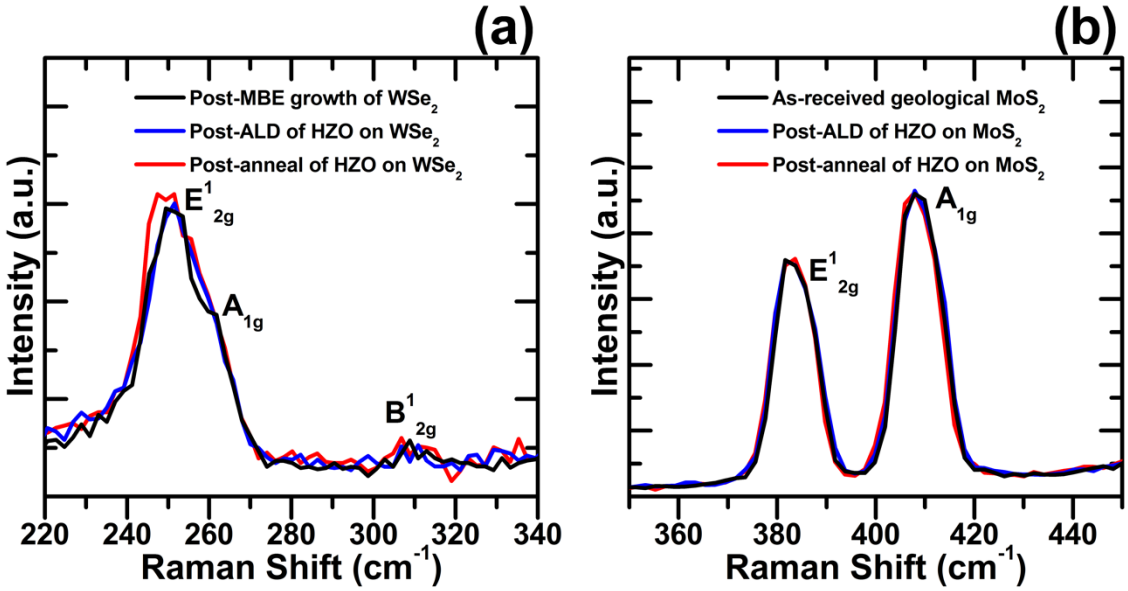

Figure 5.1.12. Raman spectra of (a) WSe_2 and (b) MoS_2 substrates used for ALD of HZO.

5.1.4.4 Oxygen Vacancies in HZO

The Hf 4*f* spectra presented above (Figure 5.1.4 and Figure 5.1.10) show that the 400 °C spectra for all three samples (untreated MoS_2, UV-O_3 treated MoS_2, and as-grown WSe_2) are shifted to higher binding energy (+0.3 eV) with respect to their positions from the as-deposited spectra. It should also be noted that at 400 °C, the Zr 3*d* peaks (Figure 5.1.5) shift to higher binding energy together with the Hf peaks. Such identical shifts in both Hf and Zr are indicative of an electronic change such as charging or Fermi level shifts. These shifts can be attributed to a loss of oxygen in the HZO with initial heating. Shifts to higher binding energy after one annealing step is consistent with previous observations on TiO_2, HfO_2, and ZrO_2 deposited on Si (100) [65, 66].

It has been reported previously that heating of oxide films causes a loss of some oxygen [65-67], which corresponds to introduction of oxygen vacancies. Oxygen vacancies can serve as n-type dopants in HfO_2 [68, 69] and ZrO_2 [69]. However, after anneals at 500 °C and higher, the Hf 4*f* peaks shift back to lower binding energy, which signifies that the Fermi level moves closer to the valence band, and is thus characteristic of a decrease in n-type charge carriers. Therefore,

this shift to lower binding energy at the high temperatures is attributed to passivation of oxygen vacancies in the HZO film. This requires a source of atoms responsible for oxygen vacancy passivation, and we propose two possibilities: one using oxygen atoms and the other using chalcogen atoms. We discuss both possibilities in this section.

We first discuss the proposed vacancy passivation mechanism involving oxygen atoms. Figure 5.1.13 shows the O 1*s* spectra of HZO on functionalized MoS_2 at different annealing stages. For comparison, the O 1*s* spectra of the other two samples (untreated MoS_2 and WSe_2) are shown in Figure 5.1.14. The peaks seen in the O 1*s* spectra can be classified into three main features, as labeled in the figure. The high intensity oxygen peak at the low binding energy side corresponds to metal oxide; the intermediate peak between 532-533 eV is assigned to non-lattice oxygen (O^{2-}) present in the material [70-72]; and the high binding energy feature is from adventitious oxygen species adsorbed on the surface, likely from residual hydroxide from the ALD process as well as atmospheric exposure after HZO deposition.

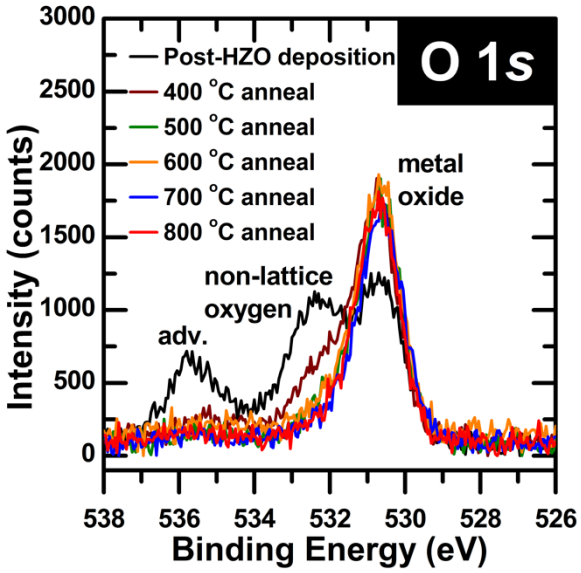

Figure 5.1.13. O 1s spectra of HZO on the functionalized MoS_2 sample.

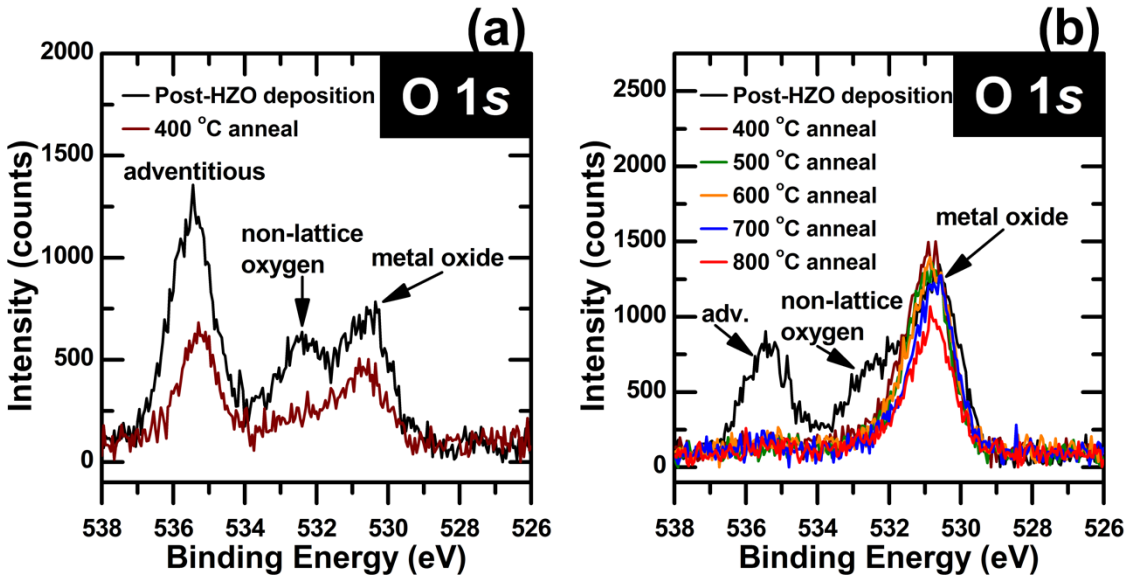

Figure 5.1.14. O 1s spectra of HZO on (a) untreated MoS_2 and (b) WSe_2 at different annealing stages. We note that for the untreated MoS_2 sample, there are no discernable features in the O 1s spectra at anneals higher than 400 ℃ because of removal of adventitious contaminants and most of the HZO overlayer film (non-lattice oxygen and metal oxide components).

We draw attention to the non-lattice oxygen feature. Here we note that the as-deposited HZO films are amorphous and therefore do not have a lattice arrangement of atoms. Crystallization of these films is discussed in section 5.1.4.5. In the case that the HZO does not have a lattice, it should be noted that the non-lattice oxygen component corresponds to oxygen atoms that are coordinated differently. For HfO_2, the oxygen atoms can have a coordination number of 3 or 4 [73]. We assume non-lattice oxygen to have a non-threefold and non-fourfold coordination. We report that after the HZO deposition, there is an excess of oxygen anions in the material, based on the large non-lattice oxygen peak. Negatively charged excess oxygen after oxide deposition has been previously reported by Fulton et al. [65, 66]. Although some amount of non-lattice oxygen is removed from the film after the first anneal at 400 °C, there is still O^{2-} remaining after this initial anneal. It is known that non-lattice oxygen can react with oxygen vacancies, ultimately passivating the defects and neutralizing charge [70, 71], so it is possible that the non-lattice oxygen is being consumed by the HZO film to passivate oxygen vacancies. We thus speculate that the remaining

non-lattice oxygen, or O^{2-} anions, after an initial UHV anneal are more tightly bound to the oxide film, and could act as an oxygen source for passivating oxygen vacancies.

We note that for the HZO on WSe_2 sample, the WO_3 could also be playing a role in vacancy passivation. As mentioned earlier, it is seen in Figure 5.1.11(a) that the WO_3 features decrease in intensity with increasing temperature. Thus, another potential oxygen source for passivating oxygen vacancies at the higher temperature anneals is this WO_3 at the HZO/WSe_2 interface. Sowinska et al. [72] and Bertaud et al. [74] have shown that oxygen vacancies in HfO_2 are passivated by a metal oxide (TiO_y) interfacial layer between their HfO_2 film and a Ti top electrode. In the present study, it is possible that the oxygen from the WO_3 is being consumed to passivate oxygen vacancies, which makes the HZO less n-type after higher temperature anneals (500-800 °C).

For both HZO on MoS_2 and HZO on WSe_2, a second potential source for passivating atoms is the TMDC underlayer. Because the HZO is in contact with a TMDC, it cannot be discounted that the chalcogen atoms from the TMDC substrate could be diffusing into the HZO film and passivating any oxygen vacancies in it. Sulfur (from MoS_2) and selenium (from WSe_2) have the same valence as oxygen, making them both a likely candidate for being a substitutional atom for oxygen in the HZO lattice. For this proposed vacancy passivation mechanism, we speculate that at 400 °C, there is not enough thermal energy for diffusion of excess S or Se from the TMDC into the HZO. This is why the HZO becomes more n-type, signifying an increase in oxygen vacancies, at this annealing temperature. The vacancy passivation occurs at higher temperature anneals, wherein any excess chalcogen atoms, such as interstitials or intercalants in the TMDC, may have enough energy to diffuse away from the TMDC substrate and into the HZO. We report that changes in the widths of the XPS features due to this potential phenomenon are not detected in these samples because the concentration of oxygen vacancies is outside the detection limit of XPS. Based on our XPS data, it is not possible to differentiate between oxygen or chalcogen atoms as the source of vacancy passivation.

5.1.4.5 Crystallization of HZO

Crystallization of the amorphous as-deposited HZO is expected to occur within the temperature range used in this work. With a 10 nm $Hf_{0.5}Zr_{0.5}O_2$ film, Park et al. report a mixture

of the orthorhombic and tetragonal phases after annealing at 400-500 °C, and a mixture of the monoclinic, orthorhombic, and tetragonal phases after annealing at 600-700 °C. They state that the start of crystallization occurs with the formation of the tetragonal phase, followed by the transformation of some grains into the orthorhombic phase because of a two-dimensional stress effect. At higher temperatures, the monoclinic phase is formed, primarily from the tetragonal phase, as the grain size increases. [36] A study by Hsain et al. confirms these phase transitions through in-situ high-temperature XRD, which allowed them to study the phases present in 30 nm films of different HZO compositions as they develop during heating and cooling. Additionally, they revealed that for annealing temperatures of 500-1000 °C, the monoclinic phase fraction increases linearly with increasing temperature. [75]

Using XPS, we have found the HZO to show qualitative signs of ordering after annealing at 500 °C and higher. Figure 5.1.15 shows the Hf 4*f* data from Figure 5.1.4(b) normalized and energy corrected. It is clear from the peak-to-valley ratio, which is the ratio between the maximum intensity and the value between the doublet feature, that the full width at half maximum of the individual components has decreased after annealing at temperatures of 500 °C and higher. This sharpening of the peaks typically indicates some degree of increased ordering of the material. We report that this ordering phenomenon is because of the onset of crystallization of the HZO.

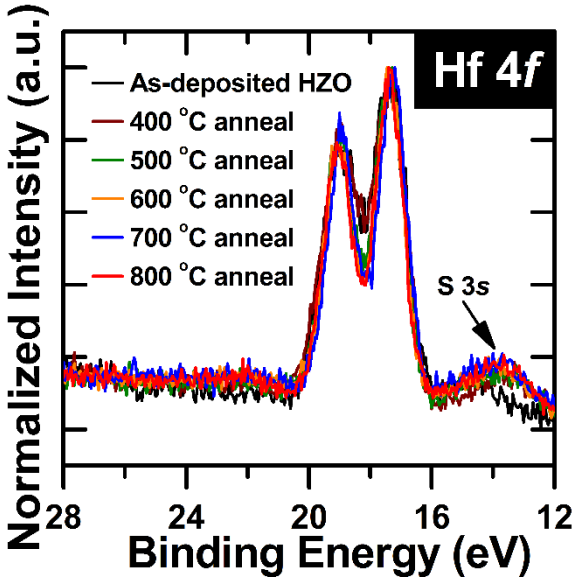

Figure 5.1.15. Normalized and overlaid Hf 4f spectra of HZO on functionalized MoS_2 (from Figure 5.1.4(b)).

All three samples discussed above comprised a very thin layer (~1 nm) of HZO, which is much thinner than typical HZO films used in devices, as these samples were primarily used for XPS interfacial studies. These 1 nm HZO films were also too thin to get sufficient XRD signal, therefore, thicker HZO samples were required to obtain strong and meaningful diffraction peaks that show crystallization. We thus fabricated two separate samples for XRD. Approximately 10 layers of WSe_2 was MBE-grown on an AlN/Si (111) substrate using the same method described for the WSe_2 growth on HOPG. After MBE growth, nominally 20 nm of HZO was deposited on top of the WSe_2 through ALD.

The first sample (HZO/WSe_2/AlN sample 1) was subjected to a series of anneals in UHV for 40 min at each of the following temperatures: 400 °C, 500 °C, and 600 °C. This annealing procedure replicates that of the samples in the XPS study. GIXRD measurements were performed after each annealing step. No peaks were observed in any of the diffraction measurements; the pattern measured after the 600 °C anneal is shown in blue in Figure 5.1.16.

The second sample (HZO/WSe_2/AlN sample 2) was subjected to a 600 °C anneal in UHV for 80 min rather than 40 min to allow more time for grain growth. The GIXRD pattern for this sample after the 600 °C anneal is shown in black in Figure 5.1.16. The pattern indicates that the HZO has crystallized and demonstrates mixed phase assemblage due to the presence of both monoclinic and orthorhombic and/or tetragonal peaks. The peak at 30.5° presents challenges in indexing due to similar *d*-spacings of the orthorhombic and tetragonal phases; therefore, this peak could be the result of the orthorhombic (111) reflection, the tetragonal (101) reflection, or both. The peak at 31.7° can be attributed to the monoclinic (111) reflection. It is interesting to note that the monoclinic ($\bar{1}11$) reflection at 28.3° is of much lower intensity than the monoclinic (111) reflection, suggesting that some degree of crystallographic texture exists, or that the strain state of the film has resulted in preferred orientation of the monoclinic phase, as the (111) and ($\bar{1}11$) reflections represent planes of the same family that are related by a ferroelastic transformation.

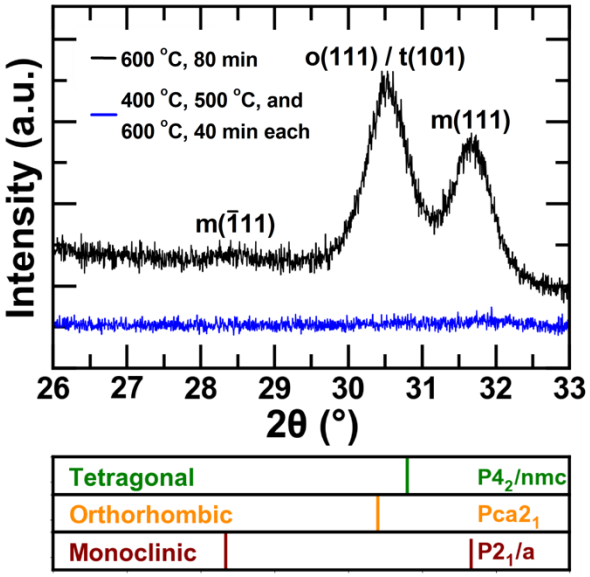

Figure 5.1.16. GIXRD patterns of the 20 nm thick HZO on WSe_2 samples. For these measurements, the X-ray incident angle was fixed at 0.7°, and the 2θ range of 26-33° was measured. Markers designate reflections for tetragonal, orthorhombic, and monoclinic phases.

We note that while a 40 min anneal, used for HZO/WSe_2/AlN sample 1, was sufficient to observe peak narrowing by XPS, it did not yield detectable peaks in XRD (blue curve in Figure 5.1.16). We speculate that 40 min was sufficient to generate short-range atomic order, possibly in the near-surface region to which XPS is most sensitive, but was insufficient to suitably coarsen them. In previous work, it was shown that newly formed grains in 2.8 nm thick HfO_2 were ~1-2 nm in size [67]. These grain sizes would be expected to produce peaks that are too broad (~10 degrees in 2θ) to be observable by XRD. For HZO/WSe_2/AlN sample 2, the anneal time was longer to allow grain coarsening, such that XRD peaks are observable (black curve in Figure 5.1.16). In Chapter 5.2 (section 5.2.4.2.1), we present further evidence of the relationship between XPS peak widths and crystallization onset, observed with electron diffraction, for HfO_2 thin films that were similarly deposited through ALD.

5.1.5 Conclusions

We have examined the thermal stability of HZO grown directly atop TMDCs (MoS_2 and WSe_2) of interest for next generation non-volatile memories and advanced low power transistors. For MoS_2, the importance of functionalizing the MoS_2 prior to ALD, in order to produce a high-quality and thermally stable oxide film, was demonstrated. The HZO film deposited on a non-functionalized MoS_2 substrate was unstable with temperature, wherein removal of the HZO overlayer began at a 400 °C anneal. ZrO_2 species were fully removed after a 500 °C anneal, leaving behind trace amounts of hafnium oxide, which shows that HfO_2 sticking on the MoS_2 surface is preferred over the sticking of ZrO_2. HZO on a functionalized UV-O_3 treated MoS_2 substrate, on the other hand, did not show signs of decomposition, and both the HZO and the MoS_2 were stable between 400-800 °C. For the as-grown WSe_2 film, a thermal budget of 700 °C is reported. The W 4*f* spectra showed an asymmetry in the low binding energy side after an 800 °C anneal, which signifies the appearance of a sub-stoichiometric state, WSe_{2-x}. We also report on possible mechanisms for passivating oxygen vacancies in the HZO. Lastly, crystallization of the HZO was examined, and the monoclinic, tetragonal, and orthorhombic phases were observed via XRD after annealing for 80 min at 600 °C, demonstrating that functional crystalline films can be directly integrated on TMDCs.

5.2 Effects of Atmospheric UV-O_3 Exposure of WSe_2 on the Properties of the HfO_2/WSe_2 Interface

5.2.1 Abstract

In device applications, transition metal dichalcogenides (TMDCs), such as semiconducting WSe_2, are typically interfaced with a high-quality dielectric layer. The unreactive basal plane of TMDCs makes the standard technique for deposition of dielectric oxides, atomic layer deposition (ALD), challenging on TMDC surfaces. In this work, we make use of atmospheric ultraviolet-ozone (UV-O_3) exposure of WSe_2 to functionalize its surface and promote uniform ALD of HfO_2. We report two classifications depending on the UV-O_3 exposure time. Low exposures do not result in detectable WSe_2 surface oxidation, while high exposures result in a self-limiting and amorphous tungsten oxyselenide top layer. Following ALD of HfO_2, low exposure samples have an abrupt HfO_2/WSe_2 interface with no interfacial oxide, while high exposure results in an interfacial WO_3 layer between the HfO_2 and the WSe_2, as well as evidence of two doping states observed in the underlying WSe_2. Despite differences in the interface chemistry, both low and high exposures result in uniform and smooth HfO_2 films directly deposited by ALD. We report that our atmospheric UV-O_3 exposure technique on WSe_2 is an avenue for allowing direct ALD of thin uniform oxide films on WSe_2, and the UV-O_3 exposure time provides unique tunability and flexibility in interface design within devices. However, top-gated device fabrication using UV-O_3 functionalization of WSe_2 requires further process optimization.

5.2.2 Introduction

Transition metal dichalcogenides (TMDCs) are a class of two-dimensional (2D) layered materials, in which each layer is held in-plane by strong chemical bonds but held in the out-of-plane direction by weak van der Waals forces. WSe_2 is a semiconducting TMDC offering fundamentally unique charge carrier and transport properties, such as its propensity for p-type doping and its enhanced spin-orbit coupling compared with other TMDCs [76-78]. These attributes make WSe_2 an attractive channel candidate for use in various applications, such as field-effect transistors and low power memory devices. [79, 80]

In an electronic device, TMDC channels, like WSe_2, are typically capped in the gate region with a high-quality dielectric layer, where ultrathin (sub-5 nm) dielectric thicknesses are desired to achieve sufficient gate-to-channel electrostatic coupling. Atomic layer deposition (ALD) is a widely adapted method for depositing dielectric films, and it is a technique that is compatible with semiconducting manufacturing processes. ALD offers excellent film conformality, low roughness, good uniformity, and precise thickness control due to the layer-by-layer nature of the deposition. [81, 82] However, since initial nucleation during ALD relies on the precursors reacting with the growth substrate, i.e., the channel surface, ALD of uniform and conformal films is hard to achieve on 2D materials due to their unreactive basal plane [58, 83, 84]. Some ways to circumvent this issue of non-uniform ALD on 2D materials include the use of buffer layers [85-87], plasma-enhanced ALD (PEALD) [88, 89], surface treatment with O_2 plasma [90, 91], and functionalization with ultraviolet-ozone (UV-O_3) [43, 44, 62].

Azcatl et al. [44] have compared the properties of different UV-O_3 exposed TMDCs, including WSe_2. They studied the characteristics of the ALD oxide and the interface chemistry following ALD of HfO_2 on these UV-O_3 exposed TMDCs. Uniform ALD on the UV-O_3 exposed WSe_2 surface was not achieved in that study. The ALD proceeded in a triangular cluster growth mechanism, which was attributed to "self-cleaning" [92] reduction reactions during ALD. Since their starting WSe_2 surface consisted of WO_x and SeO_x species, these W and Se oxides were reduced or eliminated by reacting with the ALD precursor/s and subsequently volatilizing. This partial etching of the surface produced triangular hole-like structures on the WSe_2, which then acted as preferred nucleation sites for the ALD growth, thus resulting in the triangular island morphology of the deposited HfO_2 after ALD.

However, in Azcatl et al.'s study, the UV-O_3 exposure was performed in ultra-high vacuum (UHV), and the optimal UV-O_3 exposure time for the best WSe_2 surface conditions for ALD were not investigated. Hence, investigating how the extent of WSe_2 functionalization affects the ALD process of oxide films (i.e., HfO_2) on WSe_2 has not been explored.

In this work, we aim to study the extent of UV-O_3 functionalization of WSe_2, achieved by varying the UV-O_3 exposure time. Low and high exposure times result in different WSe_2 starting surfaces for ALD. At high exposures, the WSe_2 top surface is oxidized, and we also investigate the properties of this oxidized layer, such as its thickness, structure, air stability, and thermal

stability. We then perform ALD of HfO_2 and study the resulting interface chemistry, HfO_2 film morphology, and electrical properties at the different WSe_2 exposure times.

5.2.3 Methodology

Clean surfaces of bulk WSe_2 crystals (2D Semiconductors [93] and SPI Supplies [94]) were exposed by removing the topmost layers through mechanical exfoliation with Scotch tape. The freshly exposed crystal surfaces were then exposed to UV-O_3 in atmosphere. We previously showed that the UV-O_3 treatment in UHV demonstrated by Azcatl et al. [43, 44] can be adapted to a tabletop UV lamp in atmosphere [95], demonstrating the transferability of the functionalization process to ambient conditions. In the current study, a custom-built UV-O_3 tool, which consisted of a UV grid lamp connected to a 3 kV, 30 mA power supply (BHK, Inc.), was used in the saturation and air stability experiments (Figure 5.2.5, Figure 5.2.6, Figure 5.2.10, and Figure 5.2.11). For all other UV-O_3 exposure experiments discussed here, a UVOCS UV-O_3 system [96] was used. Following UV-O_3 treatment, the surfaces were analyzed with X-ray photoelectron spectroscopy (XPS) using a monochromated Al Kα X-ray source. For Figure 5.2.1, Figure 5.2.3, and Figure 5.2.12, XPS spectra were collected with a PHI VersaProbe III system using a 130 W X-ray source, 100 μm X-ray spot size, 26 eV pass energy, and standard lens mode settings. All other XPS spectra in this work were collected using a 300 W X-ray source, a 0.8 mm slit, and a Scienta Omicron R3000 analyzer at a pass energy of 50 eV. This same Scienta Omicron UHV system, which is described elsewhere [48], was used for low energy electron diffraction (LEED) analysis. Atomic force microscopy (AFM) measurements were also carried out on the UV-O_3 treated WSe_2 surfaces using a Bruker Dimension Icon AFM.

ALD of HfO_2 was performed using a Kurt J. Lesker ALD 150LX. Tetrakis(dimethylamido)hafnium (TDMA-Hf) and H_2O were used as metal precursor and oxidant, respectively. The ALD was performed at 200 °C, and to stabilize the substrate temperature at the start of the ALD process, the growth substrate was held at 200 °C for 10 min before any precursor pulse. The growth rate per cycle (GPC) of the HfO_2 ALD recipe, calibrated on a bare silicon wafer, was 0.1 nm/cycle. For XPS measurements of the HfO_2/WSe_2 interface, approximately 3 nm of HfO_2 (30 ALD cycles) was deposited. For AFM characterization of the deposited film, 60 HfO_2 ALD cycles were deposited on the WSe_2 samples. AFM images of the HfO_2 films were obtained

using a Hitachi AFM 5300 in ambient mode. Cross-section samples were prepared for transmission electron microscopy (TEM) using a ThermoFisher Helios G4 UX dual beam focused ion beam-scanning electron microscope (FIB-SEM). Prior to FIB preparation, the samples were sputter coated with 2 nm of IrO_x to improve surface conductivity and prevent charging. TEM characterization was performed using a probe-corrected JEOL ARM200F operated at 200 kV.

For electrical characterization, targeted lithography was performed via e-beam lithography (Vistec EBPG 5000+) using poly(methyl methacrylate) (PMMA) (950A4, MicroChem) and a base dose of 750 μC/cm^2. Samples were developed in methyl isobutyl ketone / isopropyl alcohol (10 mL / 25 mL) for 75 seconds, then dried with nitrogen. Metals were deposited by thermal evaporation (Bi at 1 Å/s) or e-beam (Pd at 2 Å/s) at 10^{-6} to 10^{-7} Torr, followed by lift-off in acetone. Devices were tested in a Lake Shore vacuum probe station using a Keithley 4200-SCS.

Spectral deconvolution of XPS data was performed using kolXPD software [97]. All peaks were fit with Voigt lineshapes. Gwyddion software [98] was used to process AFM images and generate line profiles.

5.2.4 Results and Discussion

5.2.4.1 Atmospheric UV-O_3 Exposure of WSe_2

5.2.4.1.1 Extent of UV-O_3 Functionalization

To determine how the extent of UV-O_3 exposure affects the chemistry of the WSe_2 surface, we exposed four different WSe_2 samples to UV-O_3 for different amounts of time – 10 min, 13 min, 17 min, and 20 min. Overlaid XPS spectra for these four exposure times are shown in Figure 5.2.1.

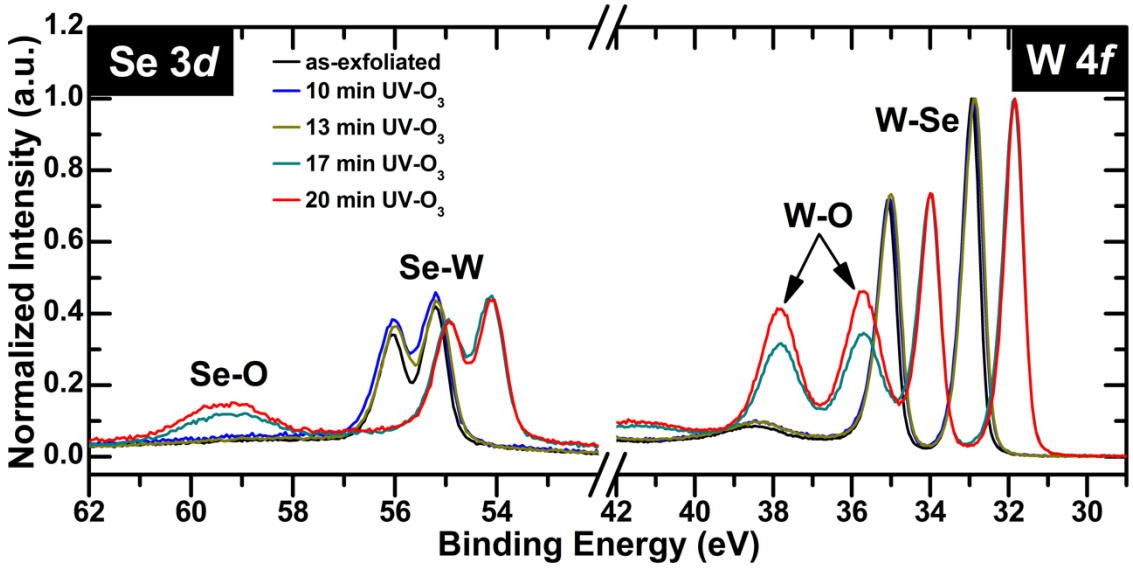

Figure 5.2.1. W 4f and Se 3d spectra of different WSe_2 samples that underwent different amounts of UV-O_3 exposure. All times indicated are single exposures. 10 min and 13 min are classified as low exposure, while 17 min and 20 min are classified as high exposure.

With XPS, we found two distinct results which allow us to classify the UV-O_3 functionalization into two categories. With lower exposure times (10 and 13 min), we observe no oxide formation, and higher exposure times (17 and 20 min) result in tungsten oxyselenide layer formation. Shown in Figure 5.2.2 are the O 1*s* spectra of the same samples, where it can be seen that low and high UV-O_3 exposure times result in different oxygen signatures.

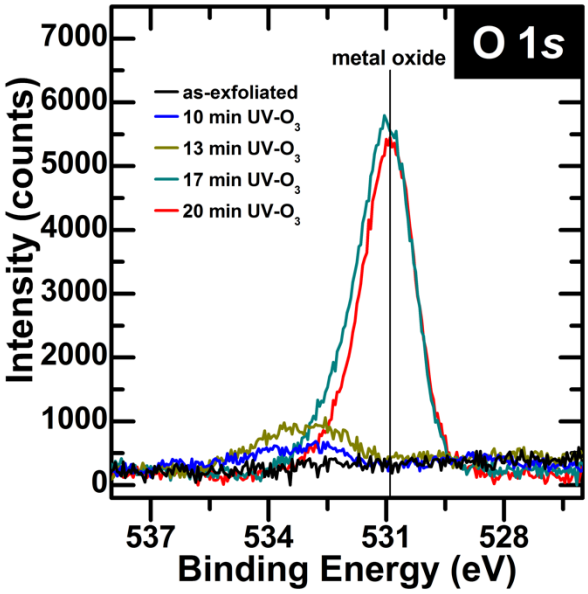

Figure 5.2.2. O 1s spectra of the same samples in Figure 5.2.1. 10 min and 13 min are classified as low exposure, while 17 min and 20 min are classified as high exposure.

Oxygen species accumulate on the surface for both low and high exposures, but the O 1*s* peak intensities (indicative of amount of oxygen) and binding energy positions (indicative of oxygen chemical state) differ with exposure time. The position of the oxygen peak for low exposures (10 and 13 min) is approximately 2 eV higher than the peak position expected for metal oxide, so this oxygen cannot be attributed to WO_x or SeO_x species. This agrees with what we observe in the W 4*f* and Se 3*d* spectra (Figure 5.2.1), where no tungsten or selenium oxide is detected for 10 and 13 min. We speculate that the oxygen species detected on the low exposure samples occupy Se vacancies, step edges, and other defect sites on the WSe_2 surface. In contrast, for high UV-O_3 exposures (17 and 20 min), the O 1*s* intensity is ~5 times higher than the low exposure signal, and their binding energy position at 530.9 eV matches that of metal oxide. This tall metal oxide feature makes sense since as shown in Figure 5.2.1, we know that high UV-O_3 exposures result in the formation of tungsten and selenium oxides on the surface. Further differences between our low and high exposure classifications are seen by deconvoluting the W 4*f* and Se 3*d* spectra, as shown in Figure 5.2.3.

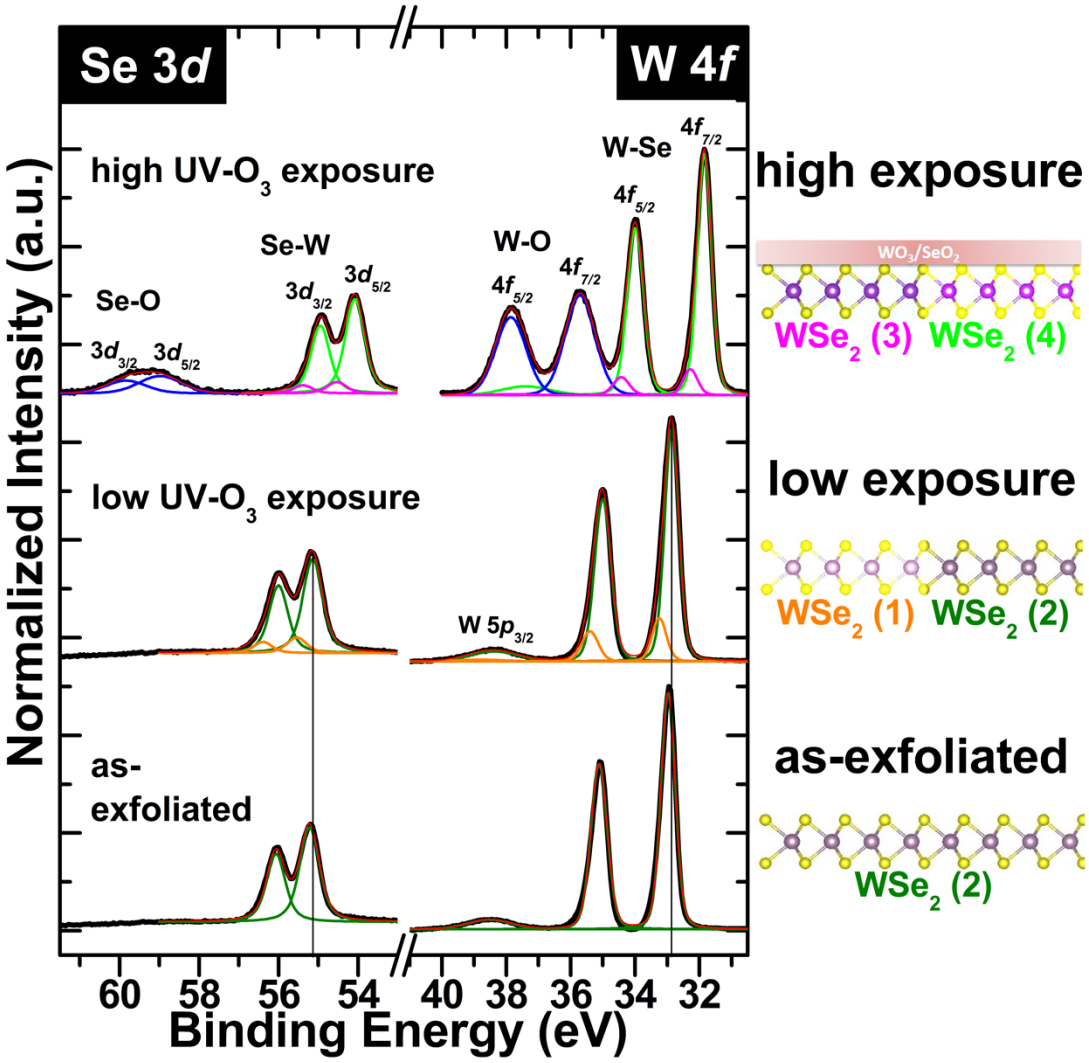

Figure 5.2.3. W 4f and Se 3d spectral fits and schematic representation of the surface/interface structure for as-exfoliated, low exposure, and high exposure WSe2 samples. More details on the spectral deconvolution can be found in Appendix C. The different WSe_2 components are classified based on their binding energy positions. In order of highest to lowest binding energy, the W $4f_{7/2}$ peak for WSe_2 (1) is at ~33.3 eV, WSe_2 (2) is at 32.9 to 33.0 eV, WSe_2 (3) is at ~32.3 eV, and WSe_2 (4) is at ~31.9 eV. Drop lines are a guide to more clearly visualize the 0.1 eV shift to lower binding energy of WSe_2 (2) in the low exposure spectra.

Through spectral deconvolution, we see that with low UV-O_3 exposure, there are two WSe_2 components. The lower intensity component, "WSe_2 (1)", is located 0.4 eV above the main higher intensity component, "WSe_2 (2)". As can be seen by the drop line in Figure 5.2.3, WSe_2 (2) in the

low exposure spectra is shifted to slightly lower binding energy (~0.1 eV lower) than WSe_2 (2) in the as-exfoliated spectra. The equal shift of both the W 4*f* and Se 3*d* peaks to lower (or higher) binding energy means that the core levels and valence band of that WSe_2 component are closer to (or further from) the Fermi level, which serves as evidence that the WSe_2 is p-type (or n-type) doped relative to the as-exfoliated material.

We report that at the initial stages of UV-O_3 exposure pertinent to low exposure times, the UV-O_3 likely interacts with both adventitious surface contaminants and the WSe_2 material. We show C 1*s* spectra in Figure 5.2.4, where it can be seen that UV-O_3 exposures reduce the amount of carbon on the surface.

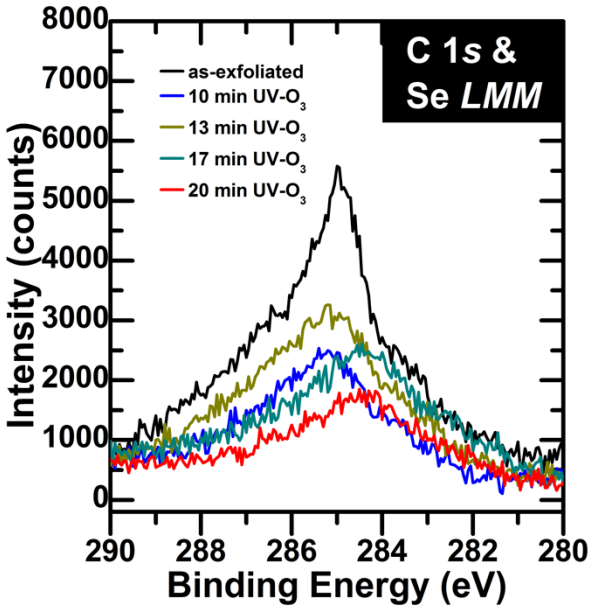

Figure 5.2.4. C 1s region of the same samples in Figure 5.2.1 and Figure 5.2.3. In general, the amount of carbon on the surface of the WSe_2 is reduced upon exposure to UV-O_3. We note that the shape of the background is due to a broad Se LMM Auger feature that overlaps with the C 1s region.

Surface hydrocarbons are known to be p-type dopants in 2D materials [99], so cleaning off these surface contaminants can induce an n-type shift in the WSe_2, which may be a reason for the appearance of the small WSe_2 (1) component for low UV-O_3 exposure. However, the slight shift of the primary component, WSe_2 (2), relative to the as-exfoliated curve is p-type in nature. We attribute this to an onset of the doping effect induced by the UV-O_3 interacting with the WSe_2. In

addition, we do not see any detectable tungsten or selenium oxide formation with low exposure. We note that the chemical detection limit of XPS is ~0.1 to 1 atomic % [100]; however, it is able to detect Fermi level shifts and electronic changes arising from interfacial defects, dopant atoms, vacancies, etc., that may be below this chemical/elemental detection limit. This makes us more sensitive to Fermi level shifts than to changes in the chemical bonding environment, especially close to the limit of chemical resolution. The schematic picture of the functionalized surface in Figure 5.2.3 shows the different WSe_2 components labeled with colors matching the colors of their respective peaks in the XPS fit.

In contrast, high UV-O_3 exposures resulted in tungsten and selenium oxides, as well as a uniform ~1 eV shift to lower binding energy of the two sets of W 4*f* and Se 3*d* peaks. As shown in the high exposure spectra in Figure 5.2.3, the lower intensity WSe_2 component is classified as "WSe_2 (3)", and the WSe_2 state that is observed at the lowest binding energy is assigned "WSe_2 (4)". Based on the shift of the WSe_2 peaks to even lower binding energies, we can say that high exposure WSe_2 is even more p-type doped than low exposure. Also evident from the XPS spectra of high exposure samples is the presence of WO_x and SeO_x. We assume these oxides to be WO_3 and SeO_2 based on their binding energy positions [95, 101-103]. The phenomenon of p-doping and oxide formation that we observe with high exposures is similar to what has been previously shown in other literature reports, for both WSe_2 and MoS_2. Previous studies have reported this p-type shift in WSe_2 and MoS_2 upon oxidation of the top layer. Yamamoto et al. [104] showed this with O_3-oxidized WSe_2; Addou et al. [105] showed this p-type shift in aged WSe_2 which has formed WO_3; Hoffman et al. [103] and Lin et al. [106] demonstrated this in WSe_2 oxidized using O_2 plasma; Nipane et al. [107] showed a p-type shift in WSe_2 with a tungsten oxyselenide layer formed through UV-O_3 exposure; Zhu et al. [108] reported a similar effect for MoS_2 that was exposed to remote O_2 plasma. It is noted that this p-type doping that is observed upon oxide formation is likely due to electron transfer from the WSe_2 (MoS_2) to the top WO_x (MoO_x) oxide layer [104, 105, 108].

We also observed that with high exposure, the thickness of the oxide layer has a saturation point. Figure 5.2.5 shows the W 4*f* and Se 3*d* spectra of a sample exposed to UV-O_3 for 30 min, overlaid with the spectra of two samples with doubled UV-O_3 exposure times (60 min). The ratio of the intensity of the W-O peak to the W-Se peak (and/or Se-O to Se-W) can be used as a measure of how much of the bulk WSe_2 crystal was oxidized. It is seen in Figure 5.2.5 that the intensities

of the W-O and Se-O peaks relative to the WSe_2 peaks are constant across the different samples. The doubled exposure time did not result in more WO_3/SeO_2 formed on the sample surface, indicating that a maximum/saturation point in the oxide thickness was reached at 30 min.

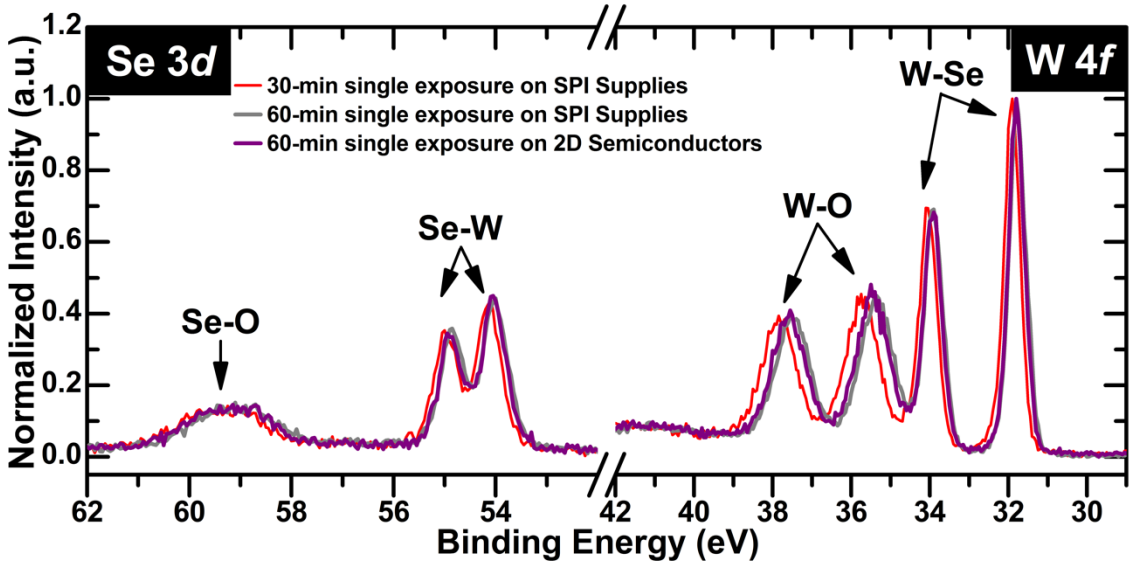

Figure 5.2.5. W 4f and Se 3d spectra of samples exposed to 60 min of UV-O_3, overlaid with spectra of a 30-min exposed sample, showing that doubling the UV-O_3 exposure time did not create more WO_3/SeO_2.

We note that this oxide thickness saturation is repeatable, as we show with different 30 min UV-O_3 exposures all resulting in the same amount of oxide formed (see Figure 5.2.6). The saturated tungsten oxyselenide layer thickness was calculated and found to be 1.11 $\pm$ 0.05 nm, assuming a compound overlayer of WO_3-SeO_2. This is the average of the six thicknesses found for each of the spectra in Figure 5.2.6, which are outlined in Table 5.2.1. Details of this calculation can be found in Appendix D. These findings agree with other studies that have shown that oxidation of WSe_2 is self-limiting. This is because once the first layer is oxidized, the vertical diffusion barrier for oxygen and/or oxygen radicals is high, preventing them from penetrating through the top oxide layer and reacting with the underlying WSe_2 layers. [104, 106, 107, 109]

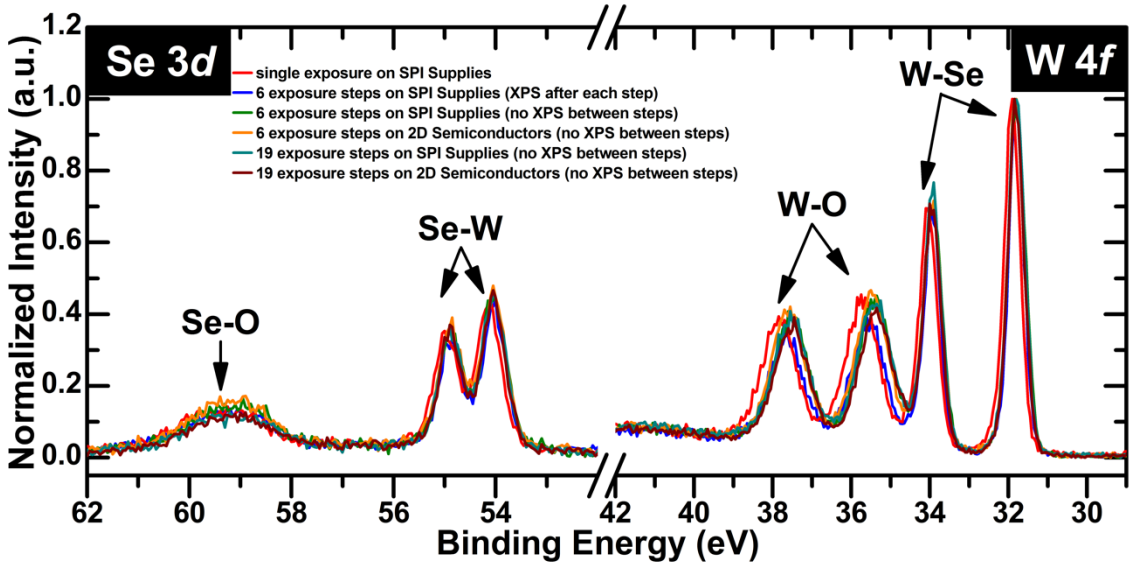

Figure 5.2.6. W 4f and Se 3d spectra of various WSe_2 samples all exposed to a total of 30 min of UV-O_3 exposure. The amount of W-O and Se-O formed is independent of the number of UV-O_3 exposure steps and WSe_2 vendor; all 30-min exposures resulted in nominally the same amount of tungsten oxyselenide.

Table 5.2.1. Calculated effective WO_3 and SeO_2 thicknesses and compound tungsten oxyselenide layer thickness for each of the spectra shown in Figure 5.2.6.

Spectra from Figure 5.2.6	**Effective WO_3 Thickness (d_{WO_3}, Å)**	**Effective SeO_2 Thickness (d_{SeO_2}, Å)**	**Compound Overlayer Thickness (d_{WO_3} + d_{SeO_2}, Å)**
single exposure on SPI Supplies	8.0	3.3	11.3
6 exposure steps on SPI Supplies (XPS after each step)	7.4	3.2	10.6
6 exposure steps on SPI Supplies (no XPS between steps)	7.6	3.8	11.4

6 exposure steps on 2D Semiconductors (no XPS between steps)	7.9	3.9	11.8
19 exposure steps on SPI Supplies (no XPS between steps)	7.4	3.3	10.7
19 exposure steps on 2D Semiconductors (no XPS between steps)	7.3	3.8	11.1

5.2.4.1.2 High Exposure: Properties of the Tungsten Oxyselenide Layer

We examined the structure, air stability, and thermal stability of this tungsten oxyselenide layer. We found through TEM and LEED that the oxide layer formed through UV-O_3 exposures is amorphous. Figure 5.2.7 shows a cross-sectional TEM micrograph of a WSe_2 crystal exposed to 30 min of UV-O_3. This UV-O_3 exposure time was sufficiently long to form a saturated tungsten oxyselenide layer, which our TEM micrograph reveals to have a disordered structure.

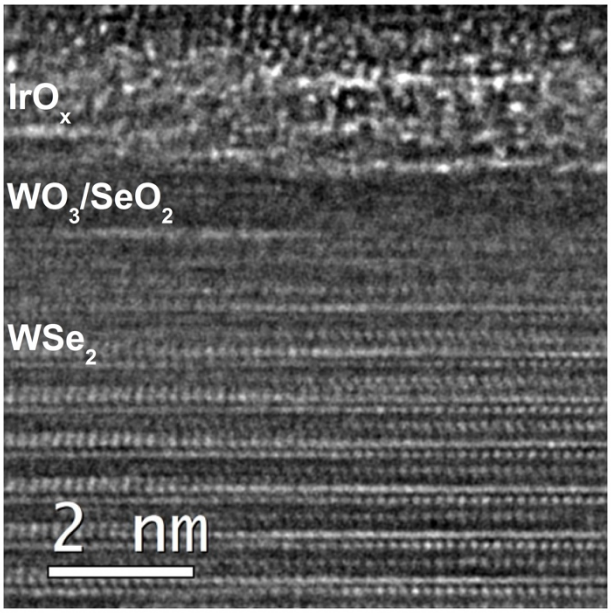

Figure 5.2.7. Cross-sectional TEM of a WSe_2 crystal exposed to UV-O_3 for 30 min showing the disordered nature of the tungsten oxyselenide layer (WO_3/SeO_2).

LEED images are shown in Figure 5.2.8. We see with LEED that the hexagonal diffraction pattern from the symmetry of the WSe_2 crystal is no longer present after 30 min of UV-O_3 exposure. Since the probing depth of LEED is ~1 nm or less [110], we know that after the 30 min UV-O_3 exposure, only the oxide layer formed will have contributions to the LEED image, and the absence of a diffraction pattern after UV-O_3 is indicative of an amorphous surface oxide layer.

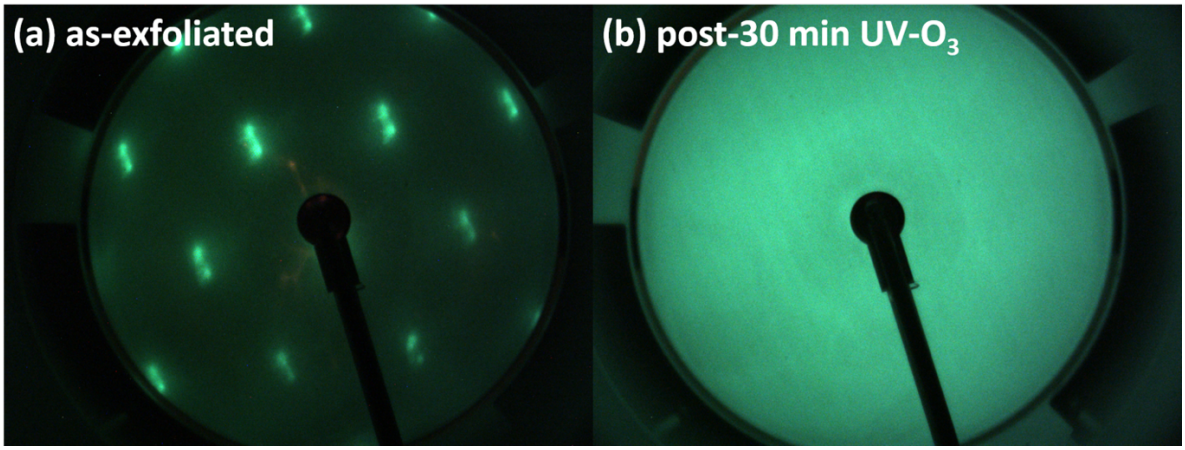

Figure 5.2.8. Low energy electron diffraction (LEED) images of (a) an as-exfoliated WSe_2 sample, and (b) a WSe_2 sample after a straight 30-min UV-O_3 exposure.

Additionally, AFM characterization of as-exfoliated and UV-O_3 treated WSe_2 (Figure 5.2.9) also reveals that the WSe_2 surface has an increased roughness after oxidation with UV-O_3. Our findings agree with prior reports that have also shown the amorphous nature of an oxide layer formed by O_3 exposure of WSe_2 without UV illumination [104], O_2 plasma oxidation of WSe_2 [103, 109], UV-O_3 exposure of WSe_2 [106], and remote O_2 plasma treatment of MoS_2 [108].

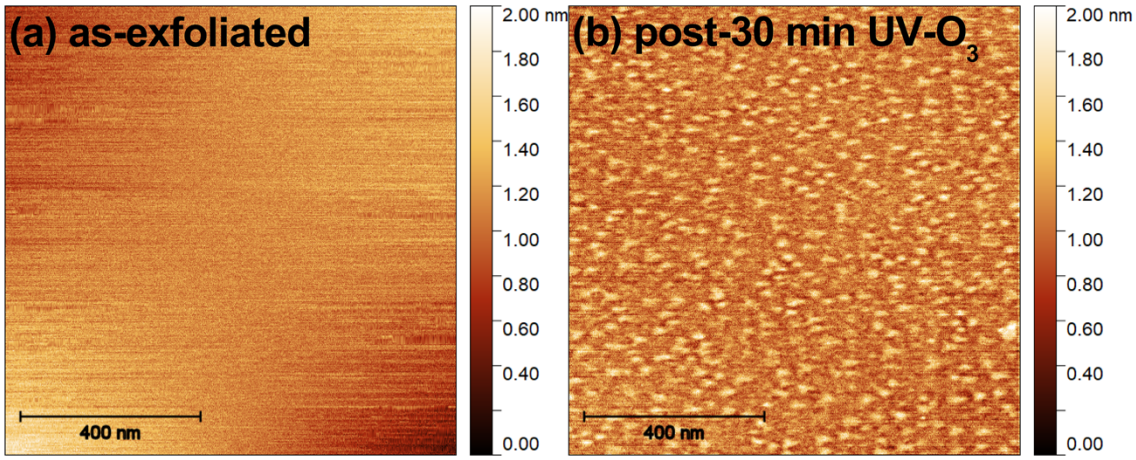

Figure 5.2.9. Atomic force micrographs of (a) as-exfoliated WSe_2, and (b) WSe_2 after a straight 30-min UV-O_3 exposure. The tungsten oxyselenide layer formed after UV-O_3 exposure results in an increased surface roughness.

We show through atmospheric exposure of a UV-O_3 oxidized sample (30 min exposure) that the tungsten oxyselenide layer is stable after 3 h, 1 day, and 6 days in ambient. It should be noted that a bare WSe_2 crystal does not easily oxidize in atmosphere, similar to what has been reported for MoS_2 [111]; the XPS spectra of as-exfoliated WSe_2 left in air for 3 h is shown in Figure 5.2.10 for reference.

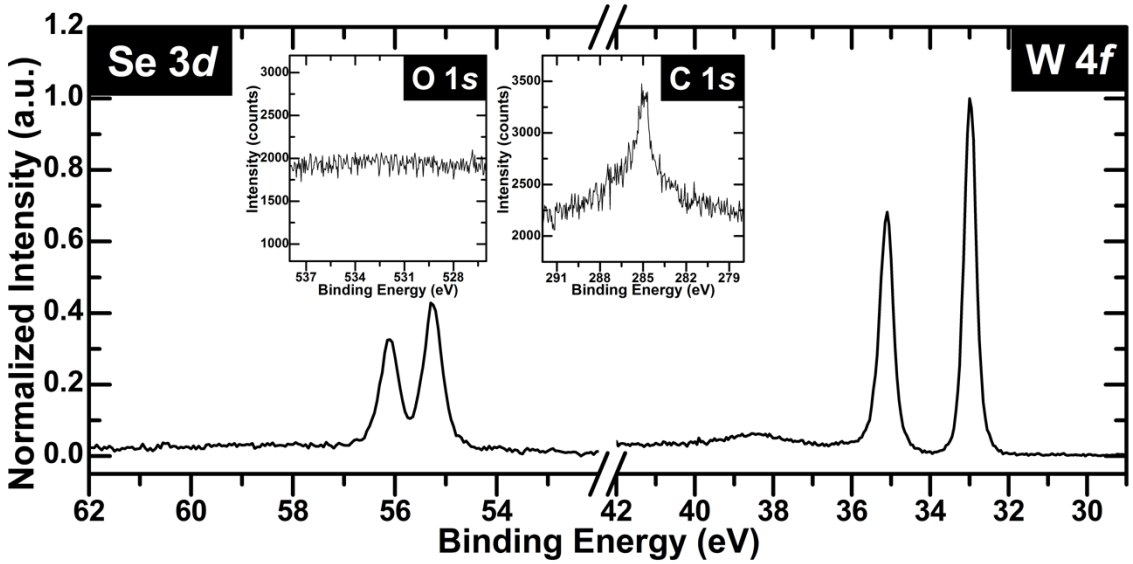

Figure 5.2.10. W 4f and Se 3d spectra of a WSe_2 crystal left in air for 3 h after mechanical exfoliation. Aside from the expected peaks for WSe_2, no other W or Se chemical states are detected. O 1s and C 1s spectra are shown as insets, where we see some adventitious carbon, but no oxygen, on the surface after the 3 h air exposure.

The W 4*f* and Se 3*d* spectra of a UV-O_3 exposed sample that was left in air for increasing amounts of time are shown in Figure 5.2.11, wherein the inset shows a plot of the calculated tungsten oxyselenide overlayer thickness. The average thickness of the four data points shown in Figure 5.2.11 is 1.07 nm $\pm$ 0.02 nm, which is within the error of our reported saturated oxide layer thickness in section 5.2.4.1.1. The calculated tungsten oxyselenide thicknesses after various air exposures only vary by less than 0.1 nm, as shown in Figure 5.2.11, so we report that this surface oxide layer is stable in atmosphere for the length of time we investigated. Despite the atmospheric stability of the high exposure WSe_2 surface, adventitious contamination still builds up on the surface when left in air. Therefore, for subsequent ALD after UV-O_3 exposure, which is discussed later, the samples are immediately transferred into the ALD load lock following UV-O_3 treatment to minimize adventitious carbon build-up.

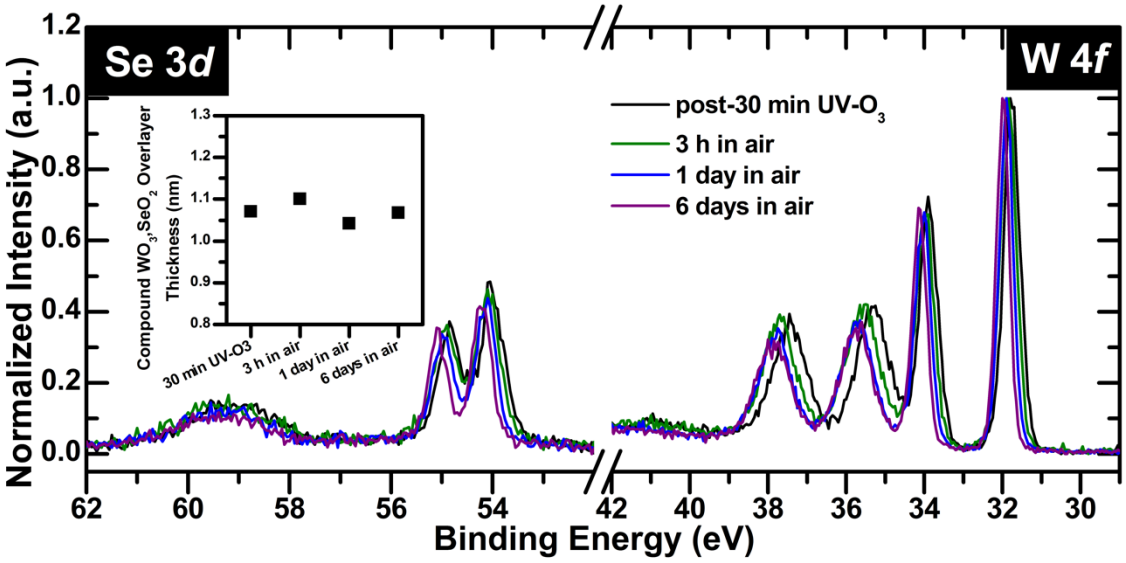

Figure 5.2.11. W 4f and Se 3d spectra of a WSe_2 sample after 30 min of UV-O_3 exposure and after subsequent increasing lengths of air exposure. Inset shows a plot of the compound oxide overlayer thickness as a function of time in atmosphere.

We also studied the thermal stability of this oxide layer and found that it changes upon heating to the ALD temperature for HfO_2 deposition. Figure 5.2.12 shows the spectra of a 30-min UV-O_3 exposed sample that was subsequently annealed in the ALD chamber at 200 °C, which is the substrate temperature for the HfO_2 ALD recipe used in section 5.2.4.2. Note that for this HfO_2 ALD recipe, as mentioned in the Methodology, the samples are held at deposition temperature for 10 min prior to any pulse step, so the 10-min anneal performed in this experiment mimics that of real pre-deposition conditions. This allowed us to examine the actual WSe_2 starting surface that exists just prior to the first HfO_2 ALD precursor pulse.

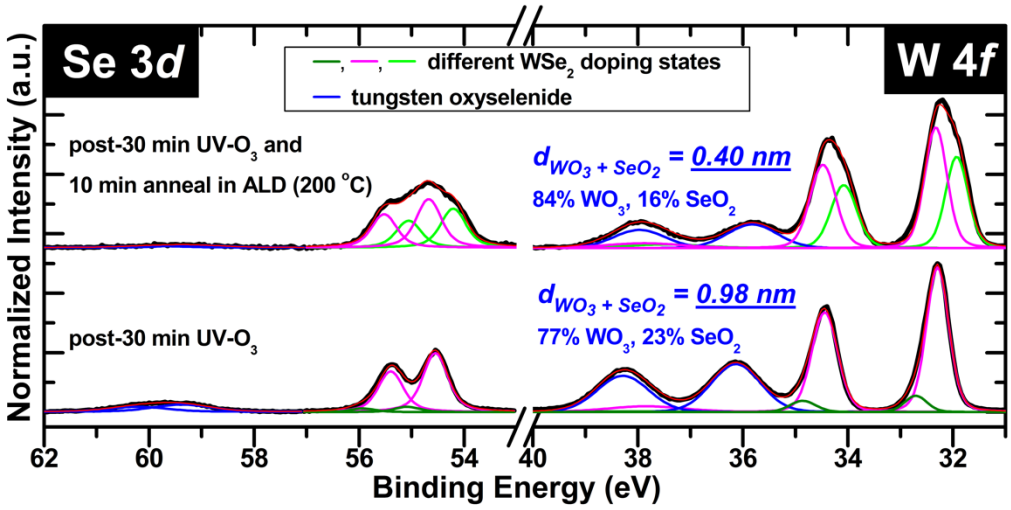

Figure 5.2.12. W 4f and Se 3d spectra of a WSe_2 crystal after 30 min of UV-O_3 exposure and after a subsequent 10-min anneal in the ALD at 200 °C (HfO_2 deposition temperature used in section 5.2.4.2). The calculated thickness of the tungsten oxyselenide on the surface for each spectrum is also noted in the figure. The % WO_3 and % SeO_2 indicated represent the percentage of the tungsten oxyselenide thickness coming from the effective WO_3 and effective SeO_2 thicknesses, respectively. We note that these spectra were collected at a photoelectron take-off angle of 60°.

It is evident that after this thermal treatment, there is less tungsten oxyselenide on the surface, and there is less SeO_2 relative to WO_3 within this tungsten oxyselenide layer. Based on thickness calculations using intensity ratios (as described in Chapter 2 and Appendix D), we report an approximate 0.6 nm reduction in the tungsten oxyselenide thickness after annealing. We also observe that the amount of both tungsten and selenium oxide decreased, but SeO_2 was removed at a faster rate than WO_3. In addition, we observe Fermi level shifts in the WSe_2, as seen by the different WSe_2 components present before and after the 10-min ALD anneal. This annealing experiment informed us of the chemical and electronic changes that take place with high exposure WSe_2 between the UV-O_3 functionalization and the HfO_2 deposition steps. In the following section, we report on ALD of HfO_2 on UV-O_3 functionalized WSe_2 and discuss the properties of the HfO_2 film and the interface chemistry between the HfO_2 film and underlying WSe_2.

5.2.4.2 HfO_2 ALD on UV-O_3 Functionalized WSe_2

5.2.4.2.1 Interface Chemistry and Structure

To study the interface between ALD HfO_2 and WSe_2, we used bulk WSe_2 crystals and exposed them to a range of UV-O_3 exposure times: 10, 17, and 30 min under identical conditions to those discussed in section 5.2.4.1.1. Along with a "control" untreated sample, the bulk WSe_2 crystals were then immediately transferred to the ALD chamber and loaded side-by-side in order to ensure that they all underwent the same HfO_2 deposition conditions. UV-O_3 start times were staggered, and the "control" sample was exfoliated right before loading into the ALD to ensure no differences in air exposure times between treatment and ALD.

We first discuss the interfacial characteristics of the WSe_2 based on XPS, as shown in Figure 5.2.13. For low exposure (10 min UV-O_3), it is noticeable that the W 4*f* and Se 3*d* features after ALD are comparable to the non-functionalized WSe_2 surface, in terms of both linewidth/lineshape and peak position. As seen in the deconvoluted spectra in Figure 5.2.13(b), we only see one WSe_2 component in the W 4*f* and Se 3*d* features, WSe_2 (2). Also, the ALD on a low exposure WSe_2 surface results in no interfacial WO_3 layer. On the other hand, the high exposure surface (17 min and 30 min UV-O_3) after ALD has an interfacial WO_3 layer and multiple WSe_2 related features, which can be seen in the lineshape of the W 4*f* and Se 3*d* peaks. Spectral deconvolution (Figure 5.2.13(b)) reveals that there are two WSe_2 states for high UV-O_3 exposures post-ALD – WSe_2 (2) and WSe_2 (3). We know that these two sets of W-Se peaks are not due to a change in the chemical bonding environment of W or Se because both components have a Se/W stoichiometry consistent with the WSe_2 peaks for 0 min and 10 min UV-O_3. The presence of WSe_2 (2) and WSe_2 (3) on the same sample is thus the result of variable doping states in the WSe_2. The 0.4 eV separation between these two doping states is consistent with the separation of the two WSe_2 components in the as-UV-O_3 exposed XPS (Figure 5.2.3) and the ALD-annealed XPS (Figure 5.2.12).

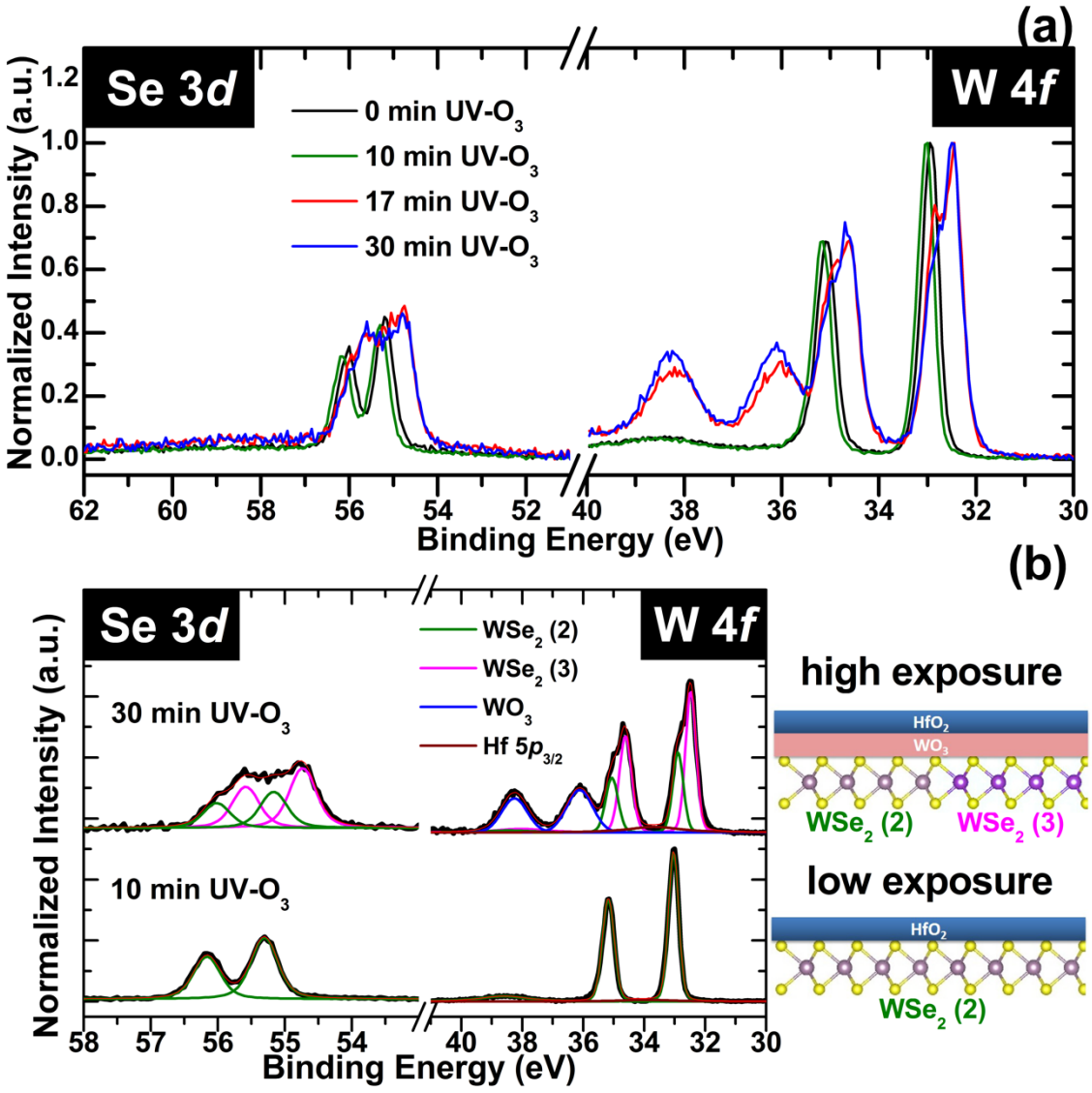

Figure 5.2.13. (a) W 4f and Se 3d spectra after ALD of HfO_2 on WSe_2 exposed to UV-O_3 for different amounts of time. (b) Deconvoluted spectra from (a) and accompanying pictorial representation, showing the post-ALD characteristics of a low and high exposure WSe_2 surface.

We investigated the HfO_2 films deposited on our samples by comparing their Hf 4*f* peaks. We note that there is a difference in the peak-to-valley ratio of the Hf 4*f* core level spectra between the four WSe_2 samples exposed to different amounts of UV-O_3 before HfO_2 deposition. This can be seen in the plot where the maximum intensity of each spectrum is aligned and normalized to 1, as shown in Figure 5.2.14(a). The peak-to-valley ratio is the ratio of the maximum intensity of the

Hf $4f_{7/2}$ peak at ~18 eV to the value between the Hf 4*f* doublet (valley at ~19 eV), and this ratio is a visual indicator of the full width at half maximum (FWHM) of the individual Hf 4*f* components. We plot the measured FWHM as a function of the UV-O_3 exposure time in Figure 5.2.14(b). It is evident in Figure 5.2.14 that the FWHM of the 0 min and 10 min samples (untreated and low exposure) are wider than the 17 min and 30 min samples (high exposure). XPS peak narrowing, as we observe in the high exposure samples, is typically indicative of increased order in the material. We hypothesize that this is due to the onset of crystallization of the deposited HfO_2 film on the 17 min and 30 min samples. This interpretation of the XPS FWHM is consistent with our prior report which showed the onset of hafnium zirconium oxide crystallization through the sharpening of the Hf 4*f* peaks [95].

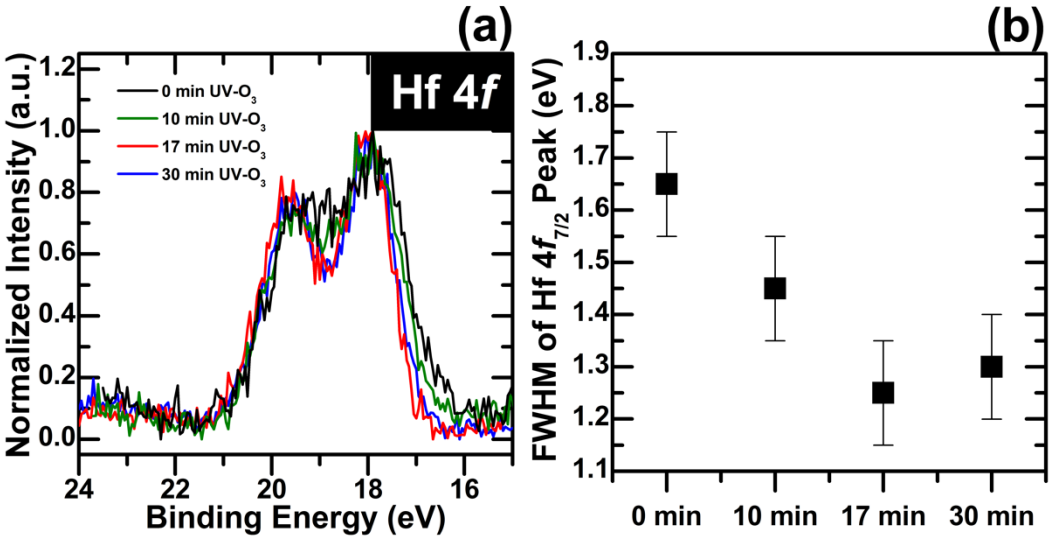

Figure 5.2.14. (a) Hf 4f spectra of HfO_2 films deposited on WSe_2 samples that were exposed to varying amounts of UV-O_3 prior to HfO_2 ALD. (b) FWHM of the Hf $4f_{7/2}$ peaks for each UV-O_3 exposure time in panel (a).

This hypothesis is supported by the TEM diffraction patterns shown in Figure 5.2.15. For the diffraction patterns of HfO_2 on untreated and low exposure WSe_2, only the diffraction spots for WSe_2 are visible, but for HfO_2 deposited on high exposure WSe_2, the presence of other weak diffraction spots, attributed to the presence of some HfO_2 crystallites, can be observed.

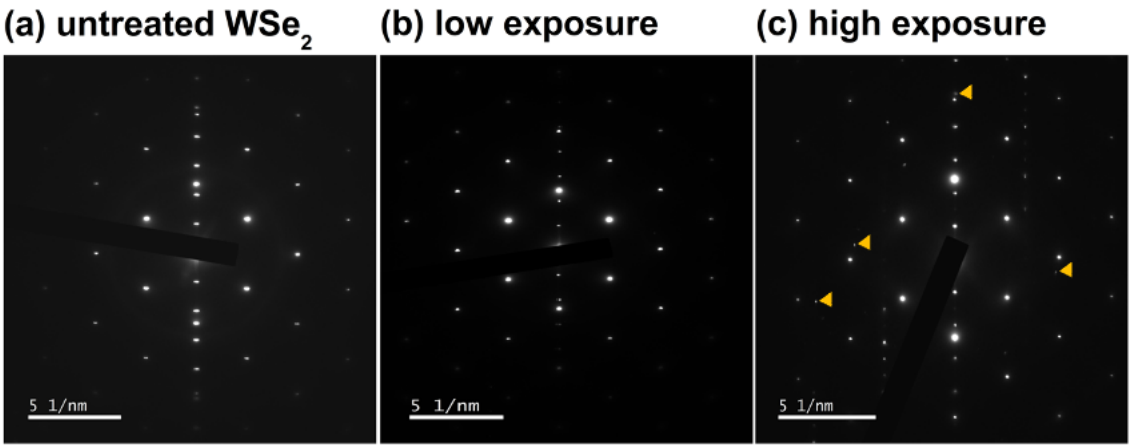

Figure 5.2.15. TEM diffraction patterns of HfO_2-on-WSe_2 samples (same samples as Figure 5.2.17). The WSe_2 underwent different amounts of UV-O_3 exposure prior to HfO_2 ALD: (a) no UV-O_3 exposure, (b) 10 min UV-O_3, and (c) 30 min UV-O_3.

The diffraction spots for Figure 5.2.15(a) and (b) correspond to the WSe_2 layers and the Si substrate. All patterns show spots consistent with the $[\bar{1}10]$ Si zone axis. The WSe_2 layer is not on zone axis for (a) and (b), but we can see diffraction from their (0002) hexagonal growth direction planes in line with the (002) Si planes. In (c), we see the growth direction WSe_2 spots as well as those resulting from the WSe_2 being oriented closer to its $[2\bar{1}\bar{1}0]$ zone axis; there are also additional weaker diffraction spots (labeled with orange triangles), which provide evidence for the onset of crystallization of the HfO_2 film deposited on high exposure WSe_2.

5.2.4.2.2 HfO_2 Film Morphology

We investigated the surface morphology of the deposited HfO_2 film using AFM. Few-layer WSe_2 flakes were exfoliated onto SiO_2 wafers, which then underwent UV-O_3 exposure and subsequent ALD of HfO_2. Consistent with our methodology for the XPS studies, all of these samples were adjacent to each other during ALD in order to ensure that they all underwent the exact same deposition conditions. Shown in Figure 5.2.16 are 2 μm × 2 μm AFM micrographs of the WSe_2 flakes on SiO_2 after HfO_2 deposition. We also show line profiles across the flake edge

to compare the uniformity of the HfO_2 film on-flake vs. off-flake (on the SiO_2 substrate). It is clear that all UV-O_3 exposed WSe_2 surfaces had a smooth and uniform HfO_2 film deposited on top, which all have nominally the same uniformity as the deposited film on bare SiO_2 (off-flake). This contrasts with the AFM image and line profile for the untreated sample, which shows non-uniformities and pinholes across the entire WSe_2 flake surface, showing incomplete HfO_2 coverage. For the untreated WSe_2, the dips in the line profile are ~5 nm deep, which was the targeted HfO_2 film thickness, so this reveals that these non-uniformities are indeed discontinuities in the film that result in exposed WSe_2 areas.

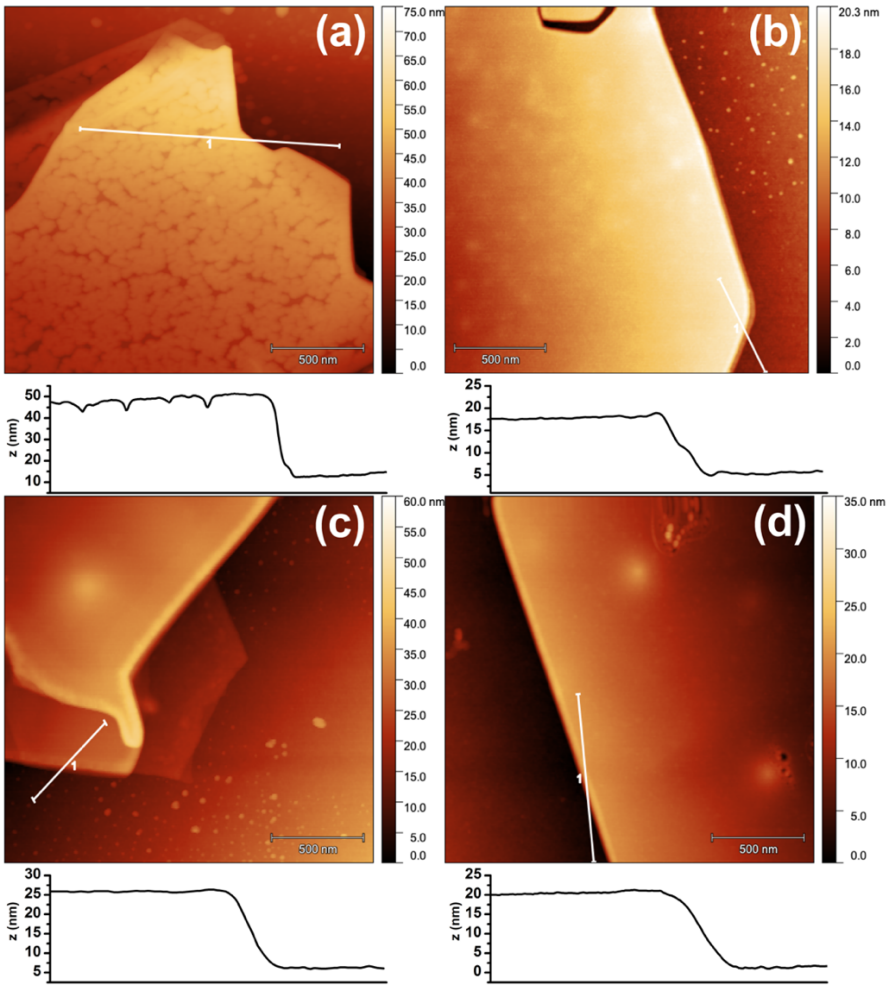

Figure 5.2.16. AFM micrographs and line profiles of ~5 nm of HfO_2 deposited on WSe_2/SiO_2. Line profiles are drawn across the WSe_2 flake edge. Prior to ALD, the WSe_2 flakes were UV-O_3 functionalized for different amounts of time: (a) control/untreated, (b) 10 min UV-O_3, (c) 17 min UV-O_3, (d) 30 min UV-O_3.

Cross-sectional TEM was also performed on an equivalent set of samples, and the micrographs are shown in Figure 5.2.17. It is evident that both low and high UV-O_3 exposures of WSe_2 resulted in a sharp interface with the deposited HfO_2 film and a uniform thickness of the HfO_2. From the micrographs collected, the average HfO_2 thickness was 5.4 $\pm$ 0.5 nm for low exposure WSe_2 and 5.4 $\pm$ 0.8 nm for high exposure WSe_2. The uniformity of HfO_2 on these functionalized WSe_2 surfaces is shown to be true across a large area, which we show up to at least 150 nm across (see Appendix E).

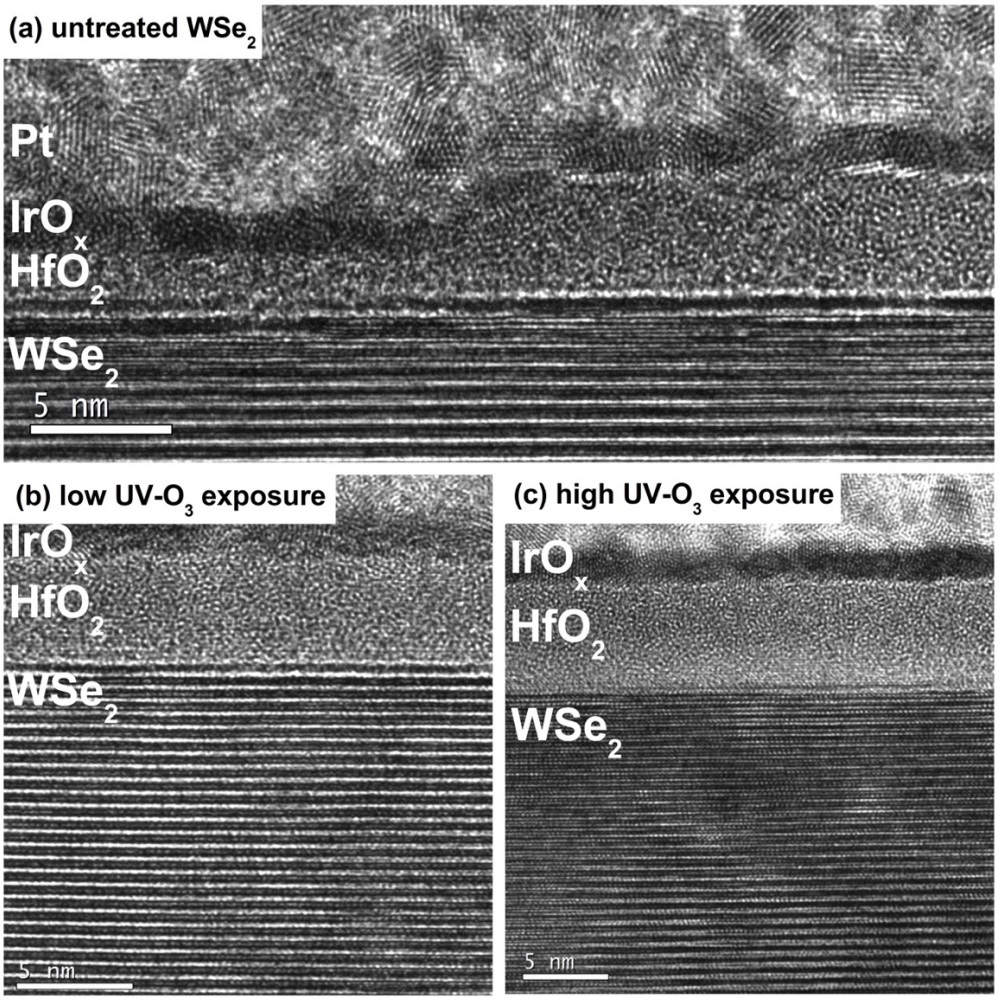

Figure 5.2.17. Cross-sectional TEM micrographs of ~5 nm of HfO_2 deposited on WSe_2 which underwent different pre-treatment conditions: (a) control/untreated, (b) 10 min UV-O_3, and (c) 30 min UV-O_3. The IrO_x layer was sputter deposited to make the surface conducting, and the Pt was deposited in the FIB as a surface protection layer.

We note that for the high exposure WSe_2 sample, the WO_3 layer which we observe with XPS (Figure 5.2.13) is not clearly distinguishable in cross-sectional TEM (Figure 5.2.17(c)). Thickness calculations using XPS indicate that this interfacial WO_3 layer between high exposure WSe_2 and HfO_2 is only 4.8 Å thick. We note that this thin layer is difficult to distinguish in the cross-sectional TEM micrograph because at the interface, the image is an average of the WSe_2, WO_3, and HfO_2 layers. The amorphous nature of both the WO_3 and HfO_2 layers make them difficult to differentiate from each other, and in addition, the contrast from the highly ordered nature of the WSe_2 overwhelms the signal at the interface. Nonetheless, consistent with the AFM micrographs, TEM shows that this WO_3 layer on the high exposure WSe_2 surface promotes smooth and uniform ALD of HfO_2.

For HfO_2 deposited on untreated WSe_2, the roughness and non-uniformity of the ALD HfO_2 is evident in Figure 5.2.17(a). The IrO_x layer was deposited to make the surface conductive, and we note that the IrO_x deposition was performed before any other processing steps for TEM sample preparation. Thus, we know that the IrO_x layer conforms to the true surface of the HfO_2 layer. Figure 5.2.17(a) clearly shows the roughness of the HfO_2 film deposited on untreated WSe_2, which is apparent based on the roughness of the IrO_x layer on top. This roughness of the HfO_2 is shown to be true across a large area (at least 180 nm) in the micrographs of the same sample shown in Figure 5.2.18(b). Additionally, in Figure 5.2.18(a), we also show evidence that the interface between the HfO_2 and the untreated WSe_2 is not sharp, unlike that shown for HfO_2 on UV-O_3 functionalized WSe_2.

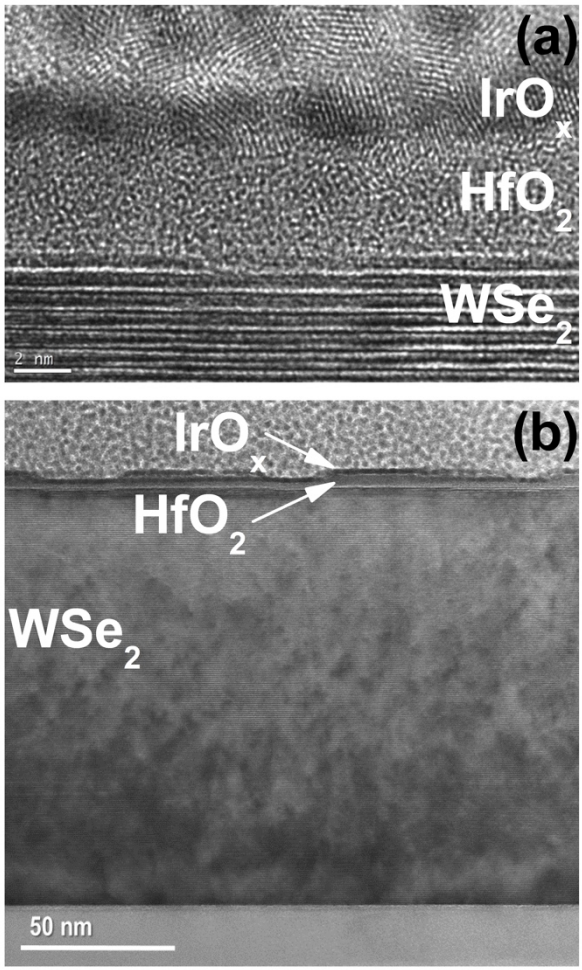

Figure 5.2.18. Cross-sectional TEM of ALD HfO_2 deposited on untreated WSe_2. (a) Smaller field of view micrograph showing that the HfO_2/WSe_2 interface has some roughness associated with it. (b) Larger field of view micrograph demonstrating the non-uniformity of the HfO_2 film across a large area of at least 180 nm.

These observations from TEM agree with our findings from AFM. The top-down AFM image for HfO_2 on untreated WSe_2 (Figure 5.2.16(a)) reveals random discontinuities in the dielectric film across the entire surface over the 4 μm^2 area. We note that based on Figure 5.2.16(a), the widest discontinuities are in the order of tens of nm in width, and since cross-sectional TEM micrographs show an average along the beam direction (along ~100 nm of sample thickness), we never see areas with complete absence of HfO_2 in our TEM analyses. Instead, this discontinuous film morphology, when averaged along the beam direction, manifests itself as a rough layer, as we

see in Figure 5.2.17(a) and Figure 5.2.18. We caveat this statement with a reminder that the field of view allowed by TEM is substantially smaller than AFM.

Discontinuities in the ALD oxide film will present leakage issues when used as a dielectric layer in a device. Our investigations of the HfO_2 film morphology (through AFM and TEM) show us that WSe_2 processing using atmospheric UV-O_3 is an avenue for achieving uniform oxide films deposited by ALD on WSe_2. Additionally, we present two different routes for achieving a uniform ALD oxide film on WSe_2, depending on the desired interfacial properties between the WSe_2 and the oxide film. Low UV-O_3 exposures will result in a direct interface between WSe_2 and HfO_2, while high exposures will provide an interfacial WO_3 layer. The HfO_2-on-WO_3 stack, i.e., the high exposure interface, has been used in metal oxide-based electro-chemical random-access memory [112] and protonic programmable resistor devices [113]. Our atmospheric UV-O_3 exposure technique thus provides unique flexibility in device design and pathways for the realization of various electronic and memory devices.

5.2.4.3 Electrical Characterization

We investigated the impact of the extent of UV-O_3 functionalization on the electrical properties of WSe_2 via the fabrication and characterization of field-effect transistors (FETs) using multilayer WSe_2 as the semiconducting channel. Initial FETs (Figure 5.2.19(a)) were fabricated using Bi/Au contacts and were tested after drain/source metal deposition without exposure to UV-O_3 or ALD (back-gated), and after top-gate metal (Ni/Au) deposition following UV-O_3 exposure and ALD of HfO_2 (top-gated). UV-O_3 exposure times prior to ALD of HfO_2 were varied. We fabricated untreated (0 min UV-O_3), low exposure (10 min UV-O_3), and high exposure (30 min UV-O_3) WSe_2 FETs. As seen in Figure 5.2.19(b), without any UV-O_3 exposure, the I_{DS}-V_{GS} curves (back- and top-gated) demonstrated predominantly n-type conduction with an on/off ratio greater than 10^6. Additionally, linear I_{DS}-V_{DS} behavior (Figure 5.2.20(a)) was exhibited without any UV-O_3 exposure. However, with UV-O_3 exposure, the I_{DS}-V_{GS} characteristics change to show p-type conduction and a reduced on/off ratio (Figure 5.2.19(b)), along with a nonlinear I_{DS}-V_{DS} relationship (Figure 5.2.20(b)).

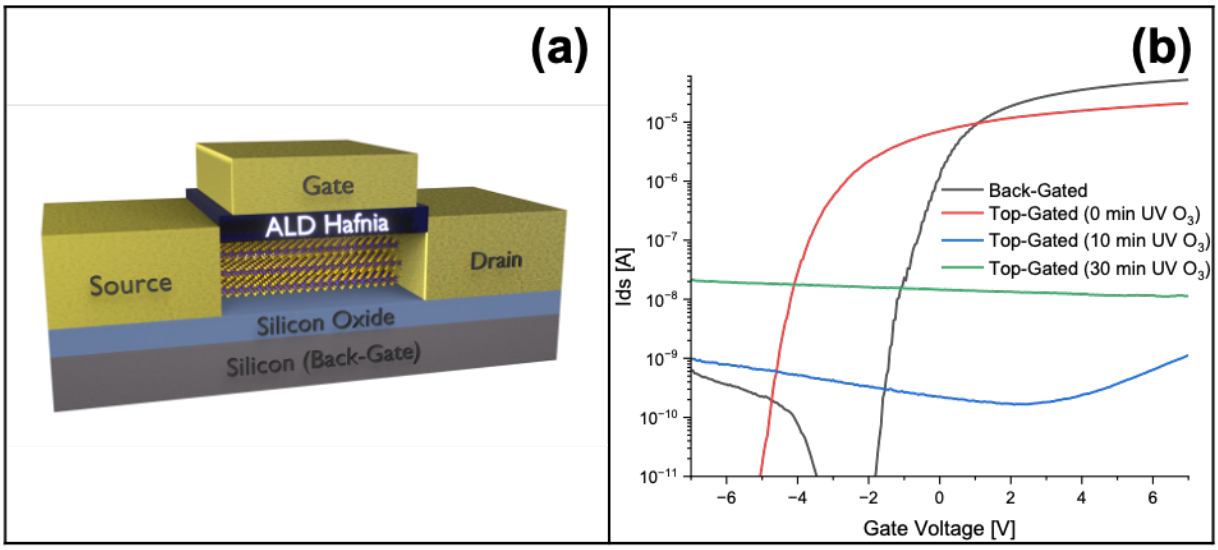

Figure 5.2.19. (a) Schematic of FETs fabricated with WSe_2 exposed to varying UV-O_3 treatment times prior to HfO_2 ALD. (b) Measured back-gated and top-gated I_{DS} vs. V_{GS} curves at a V_{DS} of 100 mV.

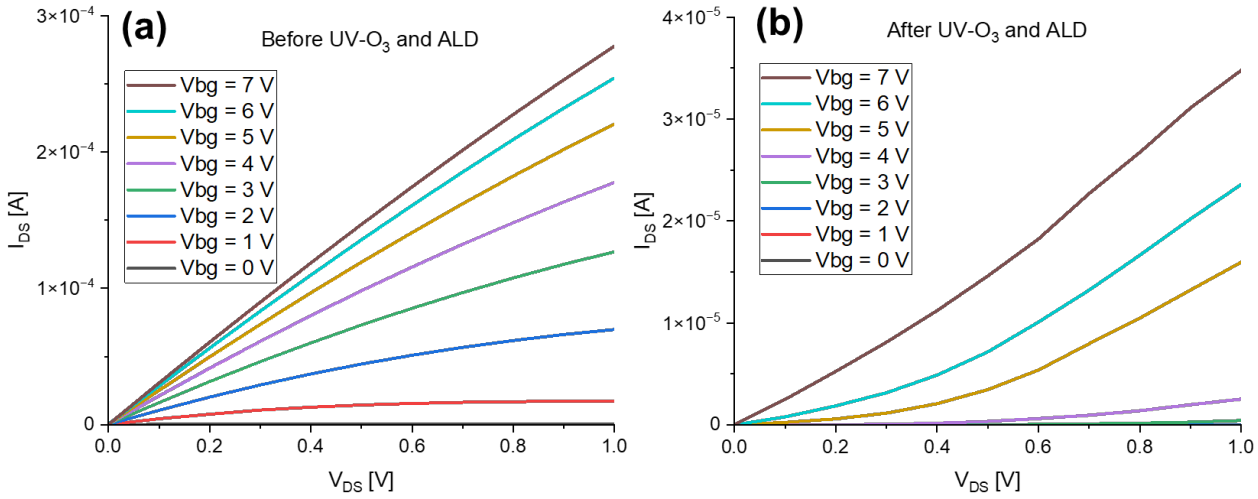

Figure 5.2.20. Example back-gated I_{DS}-V_{DS} curves for a device with Bi/Au contacts (a) before and (b) after a 10-minute UV-O_3 exposure and HfO_2 deposition, highlighting the change in low-field conduction from linear I_{DS}-V_{DS} behavior to a non-linear relationship.

This agrees with results in the literature [114-116], however, those studies did not investigate the role of seeding an ALD dielectric or top-gated FET performance. To achieve large on/off ratios, either selective doping of only the contact region [114, 117] or removing the layer exposed to UV-O_3 with an etching process [115] was performed.

Since our AFM data show improved HfO_2 nucleation with increased UV-O_3 exposure, there may be a fundamental trade-off between dielectric scalability and electrical performance of the FET. Given the Schottky I_{DS}-V_{DS} behavior and p-type transfer curve, we changed our contact metal to Pd/Au. More UV-O_3 exposure times (0, 5, 7.5, 10, and 30 min) were investigated, along with a thinner HfO_2 layer (10 nm) to explore the potential trade-off described above.

A trend in gate leakage, consistent with our AFM results, was observed as every device with exposure times of 0 or 5 min leaked and every device with 10 or 30 min of UV-O_3 exposure could withstand +/- 2 V on the gate (Figure 5.2.21). However, although the switch to Pd/Au contacts increased the current measured in the p-type FETs, poor switching behavior was generally observed in devices that did not suffer from gate leakage. This implies that selection of UV-O_3 exposure time alone may not resolve the issue of low on/off ratios, prompting additional study into treatments such as annealing [118]. Nucleating HfO_2 ALD on WSe_2 via UV-O_3 without degrading the top-gated semiconducting characteristics is an area for further exploration.

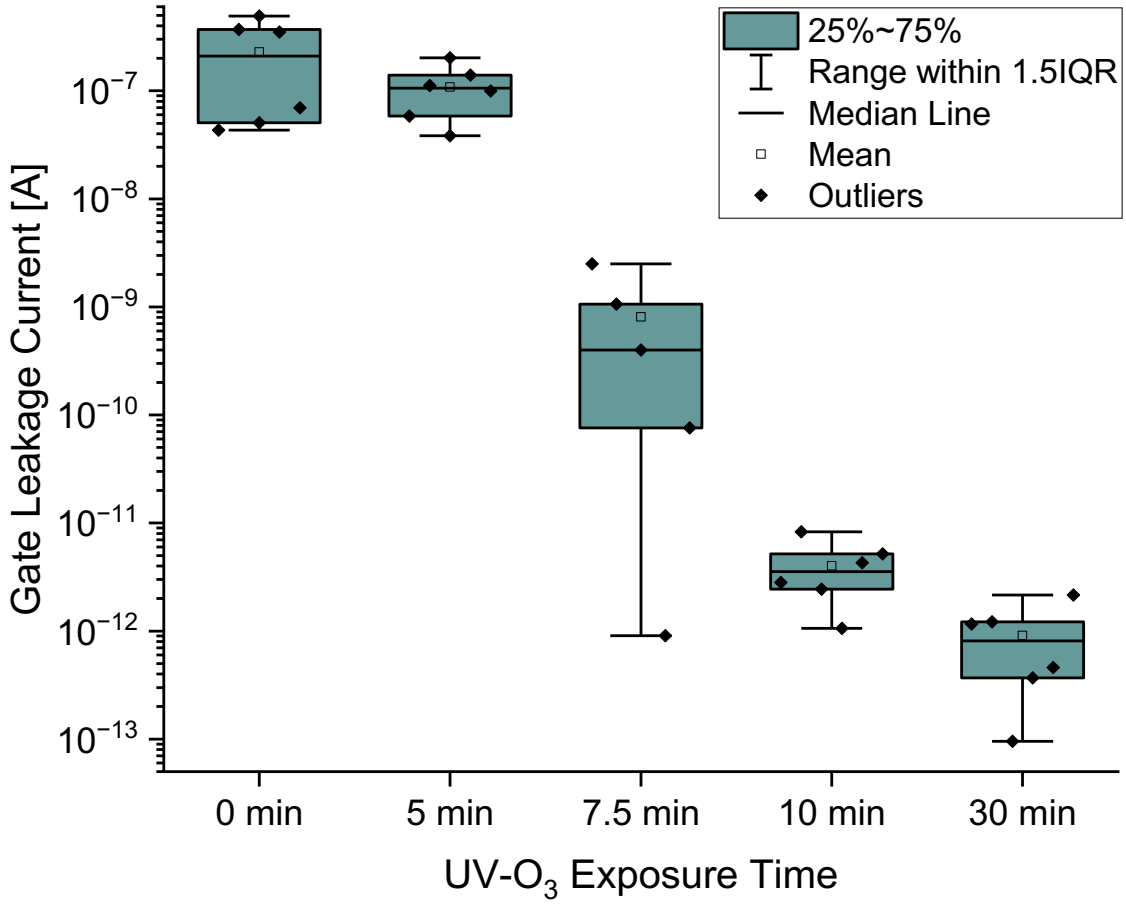

Figure 5.2.21. Maximum gate current measured within the V_{GS} range of +/- 0.5 V.

Prior work on the fabrication of top-gated MoS_2 FETs using UV-O_3 functionalization have had success with achieving low leakage currents at scaled dielectric thicknesses (at least 6 nm) and linear I_{DS}-V_{DS} curves [119]. Zhao et al. demonstrated that the high-κ/MoS_2 interface was highly improved, and the devices exhibited ultralow gate leakage and excellent on/off ratio when UV-O_3 functionalization was performed in-situ on few-layer MoS_2 [47] as opposed to ex-situ on bulk MoS_2 [45]. Additionally, Zhao et al. [120] and Bolshakov et al. [46] showed improved dielectric leakage, I-V hysteresis, and interface trap density of the high-κ interfaces by annealing the devices in UHV and in forming gas. For future applicability of UV-O_3 functionalization of WSe_2 in FETs, some of these techniques that have been used to improve the performance of top-gated UV-O_3 treated MoS_2 may be adapted for improved WSe_2 FET performance.

5.2.5 Conclusions

In this work, we demonstrated the effects of atmospheric exposure of WSe_2 to UV-O_3. Based on XPS results, with low exposure times, we observe an onset of WSe_2 doping without formation of any tungsten or selenium oxide. Higher exposure times result in the formation of a top layer of tungsten oxyselenide and more heavily p-doped WSe_2 underneath. We found that this tungsten oxyselenide layer has a thickness saturation, is non-crystalline, is stable in ambient, but is unstable at the ALD deposition temperature of 200 °C.

We found that after ALD of HfO_2 on these functionalized WSe_2 surfaces, low exposure WSe_2 remained unoxidized, but the WSe_2 changed from having two doping states (following UV-O_3 exposure), to only one after ALD was performed. In contrast, after ALD on high exposure WSe_2, there was an interfacial WO_3 layer between the WSe_2 and the deposited HfO_2 film. For high exposures, the WSe_2 also appeared to retain the two doping states that were induced by the UV-O_3 exposure – two WSe_2 components with a binding energy difference of 0.4 eV in XPS. We found that high exposure WSe_2 resulted in a higher degree of order in the HfO_2 film compared to low exposure WSe_2. Lastly, we note that ALD HfO_2 deposited on both low and high exposure WSe_2 resulted in a smooth and uniform film free of discontinuities. We demonstrate the feasibility of using our atmospheric UV-O_3 functionalization technique as a way to directly deposit oxide films on WSe_2 through ALD. Additionally, the different exposure times allow for tunability of the

interface chemistry between WSe_2 and HfO_2, providing unique flexibility in the design and fabrication of WSe_2-based devices. However, to fabricate top-gated WSe_2 FETs with good switching behavior, further process optimization using the UV-O_3 functionalization technique is required.

5.3 Chapter 5 References

[1] D. J. Late, B. Liu, H. S. S. R. Matte, V. P. Dravid, and C. N. R. Rao, "Hysteresis in Single-Layer MoS_2 Field Effect Transistors," *ACS Nano,* vol. 6, no. 6, pp. 5635-5641, 2012/06/26 2012, doi: 10.1021/nn301572c.

[2] D. Kufer and G. Konstantatos, "Highly Sensitive, Encapsulated MoS_2 Photodetector with Gate Controllable Gain and Speed," *Nano Letters,* vol. 15, no. 11, pp. 7307-7313, 2015/11/11 2015, doi: 10.1021/acs.nanolett.5b02559.

[3] J. Gao, B. Li, J. Tan, P. Chow, T.-M. Lu, and N. Koratkar, "Aging of Transition Metal Dichalcogenide Monolayers," *ACS Nano,* vol. 10, no. 2, pp. 2628-2635, 2016/02/23 2016, doi: 10.1021/acsnano.5b07677.

[4] M. Si *et al.*, "A ferroelectric semiconductor field-effect transistor," *Nature Electronics,* vol. 2, no. 12, pp. 580-586, 2019/12/01 2019, doi: 10.1038/s41928-019-0338-7.

[5] J. F. Scott and C. A. Paz de Araujo, "Ferroelectric Memories," *Science,* vol. 246, no. 4936, p. 1400, 1989, doi: 10.1126/science.246.4936.1400.

[6] J. F. Ihlefeld, D. T. Harris, R. Keech, J. L. Jones, J.-P. Maria, and S. Trolier-McKinstry, "Scaling Effects in Perovskite Ferroelectrics: Fundamental Limits and Process-Structure-Property Relations," *Journal of the American Ceramic Society,* vol. 99, no. 8, pp. 2537-2557, 2016/08/01 2016, doi: 10.1111/jace.14387.

[7] K. R. Udayakumar *et al.*, "Manufacturable High-Density 8 Mbit One Transistor–One Capacitor Embedded Ferroelectric Random Access Memory," *Japanese Journal of Applied Physics,* vol. 47, no. 4, pp. 2710-2713, 2008/04/25 2008, doi: 10.1143/jjap.47.2710.

[8] T. S. Böscke, J. Müller, D. Bräuhaus, U. Schröder, and U. Böttger, "Ferroelectricity in hafnium oxide thin films," *Applied Physics Letters,* vol. 99, no. 10, p. 102903, 2011/09/05 2011, doi: 10.1063/1.3634052.

[9] S. Mueller, S. R. Summerfelt, J. Muller, U. Schroeder, and T. Mikolajick, "Ten-Nanometer Ferroelectric Si:HfO_2 Films for Next-Generation FRAM Capacitors," *IEEE Electron Device Letters,* vol. 33, no. 9, pp. 1300-1302, 2012, doi: 10.1109/LED.2012.2204856.

[10] H. Mulaosmanovic *et al.*, "Switching Kinetics in Nanoscale Hafnium Oxide Based Ferroelectric Field-Effect Transistors," *ACS Applied Materials & Interfaces,* vol. 9, no. 4, pp. 3792-3798, 2017/02/01 2017, doi: 10.1021/acsami.6b13866.

[11] H. Mulaosmanovic, T. Mikolajick, and S. Slesazeck, "Accumulative Polarization Reversal in Nanoscale Ferroelectric Transistors," *ACS Applied Materials & Interfaces,* vol. 10, no. 28, pp. 23997-24002, 2018/07/18 2018, doi: 10.1021/acsami.8b08967.

[12] F. A. McGuire *et al.*, "Sustained Sub-60 mV/decade Switching via the Negative Capacitance Effect in MoS_2 Transistors," *Nano Lett.,* vol. 17, no. 8, pp. 4801-4806, 2017/08/09 2017, doi: 10.1021/acs.nanolett.7b01584.

[13] M. Si, C. Jiang, W. Chung, Y. Du, M. A. Alam, and P. D. Ye, "Steep-Slope WSe_2 Negative Capacitance Field-Effect Transistor," *Nano Letters,* vol. 18, no. 6, pp. 3682-3687, 2018/06/13 2018, doi: 10.1021/acs.nanolett.8b00816.

[14] X. Sang, E. D. Grimley, T. Schenk, U. Schroeder, and J. M. LeBeau, "On the structural origins of ferroelectricity in HfO_2 thin films," *Applied Physics Letters,* vol. 106, no. 16, p. 162905, 2015/04/20 2015, doi: 10.1063/1.4919135.

[15] H. J. Kim *et al.*, "Grain size engineering for ferroelectric $Hf_{0.5}Zr_{0.5}O_2$ films by an insertion of Al_2O_3 interlayer," *Applied Physics Letters,* vol. 105, no. 19, p. 192903, 2014/11/10 2014, doi: 10.1063/1.4902072.

[16] C. Künneth, R. Materlik, and A. Kersch, "Modeling ferroelectric film properties and size effects from tetragonal interlayer in $Hf_{1-x}Zr_xO_2$ grains," *Journal of Applied Physics,* vol. 121, no. 20, p. 205304, 2017/05/28 2017, doi: 10.1063/1.4983811.

[17] T. Shiraishi *et al.*, "Impact of mechanical stress on ferroelectricity in $(Hf_{0.5}Zr_{0.5})O_2$ thin films," *Applied Physics Letters,* vol. 108, no. 26, p. 262904, 2016/06/27 2016, doi: 10.1063/1.4954942.

[18] S. J. Kim *et al.*, "Large ferroelectric polarization of $TiN/Hf_{0.5}Zr_{0.5}O_2/TiN$ capacitors due to stress-induced crystallization at low thermal budget," *Applied Physics Letters,* vol. 111, no. 24, p. 242901, 2017/12/11 2017, doi: 10.1063/1.4995619.

[19] S. J. Kim *et al.*, "Stress-Induced Crystallization of Thin $Hf_{1-X}Zr_XO_2$ Films: The Origin of Enhanced Energy Density with Minimized Energy Loss for Lead-Free Electrostatic Energy Storage Applications," *ACS Applied Materials & Interfaces,* vol. 11, no. 5, pp. 5208-5214, 2019/02/06 2019, doi: 10.1021/acsami.8b17211.

[20] E. D. Grimley *et al.*, "Structural Changes Underlying Field-Cycling Phenomena in Ferroelectric HfO_2 Thin Films," *Advanced Electronic Materials,* vol. 2, no. 9, p. 1600173, 2016/09/01 2016, doi: 10.1002/aelm.201600173.

[21] S. Starschich, S. Menzel, and U. Böttger, "Pulse wake-up and breakdown investigation of ferroelectric yttrium doped HfO_2," *Journal of Applied Physics,* vol. 121, no. 15, p. 154102, 2017/04/21 2017, doi: 10.1063/1.4981893.

[22] S. Mueller *et al.*, "Incipient Ferroelectricity in Al-Doped HfO_2 Thin Films," *Advanced Functional Materials,* vol. 22, no. 11, pp. 2412-2417, 2012/06/06 2012, doi: 10.1002/adfm.201103119.

[23] J. Müller *et al.*, "Ferroelectricity in Simple Binary ZrO_2 and HfO_2," *Nano Lett.,* vol. 12, no. 8, pp. 4318-4323, 2012/08/08 2012, doi: 10.1021/nl302049k.

[24] J. Müller *et al.*, "Ferroelectricity in yttrium-doped hafnium oxide," *Journal of Applied Physics,* vol. 110, no. 11, p. 114113, 2011/12/01 2011, doi: 10.1063/1.3667205.

[25] S. Mueller, C. Adelmann, A. Singh, S. Van Elshocht, U. Schroeder, and T. Mikolajick, "Ferroelectricity in Gd-Doped HfO_2 Thin Films," *ECS Journal of Solid State Science and Technology,* vol. 1, no. 6, pp. N123-N126, 2012, doi: 10.1149/2.002301jss.

[26] H. Yu *et al.*, "Flexible Inorganic Ferroelectric Thin Films for Nonvolatile Memory Devices," *Adv. Funct. Mater.,* vol. 27, no. 21, p. 1700461, 2017, doi: 10.1002/adfm.201700461.

[27] M. Hyuk Park, H. Joon Kim, Y. Jin Kim, W. Lee, H. Kyeom Kim, and C. Seong Hwang, "Effect of forming gas annealing on the ferroelectric properties of $Hf_{0.5}Zr_{0.5}O_2$ thin films with and without Pt electrodes," *Applied Physics Letters,* vol. 102, no. 11, p. 112914, 2013/03/18 2013, doi: 10.1063/1.4798265.

[28] A. Lipatov, P. Sharma, A. Gruverman, and A. Sinitskii, "Optoelectrical Molybdenum Disulfide (MoS_2)—Ferroelectric Memories," *ACS Nano,* vol. 9, no. 8, pp. 8089-8098, 2015/08/25 2015, doi: 10.1021/acsnano.5b02078.

[29] C. H. Li, K. M. McCreary, and B. T. Jonker, "Spatial Control of Photoluminescence at Room Temperature by Ferroelectric Domains in Monolayer WS_2/PZT Hybrid Structures," *ACS Omega,* vol. 1, no. 6, pp. 1075-1080, 2016/12/31 2016, doi: 10.1021/acsomega.6b00302.

[30] J. P. B. Silva, C. Almeida Marques, J. A. Moreira, and O. Conde, "Resistive switching in $MoSe_2/BaTiO_3$ hybrid structures," *Journal of Materials Chemistry C,* 10.1039/C7TC03024J vol. 5, no. 39, pp. 10353-10359, 2017, doi: 10.1039/C7TC03024J.

[31] H. S. Lee *et al.*, "MoS_2 Nanosheets for Top-Gate Nonvolatile Memory Transistor Channel," *Small,* vol. 8, no. 20, pp. 3111-3115, 2012/10/22 2012, doi: 10.1002/smll.201200752.

[32] E. Preciado *et al.*, "Scalable fabrication of a hybrid field-effect and acousto-electric device by direct growth of monolayer $MoS_2/LiNbO_3$," *Nature Communications,* Article vol. 6, p. 8593, 10/23/online 2015, doi: 10.1038/ncomms9593.

[33] I. P. Batra, P. Wurfel, and B. D. Silverman, "Depolarization Field and Stability Considerations in Thin Ferroelectric Films," *Journal of Vacuum Science and Technology,* vol. 10, no. 5, pp. 687-692, 1973/09/01 1973, doi: 10.1116/1.1318414.

[34] H. Ishiwara, "Recent progress of FET-type ferroelectric memories," *Integrated Ferroelectrics,* vol. 34, no. 1-4, pp. 11-20, 2001/02/01 2001, doi: 10.1080/10584580108012869.

[35] H. Ishiwara, "Current status and prospects of FET-type ferroelectric memories," *Journal of Semiconductor Technology and Science,* vol. 1, no. 1, pp. 1-14, 2001, doi: 10.1109/IEDM.2001.979615.

[36] M. Hyuk Park, H. Joon Kim, Y. Jin Kim, W. Lee, T. Moon, and C. Seong Hwang, "Evolution of phases and ferroelectric properties of thin $Hf_{0.5}Zr_{0.5}O_2$ films according to the thickness and annealing temperature," *Applied Physics Letters,* vol. 102, no. 24, p. 242905, 2013/06/17 2013, doi: 10.1063/1.4811483.

[37] D. S. Macintyre, O. Ignatova, S. Thoms, and I. G. Thayne, "Resist residues and transistor gate fabrication," *Journal of Vacuum Science & Technology B: Microelectronics and Nanometer Structures Processing, Measurement, and Phenomena,* vol. 27, no. 6, pp. 2597-2601, 2009/11/01 2009, doi: 10.1116/1.3243176.

[38] A. Pirkle *et al.*, "The effect of chemical residues on the physical and electrical properties of chemical vapor deposited graphene transferred to SiO_2," (in English), *Appl. Phys. Lett.,* vol. 99, no. 12, p. 122108, Sep 19 2011, doi: Artn 122108 Doi 10.1063/1.3643444.

[39] Y.-C. Lin, C.-C. Lu, C.-H. Yeh, C. Jin, K. Suenaga, and P.-W. Chiu, "Graphene Annealing: How Clean Can It Be?," *Nano Letters,* vol. 12, no. 1, pp. 414-419, 2012/01/11 2012, doi: 10.1021/nl203733r.

[40] R. Li *et al.*, "Determination of PMMA Residues on a Chemical-Vapor-Deposited Monolayer of Graphene by Neutron Reflection and Atomic Force Microscopy," *Langmuir,* vol. 34, no. 5, pp. 1827-1833, 2018/02/06 2018, doi: 10.1021/acs.langmuir.7b03117.

[41] K. M. Freedy *et al.*, "MoS_2 cleaning by acetone and UV-ozone: Geological and synthetic material," *Applied Surface Science,* vol. 478, pp. 183-188, 2019, doi: 10.1016/J.APSUSC.2019.01.222.

[42] "SPI Supplies." https://www.2spi.com/ (accessed.

[43] A. Azcatl *et al.*, "MoS_2 functionalization for ultra-thin atomic layer deposited dielectrics," *Applied Physics Letters,* vol. 104, no. 11, p. 111601, 2014/03/17 2014, doi: 10.1063/1.4869149.

[44] A. Azcatl *et al.*, "HfO_2 on UV–O_3 exposed transition metal dichalcogenides: interfacial reactions study," *2D Materials,* vol. 2, no. 1, p. 014004, 2015/01/13 2015, doi: 10.1088/2053-1583/2/1/014004.

[45] P. Zhao *et al.*, "Electrical characterization of top-gated molybdenum disulfide metal–oxide–semiconductor capacitors with high-k dielectrics," *Microelectronic Engineering,* vol. 147, pp. 151-154, 2015/11/01/ 2015, doi: https://doi.org/10.1016/j.mee.2015.04.078.

[46] P. Bolshakov, P. Zhao, A. Azcatl, P. K. Hurley, R. M. Wallace, and C. D. Young, "Electrical characterization of top-gated molybdenum disulfide field-effect-transistors with high-k dielectrics," *Microelectronic Engineering,* vol. 178, pp. 190-193, 2017/06/25/ 2017, doi: https://doi.org/10.1016/j.mee.2017.04.045.

[47] P. Zhao *et al.*, "Probing Interface Defects in Top-Gated MoS_2 Transistors with Impedance Spectroscopy," *ACS Applied Materials & Interfaces,* vol. 9, no. 28, pp. 24348-24356, 2017/07/19 2017, doi: 10.1021/acsami.7b06204.

[48] K. M. Freedy, P. M. Litwin, and S. J. McDonnell, "(Invited) In-Vacuo Studies of Transition Metal Dichalcogenide Synthesis and Layered Material Integration," (in en), *ECS Transactions,* vol. 77, no. 8, pp. 11-25, 2017-05-03 2017, doi: 10.1149/07708.0011ecst.

[49] H. Yamamoto, K. Yoshii, K. Saiki, and A. Koma, "Improved heteroepitaxial growth of layered $NbSe_2$ on GaAs (111)B," *Journal of Vacuum Science & Technology A,* vol. 12, no. 1, pp. 125-129, 1994/01/01 1994, doi: 10.1116/1.578906.

[50] L. A. Walsh *et al.*, "WTe_2 thin films grown by beam-interrupted molecular beam epitaxy," *2D Materials,* vol. 4, no. 2, p. 025044, 2017/03/08 2017, doi: 10.1088/2053-1583/aa61e1.

[51] M. Nakano, Y. Wang, Y. Kashiwabara, H. Matsuoka, and Y. Iwasa, "Layer-by-Layer Epitaxial Growth of Scalable WSe_2 on Sapphire by Molecular Beam Epitaxy," *Nano Letters,* vol. 17, no. 9, pp. 5595-5599, 2017/09/13 2017, doi: 10.1021/acs.nanolett.7b02420.

[52] X. Zhang *et al.*, "Diffusion-Controlled Epitaxy of Large Area Coalesced WSe_2 Monolayers on Sapphire," *Nano Letters,* vol. 18, no. 2, pp. 1049-1056, 2018/02/14 2018, doi: 10.1021/acs.nanolett.7b04521.

[53] G. Delie, P. M. Litwin, S. J. McDonnell, D. Chiappe, M. Houssa, and V. V. Afanas'ev, "Energy Band Alignment of Few-Monolayer WS2 and WSe2 with SiO2 UsingInternal Photoemission Spectroscopy," *ECS Journal of Solid State Science and Technology,* 2020.

[54] W. H. Blades, N. J. Frady, P. M. Litwin, S. J. McDonnell, and P. Reinke, "Thermally Induced Defects on WSe2," *The Journal of Physical Chemistry C,* vol. 124, no. 28, pp. 15337-15346, 2020.

[55] P. M. Litwin, M. G. Sales, V. Nilsson, P. V. Balachandran, C. Constantin, and S. McDonnell, "The effect of growth temperature and metal-to-chalcogen on the growth of WSe2 by molecular beam epitaxy," in *Low-Dimensional Materials and Devices 2019*, 2019, vol. 11085: International Society for Optics and Photonics, p. 110850U.

[56] *Standard Practice for Calibration of the Electron Binding-Energy Scale of an X-Ray Photoelectron Spectrometer*, A. International, West Conshohocken, PA, 2016.

[57] "Kolibrik.net, s.r.o. - Custom develompent of electronics and software." http://www.kolibrik.net/ (accessed.

[58] S. McDonnell *et al.*, "HfO_2 on MoS_2 by Atomic Layer Deposition: Adsorption Mechanisms and Thickness Scalability," *ACS Nano,* vol. 7, no. 11, pp. 10354-10361, 2013/11/26 2013, doi: 10.1021/nn404775u.

[59] V. V. Afanas'ev *et al.*, "Band alignment at interfaces of few-monolayer MoS_2 with SiO_2 and HfO_2," *Microelectronic Engineering,* vol. 147, pp. 294-297, 2015/11/01/ 2015, doi: https://doi.org/10.1016/j.mee.2015.04.106.

[60] K. M. Price and A. D. Franklin, "Integration of 3.4 nm HfO_2 into the gate stack of MoS_2 and WSe_2 top-gate field-effect transistors," in *2017 75th Annual Device Research Conference (DRC)*, 25-28 June 2017 2017, pp. 1-2, doi: 10.1109/DRC.2017.7999405.

[61] S. K. Pradhan, B. Xiao, and A. K. Pradhan, "Energy band alignment of high-k oxide heterostructures at MoS_2/Al_2O_3 and MoS_2/ZrO_2 interfaces," *Journal of Applied Physics,* vol. 120, no. 12, p. 125305, 2016/09/28 2016, doi: 10.1063/1.4963289.

[62] S. J. McDonnell and R. M. Wallace, "UV-Ozone Functionalization of 2D Materials," *JOM,* vol. 71, no. 1, pp. 224-237, 2019/01/01 2019, doi: 10.1007/s11837-018-3156-x.

[63] K. M. Freedy *et al.*, "Interface chemistry and thermoelectric characterization of Ti and TiO_x Contacts to MBE-Grown WSe_2," *2D Materials,* 2020, doi: https://doi.org/10.1088/2053-1583/ab834b.

[64] W. Chen *et al.*, "Growth and Thermo-driven Crystalline Phase Transition of Metastable Monolayer 1T′-WSe_2 Thin Film," *Scientific Reports,* vol. 9, no. 1, p. 2685, 2019/02/25 2019, doi: 10.1038/s41598-019-39238-7.

[65] C. C. Fulton, G. Lucovsky, and R. J. Nemanich, "Process-dependent band structure changes of transition-metal (Ti,Zr,Hf) oxides on Si (100)," *Applied Physics Letters,* vol. 84, no. 4, pp. 580-582, 2004/01/26 2004, doi: 10.1063/1.1639944.

[66] C. C. Fulton, T. E. Cook, G. Lucovsky, and R. J. Nemanich, "Interface instabilities and electronic properties of ZrO_2 on silicon (100)," *Journal of Applied Physics,* vol. 96, no. 5, pp. 2665-2673, 2004/09/01 2004, doi: 10.1063/1.1776313.

[67] D. Lim and R. Haight, "Temperature dependent defect formation and charging in hafnium oxides and silicates," *Journal of Vacuum Science & Technology B: Microelectronics and Nanometer Structures Processing, Measurement, and Phenomena,* vol. 23, no. 1, pp. 201-205, 2005/01/01 2005, doi: 10.1116/1.1850105.

[68] K. Xiong, J. Robertson, M. C. Gibson, and S. J. Clark, "Defect energy levels in HfO_2 high-dielectric-constant gate oxide," *Applied Physics Letters,* vol. 87, no. 18, p. 183505, 2005/10/31 2005, doi: 10.1063/1.2119425.

[69] J. Robertson, K. Xiong, and S. J. Clark, "Band gaps and defect levels in functional oxides," *Thin Solid Films,* vol. 496, no. 1, pp. 1-7, 2006/02/01/ 2006, doi: https://doi.org/10.1016/j.tsf.2005.08.175.

[70] M. K. Yang, G. H. Kim, H. Ju, J.-K. Lee, and H.-C. Ryu, "An analysis of “non-lattice” oxygen concentration effect on electrical endurance characteristic in resistive switching MnO_x thin film," *Applied Physics Letters,* vol. 106, no. 5, p. 053504, 2015/02/02 2015, doi: 10.1063/1.4907704.

[71] M. K. Yang, J.-W. Park, T. K. Ko, and J.-K. Lee, "Bipolar resistive switching behavior in Ti/MnO_2/Pt structure for nonvolatile memory devices," *Applied Physics Letters,* vol. 95, no. 4, p. 042105, 2009/07/27 2009, doi: 10.1063/1.3191674.

[72] M. Sowinska *et al.*, "Hard x-ray photoelectron spectroscopy study of the electroforming in Ti/HfO_2-based resistive switching structures," *Applied Physics Letters,* vol. 100, no. 23, p. 233509, 2012/06/04 2012, doi: 10.1063/1.4728118.

[73] M. H. Park *et al.*, "A comprehensive study on the structural evolution of HfO_2 thin films doped with various dopants," *Journal of Materials Chemistry C,* 10.1039/C7TC01200D vol. 5, no. 19, pp. 4677-4690, 2017, doi: 10.1039/C7TC01200D.

[74] T. Bertaud *et al.*, "In-operando and non-destructive analysis of the resistive switching in the Ti/HfO_2/TiN-based system by hard x-ray photoelectron spectroscopy," *Applied Physics Letters,* vol. 101, no. 14, p. 143501, 2012/10/01 2012, doi: 10.1063/1.4756897.

[75] H. A. Hsain, Y. Lee, G. Parsons, and J. L. Jones, "Compositional dependence of crystallization temperatures and phase evolution in hafnia-zirconia (Hf_xZr_{1-x})O_2 thin films," *Applied Physics Letters,* vol. 116, no. 19, p. 192901, 2020/05/11 2020, doi: 10.1063/5.0002835.

[76] D. Xiao, G.-B. Liu, W. Feng, X. Xu, and W. Yao, "Coupled Spin and Valley Physics in Monolayers of MoS_2 and Other Group-VI Dichalcogenides," *Physical Review Letters,* vol. 108, no. 19, p. 196802, 05/07/ 2012, doi: 10.1103/PhysRevLett.108.196802.

[77] H. Yuan *et al.*, "Zeeman-type spin splitting controlled by an electric field," *Nature Physics,* vol. 9, no. 9, pp. 563-569, 2013/09/01 2013, doi: 10.1038/nphys2691.

[78] F. Withers *et al.*, "WSe_2 Light-Emitting Tunneling Transistors with Enhanced Brightness at Room Temperature," *Nano Letters,* vol. 15, no. 12, pp. 8223-8228, 2015/12/09 2015, doi: 10.1021/acs.nanolett.5b03740.

[79] A. Eftekhari, "Tungsten dichalcogenides (WS_2, WSe_2, and WTe_2): materials chemistry and applications," *Journal of Materials Chemistry A,* 10.1039/C7TA04268J vol. 5, no. 35, pp. 18299-18325, 2017, doi: 10.1039/C7TA04268J.

[80] Q. Cheng *et al.*, "WSe_2 2D p-type semiconductor-based electronic devices for information technology: Design, preparation, and applications," *InfoMat,* https://doi.org/10.1002/inf2.12093 vol. 2, no. 4, pp. 656-697, 2020/07/01 2020, doi: https://doi.org/10.1002/inf2.12093.

[81] D. M. Hausmann, E. Kim, J. Becker, and R. G. Gordon, "Atomic Layer Deposition of Hafnium and Zirconium Oxides Using Metal Amide Precursors," *Chemistry of Materials,* vol. 14, no. 10, pp. 4350-4358, 2002/10/01 2002, doi: 10.1021/cm020357x.

[82] D. M. Hausmann and R. G. Gordon, "Surface morphology and crystallinity control in the atomic layer deposition (ALD) of hafnium and zirconium oxide thin films," *Journal of Crystal Growth,* vol. 249, no. 1, pp. 251-261, 2003/02/01/ 2003, doi: https://doi.org/10.1016/S0022-0248(02)02133-4.

[83] D. B. Farmer and R. G. Gordon, "Atomic Layer Deposition on Suspended Single-Walled Carbon Nanotubes via Gas-Phase Noncovalent Functionalization," *Nano Letters,* vol. 6, no. 4, pp. 699-703, 2006/04/01 2006, doi: 10.1021/nl052453d.

[84] H. Liu, K. Xu, X. Zhang, and P. D. Ye, "The integration of high-k dielectric on two-dimensional crystals by atomic layer deposition," *Applied Physics Letters,* vol. 100, no. 15, p. 152115, 2012/04/09 2012, doi: 10.1063/1.3703595.

[85] J. H. Park *et al.*, "Atomic Layer Deposition of Al_2O_3 on WSe_2 Functionalized by Titanyl Phthalocyanine," *ACS Nano,* vol. 10, no. 7, pp. 6888-6896, 2016/07/26 2016, doi: 10.1021/acsnano.6b02648.

[86] W. J. Woo *et al.*, "Bi-layer high-k dielectrics of Al_2O_3/ZrO_2 to reduce damage to MoS_2 channel layers during atomic layer deposition," *2D Materials,* vol. 6, no. 1, p. 015019, 2018/11/22 2018, doi: 10.1088/2053-1583/aaef1e.

[87] W. Li *et al.*, "Uniform and ultrathin high-κ gate dielectrics for two-dimensional electronic devices," *Nature Electronics,* vol. 2, no. 12, pp. 563-571, 2019/12/01 2019, doi: 10.1038/s41928-019-0334-y.

[88] K. M. Price, K. E. Schauble, F. A. McGuire, D. B. Farmer, and A. D. Franklin, "Uniform Growth of Sub-5-Nanometer High-κ Dielectrics on MoS_2 Using Plasma-Enhanced Atomic Layer Deposition," *ACS Applied Materials & Interfaces,* vol. 9, no. 27, pp. 23072-23080, 2017/07/12 2017, doi: 10.1021/acsami.7b00538.

[89] K. M. Price, S. Najmaei, C. E. Ekuma, R. A. Burke, M. Dubey, and A. D. Franklin, "Plasma-Enhanced Atomic Layer Deposition of HfO_2 on Monolayer, Bilayer, and Trilayer MoS_2 for the Integration of High-κ Dielectrics in Two-Dimensional Devices," *ACS Applied Nano Materials,* vol. 2, no. 7, pp. 4085-4094, 2019/07/26 2019, doi: 10.1021/acsanm.9b00505.

[90] J. Yang *et al.*, "Improved Growth Behavior of Atomic-Layer-Deposited High-k Dielectrics on Multilayer MoS_2 by Oxygen Plasma Pretreatment," *ACS Applied Materials & Interfaces,* vol. 5, no. 11, pp. 4739-4744, 2013/06/12 2013, doi: 10.1021/am303261c.

[91] W. Yang *et al.*, "The Integration of Sub-10 nm Gate Oxide on MoS_2 with Ultra Low Leakage and Enhanced Mobility," *Scientific Reports,* vol. 5, no. 1, p. 11921, 2015/07/06 2015, doi: 10.1038/srep11921.

[92] C. L. Hinkle *et al.*, "GaAs interfacial self-cleaning by atomic layer deposition," *Applied Physics Letters,* vol. 92, no. 7, p. 071901, 2008/02/18 2008, doi: 10.1063/1.2883956.

[93] "2D Semiconductors." https://www.2dsemiconductors.com (accessed.

[94] "SPI Supplies." https://www.2spi.com/ (accessed.

[95] M. G. Sales, S. T. Jaszewski, S. S. Fields, P. M. Litwin, J. F. Ihlefeld, and S. J. McDonnell, "Thermal stability of hafnium zirconium oxide on transition metal dichalcogenides," *Applied Surface Science,* vol. 546, p. 149058, 2021/04/30/ 2021, doi: https://doi.org/10.1016/j.apsusc.2021.149058.

[96] "UVOCS Inc. - Ultraviolet (UV) Ozone cleaning systems." http://www.uvocs.com (accessed.

[97] "Kolibrik.net, s.r.o. - Custom develompent of electronics and software." http://www.kolibrik.net/ (accessed.

[98] D. Nečas and P. Klapetek. "Gwyddion – Free SPM (AFM, SNOM/NSOM, STM, MFM, …) data analysis software." http://gwyddion.net (accessed.

[99] J. Liang *et al.*, "Impact of Post-Lithography Polymer Residue on the Electrical Characteristics of MoS_2 and WSe_2 Field Effect Transistors," *Advanced Materials Interfaces,* vol. 6, no. 3, p. 1801321, 2019.

[100] A. G. Shard, "Detection limits in XPS for more than 6000 binary systems using Al and Mg Kα X-rays," *Surface and Interface Analysis,* https://doi.org/10.1002/sia.5406 vol. 46, no. 3, pp. 175-185, 2014/03/01 2014, doi: https://doi.org/10.1002/sia.5406.

[101] M. Shenasa, S. Sainkar, and D. Lichtman, "XPS study of some selected selenium compounds," *Journal of Electron Spectroscopy and Related Phenomena,* vol. 40, no. 4, pp. 329-337, 1986/01/01/ 1986, doi: https://doi.org/10.1016/0368-2048(86)80043-3.

[102] A. J. Green *et al.*, "Surface oxidation of the topological insulator Bi_2Se_3," *Journal of Vacuum Science & Technology A,* vol. 34, no. 6, p. 061403, 2016/11/01 2016, doi: 10.1116/1.4964637.

[103] A. N. Hoffman *et al.*, "Tuning the electrical properties of WSe_2 via O_2 plasma oxidation: towards lateral homojunctions," *2D Materials,* vol. 6, no. 4, p. 045024, 2019/07/24 2019, doi: 10.1088/2053-1583/ab2fa7.

[104] M. Yamamoto *et al.*, "Self-Limiting Layer-by-Layer Oxidation of Atomically Thin WSe_2," *Nano Letters,* vol. 15, no. 3, pp. 2067-2073, 2015/03/11 2015, doi: 10.1021/nl5049753.

[105] R. Addou *et al.*, "One dimensional metallic edges in atomically thin WSe_2 induced by air exposure," *2D Materials,* vol. 5, no. 2, p. 025017, 2018/03/09 2018, doi: 10.1088/2053-1583/aab0cd.

[106] Y. C. Lin *et al.*, "Modification of the Electronic Transport in Atomically Thin WSe_2 by Oxidation," *Advanced Materials Interfaces,* vol. 7, no. 18, p. 2000422, 2020.

[107] A. Nipane *et al.*, "Damage-Free Atomic Layer Etch of WSe_2: A Platform for Fabricating Clean Two-Dimensional Devices," *ACS Applied Materials & Interfaces,* vol. 13, no. 1, pp. 1930-1942, 2021/01/13 2021, doi: 10.1021/acsami.0c18390.

[108] H. Zhu, X. Qin, L. Cheng, A. Azcatl, J. Kim, and R. M. Wallace, "Remote Plasma Oxidation and Atomic Layer Etching of MoS_2," *ACS Applied Materials & Interfaces,* vol. 8, no. 29, pp. 19119-19126, 2016/07/27 2016, doi: 10.1021/acsami.6b04719.

[109] Z. Li *et al.*, "Layer Control of WSe_2 via Selective Surface Layer Oxidation," *ACS Nano,* vol. 10, no. 7, pp. 6836-6842, 2016/07/26 2016, doi: 10.1021/acsnano.6b02488.

[110] G. N. Derry, "Chapter 5 - SURFACE SEGREGATION IN BINARY METAL ALLOYS," in *Handbook of Surfaces and Interfaces of Materials*, H. S. Nalwa Ed. Burlington: Academic Press, 2001, pp. 329-382.

[111] S. S. Jo *et al.*, "Growth Kinetics and Atomistic Mechanisms of Native Oxidation of ZrS_xSe_{2-x} and MoS_2 Crystals," *Nano Letters,* vol. 20, no. 12, pp. 8592-8599, 2020/12/09 2020, doi: 10.1021/acs.nanolett.0c03263.

[112] S. Kim *et al.*, "Metal-oxide based, CMOS-compatible ECRAM for Deep Learning Accelerator," in *2019 IEEE International Electron Devices Meeting (IEDM)*, 7-11 Dec. 2019 2019, pp. 35.7.1-35.7.4, doi: 10.1109/IEDM19573.2019.8993463.

[113] M. Onen, N. Emond, J. Li, B. Yildiz, and J. A. del Alamo, "CMOS-Compatible Protonic Programmable Resistor Based on Phosphosilicate Glass Electrolyte for Analog Deep Learning," *Nano Letters,* vol. 21, no. 14, pp. 6111-6116, 2021/07/28 2021, doi: 10.1021/acs.nanolett.1c01614.

[114] A. Borah, A. Nipane, M. S. Choi, J. Hone, and J. T. Teherani, "Low-Resistance p-Type Ohmic Contacts to Ultrathin WSe_2 by Using a Monolayer Dopant," *ACS Applied Electronic Materials,* vol. 3, no. 7, pp. 2941-2947, 2021/07/27 2021, doi: 10.1021/acsaelm.1c00225.

[115] D. Lee, Y. Choi, J. Kim, and J. Kim, "Recessed-Channel WSe_2 Field-Effect Transistor via Self-Terminated Doping and Layer-by-Layer Etching," *ACS Nano,* vol. 16, no. 5, pp. 8484-8492, 2022/05/24 2022, doi: 10.1021/acsnano.2c03402.

[116] M. S. Choi *et al.*, "High carrier mobility in graphene doped using a monolayer of tungsten oxyselenide," *Nature Electronics,* vol. 4, no. 10, pp. 731-739, 2021/10/01 2021, doi: 10.1038/s41928-021-00657-y.

[117] S. Yang, G. Lee, and J. Kim, "Selective p-Doping of 2D WSe_2 via UV/Ozone Treatments and Its Application in Field-Effect Transistors," *ACS Applied Materials & Interfaces,* vol. 13, no. 1, pp. 955-961, 2021/01/13 2021, doi: 10.1021/acsami.0c19712.

[118] C. J. McClellan, E. Yalon, K. K. H. Smithe, S. V. Suryavanshi, and E. Pop, "High Current Density in Monolayer MoS_2 Doped by AlO_x," *ACS Nano,* vol. 15, no. 1, pp. 1587-1596, 2021/01/26 2021, doi: 10.1021/acsnano.0c09078.

[119] J. Wang *et al.*, "Integration of High-k Oxide on MoS_2 by Using Ozone Pretreatment for High-Performance MoS_2 Top-Gated Transistor with Thickness-Dependent Carrier Scattering Investigation," *Small,* https://doi.org/10.1002/smll.201501260 vol. 11, no. 44, pp. 5932-5938, 2015/11/01 2015, doi: https://doi.org/10.1002/smll.201501260.

[120] P. Zhao *et al.*, "Effects of annealing on top-gated MoS_2 transistors with HfO_2 dielectric," *Journal of Vacuum Science & Technology B,* vol. 35, no. 1, p. 01A118, 2017/01/01 2017, doi: 10.1116/1.4974220.

6 Conclusions, Implications, and Future Work

6.1 Conclusions and Implications of This Work

6.1.1 Overall Goal and Motivation: Spectroscopic Studies of TMDC Crystals

The general goal of this dissertation is to study the interfaces formed through direct deposition methods for the fabrication of 2D semiconductor/oxide stacks for field-effect transistors (FETs), particularly FET devices with applications in memory and data storage. To assess the feasibility of using these material systems and processes in real-world devices, we investigated direct integration techniques that are scalable to wafer processing.

Our work presented in Chapter 3 motivates the need for direct growth methods for 2D transition metal dichalcogenides (TMDCs). We performed spectroscopic studies that showed the presence of large clusters of bismuth impurities in geological MoS_2. We showed that random spots across the MoS_2 surface can contain bismuth with measured concentrations ranging from 0.1 to 4%. Laterally, these bismuth clusters were in the order of tens of microns in approximate diameter. Through chemical analysis, we concluded that they exist as bismuth oxide or bismuth sulfate compounds in the MoS_2 crystal. While bismuth and other impurity elements have been known to exist in geological MoS_2, our published report stemming from this chapter is the first in literature to show their presence in large micron-scale clusters. This finding has important implications in electronic devices where micrometer-sized contacts are used on geological MoS_2 flakes, as the unintended presence of a bismuth impurity in the MoS_2 channel can potentially dominate the measured device properties. This chapter demonstrates the difficulty of obtaining large areas of geological MoS_2 without chemical variation, shedding light on the importance of developing controlled synthesis methods for high-purity TMDCs with uniform properties.

6.1.2 TMDC-on-Dielectric by Molecular Beam Epitaxy

In Chapter 4, we present our work using one such growth technique, molecular beam epitaxy (MBE), to deposit semiconducting TMDCs directly onto various dielectric and

ferroelectric oxides. For the work in this chapter, we focused on another prototypical semiconducting TMDC material, WSe_2, for which we had previously established a growth process in our MBE system. In Chapter 4.1, we demonstrated that we can successfully and repeatably deposit large-area, chemically homogeneous WSe_2 films on hafnium zirconium oxide (HZO) substrates. We show this for both 58:42 Hf:Zr and 36:64 Hf:Zr compositions of HZO. We also studied the impact of the MBE growth conditions on the structure, chemistry, and electrical properties of HZO. The high substrate temperature (500 °C) required during WSe_2 growth resulted in in-situ crystallization of the amorphous as-loaded HZO substrates into a mixed phase assemblage of the monoclinic, tetragonal, and orthorhombic phases. Due to the presence of the orthorhombic phase responsible for ferroelectricity, we measured a ferroelectric response in our HZO substrates post-MBE processing. We also observed that the MBE growth process resulted in Se incorporation into the HZO, as Se atoms filled oxygen vacancy sites in the HZO lattice. The amount of incorporated Se was affected by both the Hf:Zr content of the HZO film and its crystallinity prior to MBE processing; these two factors were important because they dictated the oxygen vacancy concentration and Se diffusivity in the HZO film, respectively. We found that the presence of Se in the HZO films did not have detrimental effects on its remanent polarization or leakage current. Overall, the work presented in Chapter 4.1 successfully validated the feasibility of using our MBE WSe_2 process on device-relevant stacks, without compromising the device properties. This work was our first demonstration of direct MBE deposition to fabricate TMDC-on-dielectric structures for use in an FET device.

Chapter 4.2 discussed further investigations of the opportunities and challenges with this MBE WSe_2 process on HZO and other dielectric oxides. In this chapter, we showed the temperature dependence of Se incorporation in HZO, and we found that lower MBE substrate temperatures inhibit the incorporation or chemisorption of Se into HZO. We performed depth profiling studies and determined that the incorporated Se atoms are found near the top surface of the HZO, and they are not stable in ambient conditions. We note that a WSe_2 film deposited on top of the HZO through MBE likely acts as a protection barrier for the underlying Se-incorporated HZO, which means that when actual TMDC growth is performed, we expect the incorporated Se to be more robust with air exposure. The latter part of Chapter 4.2 discussed studies of state-of-the-art linear dielectrics, SiO_2 and HfO_2, as substrates for MBE WSe_2. The studies on SiO_2 and HfO_2 were performed at 400 °C to maintain back-end-of-the-line (BEOL) compatibility of the

MBE process. We showed that the MBE growth conditions at 400 °C did not have a significant effect on the chemistry of SiO_2 and HfO_2. Further, we note that the 400 °C MBE process does not induce crystallization of our dielectric substrates. Leakage through a dielectric layer is known to occur along grain boundaries, so the absence of large grains in our dielectric substrate potentially eliminates this leakage contribution in a real device. Lastly, we showed that at this 400 °C substrate temperature, we can successfully deposit chemically homogeneous WSe_2 on both SiO_2 and HfO_2. The results from our studies on these linear dielectric substrates point towards the potential of this MBE process as a BEOL-compatible 2D channel growth technique that can be integrated into wafer-scale device fabrication.

6.1.3 Dielectric-on-TMDC by Atomic Layer Deposition

In our last experimental chapter, we flip the TMDC/dielectric stack and instead explore dielectric-on-TMDC interfaces formed by atomic layer deposition (ALD) of dielectric oxides directly onto 2D TMDCs. The dielectric-on-TMDC structure is of relevance for top-gated TMDC-based FETs as well as other device designs utilizing a dielectric layer to encapsulate a TMDC channel for environmental protection.

In the first part of this chapter, Chapter 5.1, we deposit HZO thin films directly onto MoS_2 and WSe_2 and examine the thermal stability of the interfaces formed. This is important for ferroelectric FET (FeFET) applications because HZO films typically require an annealing step post-deposition in order to induce the ferroelectric orthorhombic phase. Our studies of the interface between HZO and MoS_2/WSe_2 as a function of temperature (400-800 °C) have implications for device fabrication processes requiring HZO deposition on top of a TMDC channel, where exposure of the HZO/TMDC interface to these elevated temperatures necessary for HZO crystallization would be inevitable. Through our results in Chapter 5.1, we report on the importance of surface functionalization of geological MoS_2 for improved thermal stability of an ALD oxide film directly deposited on top. We demonstrated that HZO on ultraviolet-ozone (UV-O_3) functionalized MoS_2 was stable at all temperatures investigated, but HZO on an untreated MoS_2 surface resulted in desorption of HZO starting at 400 °C. We also examined the thermal stability of HZO deposited on our MBE-grown WSe_2 material, and we report that our HZO/WSe_2 interface has a thermal budget of 700 °C; above this temperature, we observe evidence of some Se being driven off of the

WSe_2, forming a sub-stoichiometric WSe_{2-x} component in the film. In this work, we also demonstrate the annealing parameters necessary for nucleation and growth of grains in HZO that is crystallized in an ultra-high vacuum (UHV) environment. We showed that 400-600 °C anneals for 40 min each only resulted in short-range atomic order suggested by X-ray photoelectron spectroscopy (XPS) measurements, but doubling the annealing time (80 min) at 600 °C resulted in large grains that can be measured with X-ray diffraction (XRD), and includes a phase fraction of the orthorhombic phase responsible for ferroelectricity. Our work in Chapter 5.1 successfully demonstrates that functional crystalline ferroelectric films can be directly integrated onto TMDC channels for FeFET applications.

The second part of the chapter, Chapter 5.2, has implications not limited to FeFETs, but has more general applications to most FET device architectures. In this work, we investigate direct ALD of dielectric HfO_2 onto UV-O_3 exposed WSe_2. Direct ALD onto van der Waals surfaces, such as TMDCs, are known to be a challenge without the use of surface functionalization methods or buffer layers that help promote ALD film nucleation. Without these techniques, ALD on 2D materials results in extremely rough and discontinuous oxide films without full coverage of the underlying 2D material. In Chapter 5.2, we demonstrate the use of atmospheric UV-O_3 exposure to functionalize the WSe_2 surface for oxide ALD. We show two distinct resulting WSe_2 surfaces based on UV-O_3 exposure time; low exposures resulted in an onset of WSe_2 doping, and high exposures resulted in a tungsten oxyselenide top layer due to surface oxidation, as well as more dramatic p-doping of the underlying WSe_2. The tungsten oxyselenide layer for high exposure WSe_2 saturates at a thickness of ~1 nm, is amorphous, is stable in atmosphere, but is unstable and exhibits thinning when exposed to the 200 °C deposition temperature during HfO_2 ALD. Despite differences in their surface chemistry, we show through multi-scale characterization of directly deposited HfO_2 films that both low and high exposure WSe_2 provide an optimal surface for ALD that results in a smooth and uniform large-area HfO_2 film. Because of this improved film uniformity at scaled thicknesses, lower gate leakage is demonstrated by these HfO_2 gate oxides deposited on UV-O_3 exposed WSe_2. Furthermore, our low vs. high exposure conditions provide unique flexibility in interfacial design in devices, as low exposure results in an abrupt HfO_2/WSe_2 interface, while high exposure results in an interfacial tungsten oxide layer between HfO_2 and WSe_2, i.e., $HfO_2/WO_3/WSe_2$. We demonstrate that our low and high UV-O_3 exposures of WSe_2

can provide pathways for the realization of different interfaces needed for a range of electronic and memory devices.

6.2 Future Work

6.2.1 Material – Device Gap

A general area for future work involves closing the gap between materials characterization and device performance. In between the deposition techniques for fabricating our oxide/semiconductor layers and actual electrical testing, there are a multitude of processing steps that our fabricated TMDC-on-dielectric or dielectric-on-TMDC stacks have to undergo for effective measurement of their performance in a device. For instance, typical metal contact deposition performed by our collaborators at the Army Research Laboratory (ARL) is a multi-step process that involves spin-coating of poly(methyl methacrylate) or PMMA, mild annealing, electron beam lithography for patterning, soaking in developer solutions, and PMMA liftoff in solvents, among others. All of these intermediate steps could introduce variables that result in discrepancies between the expected electrical result based on measured material properties, and the actual measurement from a fabricated device. The impact of each of these lithography process steps on our deposited TMDC or oxide can be investigated through various surface and interface characterization techniques.

6.2.1.1 TMDC-on-Dielectric Stack

Furthermore, tweaking and optimization of the deposition conditions should be performed based on measured electrical properties from a device. For Chapter 4.1, devices fabricated from MBE-WSe_2/HZO showed high leakage, potentially due to oxygen vacancies in the HZO layer. Ways to circumvent this, such as annealing the HZO substrate under a Se flux prior to WSe_2 growth, should be explored. Knowing that incorporated Se passivates oxygen vacancies in HZO, this pre-growth Se flux anneal would potentially minimize oxygen vacancy-mediated leakage and improve device characteristics.

In Chapter 4.2, we demonstrated successful BEOL-compatible WSe_2 growth on common linear dielectric oxides, SiO_2 and HfO_2. However, our BEOL-compatible WSe_2 material has yet to be tested as a channel in an FET. This directly grown channel should be benchmarked against our "best" WSe_2 material, which is grown on an ideal single-crystal growth substrate, and then transferred onto an FET device for electrical testing.

6.2.1.2 Dielectric-on-TMDC Stack

For the devices fabricated in Chapter 5.2, poor switching behavior was demonstrated by top-gated WSe_2 FETs that underwent UV-O_3 exposure, suggesting a potential tradeoff between improving ALD nucleation and maintaining good semiconducting behavior. Strategies that have been used for improving the characteristics of top-gated UV-O_3 functionalized MoS_2 FETs can be adapted to our UV-O_3 WSe_2 devices. Examples of such strategies include in-situ UV-O_3 functionalization rather than UV-O_3 exposure in atmosphere, use of few-layer TMDC channels rather than bulk thicknesses, and post-annealing of the devices for improved interface quality.

Another avenue for improving these UV-O_3 exposed WSe_2 FETs is to explore the effect of UV-O_3 exposure on the existing device structure (i.e., back-gated) that the WSe_2 channel is on. Specifically, interface chemistry studies could be performed to examine how the drain/source contacts interfaced with the WSe_2 are affected by the UV-O_3 functionalization step.

6.2.1.3 Direct Measurement of Band Alignments

All of the processes described and used in this dissertation result in varied interfacial qualities between our semiconducting TMDC and dielectric oxide. These processes may induce different kinds of interfacial defects, slightly different oxygen:metal ratios in the dielectric oxide, or varied WSe_2 grain size and roughness, among others. These variables would result in changes in the band alignment at these oxide/semiconductor interfaces, which would then have consequences on FET performance. Band alignments of fabricated interfacial stacks can be experimentally measured spectroscopically, and this would allow determination of the valence and conduction band offsets of these interfaces, which dictate leakage and translate to device performance. Band alignments measured as a function of different growth/processing conditions

would potentially provide a direct explanation for the measured electrical properties of fabricated FET devices.

6.2.2 Dielectric-on-TMDC-on-Dielectric Multi-Step Integration

The work presented in this dissertation discussed various integration techniques for TMDC-on-dielectric and dielectric-on-TMDC structures. While the studies for these two stacking configurations were performed exclusively, providing proofs of concept for our oxide/semiconductor deposition and processing methods, this does not mimic real-world device fabrication, in which fabrication steps are highly interdependent and required to be compatible with each other. A logical step moving forward is to combine our most important findings from the processes we studied in Chapters 4 and 5. For instance, the atmospheric UV-O_3 exposure technique can be used on our MBE WSe_2 material to investigate if it results in the same marked improvement in the quality of ALD oxide films directly deposited on top, as observed with commercial single-crystal WSe_2.

Appendix A Surface Coverage Analysis and Correlation with XPS Intensities

We now analyze the surface coverage of the remaining HfO_2 clusters on untreated MoS_2 seen with AFM and correlate it with the Hf 4*f* peak intensity from XPS. The integrated intensity of the Hf 4*f* peak from a HfO_2 overlayer, as in our case, is given by Eq. 1 [1]:

$$I_{HfO_2,film} = I^{\infty}_{HfO_2}[1 - \exp\left(-\frac{d}{\ell cos\theta}\right)] \qquad (1)$$

In this equation, $I^{\infty}_{HfO_2}$ is the intensity of Hf 4*f* from bulk HfO_2, d is the thickness of the HfO_2 overlayer, ℓ is the effective attenuation length (EAL) of a Hf $4f_{7/2}$ photoelectron traveling through the overlayer, for which we use 2.6 nm [2], and θ is the photoelectron take-off angle with respect to the surface normal, which is 45° for the geometry of our XPS system. Eq. 1 assumes a uniform coverage of HfO_2. For incomplete HfO_2 coverage, as seen with the untreated MoS_2 surface post-anneal (Chapter 5.1), the right-hand side of Eq. 1 is multiplied by the fraction of the surface covered by the clusters, x. Taking the ratio of the equation for clusters, $I_{HfO_2,clusters}$, and the equation for a complete layer, $I_{HfO_2,film}$, gives the surface coverage estimated with XPS (Eq. 3).

$$\frac{I_{HfO_2,clusters}}{I_{HfO_2,film}} = \frac{x\{I^{\infty}_{HfO_2}[1-\exp\left(-\frac{d_{clusters}}{\ell cos\theta}\right)]\}}{I^{\infty}_{HfO_2}[1-\exp\left(-\frac{d_{film}}{\ell cos\theta}\right)]} \qquad (2)$$

$$x = \frac{I_{HfO_2,clusters}}{I_{HfO_2,film}} \frac{[1-\exp\left(-\frac{d_{film}}{\ell cos\theta}\right)]}{[1-\exp\left(-\frac{d_{clusters}}{\ell cos\theta}\right)]} \qquad (3)$$

The Hf 4*f* XPS intensities were obtained by fitting the pertinent Hf 4*f* spectra with Voigt lineshapes using kolXPD software. $I_{HfO_2,clusters}$ was the Hf 4*f* intensity of the remaining HfO_2 clusters on untreated MoS_2 after annealing, and $I_{HfO_2,film}$ was taken from a separate thicker as-deposited film that fully covered the MoS_2 substrate. The thickness of the film, d_{film}, was estimated as 5 nm based on the growth rate per cycle of the ALD recipe. The thickness of the clusters was obtained from the average peak heights in the line profile.

Using Eq. 3, we calculate an expected surface coverage of 7% based on the HfO_2 XPS signal. We obtained an actual surface coverage of approximately 27% by analysis of the AFM micrograph using Gwyddion software. The discrepancy between our calculated value using XPS and our actual value from AFM can be due to several reasons: 1) In the XPS intensity equations,

the EAL is assumed to be a known value, but the EAL that was used from the NIST database [2] is actually a result of modeling the experimental XPS setup. 2) The equation for $I_{HfO_2,clusters}$ assumes a uniform cluster thickness, which we know from the AFM line profiles is not true. Clusters thinner than the average cluster thickness may significantly be affecting the calculation due to the exponential dependence of the intensity on the thickness, resulting in a vastly reduced calculated surface coverage, x. 3) AFM was performed ex-situ after several hours of atmospheric exposure of the samples. This could result in adventitious contaminants adsorbed on the surface which are seen with AFM, but not accounted for in our in-situ XPS measurements.

Appendix B Atmospheric Stability WSe_2 Grown on HOPG by MBE

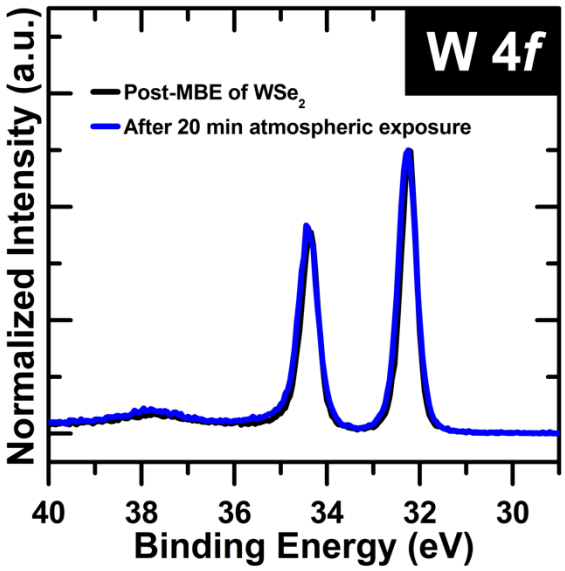

Figure B.1. W 4f spectra of MBE-grown WSe_2 before and after 20 minutes of atmospheric exposure. It is shown that a brief exposure to atmosphere does not cause significant oxidation of the WSe_2 film.

Appendix C Details of Spectral Deconvolution in Chapter 5.2

*Table C.1. Binding energy positions of fitted peaks in W 4f and Se 3d spectra of WSe_2 samples **after UV-O_3 exposure**.*

	W $4f_{7/2}$ / Se $3d_{5/2}$				W $4f_{7/2}$	Se $3d_{5/2}$
	WSe_2 (1)	WSe_2 (2)	WSe_2 (3)	WSe_2 (4)	W-O	Se-O
As-exfoliated		32.97 eV / 55.22 eV				
10 min UV-O_3	33.27 eV / 55.56 eV	32.88 eV / 55.18 eV				
13 min UV-O_3	33.25 eV / 55.54 eV	32.86 eV / 55.14 eV				
17 min UV-O_3			32.27 eV / 54.51 eV	31.86 eV / 54.10 eV	35.70 eV	58.95 eV
20 min UV-O_3			32.28 eV / 54.54 eV	31.85 eV / 54.08 eV	35.71 eV	58.98 eV

*Table C.2. Binding energy positions of fitted peaks in W 4f and Se 3d spectra of WSe_2 samples **after HfO_2 ALD**.*

	W $4f_{7/2}$ / Se $3d_{5/2}$				W $4f_{7/2}$	Se $3d_{5/2}$
	WSe_2 (1)	WSe_2 (2)	WSe_2 (3)	WSe_2 (4)	W-O	Se-O
0 min UV-O_3		32.94 eV / 55.20 eV				
10 min UV-O_3		33.04 eV / 55.31 eV				
17 min UV-O_3		32.87 eV / 55.15 eV	32.45 eV / 54.74 eV		36.05 eV	
30 min UV-O_3		32.89 eV / 55.17 eV	32.47 eV / 54.73 eV		36.12 eV	

In all of the figures where we show deconvoluted spectra in Chapter 5.2, the backgrounds of the spectra were also fit, but were subtracted in the plots for clarity. All of our spectra were fit with Shirley backgrounds, with the exception of the SeO_2 component.

Because of a loss feature from the W 4*f* that overlaps with the Se 3*d* region, specifically in the region between the Se-W and Se-O components, a Shirley background cannot fit the entire spectrum from 52 to 62 eV binding energy. In order to properly capture the background, the features from 52 to 57 eV (WSe_2 components) were fit with a Shirley background, and the features from 57 to 62 eV (SeO_2 component) were fit with a linear background, as shown in Figure C.1.

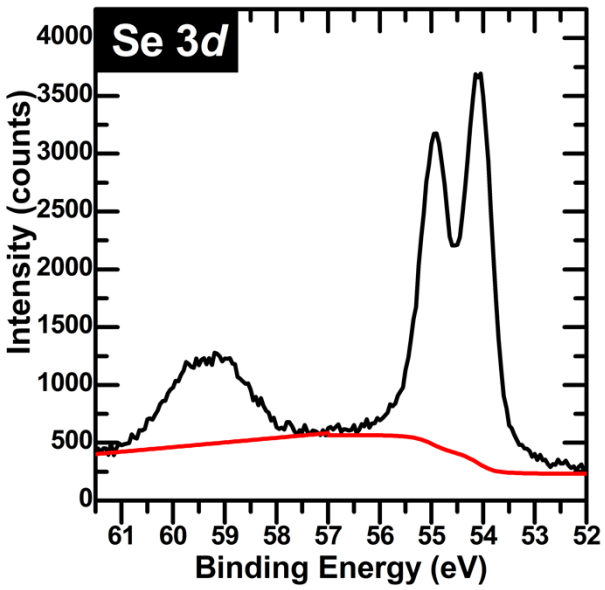

Figure C.1. High UV-O_3 exposure Se 3d spectrum from Chapter 5.2.4.1. Shown in black is the raw data, and in red is the background that was subtracted in the figure showing the fitted spectrum.

Appendix D WO_3-SeO_2 Compound Overlayer Thickness Calculation

We find with XPS that UV-O_3 exposures result in the formation of both WO_3 and SeO_2 on the WSe_2 surface. We assume these oxide components to be homogeneously mixed within the same layer rather than being stacked on top of each other. Overlayer thickness calculations using XPS results are typically performed using the ratio of the overlayer intensity (i.e., SiO_2) to the substrate intensity (i.e., Si) taken from the same core level spectrum [1, 3]. This overlayer to substrate intensity ratio is proportional to the overlayer thickness. In our case with the assumption of a compound oxide overlayer (WO_3-SeO_2), we have to account for the fact that our WSe_2 signal, in both the W 4*f* and Se 3*d* regions, are attenuated by both WO_3 and SeO_2, whose signals come from two different core level spectra. To calculate our compound overlayer thickness, we use two separate equations for the overlayer/substrate intensity ratios – one for WO_3 on WSe_2, and one for SeO_2 on WSe_2, as shown in Eq. 4 and 5, respectively. In these equations, we have an "effective" WO_3 thickness, d_{WO_3}, and an "effective" SeO_2 thickness, d_{SeO_2}. We take our compound oxide overlayer thickness to be the sum of these two effective thicknesses.

$$\frac{I_{WO_3}}{I_{WSe_2}} = \frac{I^{\infty}_{WO_3}}{I^{\infty}_{WSe_2}} \left[\frac{1-\exp\left(\frac{-d_{WO_3}}{(\ell_{W\,4f\,in\,WO_3})(cos\theta)}\right)}{\exp\left(\frac{-d_{WO_3}}{(\ell_{W\,4f\,in\,WO_3})(cos\theta)}+\frac{-d_{SeO_2}}{(\ell_{W\,4f\,in\,SeO_2})(cos\theta)}\right)}\right] \qquad (4)$$

$$\frac{I_{SeO_2}}{I_{WSe_2}} = \frac{I^{\infty}_{SeO_2}}{I^{\infty}_{WSe_2}} \left[\frac{1-\exp\left(\frac{-d_{SeO_2}}{(\ell_{Se\,3d\,in\,SeO_2})(cos\theta)}\right)}{\exp\left(\frac{-d_{WO_3}}{(\ell_{Se\,3d\,in\,WO_3})(cos\theta)}+\frac{-d_{SeO_2}}{(\ell_{Se\,3d\,in\,SeO_2})(cos\theta)}\right)}\right] \qquad (5)$$

Here, I_x represents the measured XPS intensity of specie x, $\ell_{W\,4f/Se\,3d\,in\,x}$ is the effective attenuation length (EAL) of the specified core level photoelectrons traveling through an overlayer of specie x, and θ is the photoelectron take-off angle with respect to the surface normal, which is 45° in the XPS system we used.

The EALs that we used in our calculations were obtained from the NIST EAL database [2, 4]. Given our 45° take-off angle, the EALs used were 23.388 Å for $\ell_{W\,4f\,in\,WO_3}$, 31.178 Å for

$\ell_{W\ 4f\ in\ SeO_2}$, 30.739 Å for $\ell_{Se\ 3d\ in\ SeO_2}$, and 23.073 Å for $\ell_{Se\ 3d\ in\ WO_3}$. One of the XPS measurements we discuss was performed at a photoelectron take-off angle of 60°, as noted in the appropriate figure caption. For these spectra, the EALs that we used in our thickness calculations were specific to a 60° take-off angle: 22.688 Å for $\ell_{W\ 4f\ in\ WO_3}$, 30.653 Å for $\ell_{W\ 4f\ in\ SeO_2}$, 30.212 Å for $\ell_{Se\ 3d\ in\ SeO_2}$, and 22.372 Å for $\ell_{Se\ 3d\ in\ WO_3}$.

The ratio $\frac{I^{\infty}_{overlayer}}{I^{\infty}_{substrate}}$, commonly referred to as R_o, is the intensity ratio of an "infinitely thick" pure overlayer to an "infinitely thick" pure substrate material, which can be experimentally measured if pure bulk samples of the materials of interest are available. For our calculations, we used a theoretical R_o value. Using the equation for R_o provided by Seah and Spencer [5], we calculated an R_o of 1.25 for Eq. 4 (WO_3 on WSe_2) and 1.92 for Eq. 5 (SeO_2 on WSe_2). It is known that, for the case of SiO_2 on Si, theoretical and experimental R_o values differ by more than 50%. However, we should note that such an error is systematic, and as such will impact the accuracy, but not the precision of our measurement.

To calculate the overlayer thickness, d, we use an iterative process. We start with an educated guess for d_{SeO_2} to use in Eq. 4, and an educated guess for d_{WO_3} to use in Eq. 5. Eq. 4 is used to solve for d_{WO_3}, and Eq. 5 is used to solve for d_{SeO_2}. The calculated separate effective thicknesses (d_{WO_3} and d_{SeO_2}) are then plugged into Eq. 5 and 4, respectively, and the procedure is repeated until the two equations have consistent effective thickness values.

Appendix E Supplementary Transmission Electron Microscopy (TEM) Results for Chapter 5.2

Low UV-O_3 Exposure of WSe_2

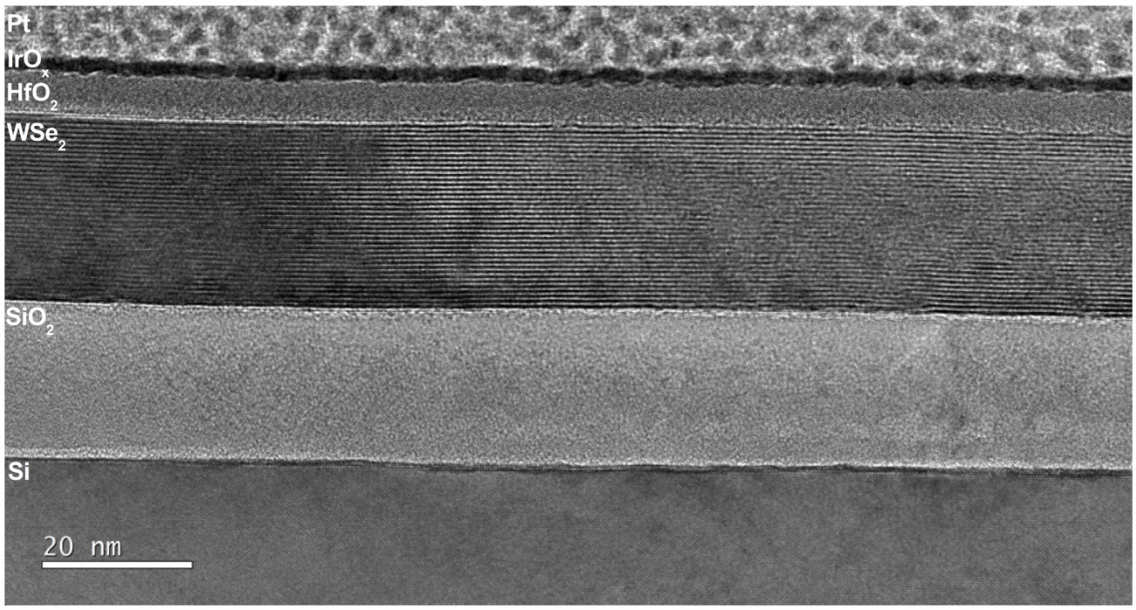

Figure E.1. Large field of view cross-sectional micrograph of ALD HfO_2 deposited on low exposure WSe_2 (10 min UV-O_3 functionalization). The HfO_2 film is shown to be smooth with a uniform thickness of 5.4 ± 0.5 nm across a large cross-sectional area.

High UV-O_3 Exposure of WSe_2

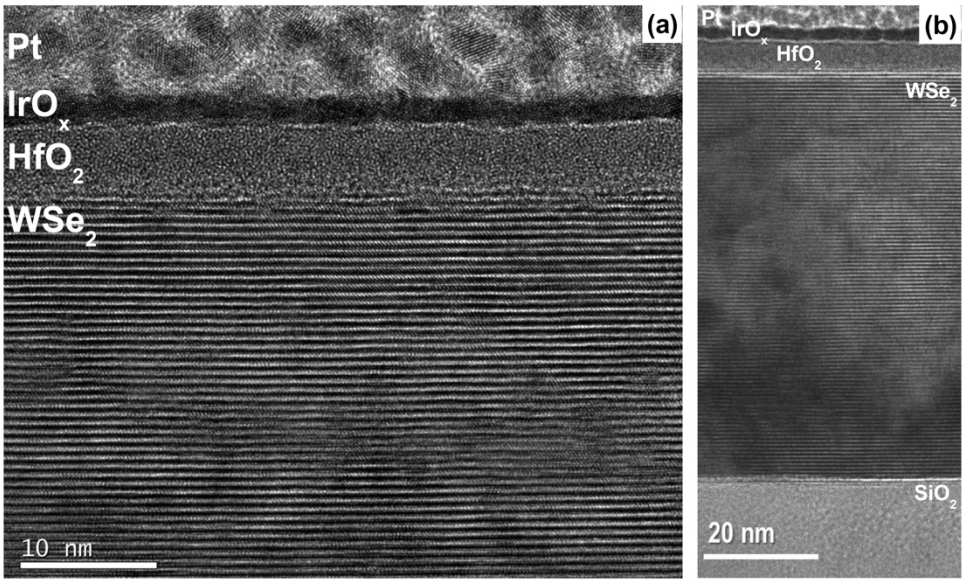

Figure E.2. Cross-sectional TEM of ALD HfO_2 on high exposure WSe_2 (30 min UV-O_3). The HfO_2 film is shown to be smooth with a uniform thickness of 5.4 ± 0.8 nm.

References for Appendices

[1] F. J. Himpsel, F. R. McFeely, A. Taleb-Ibrahimi, and J. A. Yarmoff, "Microscopic structure of the SiO_2/Si interface," *Physical Review B,* vol. 38, no. 9, pp. 6084-6096, 1988.

[2] A. Jablonski, "NIST Electron Effective-Attenuation-Length Database," 2011.

[3] Z. H. Lu *et al.*, "SiO2 film thickness metrology by x-ray photoelectron spectroscopy," *Applied Physics Letters,* vol. 71, no. 19, pp. 2764-2766, 1997/11/10 1997, doi: 10.1063/1.120438.

[4] A. Jablonski and C. J. Powell, "The electron attenuation length revisited," *Surface Science Reports,* vol. 47, no. 2, pp. 33-91, 2002/06/01/ 2002, doi: https://doi.org/10.1016/S0167-5729(02)00031-6.

[5] M. P. Seah and S. J. Spencer, "Ultrathin SiO2 on Si II. Issues in quantification of the oxide thickness," *Surface and Interface Analysis: An International Journal devoted to the development and application of techniques for the analysis of surfaces, interfaces and thin films,* vol. 33, no. 8, pp. 640-652, 2002.